Julius-Maximilians-Universität Würzburg

Graduate School of Science and Technology

Doctoral thesis / *Dissertation*

for the doctoral degree / *zur Erlangung des Doktorgrads*

Doctor rerum naturalium (Dr. rer. nat.)

Strong light-matter coupling with 2D materials

Starke Licht-Materie Kopplung mit 2D Materialien

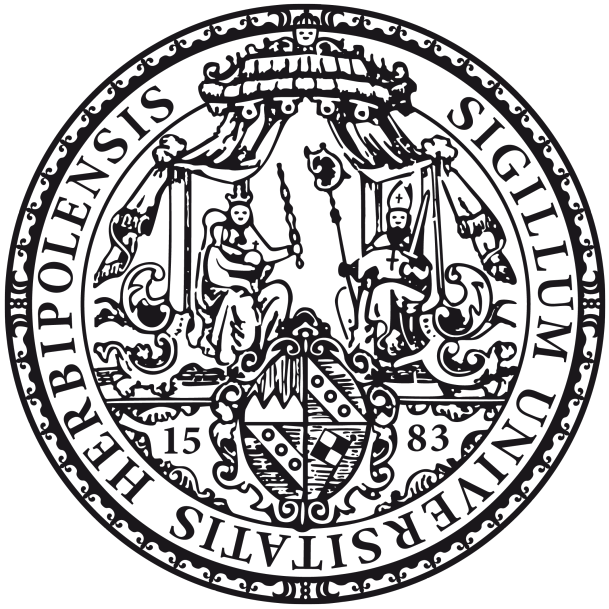

Submitted by / *Vorgelegt von*

Nils Lundt

from / aus

Burghausen

Würzburg, 2018

Submitted on / *Eingereicht am*: .....

Stamp / *Stempel* Graduate School

Members of thesis committee / *Mitglieder des Promotionskomitees*

Chairperson / *Vorsitz*:

1. Reviewer and Examiner / *1. Gutachter und Pürfer:* Dr. Christian Schneider

2. Reviewer and Examiner / *2. Gutachter und Pürfer:* Prof. Dr. Bert Hecht

3. Examiner / *3. Prüfer:* Prof. Dr. Tobias Brixner

Additional Examiners / *Weitere Prüfer*: .....

Day of thesis defense / *Tag des Promotionskolloquiums:* .....

Contents

Chapter 1

Introduction

In the year 2015, Elizabeth Gibney asked the crucial question "2D or not 2D" as the title of her latest review article [1]. This phrase refers to the possibility to stack atomically thin materials (often referred to as "2D" materials) on top of each other, which adds a third dimension ("not 2D"). According to this article, this could make up the true potential of 2D materials with respect to actual applications, giving a justification for the tremendously increasing scientific activities in this field. Thus, it is most certainly no coincidence that the title sounds like one of most cited phrases in modern English, namely "To be, or not be", the opening phrase of Shakespeares famous "Hamlet" [2]. The essence of this phrase is the justification of existence, which the author tries to draw for 2D materials in this article. However, at a time when the scientific community was still debating about very basic parameters of 2D materials such as the electronic band gap or the exciton binding energies, the raison d'être was anything else than clearly justified. Up to this day, high-quality, large-scale growth of 2D materials as well as competition with state-of-the-art bulk materials and devices remains a major challenge. Nevertheless, 2D materials, and in particular the sub-group of transition metal dichalcogenide (TMDC) monolayers, have attracted a lot of interest in the solid state physics community. The unique spin-valley physics and their very distinct excitonic resonances make these materials ideal candidates to observe new phenomena in transport and optics. Although not all details and relevant material parameters had been determined when this work was initiated, the state of knowledge indicated that these materials might be particularly interesting with respect to their light-matter interaction, because of the enormous oscillator strength.

Especially the effect of strong coupling between a light mode and an exciton resonance, also know as the formation of exciton-polaritons [3], moved in the focus of scientific interest. Exciton-polaritons are composite quasi-particles partly consisting of a light component and an excitonic "matter" component. The properties of polaritons are inherited from these two components. This leads to a very low effective mass ($m_{eff} = 10^{-5}$ m_0 with m_0 being the free electron mass [4], originating from the light component), while still

keeping the ability to interact with each other (originating form the exciton component). In addition, owing to their bosonic nature, exciton-polaritons condense in a new phase similar to a Bose-Einstein-condensate at high densities under appropriate conditions [5]. In fact, this happens even at room temperature in comparison to atomic systems, where BEC was firstly observed at temperatures of a few nano Kelvin [6]. Besides the fundamental interest in these new quasi-condensate phases, the emitted light from such phase is intriguing from a more practical perspective. It exhibits a highly monochromatic and coherent character similar to laser light [4]. However, in contrast to a laser, a polariton condensate does not require a band population inversion and exhibits therefore a threshold which is about two orders of magnitude lower [7]. According to calculations, a condensate of excitons-polaritons with TMDC monolayers can be formed even at room temperature due to the robust excitons [8]. Thus, combining polariton physics with the emerging field of 2D materials was the starting point of this work.

Additional motivation for this project is given by the unique and intriguing spin-valley physics of excitons and exciton-polaritons in TMDC monolayers. In the hexagonal crystal structure, neighboring lattice sites are occupied with different atomic species (transition metal vs. chalcogen atoms) and thus the inversion symmetry is broken. The crystal symmetry is transferred to the reciprocal space with degenerate direct band gap minima at the K points at the corners of the hexagonal Brillouin zone that are referred to as valleys. Because of the strong spin-orbit interaction and the broken inversion symmetry, both conduction and valence bands are spin-split and the splittings are inverted for opposite valleys (K and K' valley). As a result, spin and valley are locked to each other and can be selectively, optically addressed [9, 10]. This property opens up new ways to encode and process information with the spin-valley degree of freedom, a field that is often referred to as valleytronics [11]. This name is in close analogy to electronics and spintronics, where information is encoded in the charge or spin of a particle, respectively [12]. Since the origin of this property is specific to the material, strong coupling to a photon mode is not necessarily required to observe spin-valley phenomena. However, the short diffusion length of TMDC excitons, on the order of a few hundred nanometers [13, 14], might limit their use for practical applications [11]. The formation of exciton-polaritons could provide a very light effective mass and thus propagation lengths of at least one order of magnitude longer [15] in order to circumvent this limitation. Moreover, strong coupling changes the decay and scattering dynamics as compared to pure excitons [16], which could help to take full advantage of these exciting spin-valley properties.

With these introductory ideas in mind, this study evaluated which specific materials and cavity designs are most suitable to observe strong coupling between TMDC excitons and photonic modes. Based on this, TMDC monolayers were integrated into microcavities and the formation of exciton-polaritons was investigated. Here, the question whether these

quasi-particles can be observed even at room temperature was a main focus. Once the creation of exciton-polaritons was achieved, the spin-valley physics of TMDC monolayers in the strong coupling regime was studied. Finally, it was tested whether exciton-polaritons may form a condensate phase. In brief, the goal of this work was to evaluate whether the application of 2D materials in the framework of strong light-matter interaction may partly justify the enormous attention that the scientific community pays to TMDC monolayers.

This work starts with an introduction to the fundamentals of excitons in 2D materials, microcavities and strong coupling in chapter 2. The experimental methods used in this work are explained in detail in chapter 3. Chapter 4 covers basic investigations that help to select appropriate materials and cavities for the following experiments. In chapter 5, results on the formation of exciton-polaritons in various materials and cavity designs are presented. Chapter 6 covers studies on the spin-valley properties of exciton-polaritons including effects such as valley polarization, valley coherence and valley-dependent polariton propagation. Finally, the formation of hybrid-polaritons and their condensation are presented in chapter 7.

Chapter 2

Fundamentals

2.1 Crystal and band structure of TMDC monolayers

Already many decades ago, TMDC materials have been investigated in bulk and thin film form [17, 18, 19, 20, 21]. However, only in 2004 a mechanical exfoliation method for monolayers of Van der Waals materials was demonstrated, which lead to the discovery of graphene [22, 23]. Van der Waals materials are built up by a stack of planes that exhibit strong chemical bonds within the plane, but the planes are only held together by the weak Van der Waals force. This allows to mechanically isolate individual planes. Although this fabrication method was known from then on, TMDC monolayers such as MoS_2, WS_2, WSe_2 and $MoSe_2$ did not gain a lot of attention before it was observed that they were direct bandgap semiconductors in the monolayer limit [24, 25].

The structure of MoS_2, WS_2, WSe_2 and $MoSe_2$ monolayers is built up in the following way: Looking into the monolayer plane, the chalcogen atoms (X) stick out the central plane of transition metals atoms (M), forming a X-M-X layer structure as depicted in Figure 2.1a. The thickness of a monolayer was measured to be 0.65 nm [19]. From the top view, the crystal structure in the TMDC monolayer plane is composed by a hexagonal lattice as illustrated in Figure 2.1b, whereas neighboring sites are alternatingly occupied with transition metal and chalcogen atoms. The alternating occupation of crystal sites breaks the inversion symmetry, which strongly affects the electronic and optical properties. One consequence is an efficient second harmonic generation (SHG) in TMDCs monolayers for example [26]. For MoS_2, WS_2, WSe_2 and $MoSe_2$, this crystal structure results in an electronic band structure with a direct bandgap at the K-points. The band structure of a WS_2 monolayer is exemplarily depicted in Figure 2.1c, showing the direct bandgap at the K-point. The hexagonal shape of the crystal lattice transfers to a hexagonal arrangement of six K-points in reciprocal space, as illustrated in Figure 2.1d. These band extrema (also called valleys) give rise to optical interband transitions in the visible to near-infrared

range and are divided in K and K' points, which are distinguished by their valley index, as discussed below in more detail.

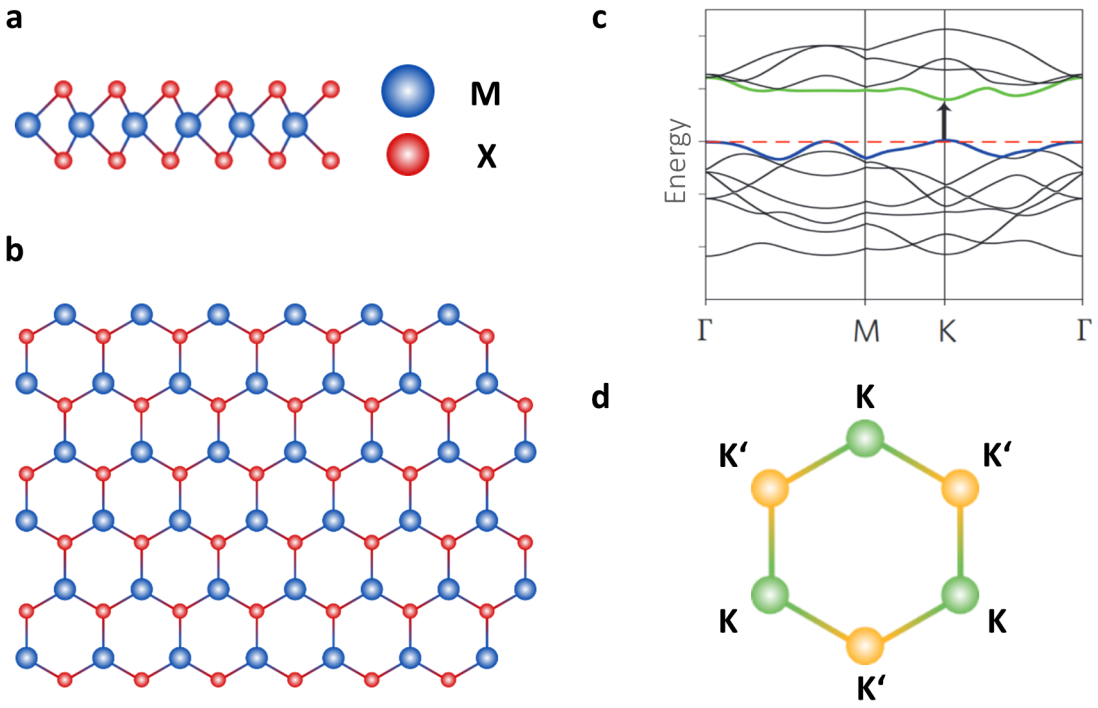

Figure 2.1: Crystal and electronic band structure of a transition metal dichalcogenide monolayer: (a) Side view of the monolayer showing the typical X-M-X layer sequence. (b) Top view of the hexagonal crystal lattice with differently occupied sites. (c) Calculated electronic band structure of a WS_2 monolayer, exhibiting a direct band gap at the K point (adapted from [27] with permission). (d) Schematic illustration of the Brillouin zone, depicting the hexagonal structure in momentum space with degenerate K and K' points, which differ by their valley index.

2.2 Excitons in TMDC monolayers

The band structure and its energy gap E_{Gap} presented in Figure 2.1c refer to single, free carriers, namely electrons or holes. However, when an electron-hole pair is created, both species are subject to Coulomb interaction because of their charge. Therefore, an electron-hole pair forms an energetically favorable, bound quasi-particle, which is called exciton as pictured in Figure 2.2a. The exciton is an essential ingredient for the formation of exciton-polaritons and is thus elaborated in more detail in this section. Besides that, an additional free particle (either electron or hole) can be bound in the particle complex,

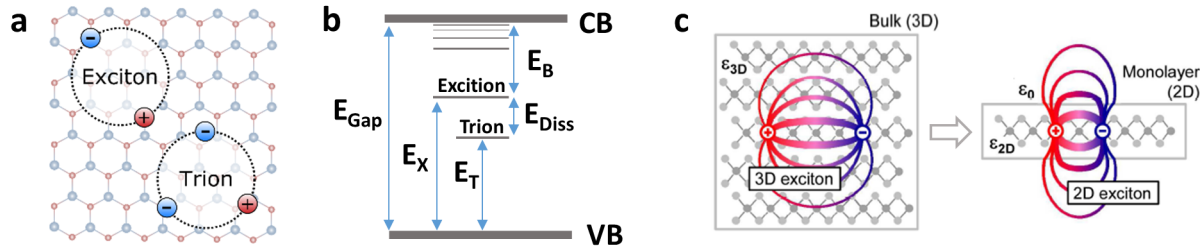

Figure 2.2: Excitons and trions in TMDC monolayers: (a) Schematic illustration of an exciton and a trion in a TMDC monolayer. (b) Energy diagram of the relevant exciton and trion energies. (c) Schematic illustration of the exciton dielectric screening in bulk and monolayer TMDC crystals, adapted from reference [28] with permission.

which leads to the formation of a trion, also indicated in Figure 2.2a. The energy that is required to separate the constituent carriers is called the binding energy E_B, which can be used to express the exciton energy E_X by [29]

$$E_X = E_{Gap} - E_B. \tag{2.1}$$

This relation is also illustrated in Figure 2.2b. In TMDC monolayers, the binding energy of an exciton can be up to several hundred meV [30], which makes them stable even under ambient conditions. The energy difference of exciton and trion is called the trion dissociation energy E_{Diss} [31]. This energy is required to separate one of the majority charge carriers from the complex, leaving an exciton and a free particle. It is important to note that the strong Coulomb interaction also affects two free charge carriers of the same kind in a repulsive way. This repulsive interaction is called the self-energy contribution and leads to an increase in the free-particle band gap [32]. This self-energy contribution and the exciton binding energy are almost equal and thus cancel out with respect to the absolute energies. This effect becomes apparent when the dielectric environment of the monolayer is changed. In this case, not only the exciton binding energy is affected, but also the self-energy contribution is changed to a similar degree. As a result, the total exciton energy E_X, which is typically observed in photoluminescence or reflectivity experiments, remains almost unaffected by the change in dielectric environment [33].

In bulk crystals, the exciton can be well described with the Bohr model of the hydrogen atom with the analogy of having a positively and a negatively charged particle bound to each other. However, the electrons and holes that compose the excitons have different effective masses in the crystal and the electric field between both charges is subject to the dielectric screening of the crystal lattice as indicated in Figure 2.2c. Taking this into account, the binding energy in bulk crystals can be approximated by [29]

$$E_B = \frac{\mu}{2\hbar}\left(\frac{e^2}{4\pi\varepsilon_r\varepsilon_0}\right)^2, \tag{2.2}$$

where $\mu = \dfrac{m_e m_h}{m_e + m_h}$ is the reduced, effective mass of the exciton with the effective masses of the electron m_e and hole m_h. e is the elementary charge, ε_0 the vacuum permittivity, and ε_r is the relative permittivity specific to the material, which accounts for the dielectric screening of the crystal [29]. The effective masses of electron and hole in TMDC monolayers are typically on the order of 0.5 m_0, yielding a reduced effective mass of 0.25 m_0 [32]. This implies that the excitons inherit the parabolic dispersion relation of valence and conduction bands at the K points with a curvature that corresponds their reduced effective mass ($E(k) = \frac{\hbar^2 k^2}{2\mu}$, with k being the wave vector).

However, the dielectric screening in monolayers is reduced to two dimensions as indicated in Figure 2.2c. Nevertheless, a 2D hydrogen-like model can be used to estimate the effects of the reduced dielectric screening and the effective mass on the binding energy [32]:

$$E_B \sim \frac{4R\mu}{m_0\varepsilon_{eff}^2}, \tag{2.3}$$

where R is the Rydberg constant (13.6 eV) and ε_{eff} accounts for the effective dielectric screening, which is averaged form the contribution of the monolayer and its environment. For an realistic $\varepsilon_{eff} = 5$, the binding energy is estimated to 500 meV [32]. In an ideal 2D system, the binding energies of higher exciton states evolve with [34]

$$E_B^n = \frac{\mu e^4}{2\hbar^2\varepsilon_{eff}^2(n-\frac{1}{2})^2}, \tag{2.4}$$

where (n = 1, 2, 3,...). However, experiments that have probed the exciton series by reflection spectroscopy show a strongly deviating behavior [28]. Because of the specific geometry of the dielectric environment shown in Figure 2.3, the dielectric screening depends on the intercharge distance r. Thus, the screened Coulomb potential strongly deviates from the usual 1/r dependence [35, 36]. The 1/r dependence is only valid for large interparticle distances, where most of the electric field lines run outside the monolayer [32] as indicated in Figure 2.3. However, at smaller interparticle distances a larger fraction of the electric field lines run within the monolayer and thus the system is no longer ideally two dimensional. As a result, the potential dependence on the interparticle distance is described with a log(r) behavior [36]. The overall potential V(r), the so-called Keldysh potential [35], is given by [28]:

$$V(r) = -\frac{\pi e^2}{2r_0}[H_0(\frac{r}{r_0}) - Y_0(\frac{r}{r_0})], \tag{2.5}$$

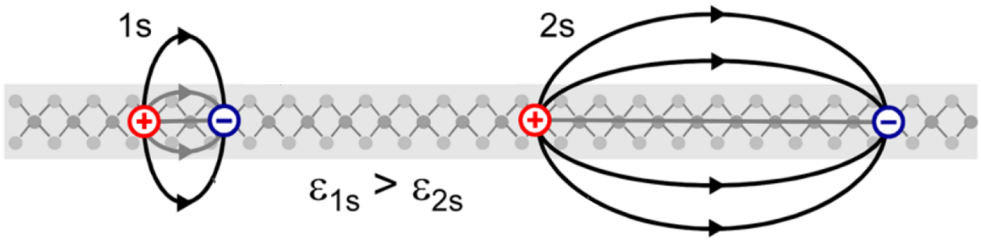

Figure 2.3: Exciton screening (adapted from reference [28] with permission): For short interparticle distances such as in the 1s exciton case more of the electric field lines run within the monolayer as compared to higher exciton states. Thus, the dielectric screening depends on the interparticle distance and the screened Coulomb potential does not follow a typical 1/r dependence, but needs to be described by a Keldysh potential.

where H_0 and Y_0 are the Struve and Neumann functions, respectively and r_0 is the effective screening length. The latter is either calculated ab initio [37] or is adjusted to fit experimental results [28]. The potential $V(r)$ is used to solve the two-particle Schröding equation for the excitons states either variationally or numerically [32].

The reduced dielectric screening leads to tightly bound excitons with Bohr radii on the order of 1 nm to 1.5 nm [38] and the binding energies on the order of a few hundred meV [28, 30, 38]. This is very high as compared to conventional bulk semiconductors such as GaAs with an exciton binding energy of a few to ten meV [7]. Because of the low monolayer thickness, the dielectric environment (substrate or capping material) strongly affects the exciton binding energy [30, 33]. Substrate or capping increase the dielectric screening and reduce in the binding energy. As described above, the single particle band gap is also renormalized in the presence additional screening. This renormalization reduces the band gap and thus compensates for reduced binding energy [30]. Ultimately, the exciton ground state energy is only weakly affected by dielectric environment.

The strong binding energy and spatial confinement has a few important consequences for excitons in TMDC monolayers. Firstly, the high binding energy makes the excitons very stable. Thus, these resonances can easily be observed as distinct and well separated resonances even under ambient conditions. Due to the spatial proximity of electron and hole, their wave functions have a large overlap, which leads to a strong interaction with light, quantified with the exciton oscillator strength f. In a system that is confined in one dimension the oscillator strength is described by [4, 39]:

$$f = \frac{2}{\mu\hbar\omega} \, |\langle u_h|\hat{e}\ \mathbf{p}|u_e\rangle|^2 \, |\langle F_h|F_e\rangle|^2 \frac{V}{\pi a_{B,2D}^3}, \tag{2.6}$$

where u_e and u_h are the lattice periodic (Bloch) parts of the electron and hole wave functions, F_e and F_h are the envelope wave functions of electron and hole, $\hat{e}$ is the polarization vector, $\mathbf{p}$ is the momentum operator and V is the quantization volume of the exciton. The term $|\langle F_h|F_e\rangle|^2$ accounts for the quantum confinement in the reduced dimension and $\frac{V}{a_{B,2D}^3}$ describes the enhancement of the electron and hole wave function overlap due to the exciton formation. However, since TMDC monolayers are so strongly confined and are therefore close-to-ideal 2D systems, the latter contribution is considered to have a $\frac{1}{a_{B,2D}^2}$ dependence [32]. The large wave function overlap also results in a very fast radiative decay time τ_0. The radiative decay time is defined by the radiative decay rate (Γ_0 as $\tau_0 = \frac{1}{\Gamma_0}$), which in turn is described by Fermis Golden rule [40]:

$$\Gamma_0 \sim |\langle f'|\hat{e}\ \mathbf{p}|i\rangle|^2\ \rho_r(\Delta E)\ \delta(\Delta E - \hbar\omega), \tag{2.7}$$

where i and f' are the initial and final states, $\rho_r(\Delta E)$ is the combined density of states and $\delta(\Delta E - \hbar\omega)$ is a delta function, which describes energy conservation. In fact, radiative lifetimes of a few hundred fs to one ps have been measured for TMDC monolayers [41, 42, 43, 44, 45, 46], which has been confirmed by first principle calculations [41, 47]. This is about two orders of magnitude lower than for excitons in GaAs quantum wells [48, 49].

Although the radiative decay is very fast, the overall exciton decay is governed by the formation, relaxation and thermalization of excitons. Due to energy and momentum conservation, the radiative decay only takes place if the excitons center-of-mass wave vector K is equal to the in-plane projection of the photon wave vector $k_{||}$. Thus, $K < k = \omega/c$ needs to be fulfilled, where ω is the photon frequency and c is the speed of light. The k-space region, where this condition is fulfilled, is therefore also referred to as the lightcone as indicated in Figure 2.4. Under non-resonant excitation at excitation energies that correspond to states outside the lightcone (energies more than a few tens of μeV larger than E_X), excitons are mainly formed by direct hot exciton photogeneration with an simultaneous emission of phonons [32]. Due to the phonon emission, they acquired a center-of-mass wave vector K larger and $k = \omega/c$ in their formation process and are consequently optically inactive ("dark"). Hence, the excitons needs to relax to (or at least close to) the ground state by phonon scattering before they decay radiatively. However, excitons do not only accumulate at the ground state (zero in-plane wave vector), but are also backscattered by phonons and occupy states with finite center-of-mass wave vectors as shown in Figure 2.4. This distribution of excitons around the ground state is determined by the temperature. As a result, the fractions of excitons inside and outside the light cone is a function of temperature, which has a linear dependence [49]. Ultimately, the radiative lifetime is weighted with the fraction of excitons inside the light cone to obtain the effective radiative decay time [32]. At cryogenic temperatures the effective radiative

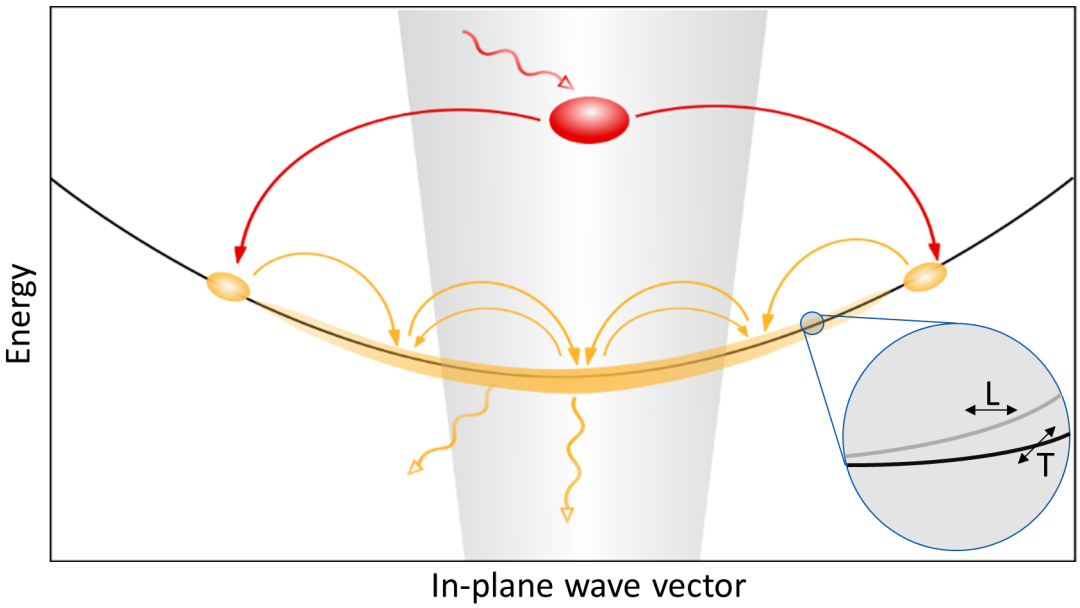

Figure 2.4: Exciton formation and dynamics: Excitons are typically formed by a hot plasma excitation with a simultaneous phonon emission. In this process, excitons acquire a finite center-of-mass momentum. Thus, they need to relax into the lightcone by phonon scattering to be optically active. At finite temperatures, excitons are also backscattered outside the lightcone and the thermal distributions extends beyond the lightcone edge. As a consequence, the effective lifetime increases towards higher temperatures. At finite k vectors, excitons are subject to an L-T splitting, which causes a valley depolarization as elaborated below.

lifetime are few to few tens of ps and can range up to the order of ns at room temperature [41, 47]. Only when excitons are excited resonantly or near-resonantly (within the light cone), the very fast temporal response is attributed the radiative recombination time [43, 45]. It should be noted that the dynamics of the bright excitons are also affected by non-radiative decay channels of the excitons outside the lightcone, for example induced by the presence of defects and disorder or by Auger-type exciton-exciton annihilation processes [50].

The tightly bound nature of excitons in TMDC monolayers also affects their high-density behavior. When the average exciton-exciton interparticle distance becomes smaller than a few Bohr radii, excitons interact by their short-range interaction. At this stage excitons are no longer considered bound states, but are described as a Coulomb-related carrier gas [32]. The density for such transition is quantified with the Mott density with $N_{Mott} = \frac{A}{\pi a_B^2}$, A being a reference area of 1 cm^2 [51]. Because of their small Bohr radius, TMDC monolayer excitons have a particular high Mott density on the order of $10^{13} - 10^{14}$ cm^{-2}. Even below the Mott density excitons interact through their long-range

interaction. This interaction can be understood as the influence of the electric field that is created by the exciton and that affects other excitons. This interaction is proportional to $\frac{1}{\mu}$ [39]. As the reduced effective mass μ is large for excitons in TMDC monolayers ($\sim$0.25 m_0 [32]) as compared to more conventional semiconductors (0.056 m_0 in GaAs quantum wells for example [4]), the long-range interaction is expected to be relatively weak [52, 53].

The spin-valley configuration in TMDC monolayers is another interesting property, which distinguishes them from conventional semiconductors. The spin-orbit interaction is strong as compared to other 2D materials, such as graphene, due to the heavy transition metal elements (atomic number Z of tungsten is 74, for example, as compared to a Z of 6 for carbon in graphene). As a result, states that are composed of transition metal d orbitals are spin-split. Since both valence and conduction band are partially composed of the d orbitals, both are subject to a spin splitting (few hundred meV in the VB and few tens meV in the CB) [54, 55] as pictured in Figure 2.5. Consequently, the

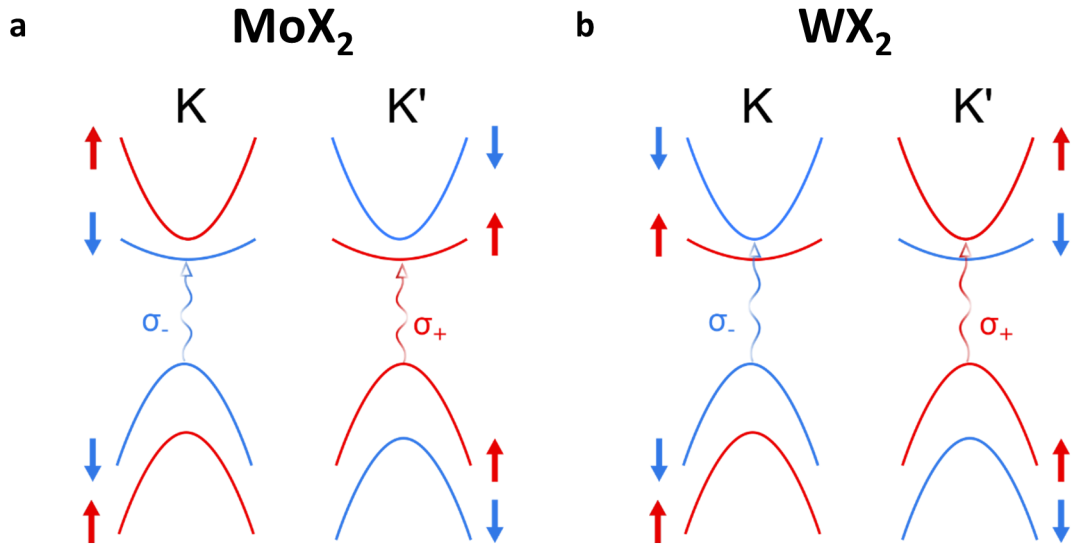

Figure 2.5: Spin- and valley-selective band configurations for molybdenum based monolayers (a) and tungsten based monolayers (b). Spin-up and spin-down are encoded in red and blue, respectively. The photon helicity for optically allowed transition is also marked in red (σ^+) and blue (σ^-), corresponding to the spin orientations of initial and final states. K and K' valleys can be addressed with opposite helicity. While the ground state is optically active in MoX_2 compounds, it is optically inactive in WX_2 compounds.

spin-allowed, optically active ("bright") transitions and spin-forbidden, optically inactive ("dark") transitions are energetically separated. Moreover, the conduction band splittings have a different sign depending on the transition metal atom (Mo vs. W) as illustrated

by the the different conduction band configurations of MoX_2 and WX_2 (Figure 2.5 a vs. b). Both effects create a distinction between MoX_2 and WX_2 based compounds: While the ground state in MoX_2 based monolayers is bright [56, 57], WX_2 based monolayers have a dark ground state [58, 59, 60]. In addition, the broken inversion symmetry of the monolayer lattice results in inverted spin splittings at opposite points in momentum space (K and K') [9, 10]. Thus, the bright transitions in opposite valleys are associated with photons of different helicity, meaning that K and K' are addressed with σ^+ and σ^- circularly polarized light, respectively. In contrast to more conventional, direct bandgap semiconductors such as GaAs, here spin and valley index are connected, which is referred to as spin-valley locking. This makes TMDC monolayers ideal materials to investigate and control spin and valley at the same time. Typical experiments are either designed to excite and detect one of the two valleys (valley polarization) or to excite a linear and coherent superposition of both valleys (valley coherence).

The valley polarization P is typically determined in a circular polarized PL experiment. The monolayer is excited with right- or left-handed (σ^+ and σ^-, respectively) circular polarized light and the intensities I of the polarization components of the PL signal are analyzed. The degree of circular (DOCP) polarization ρ is calculated by $\rho = \frac{I(\sigma^+)-I(\sigma^-)}{I(\sigma^+)+I(\sigma^-)}$ and serves as measure of the valley polarization.

Off-resonant excitation results in excitons with finite center-of-mass in-plane momentum as described above. Because of the strong Coulomb exchange interaction, exciton eigenstates with dipole moments longitudinally (L) and transversly (T) aligned to their in-plane wave vector are energetically split and the splitting depends linearly on the wave vector [61, 62] as indicated in Figure 2.4. Circular polarized excitation generates a valley-polarized exciton, which is a linear superposition of the L and T exciton eigenstates with a fixed phase relation. Since the exciton eigenstates are split in energy, their oscillation frequency is slightly different and thus the phase relation between L and T states changes over time. This change is equivalent to different L-T-superposition, which in turn means that the exciton looses its initially well-defined valley polarization. In the pseudo-spin formalism, this process is seen as an effective magnetic field, which rotates the exciton valley pseudo-spin. This process is known as the Maialle-Silva-Sham (MSS) mechanism [63] and leads to an effective depolarization time $\tau_{X,s}$, which is also interpreted as the intervalley scattering time. The degree of this valley depolarization mechanism increases with temperature, since phonons scatter excitons to higher in-plane wave vectors and outside the light cone, where the L-T splitting is more pronounced. Disorder in the monolayer also scatters excitons to high-vector with larger L-T splitting, which decreases the valley polarization as well. Finally, the resulting DOCP is determined by the dynamics of the competing processes of energy relaxation, backscattering, radiative decay and depolarization [64]. In a first empirical approximation, the valley polarization can be calculated by

[65]

$$P = \frac{P_0}{(1 + \frac{\tau}{\tau_{X,s}})}, \tag{2.8}$$

where P_0 is the initial polarization, τ is the effective decay time (energy relaxation + radiative decay) and $\tau_{X,s}$ is the depolarization time.

Valley coherence is induced by excitation with linearly polarized light, which is a superposition of σ^+ and σ^- polarized light. Hence, both valleys are equally populated and obtain a phase relation, which is determined by the polarization orientation of the exciting light. This phase relation cannot be fully conserved, because of the depolarization mechanism described above. However, if the phase relation is still conserved when the excitons decay, the original superposition of σ^+ and σ^-, equivalent to linearly polarized light of a certain orientation, is transferred to the emitted light. The valley coherence is typically determined by exciting in a linear polarization basis, for example the X-basis, and by subsequently measuring the photoluminescence in the co-polarized basis (X) and the cross-polarized basis (here, Y basis). The valley coherence is quantified by the degree of linear polarization (DOLP) $\rho_{lin} = \frac{I(X)-I(Y)}{I(X)+I(Y)}$. Interestingly, it has been shown that such coherent superposition state of K and K' may be manipulated by an external magnetic field [47] or the optical Stark effect [66]. This could potentially be used as new concept for quantum information processing [47, 66].

2.3 Microcavities

In order to facilitate the strong coupling regime/the formation of exciton-polaritons, the active material that hosts the exciton is integrated into a photonic structure. The light confinement in such a structure increases the light-matter interaction, because the optical field amplitude is enhanced in the center of the photonic structure. For this purpose, planar microcavities, also known as Fabry-Pérot cavities, are well established photonic structures [4, 7]. These consist of two planar, parallel mirrors with an adequate spacing. The mirrors can simply be metal layers, however distributed Bragg reflectors (DBR) are typically used to achieve highest reflectivity values. DBRs consist of alternating layers of two dielectric materials with layer thicknesses $d = \frac{\lambda_c}{4n_{DBR}}$, where λ_c is the wavelength of the target cavity mode and n_{DBR} is the refractive index of each layer. For this wavelength, light is reflected at each material interface and constructively interferes with light reflected at the previous interface, which ultimately leads to a high reflectivity mirror. In order to confine a photon mode in between two mirrors, the cavity thickness is designed to

$$d_c = n\frac{\lambda_c}{2n_c}, \tag{2.9}$$

with $n = 1, 2, 3, ...$ and n_c being the refractive index of the cavity material, as illustrated in Figure 2.6a. Under normal incidence, perpendicular to the cavity plane, the cavity

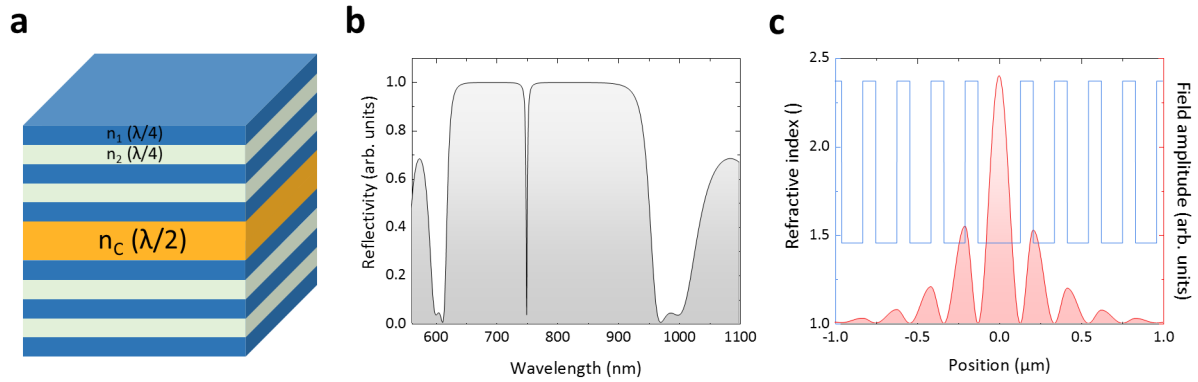

Figure 2.6: Microcavities: (a) Schematic structure of a planar microcavity consisting of bottom and top DBR with an alternating layer sequence with $\lambda/4$ thickness and a $\lambda/2$ cavity. (b) Reflectivity spectrum of a typical microcavity, calculated by the transfer matrix method [67]. The spectrum shows a broad stopband and a sharp cavity resonance. (c) Microcavity structure illustrated by the refractive indices of the alternating layers and the simulated field distribution in the structure.

exhibits a resonance with the energy $E_C = \frac{\hbar c}{\lambda_C}$. This cavity mode becomes apparent in the reflectivity spectrum of the cavity as depicted in Figure 2.6b. The reflectivity drops sharply for wavelengths that coincide with the cavity mode. The spectral width of the cavity mode Γ_C is determined by the quality factor Q (also Q-factor) of the cavity [4]:

$$Q = \frac{\lambda_C}{\Gamma_C} \approx \frac{\pi (R_1 R_2)^{\frac{1}{4}}}{1 - (R_1 R_2)^{\frac{1}{2}}}, \tag{2.10}$$

where R_1 and R_2 are the reflectivities of the upper and lower mirror. The Q-factor is a measure of the time that a photon spends on average in the cavity. The lifetime of a cavity photon τ_C can be calculated by

$$\tau_C = \frac{\hbar}{2\Gamma_C}. \tag{2.11}$$

Figure 2.6c shows the optical field distribution of the cavity mode inside the cavity. It can be seen that the optical mode is confined in the center of the cavity but penetrates into the mirrors. The optical confinement is therefore described by the effective cavity length perpendicular to the cavity plane, which is composed of the actual cavity length L_C and the penetration length into the DBRs L_{DBR} [4]:

$$L_{eff} = L_C + L_{DBR}, \tag{2.12}$$

with

$$L_{DBR} \approx \frac{\lambda_C}{2n_C} \frac{n_1 n_2}{|n_1 - n_2|}, \tag{2.13}$$

where n_1 and n_2 are the refractive indices of the two DBR mirror materials. This equation illustrates nicely that a high contrast in the refractive index leads to better mode confinement. However, this equation does not exactly reproduce the penetration length, if the refractive index contrast is high. Therefore, in this work, L_{eff} and L_{DBR} were determined by calculation the field distribution of the cavity mode in a transfer matrix approach [67]. L_{DBR} was determined by taking the distance from the cavity edge to where the envelope function of the cavity mode dropped to $1/e$.

While the optical mode is confined perpendicular to the cavity plane with a fixed wave vector of $\mathbf{k}_\perp = n_c(2\pi/\lambda_c)$, it propagates within the cavity plane with a wave vector $\mathbf{k}_{||}$. Thus, the total wave vector increases ($\mathbf{k}_{total} = \sqrt{\mathbf{k}_\perp^2 + \mathbf{k}_{||}^2}$) and so does the resonance energy ($E_C = \frac{\hbar c}{n_c} \cdot |\mathbf{k}_{total}|$). The in-plane wave vector corresponds to incident light from an angle Θ relative to the cavity plane normal, which has resonances at $\lambda_C(\Theta) = \lambda_C(0^\circ)/cos(\Theta)$. In order to relate the cavity resonance energy to its in-plane wave vector (energy dispersion), $\mathbf{k}_{||}$ needs to be expressed by its corresponding angle of incidence Θ as:

$$\mathbf{k}_{||} = n_c \frac{2\pi}{\lambda_c} \tan\left[\sin^{-1}\left(\frac{\sin\Theta}{n_c}\right)\right] \approx \frac{2\pi}{\lambda_c}\Theta \text{ with } \left|\mathbf{k}_{||}\right| \ll \left|\mathbf{k}_\perp\right|. \tag{2.14}$$

Finally, the small-angle-approximation allows to express the cavity energy as:

$$E_C \approx \frac{\hbar c}{n_c}\mathbf{k}_\perp \left(1 + \frac{\mathbf{k}_{||}^2}{2\mathbf{k}_\perp^2}\right), \tag{2.15}$$

which can be re-written to:

$$E_C(\mathbf{k}_{||}) = E_C(\mathbf{k}_{||} = 0) + \frac{\hbar^2 \mathbf{k}_{||}^2}{2m_C}, \tag{2.16}$$

where m_C is the effective cavity mass:

$$m_C = \frac{E_C(\mathbf{k}_{||} = 0)}{c^2/n_c^2}. \tag{2.17}$$

This terminology already indicates that, in contrast to a free photon, the photonic cavity mode acquires an effective mass in the cavity plane. While this behavior is qualitatively the same as for the exciton, the effective mass of the cavity photon is significantly lower on the order of 10^{-5} m_0 with $\mathrm{m_0}$ being the free electron mass [4].

In analogy to the L-T splitting of excitons at high in-plane wave vectors, a planar microcavity exhibits a splitting of the transverse electric mode (TE) and transverse magnetic mode (TM) for finite, incident angles Θ_0 with respect to the surface normal. This splitting

arises due to the birefringence of the cavity. The difference between the frequencies of TE and TM modes (ω_{TE} and ω_{TM}, respectively) is given by [68]:

$$\omega_{TE} - \omega_{TM} \approx \frac{L_C L_{DBR}}{(L_C + L_{DBR})^2} \frac{2cos(\Theta_{eff})sin^2(\Theta_{eff})}{1 - sin^2(\Theta_{eff})} \Delta_C, \tag{2.18}$$

where $\Theta_{eff} \approx arcsin(n_0/n_C)sin(\Theta)$ and Δ_C is the difference between cavity frequency ω_C and stopband center frequency ω_S. The TE-TM splitting $\Delta E_{TE-TM} = E_{TE} - E_{TM}$, where $E_{TE} = h\omega_{TE}$ and $E_{TM} = h\omega_{TM}$. When the cavity mode is excited under a finite angle Θ with circular polarized ligth, the TE-TM splitting leads to a depolarization because of the same mechanism that causes the depolarization of L-T split excitons described in the section above. If the cavity mode is excited with σ^+ polarized light (a superpositon of the TE and TM modes) for example, the cavity modes also gains σ^- fractions over time. The characteristic depolarization time $\tau_{C,s}$ depends on the magnitude of the TE-TM splitting. Furthermore, excitation under a finite angle Θ with linearly polarized light, which does not coincides with the TE or TM mode, leads to a precession of the pseudo-spin, as discussed in section 6.3 in more detail.

2.4 Strong light-matter coupling

In order to establish the regime of strong coupling between a matter oscillator (the exciton) and an optical oscillator (the microcavity photon mode), a coherent energy transfer between the two individual oscillators must be possible. If the energy transfer rate is faster or on the order of the oscillators' decoherence, the coupling is considered "strong". An exciton-polariton is a quasi-particle resulting from strong coupling between matter and light [4]. This section covers an introduction to the fundamentals of strong coupling, including a description of exciton-polaritons, hybrid-polaritons and polariton condensation.

2.4.1 Exciton-polaritons

The following description of exciton-polaritons is based on references [68, 4, 7] and applies to excitons in a material integrated into a planar microcavity, where spatial overlap between the exciton and photonic mode is given. The exciton and photon resonances are described as two independent harmonic oscillators with orthogonal degrees of freedom. The exciton X and cavity photon C are described as the fundamental vectors in a two dimensional basis [7]:

$$|X\rangle = \begin{pmatrix} 1 \\ 0 \end{pmatrix}, |C\rangle = \begin{pmatrix} 0 \\ 1 \end{pmatrix}. \tag{2.19}$$

Because of the interaction between exciton and cavity photon, a coupling term needs to be introduced in the polariton Hamiltonian $\widehat{H}_{pol}$, which is expressed by [7]:

$$\widehat{H}_{pol} = \begin{pmatrix} E_X(\mathbf{k}_{||}) & \frac{V}{2} \\ \frac{V}{2} & E_C(\mathbf{k}_{||}) \end{pmatrix}, \tag{2.20}$$

where the off diagonal terms consist of the system-specific coupling constant V. Diagonalization of this matrix leads to:

$$\widehat{H}_{pol} = \begin{pmatrix} E_{UP}(\mathbf{k}_{||}) & 0 \\ 0 & E_{LP}(\mathbf{k}_{||}) \end{pmatrix}, \tag{2.21}$$

where E_{UP} and E_{UP} are the eigenenergies for the upper and lower polariton, respectively. These can be written as:

$$E_{UP/LP} = \frac{1}{2}(E_X + E_C) \pm \frac{1}{2}\sqrt{(V)^2 + (E_X - E_C)^2}. \tag{2.22}$$

Here, the wave vector dependences were left out intentionally for clarity. The coupling constant is mainly determined by the confinement of the optical field, described by the effective cavity length L_{eff}, and the oscillator strength of the exciton f,

$$V \sim \sqrt{\frac{f n_{eff}}{L_{eff}}} \tag{2.23}$$

but also by the effective number of monolayers n_{eff} in the cavity. It should be noted that the active material is ideally situated at the field maximum of the confined optical mode, since the coupling constant is also directly proportional to the electric field amplitude $|E|^2$ [68]:

$$V \sim |E|^2. \tag{2.24}$$

The difference between exciton and cavity energy is also often referred to as the detuning $\Delta E = E_C - E_X$. Figure 2.7 illustrates typical polariton dispersions for different detunings with the distinct anti-crossing of upper and lower polariton branch (UPB and LPB). Both upper and lower polariton can be characterized by their exciton and cavity fractions, $|X|^2$ and $|C|^2$, respectively, which are also referred to as the Hopfield coefficients [4, 69]:

$$\left|X_{\mathbf{k}_{||}}\right|^2 = \frac{1}{2}\left(1 + \frac{\Delta E(\mathbf{k}_{||})}{\sqrt{\Delta E(\mathbf{k}_{||})^2 + (V)^2}}\right) \tag{2.25}$$

and

$$\left|C_{\mathbf{k}_{||}}\right|^2 = \frac{1}{2}\left(1 - \frac{\Delta E(\mathbf{k}_{||})}{\sqrt{\Delta E(\mathbf{k}_{||})^2 + (V)^2}}\right), \tag{2.26}$$

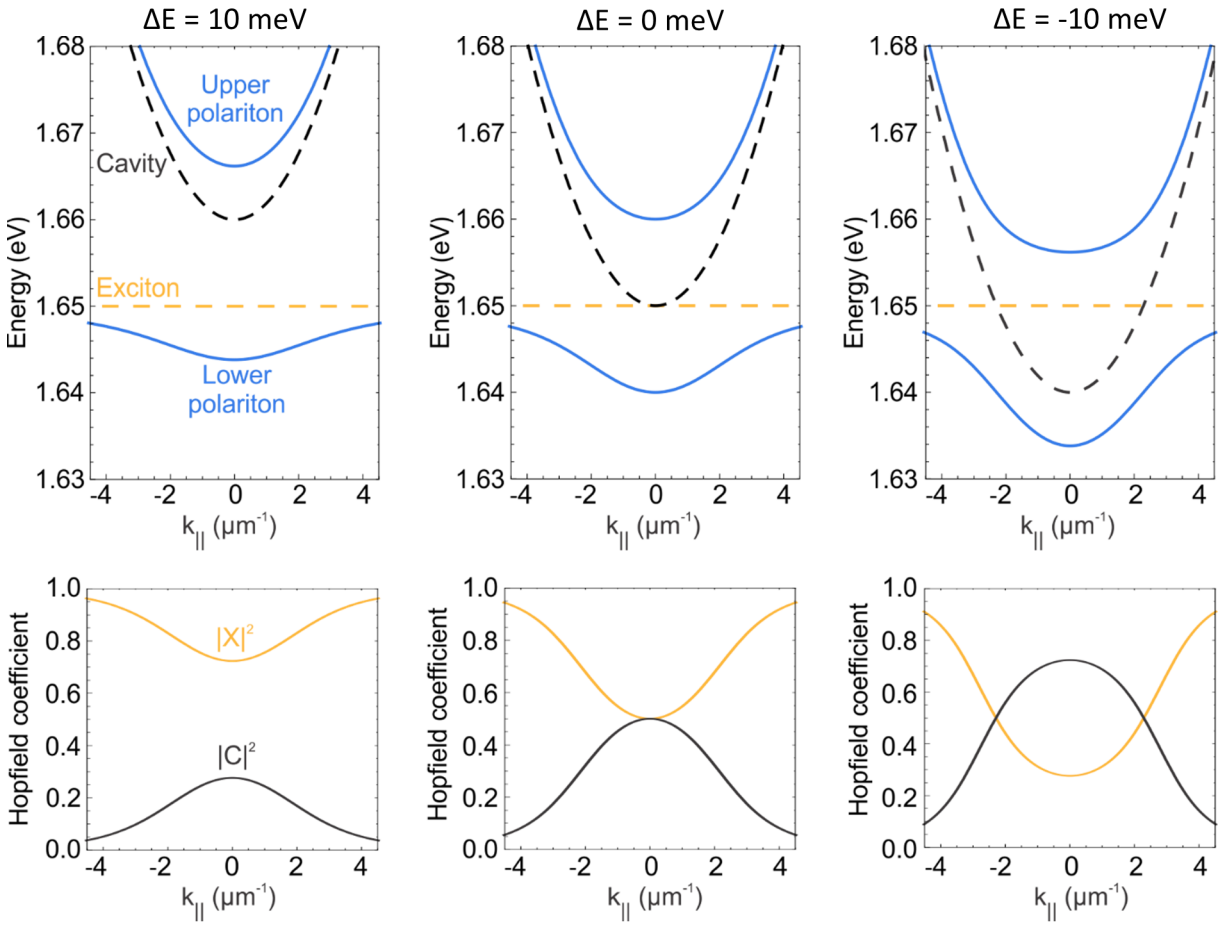

Figure 2.7: Polariton dispersions: Top diagrams: Modeled exciton-polariton dispersions for detunings of +10 meV, 0 meV and -10 meV with a coupling constant V = 20 meV. Bottom diagrams: Hopfield coefficients of the lower polariton branch corresponding to the dispersions above.

where $|X|^2 + |C|^2 = 1$.

For the actual normal mode splitting $\hbar\Omega$ (also referred to as Rabi splitting), damping terms of the exciton and cavity resonances need to be taken into account by [70]:

$$\hbar\Omega = \sqrt{V^2 - (\frac{\Gamma_C}{2} - \frac{\Gamma_X}{2})^2}, \tag{2.27}$$

where Γ_X and Γ_C are the exciton and cavity homogeneous linewidths, respectively. If note stated differently, all linewidths are denoted as the full width at half maximum (FWHM) in this work. Equation 2.27 illustrates the condition for strong coupling: For $V < |\frac{\Gamma_C - \Gamma_X}{2}|$ the square root in equation 2.27 becomes imaginary, which leave the real part of the exciton and cavity states unaffected (weak coupling). If $V > |\frac{\Gamma_C - \Gamma_X}{2}|$, the normal

mode splitting acquires real values (strong coupling) [7, 70]. This condition can be also understood as a dynamic argument, because Ω is the oscillation frequency of the energy transfer (also known as Rabi frequency Ω) and $\tau_{X/C} = \frac{\hbar}{2\Gamma_{X/C}}$ are the coherence times of exciton and cavity photon, respectively. From this perspective, the energy transfer must take place faster than decoherence of exciton and cavity resonance.

The exciton-polaritons inherit their properties from their constituent components and quantitatively depend on the quasi-particles composition. The polariton properties, such as the polariton mass as well as the radiative decay rates γ and times τ, can be therefore calculated based on the Hopfield coefficients:

$$m_{LP} = \frac{1}{\frac{|X|^2_{LP}}{m_X} + \frac{|C|^2_{LP}}{m_C}}, \tag{2.28}$$

$$\gamma_{UP/LP} = |X|^2_{UP/LP}\,\gamma_X + |C|^2_{UP/LP}\,\gamma_C, \tag{2.29}$$

and with $\tau = \frac{1}{\gamma}$:

$$\tau_{UP/LP} = \frac{1}{\frac{|X|^2_{UP/LP}}{\tau_X} + \frac{|C|^2_{UP/LP}}{\tau_C}}. \tag{2.30}$$

It should be also mentioned that both the L-T splitting of the exciton and the TE-TM splitting of the cavity are inherited by the polariton hybridization and so are the depolarization mechanisms and times. The overall polaritons depolarization time $\tau_{UP/LP,s}$ is determined by [71]

$$\tau_{UP/LP,s} = \frac{1}{\frac{|X|^2_{UP/LP}}{\tau_{X,s}} + \frac{|C|^2_{UP/LP}}{\tau_{C,s}}}. \tag{2.31}$$

.

2.4.2 Hybrid-polaritons

In principle, the cavity mode cannot only couple strongly to a single exciton resonance, but may couple to several exciton resonances. If two different, but still energetically close, exciton species are spatially overlapping with the cavity mode, they may both couple to it. The exciton species may even be spatially separated and thus they do not directly interact with one another. If the coupling to the cavity mode is strong enough for both excitonic modes, this scenario leads to a hybridization of all three modes and the formation of a so-called hybrid-polariton [72]. The system now splits into three branches, namely upper, middle and lower polariton. To describe the full system, the polariton Hamiltonian must

be extended as follows:

$$\widehat{H}_{pol}(\mathbf{k}_{||}) = \begin{pmatrix} E_{X_1}(\mathbf{k}_{||}) & 0 & V_1/2 \\ 0 & E_{X_2}(\mathbf{k}_{||}) & V_2/2 \\ V_1/2 & V_2/2 & E_{cav}(\mathbf{k}_{||}) \end{pmatrix}, \tag{2.32}$$

where V_1 and V_2 are the individual coupling constants of the exciton species X_1 and X_2, respectively. The diagonal element connecting both exciton species are set to zero, assuming that there is no direct interaction. Diagonalization of this matrix leads to:

$$\widehat{H}_{pol}(\mathbf{k}_{||}) = \begin{pmatrix} E_{LP}(\mathbf{k}_{||}) & 0 & 0 \\ 0 & E_{MP}(\mathbf{k}_{||}) & 0 \\ 0 & 0 & E_{UP}(\mathbf{k}_{||}) \end{pmatrix}, \tag{2.33}$$

where MP denotes the middle polariton. $E_{LP}(\mathbf{k}_{||})$, $E_{MP}(\mathbf{k}_{||})$ and $E_{UP}(\mathbf{k}_{||})$ are illustrated in Figure 2.8 for two different detunings. In analogy to the exciton-polariton,

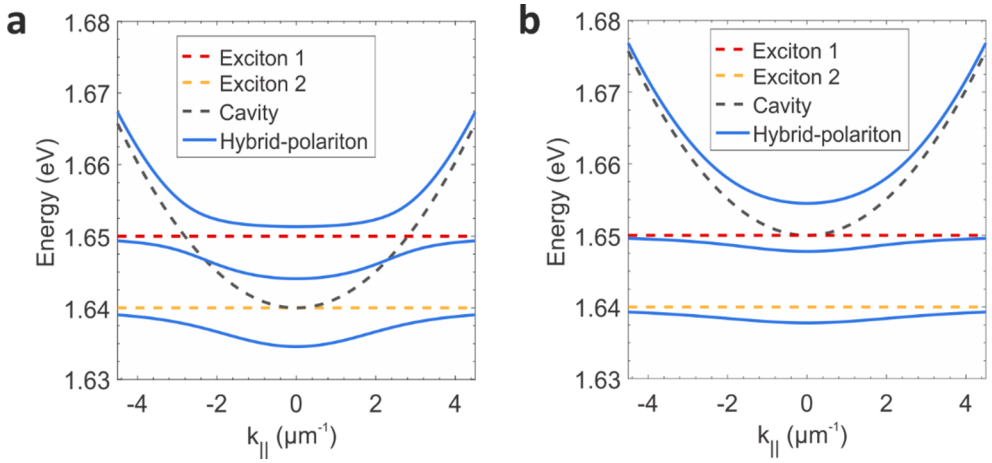

Figure 2.8: Hybrid-polariton branches plotted for zero detuning between exciton 2 and the cavity (a) and zero detuning between exciton 1 and the cavity (b).

the hybrid-polariton branches carry the properties of their individual components with the corresponding fractions $|X_1|^2$, $|X_2|^2$ and $|C|^2$, where $|X_1|^2 + |X_2|^2 + |C|^2 = 1$. Here again, the Hopfield coefficients are used to describe the polariton properties based on the properties of the individual components such as the hybrid polariton radiative life time:

$$\tau_{UP/MP/LP} = \frac{1}{\frac{|X_1|^2_{UP/MP/LP}}{\tau_{X_1}} + \frac{|X_2|^2_{UP/MP/LP}}{\tau_{X_2}} + \frac{|C|^2_{UP/MP/LP}}{\tau_C}}. \tag{2.34}$$

2.4.3 Exciton-polariton relaxation and condensation

A great motivation for exciton-polariton physics is the possibility to occupy a single macroscopic state with these very light and bosonic particles at elevated temperatures. In the low density regime, exciton-polaritons are considered composite, bosonic particles since their constituent components, namely excitons and photons, are regarded as bosonic particles as well. In the thermodynamic equilibrium, the occupation of a state with bosons F follows the Bose-Einstein-distribution [73]:

$$F = \frac{1}{e^{(E-\mu)/k_B T} - 1}, \tag{2.35}$$

where μ is the chemical potential and k_B the Boltzmann constant. For low temperatures and high densities, bosons accumulate in the ground state of the system, referred to as Bose-Einstein-Condensation (BEC) [74]. Above a critical density n_c and below a critical temperature T_c, the chemical potential approaches zero. In a three dimensional system, the critical temperature depends on the boson density n and the boson mass m according to [73]:

$$T_c = \frac{2\pi\hbar^2}{k_B m}\left(\frac{n}{\zeta(\frac{3}{2})}\right)^{\frac{2}{3}}, \tag{2.36}$$

where ζ is the Riemann zeta function with $\zeta(\frac{3}{2}) \approx 2.6124$.

In the case of exciton-polaritons, the very light effective mass is in favor for such a phenomenon and significantly increases the critical temperature. However, in addition to the temperature and density requirements, the polariton lifetime must be longer than its energy relaxation time to reach thermal equilibrium [75]. In fact, in typical polariton systems, the polariton lifetime is on the order of the thermalization time (both about 1 - 10 ps [4]) and so the system does hardly reach thermal equilibrium. This holds particularly true for exciton-polaritons in TMDC monolayers since the exciton lifetime and also the cavity life time are very short (cavity designs, which allow monolayer integration are not yet as sophisticated as epitaxially grown cavities, meaning a lower Q-factor and lifetime). Thus, the exciton-polariton lifetime is also short (see equation 2.30). Moreover, strictly speaking, bosons cannot form a BEC in a two-dimensional system since thermal fluctuations destroy the long-range order [4, 76, 77]. However, if a 2D Bose gas system is laterally confined, the density of states of the ideal 2D system is dramatically modified and the quasi-BEC phase is recovered at finite temperatures [4]. The lateral confinement can be either given by limited system extension (such as a finite monolayer size), lateral optical confinement by the photonic structure or by the finite excitation laser spot size. For such system with the lateral confinement length L, a quasi-BEC is formed for $T < T_C$ and above the critical density [4]:

$$n_c = \frac{2}{\lambda_T^2} ln\left(\frac{L}{\lambda_T}\right), \tag{2.37}$$

where λ_T is the thermal de Brouglie wavelength with

$$\lambda_T = \sqrt{\frac{2\pi\hbar^2}{mk_BT}}. \tag{2.38}$$

The described phase may also occur even if the system is not in thermal equilibrium [78, 79, 80] and is referred to as polariton-condensate [81] to clarify the distinction to a BEC. In 2D systems, there is another phase transition, namely the Berezinskii-Kosterlitz-Thouless (BKT) transition, which is characterized by the formation of bound pairs of oppositely circulating vortices. The critical density for such phase n_{BKT} is given by [4]:

$$n_{KBT} = \sqrt{\frac{\pi\hbar^2}{2m^2k_BT_{BKT}}}. \tag{2.39}$$

However, in typical polariton systems, L is small enough that the phase transition to a quasi-BEC takes place before the BKT transition [75].

As in the pure exciton case, the typical procedure to observed polariton-condensation starts with non-resonant, optical or electrical excitation of an electron-hole plasma [7], as pictured in Figure 2.9. As the carriers relax, they form excitons. Once those enter the lightcone, they may strongly couple to the cavity, forming exciton-polaritons at high in-plane wave vectors, which are also referred to as the exciton-polariton reservoir. Excitons outside the lightcone are referred to as the exciton reservoir. Since radiative decay and reabsorption is a requirement for the energy transfer between exciton and cavity mode, exciton-polaritons only form within the lightcone. The exciton-polaritons subsequently relax to the ground state by polariton-phonon, polariton-polariton or polariton-exciton scattering. It should be noted that polariton backscattering outside the lightcone and exciton thermalization is still possible, but might be suppressed because of the distinct energy lowering of the lower polariton state within the lightcone and the accelerated radiative polariton decay as compared to pure excitons. Due to the bosonic nature of exciton-polaritons, the scattering probability P to the ground state becomes more likely for each polariton N that already occupies the final state ($P \sim N+1$) [82]. This reinforcing effect, named stimulated scattering, initiates a very efficient collection of polaritons into the ground state, which ultimately leads to a macroscopic population of the final state and the condensation of polaritons [7]. The population dynamics of the plasma, exciton and lower polariton states can be modeled with a three-level, coupled rate equation system [4, 83]:

$$\frac{dN_{eh}}{dt} = N_0 - a_{eh-X}N_{eh} - \frac{N_{eh}}{\tau_{eh}} \tag{2.40}$$

$$\frac{dN_X}{dt} = a_{eh-X}N_{eh} - a_{X-LP}N_X - \frac{N_X}{\tau_X} - b_{X-LP}N_X^2(1+N_{LP}) \tag{2.41}$$

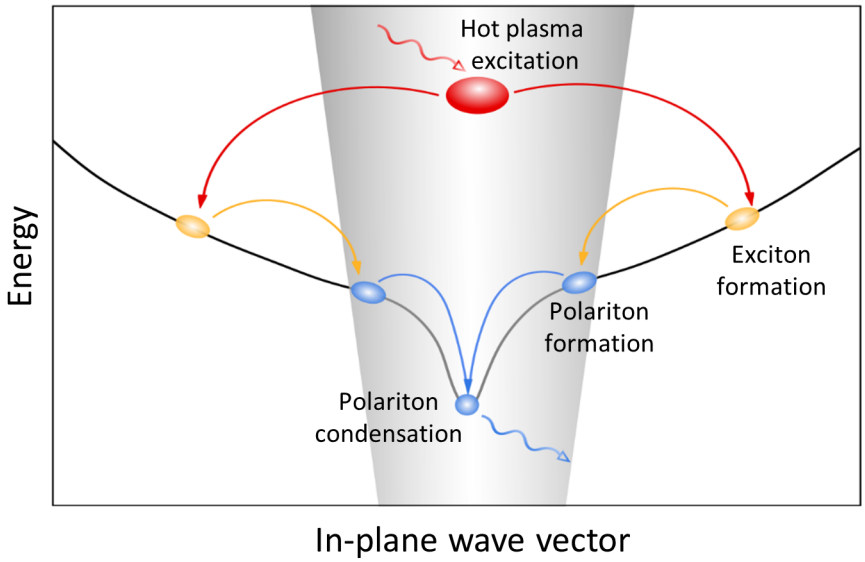

Figure 2.9: Exciton-polariton formation and condensation: First, a hot electron-hole-plasma is excited, which subsequently relaxes and forms excitons. Once excitons enter the light cone (grayly shaded here), they strongly couple to the cavity mode, forming exciton-polaritons. Polaritons may relax to the ground-state by phonon-scattering. If the ground state is significantly populated, stimulated polariton scattering is initiated, which strongly increases the relaxation efficiency of following polaritons. This leads an efficient built-up of the ground state population and ultimately to polariton condensation.

$$\frac{dN_{LP}}{dt} = a_{X-LP}N_X - \frac{N_{LP}}{\tau_{LP}} + b_{X-LP}N_X^2(1+N_{LP}), \tag{2.42}$$

where N_{eh}, N_X and N_{LP} are the population density of the electron-hole plasma, of the exciton and the lower polariton, respectively. N_0 is the initial electron-hole density (excited by a short femto second laser pulse for example). a_{eh-X} is the exciton formation and relaxation rate and a_{X-LP} is a linear scattering rate into the lower polariton ground state. τ_{eh}, τ_X and τ_{LP} are the lifetimes (non-radiative or radiative) of electron-hole plasma, exciton and lower polariton, respectively. b_{X-LP} is the non-linear scattering rate that describes the efficiency of the stimulated scattering process, which in turn is accounted for by the last terms of equations 2.41 and 2.42.

The population distribution along the polariton branch can be observed in a PL experiment since the polariton radiative lifetime is on the order of the relaxation time. Consequently, photons are emitted from all occupied states within the lightcone. When the excitation power is continuously increased, polariton condensation becomes apparent by a strong non-linear increase of the emitted photons due to the stimulated scattering

process. Moreover, the emission stems predominantly from the ground state, as states at higher in-plane wave vectors are more efficiently depopulated by stimulated scattering. Since the macroscopic population of the final state is accompanied with a dramatic increase of the spatial and temporal coherence, the spectral linewidth of the emission is strongly reduced [84]. Another typical signature of polariton condensation is a continuous blue-shift of the ground state with excitation power. Below the threshold, this blue-shift is attributed to exciton-exciton interaction of the reservoir excitons. Above the threshold, the blue-shift is explained with the polariton-polariton interaction caused by the exciton fraction of polariton [7, 85]. The nonlinear input-output characteristic, the drop in emission linewidth and the coherence of the emitted light imply a close analogy to classical lasers, which has lead to the term "polariton laser". However, the underlying amplification mechanism is not based on stimulated emission of radiation, but on stimulated scattering of polaritons. Thus, the term "laser" is misleading. Nevertheless, such system emits coherent, laser-like light at an input threshold that is one to two orders of magnitude lower than those of classical lasers, because no population inversion is required [7, 85]. However, the maximum output of a polariton laser is limited by the exciton Mott density. From this perspective, TMDC monolayer are favorable, because they have a small Bohr radius and thus a high Mott density. Although polariton lasing is not possible beyond the Mott density, the electron-hole plasma may start to emit as a conventional laser once population inversion is reached [7]. In experiments this is sometimes observed, manifesting in a second, non-linear threshold in the input-output characteristic and a spectral jump to the cavity mode [85]. With respect to polariton condensation, TMDC monolayers are challenging active materials since their short radiative life time makes the simultaneous population of the polariton ground and exciton reservoir states difficult, which would be required to initiate the stimulated scattering from the reservoir to the ground state. Nevertheless, excitons in TMDC monolayers are also very attractive for such an experiment, because of their robustness at elevated temperature and their high Mott density.

Chapter 3

Experimental methods

3.1 Material preparation

In order to achieve narrow and brightly emitting exciton resonances, the fabrication process for the TMDC monolayers is of great importance. Although TMDC monolayers can be grown by chemical vapor deposition (CVD) [86, 87, 88], molecular beam epitaxy (MBE)[30, 89], and atomic layer deposition (ALD) [90], mechanically exfoliated monolayers are still superior with respect to their optical properties (in particular the linewidth of the exciton). Apart from that, mechanical exfoliation is by far the easiest and cheapest way to fabricate individual monolayers for scientific purposes. Mechanical exfoliation, also known as the Scotch tape method, was first developed to fabricate monolayers of graphite (graphene) [22, 23] and has been optimized for TMDC monolayers [91]. This method has been used to fabricate all monolayers investigated in this work.

First, a thin (< 0.5 mm) piece of the TMDC bulk crystal (few mm in lateral extension) was placed on an adhesive tape (Tesa^{TM}) in such way that the individual material layers are aligned parallel to the tape surface. Subsequently, a second strip of the adhesive tape is brought in contact with the top surface of the bulk crystal. Tearing the tape stripes apart, as illustrated in Figure 3.1a (step 1), cleaves the bulk crystal along the weakly bound interlayer planes. This process is repeated multiple times to thin down the bulk piece. The adhesive tape is then pressed on a visco-elastic polydimethylsiloxane (PDMS) film. The adhesion to the visco-elastic film depends on the speed of detachment. Specifically, removing an object from the gel film quickly results in a strong adhesive force and vice versa for a slow detachment. When the stress is applied quickly on the PDMS film, the silicone macro-molecules have no time to rearrange and thus the strain response is fully elastic and the stress is completely transferred to the monolayer. In contrast, the macromolecules creep under slow application of stress, which results in a viscos stress response. Therefore, the applied stress relaxes in PDMS film and is not fully transferred to

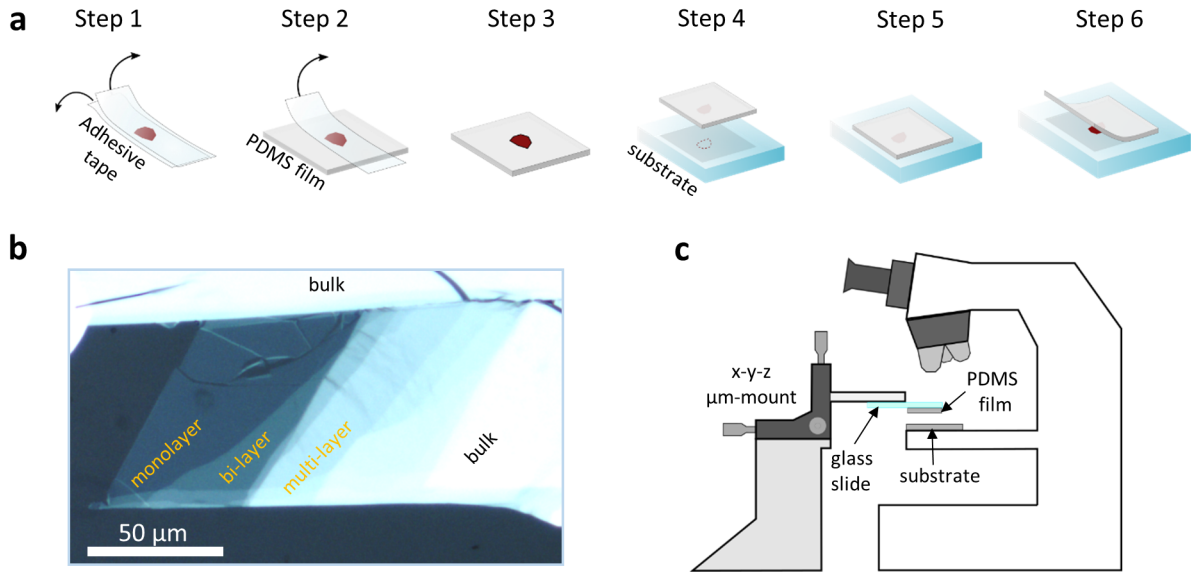

Figure 3.1: Monolayer fabrication and transfer: a) Schematic illustration of the individual fabrication and transfer steps. b) Microscope image of a $MoSe_2$ flake composed of mono-, bi- and multi-layer regions on a PDMS film. c) Schematic illustration of the transfer microscope setup.

the monolayer [92, 93]. Since it is the aim to transfer the TMDC material to the PDMS film, the adhesive tape is removed quickly (step 2). In this way, most of the TMDC material is transferred onto the PDMS film (step 3). Next, the thickness of the TMDC pieces is characterized by scanning the PDMS film in a conventional, optical microscope (reflection mode). Monolayers are identified by their optical contrast. Although the optical contrast of monolayers exhibits only subtle differences as compared to bi- or multi-layers (see Figure 3.1b with enhanced brightness and contrast, here), it is possible to distinguish the monolayer flakes from bulk material. In fact, only a very small fraction of the TMDC material on the PDMS is monolayer. Nevertheless, this method regularly yields monolayers on the order of 10 x 10 μm to 20 x 20 μm (often with elongated shape), but also exceptionally large monolayers of 50 x 100 μm have been obtained this way (see Figure 3.1b). Once a monolayer is identified, the PDMS film is placed on a glass slide, is turned upside down and is brought in close proximity to the target position on the final substrate (step 4). This procedure is carried out on a modified microscope as depicted in Figure 3.1c. Both the glass slide and the target substrate are mounted on x-y-z micrometer stages, so the monolayer on the PDMS film and substrate can be aligned with respect to each other with micrometer precision. Since the glass slide and the PDMS film are transparent, both the monolayer on the PDMS film as well as the substrate surface can be observed through the microscope during this process. This control is important to

avoid contaminated areas on the sample (such as dust grains) and allows to stack multiple flakes (see section 4.1). Once the desired position on the substrate is found, the PDMS film is gently pressed down (step 5). Most importantly, the micrometer stages provide excellent control of the speed of PDMS film detachment. As a final step, the PDMS film is removed very slowly (about 1 μm/second, step 6), meaning that the adhesion to it is weak, while the adhesion to the substrate is stronger. It should be noted that a clean and smooth surface is crucial for the described process. Therefore, the target substrates were cleaned with a reactive oxygen plasma for 3 minutes prior to the transfer process. Also, a low substrate surface roughness ($<$ 1 nm (root-mean-squared)) increases the chances for the monolayer to stick to the substrate. This way, a monolayer can be deterministically transfered to a large variety of target substrates with precise position control.

3.2 Spatial- and angle-resolved spectroscopy

Photoluminescence and reflectivity spectroscopy are the main methods to identify and investigate excitons, cavity modes and exciton-polaritons in this work. Since a typical lateral sample size is on the order of few tens of micrometers, the measurement requires a spatial resolution on the micrometer scale. At the same time, the emission angle should be resolved to acquire the in-plane dispersion relation as described in chapter 2. Both functionalities were implemented in one setup, which is schematically drawn in Figure 3.2. Various white-light and laser sources can be independently coupled into the excitation beam path (see table 3.1 for used laser systems) and various polarization optics can be added (see section 3.3). A beam splitter transmits part of the excitation light, which is

Table 3.1: Table of laser systems used in this work

Name/Brand	**Wavelength range**	**Mode** if applicable (pulse length/repetition rate)	**in-coupling**
Toptica TVIS	400-700 nm	pulsed (120 fs/ 80 MHz)	module
Nd:YAG	532 nm	cw	module
Coherent Saphire	568 nm	cw	module
Solstis M^2	695-980 nm	cw	module
Tsunami	720-980 nm	pulsed (2 ps/ 82 MHz)	module
Mira-OPO	1100-1600 nm	pulsed (2 ps/ 82 MHz)	fiber-coupled

used to measure the incident light power (if not stated differently a non-polarizing 50:50

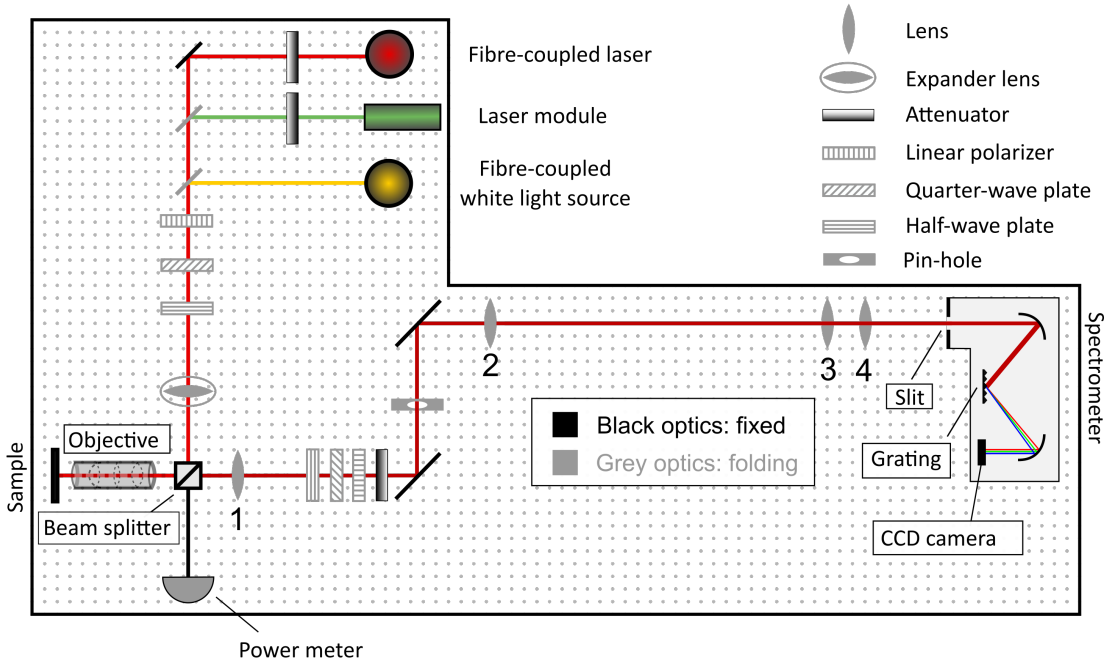

Figure 3.2: Schematic illustration of the photoluminescence and reflectivity setup

beams splitter was used). The light that is reflected at the beam splitter is directed through an objective to the sample. The latter is mounted in a liquid helium cryostat, allowing to cool the sample down to 4.2 K. Using the objective allows to probe a sample with a focus spot diameter of 2 μm for the laser excitation and 10 μm for the white-light illumination. In order to illuminate a larger area on the sample, an expander lens can be folded into the beam path, which focuses the parallel excitation beam in the back focal plane of the objective. By using an expander lens with 100 mm focal length (about 10 mm beam waist), an illumination area of about 500 μm can be achieved.

The re-emitted or reflected light is collected by the objective and propagates through a lens system to the entrance plane of the spectrometer. Depending on the configuration of the lens system, the signal can be either spatial or angle-resolved. Figure 3.3 illustrates the principles of the two lens configurations. To spatially resolve the signal, a so-called real space imaging configuration is used (Figure 3.3a). All light that is emitted from a specific spot on the sample propagates in parallel after passing through the objective, independent of its initial emission angle. The beampaths of light emitted from two different spots on the sample are drawn in blue and red. The emission angles of the light from each spot are encoded in the brightness of each color. A lens is placed in front of the imaging plane, with a distance equivalent to its focal length. Now, all parallel beams are focused at one spot in the back focal plane of this imaging lens (imaging plane). Thus, the sample surface is imaged at the imaging plane. This configuration is equivalent to a conventional

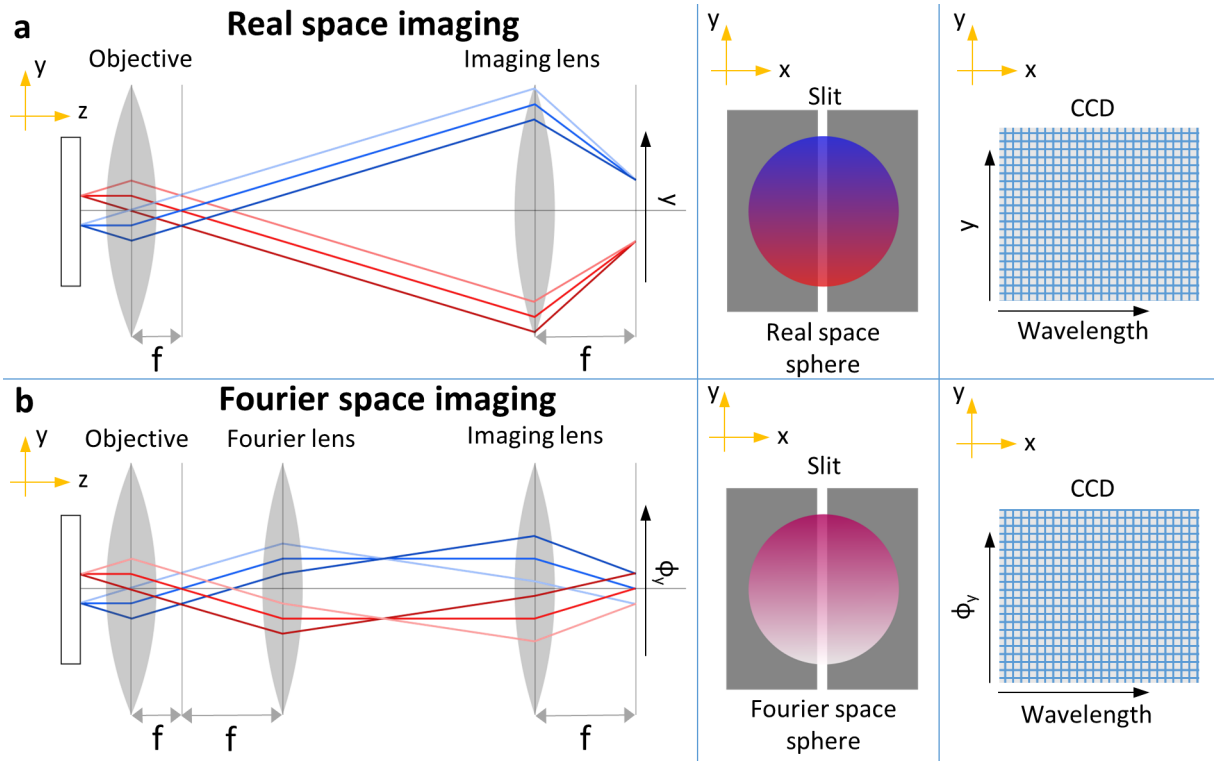

Figure 3.3: Real space (a) and Fourier space (b) imaging configurations: The left panel shows the lens positions and beam paths for each imaging configuration. Different spots on the sample are encoded with blue and red, while the emission angle is illustrated by the brightness of each color. While real space imaging results in focused rays from a specific spot of the sample (all beams of one color) in the imaging plane, the Fourier space imaging focuses all rays with the same initial emission angle (all beams with the same brightness). The central panel shows the spherical images in real and Fourier space view in propagation direction. Applying a line slit allows to cut out a strip of the images, which is subsequently, energetically dispersed by an optical grating. Finally, a CCD chip reads out the signal, which carries either spatial or angle information in y direction and wavelength/energy in x direction (right panel).

microscope, where the image of the sample surface is magnified depending on the front and back focal lengths of the objective and ocular lens. In order to switch to the angle-resolved configuration, a third lens is placed into the beam path, where its distance to the back focal plane of the objective is equivalent to its focal length. This configuration is also known as Fourier space imaging (Figure 3.3b). All light that is emitted from the sample surface under the same angle, but from different spots, is focused in the back focal plane of the objective. In this example, light that is emitted under a certain angle to the top (encoded in light color) is focused at one position and light that is emitted under the

same angle, but to the bottom (encoded in dark color) is focused at a different position. All beams that originate from one spot in the objective back focal plane are parallel after passing through the Fourier lens. In this case, the imaging lens has the same functionality, namely focusing parallel beams on one spot in the imaging plane. However, in the Fourier configuration, parallel beams correspond to an emission angle and not to a spot on the sample. In this way, the angle dependent emission characteristics of the sample is mapped in the imaging plane. It should be noted that the schematics in Figure 3.3 only illustrate the beampath in propagation direction (z) and in one of the perpendicular dimensions (y). Nevertheless, the beam propagation rules also hold true in the other perpendicular dimension (x) due of the spherical geometry of the objective and lenses. The image sizes are limited by the magnification factor of the lens configuration and the numerical aperture of the objective.

In the setup presented in Figure 3.2, the Fourier and imaging lens correspond to lens 3 and 4, respectively. It should be noted that the distance between these two lenses is not crucial for a sharp image of the Fourier space, as long as the vertical dimension of lens 4 is large enough to collect all divergent beams. Lens 1 and 2 simply project the back focal plane of objective to the back focal plane of lens 2. For lenses 1, 2 and 3, it is essential that their distances to the previous lens is equivalent to the sum of their front focal length and the back focal length of the previous lens. Although lens 1 and 2 are in principle not required for real and Fourier space imaging, the key advantage of this configuration is a real space plane in the back focal plane of lens 1. At this position, a pinhole aperture can be placed to carry out spatial filtering while operating the setup in the Fourier configuration. Thus, the emission angle characteristic from a specific spot on the sample can be determined.

Both the real space and Fourier space configurations create an image in the focus plane of the spectrometer system. In the spectrometer, this plane is projected to a charge coupled device (CCD) camera chip with two different options. For the first option, a slit in the entrance plane is closed to cut out a narrow section of the image in y direction. The emitted signal is dispersed by an optical grating with either 150, 600 or 1200 lines/mm and energy resolutions of 1.1, 0.26 and 0.11 meV (at 750 nm), respectively. Ultimately, the CCD chip acquires a data set which carries the spectral information along the x axis and either spatial position or emission angle along the y axis. Alternatively, the slit can be completely opened, the grating is aligned to act as a mirror (zero order reflection) and the CCD camera is used to acquire an energy-averaged image of the emission. In this way, the CCD chip captures the full real space or Fourier space image.

The maximum emission angle Θ_{max} (with respect to the z axis) that is collected by the objective is given by:

$$\Theta_{max} = sin^{-1}(\frac{NA}{n_{medium}}), \tag{3.1}$$

where NA is the numerical aperture of the objective and n_{medium} is the refractive index of the medium between sample and objective (n_{medium} is approx. 1 for air and vacuum). For a given wavelength λ of the emitted light, the in-plane wave vector can be calculated as:

$$k_{||} = \frac{2\pi}{\lambda} sin(\Theta). \tag{3.2}$$

For an objective with a numerical aperture of 0.65 (50 x magnification, used for all experiments in this work, if not noted differently), $\Theta_{max} = 40.5°$, which corresponds to an in-plane wave vector of 5.4 μm^{-1} for an emission wavelength of 750 nm.

3.3 Polarization-resolved spectroscopy

As outlined in chapter 2.2, the spin physics of excitons in TMDC monolayers play a special role and give these materials a unique character. Since the individual valleys can be addressed with circular polarized light, it is essential to control the polarization state of the incident beam and to analyze the polarization of the emitted signal.

To probe the sample with a well defined polarization state, a linear polarizer is placed in the excitation path. Subsequently, either a quarter- or half-wave plate are inserted. Both wave plates are composed of birefringent materials, which induce a phase shift between the two perpendicular polarization components of the transmitted light. In the appropriate orientation, the quarter-wave plate induces a phase shift of $\pi/2$ and thereby converts linearly polarized light to circularly polarized light and vice versa. Depending on which of the two components is retarded in the wave plate, the circularly polarized light is referred to as right handed (σ^+) or left handed (σ^-). The half-wave plate induces a phase shift of π, which alters the orientation of the linearly polarized light. The linearly polarized light is referred to as V and H, when the electric field of the incident wave is oriented vertically or horizontally in the propagation normal plane. Since all optical components may in principle alter the polarizations state of the incident light, a non-polarizing beam-splitter, objective and cryostat glass were used. Although the beam splitter is commercially classified as "non-polarizing, V and H still have reflection and transmission differences on the order of 2 %. Therefore, a polarimeter (Schaefter-Kirchoff SK010PA-VIS) was used to quantify the actual polarization state of the incident light at the position where the sample is placed. In this manner, the orientations of the wave plates can be slightly corrected to compensate for the polarizing effect of the beam splitter. As result, a degree of circular polarization of more than 99 % in front of the cryostat window can be achieved. In addition, it must be also considered that the reflection of the beam splitter and at the sample surface each induce an additional phase shift of π.

After excitation with light of certain polarization state, the reflected and emitted light is analyzed with respect to its polarization. Therefore, a quarter-wave plate is inserted in

the detection path and is oriented in a way that σ^+ is converted to linear polarized light in V orientation and σ^- is converted into the H orientation. Then, a linear polarizer is inserted in V orientation, which transmits all V components (originally σ^+) and blocks all H components (originally σ^-). In such manner, the intensity of the σ^+ component $I(\sigma^+)$ is measured. Analogously, the quarter-wave plate is rotated to measure the intensity of the σ^- component $I(\sigma^-)$. It should be noted that all polarization optics were placed before the first mirror in the detection path (see Figure 3.2), since the mirror may alter the polarization state. In addition, the linear polarizer in the detection is always kept at the same orientation since the sensitivity of the spectrometer depends on the polarization of the detected light. The degree of circular polarization (DOCP) ρ is then determined to be:

$$\rho = \frac{I(\sigma^+) - I(\sigma^-)}{I(\sigma^+) + I(\sigma^-)}. \tag{3.3}$$

In order to analyze the linear components of the emitted and reflected light, the quarter-wave plate in the detection path is replaced by a half-wave plate. In the first configuration, the half-wave plate is oriented in such way that V and H components are not affected. Thus, the subsequent linear polarizer in V orientation transmits the V component and blocks the H component (measurement of $I(V)$). Then, the half wave plate is rotated in order to swap H and V components, so the linear polarizer in V orientation transmits the original H component and blocks the original V component (measurement of $I(H)$). In the this configuration, the degree of linear polarization (DOLP) ρ_{lin} can be determined by:

$$\rho_{lin} = \frac{I(V) - I(H)}{I(V) + I(H)}. \tag{3.4}$$

3.4 Time-resolved spectroscopy

The valley-polarization is closely related to the relaxation and decay dynamics in TMDC monolayers [64]. Because of this, the dynamics of the investigated systems were measured by time-resolved PL experiments. The used setup is very similar to the one presented in Figure 3.2. Here, the real space configuration was used and one spot on the sample is excited with a pulsed laser. To obtain a temporal resolution, a different spectrometer with an attached streak camera (Hamamatsu C5680) was used. The excited spot on the sample is imaged at the entrance slit of the spectrometer, which contains a grating, that disperses the incident light along the x direction just like in the conventional spectrometer. However, here the dispersed light incides on a line-shaped photo-cathode. As a consequence, a photo electron is ejected, which is accelerated by an constant electric field along the propagation direction of the incident light and finally hits a cathodoluminescent screen. Perpendicular to the propagation direction and perpendicular to the wavelength direction (x axis), there

is an electric field applied which varies over time. As a result, the photo electrons are deflected in y direction depending on when the incident photons impinge on the photo cathode. The streak camera is synchronized with the pulsed laser in a way that the start of the sweeping electric field is trigged by the light pulses of the laser. Finally, the spectral information is encoded in the x direction and the time-resolved information is encoded in the y direction of the screen, which is read out by a CCD camera. For all time-resolved measurements in this work, a tunable and pulsed laser (Topitica TVIS) with a pulse length of 180 fs and a repetition rate of 80 MHz was used. The temporal resolution of the streak camera was approx. 4 ps.

Chapter 4

Basic investigations of TMDC monolayers and microcavities

4.1 2D materials and their dielectric environment

Among the TMDC monolayer materials, MoS_2, WS_2, $MoSe_2$ and WSe_2 are best investigated. In order to choose the most appropriate of these materials for either cryogenic or room temperature strong coupling experiments, the most relevant exciton properties are reviewed here. For strong coupling experiments it is important to have a narrow exciton linewidth, high oscillator strength and a high PL intensity, which are therefore compared in table 4.1. The comparison shows that the exciton linewidth depends on the substrate and capping material (see below for more details). It should be noted that the recent improvement by h-BN encapsulation, has not been known at the time when specific material were selected for the strong coupling experiments presented in this work. Thus, this selection was based on linewidth values that were measured for monolayers on SiO_2 substrate.

Based on this comparison, $MoSe_2$ and WSe_2 monolayers are the preferred candidates for low temperature experiments due to their narrow linewidth at cryogenic temperatures. Figure 4.1 presents PL spectra of both materials at 5 K. These measurements confirm the narrow linewidth stated in tabel 4.1. Although linewidth and oscillator strength are comparable for both material, $MoSe_2$ was selected as the material of choice for low temperature experiments, because it has higher PL yield at such temperatures and its PL spectrum is more clearly defined (exciton and trion resonances only).

However, the PL yield of WSe_2 grows with temperature due to its inverted band structure [97] (see also Figure 2.5), while the one of $MoSe_2$ decreases with temperature. At room temperature, the PL yield of WSe_2 has exceed the one of $MoSe_2$ (see table 4.1), which makes WSe_2 an attractive candidate for experiments under ambient condi-

Table 4.1: Exciton linewidth, relative oscillator strength and relative PL intensity for various TMDC monolayers. Values for linewidths at cryogenic temperature refer to monolayers on SiO_2 substrate and are taken from reference [94], while * indicates that linewidths were measured on monolayers with h-BN encapsulation [95]. Room temperature linewidth values are given for h-BN encapsulated monolayers, however the difference to a SiO_2 is small (few meV) at room temperature [95]. The relative oscillator strength values were determined based on the absorption data in reference [96] and have been communicated privately from the authors. The reference value for relative intensity is $MoSe_2$ at 5 K (values are taken from reference [97], where no values were states for MoS_2 and WS_2).

Material	**Linewidth (5 K)**	**Linewidth (5 K)***	**Linewidth (300 K)***	**relative oscillator strength**	**relative Intensity (5 K)**	**relative Intensity (300 K)**
MoS_2	18 meV	3.2 meV	46 meV	1.3	n/a	n/a
WS_2	18 meV	4.5 meV	24 meV	1.9	n/a	n/a
$MoSe_2$	10 meV	3.6 meV	35 meV	1	1	0.17
WSe_2	10 meV	4.0 meV	33 meV	1	0.04	0.76

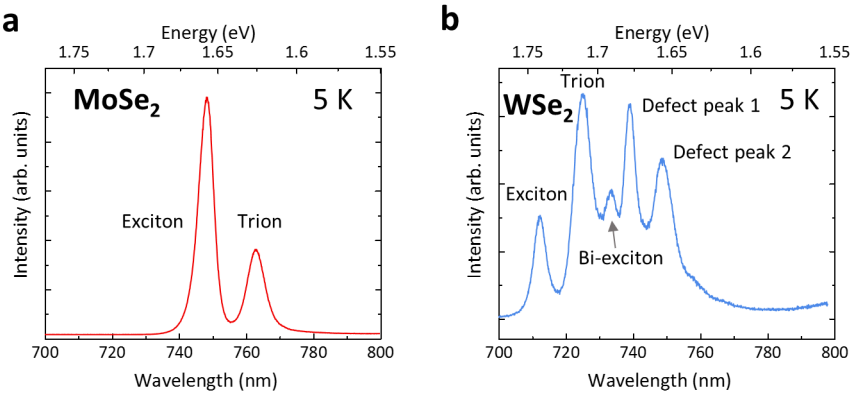

Figure 4.1: Normalized photoluminescence spectra of $MoSe_2$ and WSe_2 monolayer, taken at 5 K. (a) $MoSe_2$ shows an exciton resonances at 748.2 nm/1.657 eV with a linewidth of 11 meV and trion resonance at 763.0 nm/1.625 eV with a linewidth of 13 meV. (See appendix A.1 for details on the energy and linewidth error analysis.) (b) Besides the exciton and trion resonances at 712.4 nm/1.740 meV (10 meV) and 725.3 nm/1.709 eV (12 meV), respectively, the PL spectrum exhibits further low-energy resonances, which are typically associated with the bi-exciton and defect-related emission.

tions. Although WS_2 has a lower PL yield [94], it could be an interesting alternative for room temperature strong coupling because of its narrow linewidth and a factor of 1.9 higher oscillator strength. Figure 4.2 compares the PL spectra of WS_2 and WSe_2 at room temperature. The linewidth of the measured exciton resonances are slightly higher

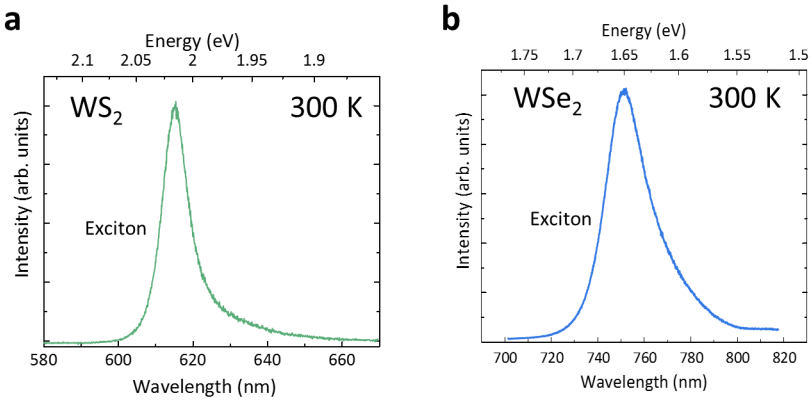

Figure 4.2: Normalized photoluminescence spectra of WS_2 and WSe_2 monolayer, taken at 300 K. (a) WS_2 shows an exciton resonances at 615.4 nm/2.015 meV with a linewidth of 30 meV. (b) WSe_2 exhibits an exciton resonance at 752.2 nm/1.648 eV with a linewidth of 37 meV.

than those presented in table 4.1, which is attributed to the different substrate materials (SiO_2 in this measurement vs. h-BN for the values presented in table 4.1). Nevertheless, WS_2 (30 meV) is still narrower than WSe_2 (37 meV). Furthermore, the exciton energy is a relevant parameter from the experimental perspective. The wavelength range around 750 nm ($MoSe_2$ at 5 K and WSe_2 at 300 K) can be covered by the accessible laser systems (typical tuning range of a titanium sapphire laser: 700 - 980 nm, also see table 3.1), while WS_2 monolayers (around 620 nm) is out of this range. Moreover, III-V semiconductors such as GaAs or AlGaAs strongly absorb in the wavelength range of sulfide based monolayers, and can therefore not be used in microcavities composed of epitaxially grown GaAs/AlGaAs DBRs. It should also be mentioned that the coinciding exciton energies for $MoSe_2$ at 5 K and for WSe_2 at 300 K, allows to use the same cavity design for both monolayers (see next section).

As indicated above, the substrate has a strong influence on the exciton properties. While the linewidth is most strongly affected by the surface roughness, emission energy and binding energy are determined by the dielectric constant and the electronic structure of the substrate [33]. Most commonly, a SiO_2 substrate is used (typically a Si wafer with a thermally oxidized SiO_2 layer of 100 nm thickness). To evaluate the influence of the substrate in more detail, the properties of a $MoSe_2$ monolayer are compared for a SiO_2

substrate and an epitaxially grown GaInP substrate. GaInP is a III-V semiconductor that is used to terminate III-V DBRs (oxidation protection layer) and is considered atomically smooth. Figure 4.3 illustrates the differences between the two substrates. The atomic

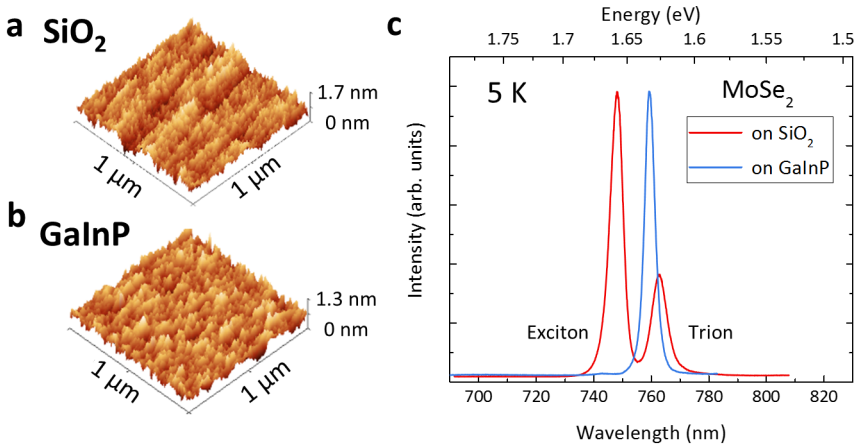

Figure 4.3: $MoSe_2$ monolayer on different substrates: (a) and (b) show AFM images of the SiO_2 and GaInP substrates, respectively. (c) PL spectra of $MoSe_2$ monolayer compared for the two substrates.

force microscopy (AFM) images presented in Figure 4.3a and b reveal surface roughness values (root-mean-squared) of 0.25 nm and 0.16 nm for SiO_2 and GaInP, respectively. In addition, the optical appearance shows uneven regions on the SiO_2 substrate. Although the roughness is higher for SiO_2, 0.25 nm is still an acceptably good value. The PL spectrum of $MoSe_2$ on GaInP (Figure 4.3c) is extremely trion dominant with a trion/exciton intensity ratio of about 80. The exciton peak is hardly visible at all, but still measurable at 743 nm. Both peaks have a linewidth of 7 meV, which is significantly less than for SiO_2 (11 meV). This difference can be attributed to the smooth surface of GaInP. The strong trion dominance on GaInP originates most likely from the band alignment, when substrate and monolayer get in contact, as illustrated in Figure 4.4. While the GaInP can be expected to be undoped, TMDC monolayers typically exhibit unintentional, intrinsic n-type doping [100, 101]. Thus, the Fermi level of the monolayer is increased [100]. While the quantitative Fermi level shift cannot be determined here, the qualitative behavior can explain a band alignment configuration, where both valence and conduction band of the $MoSe_2$ monolayer lie below the ones of GaInP. As a result, electrons are transfered from the substrate to the monolayer, which in turn favors the formation of negatively charged trions. It should be noted that the trion/exciton intensity ratio varies between individual monolayers and may also increase under continuous-wave (cw) laser exposure in the mW range due to photo-doping [102]. In addition, the dielectric environment of the two substrates differs significantly, because of the large difference in the real parts of

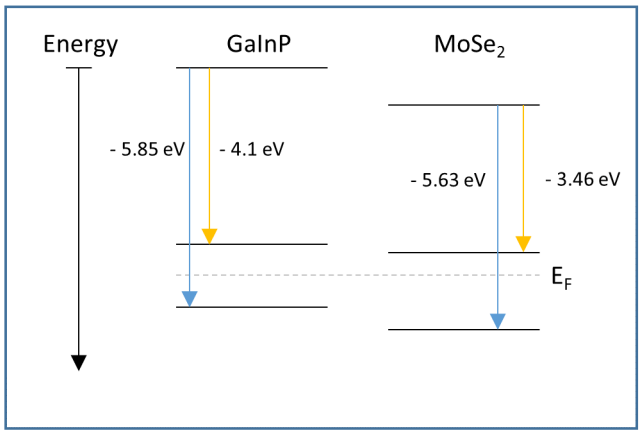

Figure 4.4: Qualitative illustration of the band alignment between GaInP and $MoSe_2$ in contact. The ionization energies for valence and conduction bands are indicated by blue and yellow arrows and have been taken from references [98, 99]. Due to natural n-type doping of the $MoSe_2$ monolayer, its estimated Fermi energy lies above the band gap center. In this configuration, both conduction and valence band of $MoSe_2$ lie below those of GaInP. As a consequence, there is a transfer electrons into the monolayer and of holes into the substrate.

the dielectric constant ε_1 (2.1 for SiO_2 and 11.4 for GaInP [103]). A higher ε_1 decreases the binding energy (see equation 2.2) and thus the exciton energy increases. However, not only the binding energy is affected, but also the electronic band gap is renormalized. Both effects almost compensate each other and therefore the exciton energy only changes by a few meV [30, 33, 32] as described in section 2.2.

In order to integrate a TMDC monolayer into a planar Fabry-Pérot microcavity, at first, a monolayer needs to be placed on a bottom DBR. Subsequently, the monolayer must be capped with some type of dielectric material and finally a top mirror (metal layer or DBR) may be deposited. However, deposition of dielectrics on TMDC monolayers is very challenging since most techniques damage or destroy the monolayer. Such deposition was tested with atomic layer deposition (ALD), physical vapor deposition (PVD/sputtering), electron beam evaporation and plasma-enhanced chemical vapor deposition (PE-CVD). All these techniques damage the monolayer during the deposition process due to a high process temperature, the impact of high energy ions or a reactive process atmosphere. The photoluminescence after such deposition monolayers is either completely quenched or strongly decreased and broadened as in the case of ALD deposition of Al_2O_3. Figure 4.5 presents $MoSe_2$ monolayer room temperature PL spectra before and after deposition of 10 nm Al_2O_3 by ALD at 36° C. The exciton resonance broadens from 39 meV to 46 meV and decreases by a factor of 28 in intensity. Nevertheless, two techniques were identified

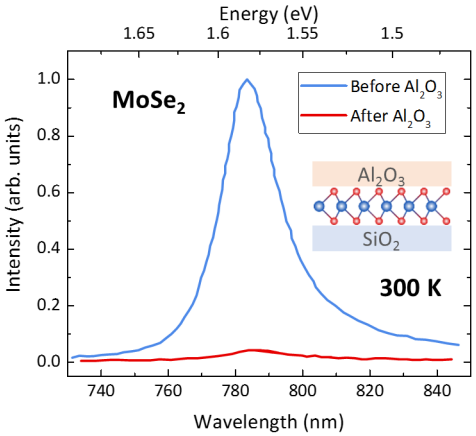

Figure 4.5: Influence of ALD depositon of Al_2O_3 on $MoSe_2$ monolayer PL: The exciton resonance broadens from 39 meV to 46 meV and decreases by a factor of 28.

during the course of this work, which only weakly affect the monolayer properties. These are spin-coating of poly-methyl-methacrylate (PMMA) and plasma-assisted evaporation (PAE) of SiO_2[1]. Figure 4.6 shows the influence of capping a WSe_2 monolayer with these materials. Figure 4.6a compares the monolayer PL before and after capping with PMMA

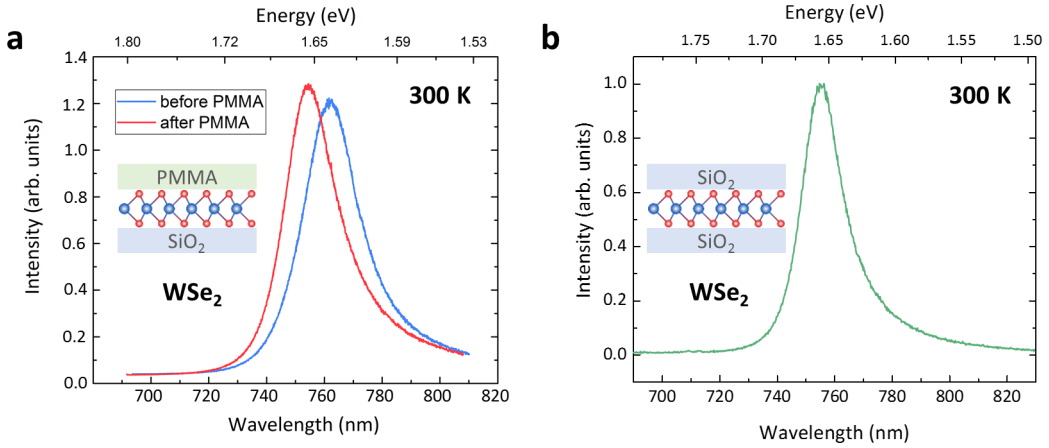

Figure 4.6: Influence of monolayer capping: (a) PL spectra of a WSe_2 monolayer at 300 K before and after PMMA capping (Normalization resembles the original intensity ratio between the spectra, which were both taken under 70 μW excitation power). (b) PL spectrum of a WSe_2 monolayer capped with SiO_2 (PAE) at 300 K.

at room temperature. A shift from 761 nm to 755 nm is observed, which can be explained by a reduced exciton binding energy due to additional dielectric screening in the

[1]The layer deposition with PAE was carried out in close collaboration with H. Knopf, F. Rickelt, U. Schulz and F. Eilenberger, Fraunhofer institute for Applied Optics and Precision Engineering, Jena.

capping layer. Here again, the effect is not very strong since the electronic bandgap is also renormalizing in a compensating way [30, 33, 32]. The shift may also stem from any strain, induced in the capping process, since the exciton energy is very sensitive to strain ($\sim 50\ meV/\%$) [104]. In terms of linewidth, the PMMA actually seems to have a beneficial influence, showing a decrease from 46 meV to 42 meV. In the case of the SiO_2 deposition (Figure 4.6b), the capping does not show a significant broadening either. Although there is no direct before/after comparison available for the identical flake that was analyzed in this measurement, the exciton feature at 754 nm with a linewidth of 36 meV is comparable with resonances of uncapped WSe_2 monolayers presented in Figures 4.1b and 4.6a (37 - 42 meV linewidth).

More recently, it has been shown that using mechanically exfoliated, atomically smooth hexagonal boron nitride (h-BN) as substrate and as capping layer may significantly reduce the linewidth of excitons [31, 105, 106]. The perfectly smooth surface prevents linewidth broadening due to monolayer wrinkles. Moreover, the capping layer prevents the adhesion of molecules on the monolayer surface, which potentially broaden the exciton by inducing charge fluctuations. This approach has been implemented in this work as well. h-BN can be exfoliated and transfered just like TMDC monolayers. However, going to the monolayer limit is not required. In fact, a h-BN monolayer is hardly visible at all under an optical microscope and thus few-layer h-BN flakes (5 - 10 nm thick) were used as substrate and capping layers. The lateral size of the h-BN flakes may easily exceed 50 x 50 μm. The transfer microscope presented in section 3.1 was used to align h-BN and TMDC flake on top of each other. After transferring the first h-BN flake, the sample is annealed at 150° C for 3 minutes in N_2 atmosphere to release a number of potentially adsorbed or trapped contamination molecules. Annealing the full stack of h-BN/TMDC monolayer/h-BN also improves the contact between individual flakes, but may also lead to bubble formation. Figure 4.7a shows a microscope image of a full stack. The PL spectrum of such h-BN encapsulated $MoSe_2$ monolayer is compared to a $MoSe_2$ monolayer on SiO_2 at 5 K in Figure 4.7b. The h-BN encapsulated $MoSe_2$ monolayer exhibits resonances with linewidths of 3 meV (as compared to 10 meV for $MoSe_2$ monolayer on SiO_2) and is shifted red by 22 meV. According to calculations presented in reference [33], the exciton binding energy should decrease by about 150 meV by the enhanced dielectric screening of the h-BN layers. However, as in the previous cases, the self-energy contribution is also strongly reduced and thus there is actually a red shift of 22 meV despite of the strongly altered dielectric screening. These results show that the quality of the monolayer can be significantly improved by h-BN encapsulation as also compared in table 4.1.

Based on previous finding and first PL experiments, $MoSe_2$ was selected for low temperature experiments, due to its narrow linewidth and its relatively high PL intensity. WS_2 and WSe_2 are more suitable for room temperature experiments. WSe_2 has a four-fold

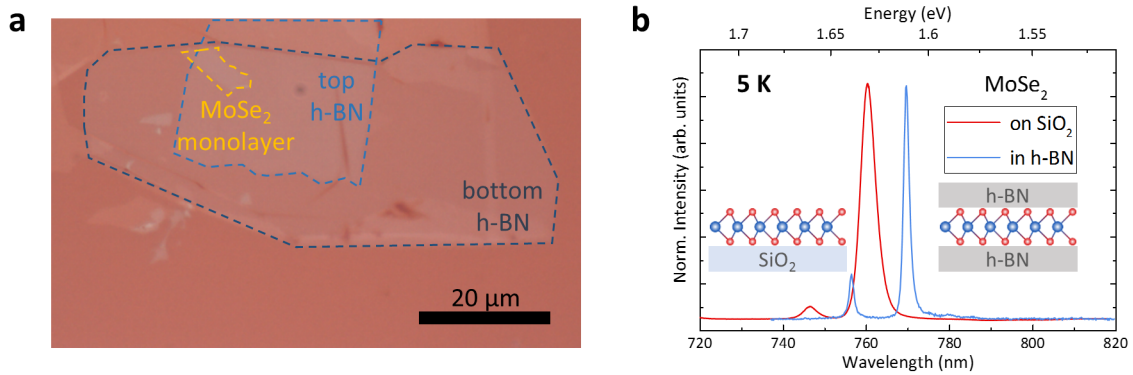

Figure 4.7: Monolayer encapsulation with h-BN: (a) Microscope image of a h-BN/$MoSe_2$/h-BN stack. (b) PL spectra of a $MoSe_2$ monolayer on SiO_2 compared to the encapsulated monolayer at 5 K.

higher PL yield under ambient conditions than $MoSe_2$. WS_2 exhibits the highest oscillator strength and the narrowest linewidth at room temperature of the compared materials, but is not well covered by the available excitation laser sources for near-resonant excitation. It has been shown that a smooth substrate is beneficial for the resonance linewidths, but also doping effects from the substrate must be considered. TMDC monolayers are challenging to overgrow, but spin-coating with PMMA and plasma-assisted evaporation of SiO_2 only weakly affect the exciton resonances. Finally, encapsulation with h-BN results in excellent optical properties and is also compatible with the previous two capping techniques. Based on these results, different cavity designs were implemented, as presented in the next section.

4.2 Microcavity designs

As shown above, integrating TMDC monolayers in planar microcavities is challenging because of the few, available approaches to overgrow the monolayers without damaging them. For the first unambiguous demonstration of strong coupling with a TMDC monolayer, this problem was circumvented by using a so-called ”open cavity” design, where a monolayer is transfered on a bottom DBR and the top mirror is approached with a piezo stage [107, 108]. This leaves an air/vacuum gap between the mirrors and therefore does not require to overgrow of the monolayer. However, the gap is typically on the order of a few micrometers, meaning that the cavity length is rather large as compared to a cavity length of about 260 nm in a fully grown design. This value depends on the target wavelength of the cavity resonance and the cavity material (see equation 2.9) and refers to $\lambda_C = 750$ nm and SiO_2 as cavity material in this case. This short cavity length is

beneficial for the coupling strength (see equation 2.23). Moreover, the open cavity approach demands extreme requirements for the mechanical stability as the cavity mode is very sensitive to the gap length. In this section, three new fabrication approaches are described to fully integrate the monolayer in compact microcavities. The cavity designs were simulated based on the transfer matrix method [67] and the required refractive indices were taken from the Filmetrics refractive index database [109] or the n,k data base of the Ioffe Physical-Technical Institute, Russia [110]. Here, the fabrication process and measurements on empty cavities (without active material) are described. Nevertheless, all presented approaches are fully compatible with monolayer integration.

4.2.1 DBR-metal design

The DBR-metal design is particularly promising because of its ease in fabrication and its low effective cavity length. First, a bottom DBR is taken, which terminates with a low refractive index material. The stopband center is preferably at the target wavelength of the cavity resonance. The monolayer can be transferred on the DBR and then the full structure is spin-coated with a $\lambda/4n$-thick layer of PMMA. Finally, a thin, semi-transparent layer of metal (typically 30-60 nm) is deposited on top as depicted in Figure 4.8a. The choice of metal depends on the cavity target wavelength. At 620 nm (exciton

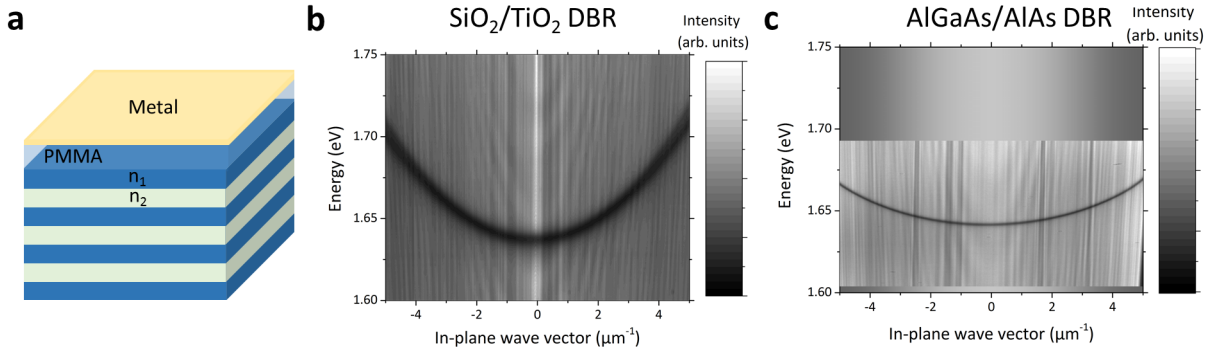

Figure 4.8: DBR-metal design: (a) Schematic illustration of a DBR-metal photonic structure. (b and c) Reflectivity dispersion relations of DBR-metal structures based on SiO_2/TiO_2 and AlGaAs/AlAs DBRs, respectively. Both diagrams are scaled in the same manner for a better comparison of the dispersion curvature.

resonance of WS_2 at 300 K), silver has a higher reflectivity than gold (96.7 % as compared to 92.5 % (see appendix A.2)). Around 750 nm (exciton resonance of $MoSe_2$ at 5 K and of WSe_2 at 300 K), gold and silver have a comparable reflectivity of 97 % (see appendix A.2), but gold is preferred because of its long term stability under ambient conditions.

DBRs based on oxide dielectric material are commercially available. A typical material combination is SiO_2/TiO_2, because of its high refractive index contrast ($n_{SiO_2} = 1.454$, $n_{SiO_2} = 2.360$ at 750 nm). Figure 4.8b presents a typical cavity dispersion of a DBR-metal cavity, measured in reflectivity. The cavity is based on a SiO_2/TiO_2 DBR and gold as the top layer. These cavities typically feature Q-factors of 50 to 350, depending on the metal layer thickness, and an effective cavity length of 300 nm (cavity resonance at 750 nm). Figure 4.9a shows reflectivity spectra of empty cavities with a different gold layer thickness, illustrating that the cavity mode linewidth is lower for a thicker gold layer and thus the Q-factor is larger (equation 2.10). This relation has been simulated

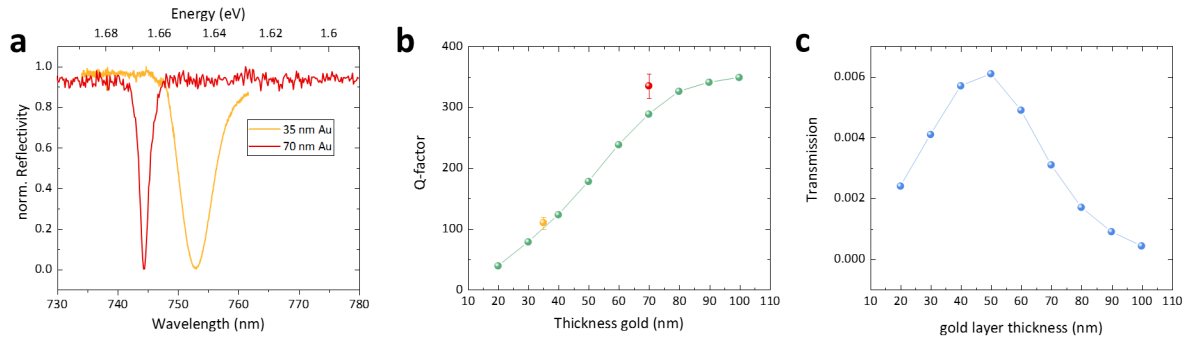

Figure 4.9: (a) Reflectivity spectra of empty SiO_2/TiO_2 DBR-metal cavities with a 35 nm and a 70 nm gold layer thickness (spectra were normalized to 1). While 35 nm of gold result in a Q-factor of 110, the increased gold thickness of 70 nm enhances the Q-factor to 335. (b) Relation of Q-factor to gold layer thickness, calculated by the transfer matrix method. Experimental values from (a) are plotted in yellow (35 nm gold) and red (70 nm gold). (c) Simulated transmission of the full structure as a function of the gold layer thickness.

by transfer matrix calculations as plotted in Figure 4.9b. The Q-factor increases linearly with the gold layer thickness and starts to saturate for layer thicknesses of more than 70 nm and converges to a value of about 350. The experimentally observed values are actually slightly larger than in the simulation, which might be explained by a difference between the assumed and real refractive index of the thin film gold. Figure 4.9c depicts the simulated transmission of the full structure. For thin, semi-transparent layers of gold, the reflectivity increases with the layer thickness. Thus, the photon stays longer in the cavity, which is equivalent to a higher Q-factor (see equations 2.10 and 2.11). This behavior also manifests in an increasing transmission of the full structure as also seen in the simulation. However, for thicker layers the absorption of gold becomes dominant and decreases the transmission through the full structure. Consequently, the transmission is a good measure for the gold absorption at high gold layers thicknesses. Although a high Q factor is desired, which suggest a thicker gold layer, the absorption from a thick gold

layer also reduces the emitted photoluminescence signal of a cavity including a TMDC monolayer. Thus, the layer thickness was kept between 35 nm and 60 nm for final devices.

Alternatively, an epitaxially grown DBR, based on III-V semiconductors, known for its extremely high reflectivity, can be taken[2]. In this particular case, a PMMA layer thickness of less than $\lambda/4n$ was used to form so-call optical Tamm modes. These optical modes were first predicted to appear at the interface between two periodic DBR structures with different periodicity [111], but also form so-called Tamm plasmon polaritons close to the interface of a DBR and a thin metal layer [112, 113]. It was also shown that these optical modes may strongly couple to excitons in GaAs quantum wells [114]. Photonic structures hosting these Tamm modes are therefore not referred to as classical Fabry-Perot microcavities, but are called Tamm structures. While the SiO_2/TiO_2-DBR based cavities have a cavity thickness (SiO_2+PMMA) of $\lambda/2n$, the design based on the AlGaAs/AlAs DBR strongly diverges from this criteria (cavity length $\sim \frac{3}{8}\lambda/n$) and is therefore referred to as a Tamm structure. Despite of this difference, Tamm structures behave like conventional microcavities with respect to the properties described in section 2.3. Figure 4.8c shows a dispersion relation for a Tamm structure based on an AlGaAs/AlAs DBR and a metal layer. Here, the linewidth is significantly reduced, corresponding to a Q-factor of 960 ± 40 (see appendix A.3 for Q-factor error analysis). In both photonic structures, the limiting factor for Q is the layer with the lower reflectivity (see also equation 2.10), which is gold in both cases. Nevertheless, the Tamm structure features a higher Q-factor. However, the Q-factor also depends on the effective cavity length [115]:

$$Q = \frac{2L_{eff}}{\lambda_C}\frac{\pi}{1 - R_1R_2}. \tag{4.1}$$

This can be understood as a longer effective cavity length increases the photon cycling time in the cavity, which in turn is equivalent to a narrow linewidth and higher Q-factor (see equations 2.10 and 2.11). The effective cavity length for the Tamm structure (750 nm) is a factor of 2.5 longer than the one of the SiO_2/TiO_2 based cavity (300 nm), because the refractive index contrast is lower in the AlGaAs/AlAs DBR (n_{AlAs} = 3.044, n_{AlGaAs} = 3.525 at 750 nm). In fact, the Q-factors of the AlGaAs/AlAs based Tamm structure are about a factor of 3 larger than for SiO_2/TiO_2 based DBR-metal cavities.

When comparing both dispersion relations, it is also striking that the parabolic dispersion of the SiO_2/TiO_2 based cavity has a stronger curvature, which is equivalent to a lower effective cavity mass (see equation 2.16). Here, the effective mass of the SiO_2/TiO_2 based cavity is 1.41 (± 0.07) x 10^{-5} m_0 compared to 4.29 (± 0.21) x 10^{-5} m_0 for the AlGaAs/AlAs based Tamm structure (see appendix A.5 for error analysis). This is not

[2] All III-V semiconductor DBRs used in this work were grown by M. Wurdack during his master project at the chair for applied physics, University of Würzburg.

surprising since the effective mass depends quadratically on the refractive index of the cavity material (see equation 2.17).

Overall, the SiO_2/TiO_2 based cavity provides a low effective cavity length (about 300 nm) and low cavity mass (about 1.4 x 10^{-5} m_0). However, its Q-factor is limited to 350 at best. Using an AlGaAs/AlAs DBR allows to significantly improve the Q-factor (up to 1200), however the effective cavity length is increased by a factor of 2.5 and the cavity mass by a factor of 3. In any case, the top gold layer is strongly absorbing. Assuming a 50 nm thick gold layer and an emission wavelength of 750 nm, about 99.4 % of the emitted light is absorbed (see figure 4.9c). This reduces the excitation and emission efficiency, making the experimental conditions more difficult. Moreover, even a Q-factor of 1200 is still relatively low as compared with more common III-V semiconductor microcavities, where Q-factors of at least 4000 are routinely achieved [4] [3]. Therefore, microcavities with bottom and top DBRs are desired to further increase the Q-factor and to eliminate the absorption of the metal layer.

4.2.2 Mechanically assembled DBR-DBR cavity

Since overgrowing a TMDC monolayer with a top DBR is challenging, an alternative approach pursues the idea of growing the DBR on a separate substrate. Subsequently, the top DBR can be placed mechanically on top of the bottom DBR. To implement this idea, a TMDC monolayer is transfered on a SiO_2/TiO_2 bottom DBR (10 pairs) that terminates with the low refractive index material. The DBR is subsequently spin-coated with PMMA ($d_{PMMA} = \lambda/4n$). Then, a sharp item, such as a screw driver, is used to scratch off small pieces of a SiO_2/TiO_2 DBR coating from a separate substrate. This procedure yields small pieces (about 50 x 50 μm) of this DBR coating (8 pairs, high refractive index termination). These pieces can be picked up with a PDMS gel film and can subsequently be transfered on the prepared bottom DBR with the same transfer method as for the TMDC monolayers (see section 3.1). The van-der-Waals force is sufficient to hold both DBRs together. The PMMA layer on top of the bottom DBR acts as spacer between the DBRs. Its thickness may be varied to adjust the cavity resonance. The full structure is illustrated in Figure 4.10a. Due to the asymmetry of DBR pair number, most light is coupled out towards the top direction, where the signal is detected. Using a top DBR also allows to eliminate light absorption of the top metal layer and thus the overall extraction efficiency is increased. The dispersion relation, measured in reflectivity as shown in Figure 4.10b, reveals a cavity mass of 1.23 ($\pm$ 0.06) x 10^{-5} m_0. This is slightly lower, but still comparable with the one of the SiO_2/TiO_2 based DBR-metal cavity.

[3] The highest, directly measured Q-factor for a cavity in a strongly coupled exciton-polariton system with GaAs quantum wells was 17000 [116].

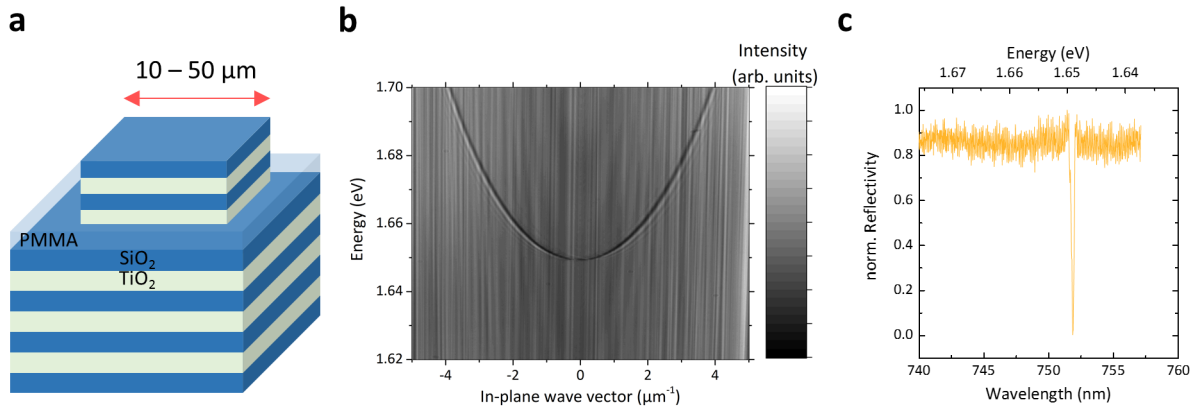

Figure 4.10: Mechanically assembled DBR-DBR cavity: (a) Schematic illustration of the cavity structure. (b) Cavity dispersion measured in reflectivity. (c) Normalized reflectivity line spectrum at $k_{||} = 0\ \mu m^{-1}$ measured with a high-resolution optical grating (See appendix A.4 for details on data treatment).

The line spectrum at $k_{||} = 0\ \mu m^{-1}$, depicted in 4.10c, shows an extremely narrow cavity mode with a linewidth of 0.163 nm. This corresponds to a Q-factor of 4600 ± 200. According to the transfer matrix calculation of this structure, the Q-factor of 25000 can be theoretically achieved, however it is presumably limited by absorption at the material interfaces or at material inhomogeneities. The calculation also yields an effective cavity length of 400 nm as compared to 300 nm for the SiO_2/TiO_2 based DBR-metal cavity. Overall, this approach significantly improves the Q-factor and avoids the use of an absorbing metal layer, while still keeping a low cavity length and mass. A slight drawback is the challenging mechanical assembly as compared to the fabrication of DBR-metal structures.

4.2.3 Fully grown DBR-DBR cavity

While the mechanically assembled DBR-DBR cavity works well on the prototype level, growing the top DBR would provide a more controlled and reproducible fabrication of more robust microcavities. Since plasma-assisted evaporation of SiO_2 is compatible with TMDC monolayers, this deposition technique can be also used to grow a full SiO_2/TiO_2 DBR on top of a bottom DBR including a monolayer[4]. The resulting, fully grown microcavity is illustrated in Figure 4.11a. Again, the cavity is designed slightly asymmetric with a bottom DBR of 10 pairs and a top DBR of 9 pairs. The dispersion relation and a line spectrum at $k_{||} = 0\ \mu m^{-1}$, measured in reflectivity (Figures 4.11b and c, respectively),

[4]The layer deposition with PAE was carried out in close collaboration with H. Knopf, F. Rickelt, U. Schulz and F. Eilenberger, Fraunhofer institute for Applied Optics and Precision Engineering, Jena.

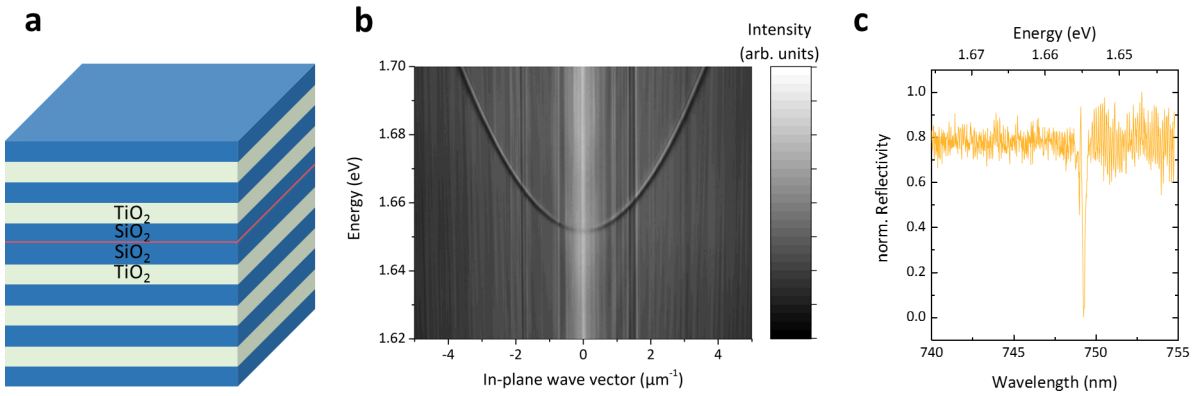

Figure 4.11: Fully grown DBR-DBR microcavity: (a) Schematic illustration of the cavity structure. The red layer in the cavity center indicates the surface of the bottom DBR. (b) Cavity dispersion measured in reflectivity. (c) Reflectivity line spectrum at $k_{||} = 0\ \mu m^{-1}$ measured with a high-resolution optical grating.

demonstrate a cavity mass of 1.32 ($\pm$ 0.07) x 10^{-5} m_0 and a sharp cavity resonance with a linewidth of 0.157 nm, which is equivalent to a Q-factor of 4700 $\pm$ 400. These values are well comparable with the mechanically assembled monolithic cavity, while the sample fabrication is more controlled and the cavity is significantly more robust.

DBR-metal based microcavities and Tamm structures are relatively easy to fabricate and provide a small effective cavity length, in particular compared to an open cavity design. However, their Q-factor is limited and the absorbing metal layer strong reduces the excitation power and emission intensity. DBR-DBR based microcavities are more challenging to fabricate, but exhibit significantly higher Q-factors and strongly improved PL extraction.

4.3 Estimation of normal mode splittings

The first clear demonstration of exciton-polaritons with a TMDC monolayer, namely $MoSe_2$, was shown at cryogenic temperatures in 2015 [107]. However, strong coupling could not be demonstrated at room temperature in this work, presumably because the normal mode splitting decreases too much with temperature. The reasons for this are a decrease of the oscillator strength and an increase of the exciton linewidth towards higher temperatures (see equation 4.4 and 2.23). In order to estimate whether exciton-polariton formation and condensation can be achieved at room temperature in principle and to select the appropriate cavity design, the temperature-dependent normal mode splitting was calculated with the transfer matrix method for a $MoSe_2$ monolayer that is

hypothetically integrated into various cavity designs.

This calculation required the dependencies of the exciton oscillator strength f and linewidth Γ_X on temperature as an input. Therefore, the reflectance contrast $\Delta R/R$ of a $MoSe_2$ monolayer on a SiO_2 substrate was measured as a function of temperature. Following the convention of references [28, 117], the reflectance contrast is obtained as $\Delta R/R = (R_{sample} - R_{substrate})/R_{substrate}$, where R_{sample} is the reflectivity measured on the monolayer position and $R_{substrate}$ is the reflectivity measured on the bare substrate (see appendix A.6 for raw data treatment). Figure 4.12a presents the exciton resonance in the reflectance contrast spectra for various temperatures. Linewidth and amplitude of the

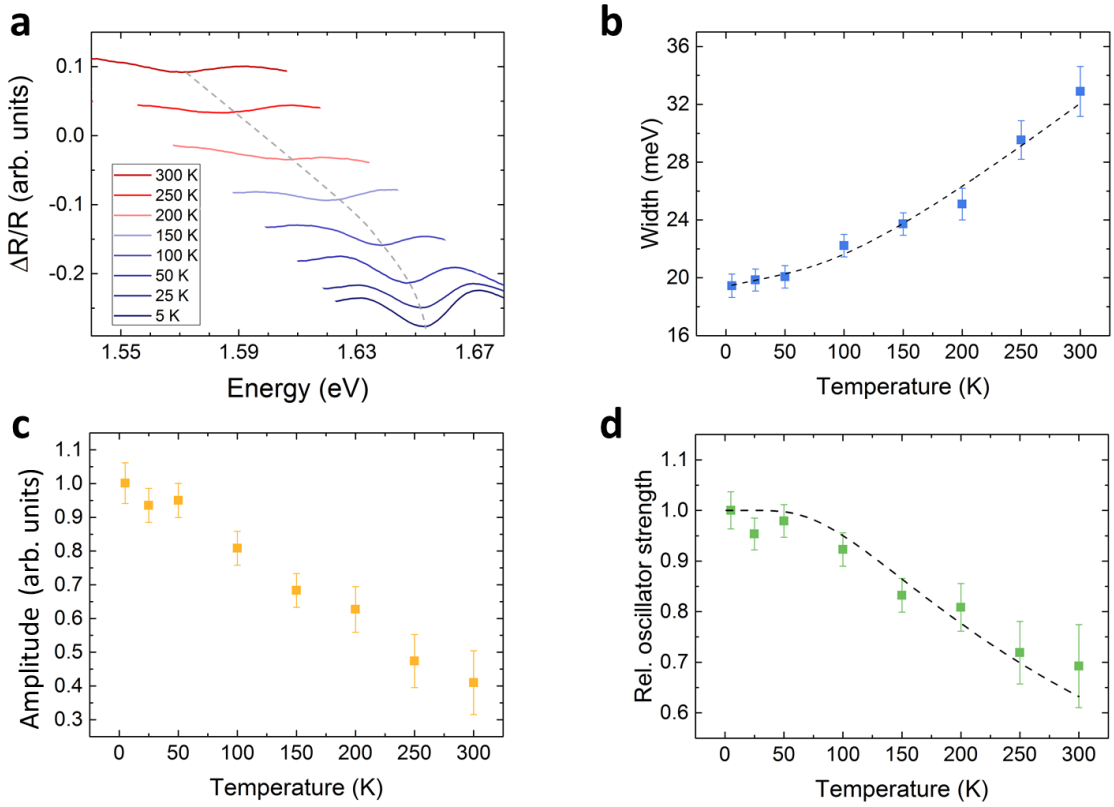

Figure 4.12: Temperature-dependent μ-reflectance contrast measurements of a $MoSe_2$ monolayer. a) exciton absorption features of the spectra for various temperatures. b) exciton linewidth (FWHM) as a function of temperature. c) amplitude of the exciton feature as a function of temperature. d) Relative oscillator strength expressed as the product of linewidth and amplitude as a function of temperature.

absorption dip were extracted from these spectra and are presented in Figures 4.12b and c (see appendix A.7 for fitting details). The linewidth dependence on temperature can be fitted by

$$\Gamma_X(T) = \Gamma_{X,0} + \Gamma_{X,AP}T + \Gamma_{X,OP}\frac{1}{e^{\frac{E_{LO}}{k_B T}} - 1}, \tag{4.2}$$

where $\Gamma_{X,0}$ is the exciton linewidth at 0 K in the presence of inhomogeneous broadening, $\Gamma_{X,AP}$ is the linear broadening constant attributed to acoustic phonon dephasing [118, 42], $\Gamma_{X,OP}$ is the broadening constant attributed to optical phonons, and E_{LO} is the optical phonon energy, where E_{LO} was fixed at 30 meV [119]. Such fitting results in parameters of $\Gamma_{X,0} = 19.4$ meV, $\Gamma_{X,AP} = 1.55 \times 10^{-2}$ meV K^{-1} and $\Gamma_{X,OP} = 8.6$ meV. The exciton linewidth at 5 K (19.4 meV $\pm$ 0.3 meV, measured by reflectance contrast) is broader than previously observed (11 meV, measured by PL), whereas the linewidth at room temperature (33 meV) is in good agreement with literature PL measurements (34 meV)[107]. The difference could stem from a higher surface roughness of the substrate or from averaging over a larger illumination area. Here, the spot size was experimentally limited to about 10 μm, which potentially contains more defects and substrate inhomogeneities that broaden the exciton resonance as compared to a smaller excitation laser spot of about 2 μm in a PL experiment. At room temperature, the linewidth is dominated by phonon broadening, which is independent of roughness or defect-induced broadening, making it less sensible to the spot size.

The resonance amplitude, presented in Figure 4.12c, decreases linearly by 60 % from 5 K to 300 K. The resonance area, approximated by the product of linewidth and amplitude, is a measure of the oscillator strength. Although, this procedure does not yield quantitative values for the oscillator strength, the relative development of oscillator strength with temperature can be extracted this way, which is presented in Figure 4.12d. The relative oscillator strength drops by 30 % towards room temperature, which is explained by a reduced fraction of excitons within the radiative light cone [44] (see appendix A.9 for modeling and fitting).

These results were used to simulate the normal mode splittings with the transfer matrix method for various cavity designs and for the temperature range from 5 K to 300 K. In order to calculate the normal mode splitting by the transfer matrix method, the dielectric function of the $MoSe_2$ monolayer $\tilde{\epsilon}(\omega)$ can be modeled as a Lorentz oscillator:

$$\tilde{\varepsilon}(\omega) = \varepsilon_b(\omega) + \frac{A}{\omega_0^2 - \omega^2 - i\Gamma_X\omega}, \tag{4.3}$$

where ε_b is the background dielectric function (value of 26 was taken from reference [120]), A is the oscillator amplitude and ω_0 is the light frequency which corresponds to the exciton resonance. Then, the complex refractive index $\tilde{n}(\omega) = n + ik$ was derived from $\tilde{n}(\omega) = \sqrt{\tilde{\epsilon}(\omega)}$, which can be subsequently used for transfer matrix calculations.

In order to obtain an initial ($T = 5K$) value for A, the normal mode splitting that had been measured in reference [107] (open cavity design) was reproduced. Since the

measured linewidth is broader (19.4 meV) as compared to reference [107] (11 meV), the reference normal mode splitting needed to be corrected. For this, equation 2.27,

$$\hbar\Omega = \sqrt{V^2 - (\frac{\Gamma_X - \Gamma_C}{2})^2}, \tag{4.4}$$

was used and values for V (36 meV) and Γ_C (1.6 meV) [107] were taken to calculate a corrected normal mode splitting of 17.5 meV, which is slightly lower than the measured normal mode splitting of 20 meV [107].

Subsequently, a transfer matrix calculation for the cavity design described in reference [107] was run and A was adjusted to 0.4×10^{15} s^{-2} to reproduce the normal mode splitting of 17.5 meV. A and Γ_X were adjusted in the subsequent transfer matrix calculations for higher temperatures according to the results presented in Figure 4.12 (see also appendix A.8).

Transfer matrix calculations were not only conducted for the open cavity design [107], but also for a SiO_2/TiO_2 based DBR-metal design and a fully monolithic DBR-DBR design. For each cavity design, the normal mode splitting was determined for the zero detuning case. The transfer matrix calculations provide simulated reflectivity spectra, as presented in Figure 4.13, which were then fitted by a double-Gaussian fit to extract the normal mode splitting. While the distinct normal mode splitting can be clearly identified

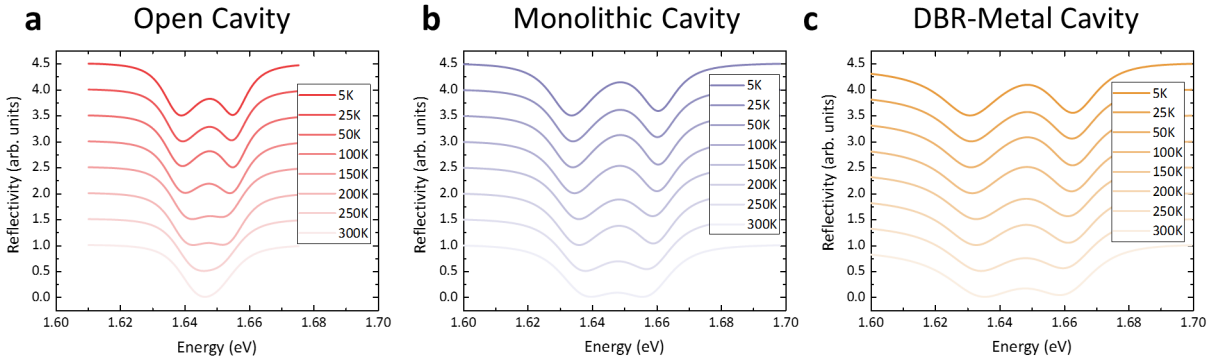

Figure 4.13: Simulated reflectivity spectra at various temperatures from 5 K to 300 K for (a) the open cavity, (b) the monolithic cavity and (c) the DBR-metal cavity. While the distinct peak splitting vanishes in the open cavity design for temperatures above 200 K, it can be clearly identified even at 300 K for the monolithic and DBR-metal cavity.

for the monolithic and DBR-metal cavity even at room temperature, the double-peak shape of the reflectivity spectrum vanishes in the open cavity case for temperatures above 200 K.

The splittings for each cavity and its dependence on temperature are presented in Figure 4.14a. The splittings for the DBR-metal cavity and the monolithic cavity are sig-

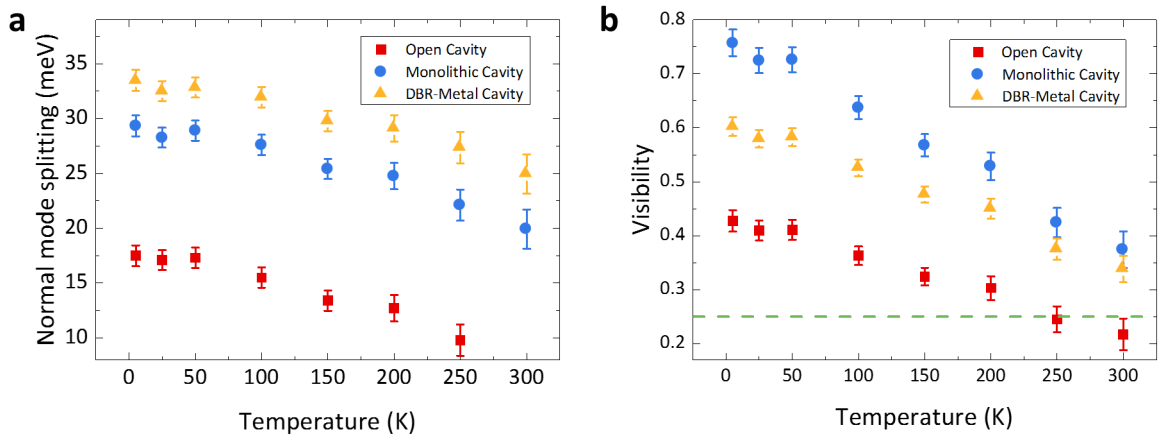

Figure 4.14: a) Simulated normal mode splittings for various cavity designs for temperatures from 5 K to 300 K. b) Corresponding, calculated visibility parameters, where the visibility threshold, required for the observation of strong coupling (0.25) is marked as green-dashed line.

nificantly larger (33 meV and 29 meV, respectively) than for the open cavity (17.5 meV). The difference can be well explained with a stronger mode confinement and lower effective cavity length of DBR-metal cavity and monolithic cavity, which are 310 nm and 410 nm, respectively, as compared to 2380 nm for the open cavity (see equations 4.4 and 2.23). Independent of the cavity, the splittings show similar, monotonously decreasing trends with increasing temperature. This reflects the decrease in oscillator strength and the increase in exciton linewidth. At 300 K, the normal mode splittings are 25 meV and 20 meV for DBR-metal cavity and monolithic cavity, respectively. It should be noted that no clear normal mode splitting can be resolved for the open cavity at this temperature.

In order to elaborate whether strong coupling can be observed for the given splittings, the visibility parameter υ is introduced as [121]

$$\upsilon = \frac{\frac{V}{4}}{\Gamma_X + \Gamma_C}. \tag{4.5}$$

This parameter takes into account that exciton and cavity linewidths must be still sufficiently narrow to observe strong coupling for a given splitting. For values of υ higher than 0.25, strong coupling can be distinctly observed [121]. Initial values ($T = 5\ K$) for V were back-calculated from the obtained splittings with equation 4.4. Figure 4.14b shows the visibility for each cavity design as a function of temperature. At 5 K, the visibility lies well above the threshold of 0.25, indicated by the green dashed line for all cavity designs. However, at above 200 K the visibility of the open cavity drops below the threshold, which is well in line with the fact that no splitting could be resolved in the simulated spectra in this case, as seen in Figure 4.13a. Nevertheless, the visibility of DBR-metal

and monolithic cavity remain above the threshold even at 300 K. Although, the DBR-metal cavity has the higher splitting of the two, the monolithic cavity exhibits the higher visibility, because of its significantly narrower cavity linewidth (0.2 meV as compared to 8.4 meV for the DBR-metal cavity). This difference reflects the high variation of Q-factors of the simulated cavities, which are 200 for the DBR-metal cavity, 3600 for the open cavity as described in reference [107] (eight pairs of SiO_2/NbO_2 for bottom and top DBR, Q of 2050 was measured) and 8250 for the monolithic cavity (eight pairs of SiO_2/TiO_2 for bottom and top DBR, Q of 4700 was measured on a cavity with ten bottom and nine top SiO_2/TiO_2 pair (section 4.2.3)). Despite of the large difference in Q-factor, the visibility of DBR-metal cavity and monolithic cavity are on a comparable level. This is because the cavity linewidth only makes up a smaller contribution to the splitting and visibility (see equations 4.4 and 2.23) as compared to the exciton linewidth on the order of 35 meV at 300 K.

According to these results, it should be possible to observe strong coupling at room temperature. The maximum temperature at which exciton-polaritons could be still observed is not limited by the thermal decomposition of the excitons, due to their large binding energies. Instead, the decrease of visibility will set the limit for strong coupling at elevated temperatures. By linear extrapolation of the visibility dependence on temperature, the threshold of 0.25 is reached at about 400 K for both the DBR-metal and the DBR-DBR monolithic cavity. These results also imply that a low effective cavity length is more relevant than a high Q-factor in order to observe strong coupling at room temperature. For this reason, the DBR-metal cavity approach, which has the lowest effective cavity length, was used for the first attempt to demonstrate strong coupling with a TMDC monolayer at room temperature (see section 5.1). However, it should be noted that the Q-factor is nevertheless a very crucial parameter for experiments beyond the pure demonstration of strong coupling such as the condensation of exciton-polaritons. The reason is that the Q-factor strongly relates to the polariton lifetime (see equations 2.10 and 2.30), which in turn is essential for such an experiment. The results of this section have shown that decreasing the effective cavity length by selecting an appropriate cavity design increases the coupling strength (see equation 2.23). Alternatively, several distinctly separated monolayers can be integrated into a microcavity as suggested in reference [107], since the coupling constant scales with the number of monolayer as $\sqrt{n_{eff}}$ (see equation 2.23)[5].

[5]The experimental data presented in this section were acquired in close collaboration with A. Maryński and G. Sek, University of Wroclaw. Results of this section were published in reference [8]

4.4 Phase diagram of exciton-polaritons

In order to evaluate if strongly coupled excitons in TMDCs monolayers could form a polariton condensate, a phase diagram for the $MoSe_2$ monolayer material system was calculated. The calculation is based on the approach described in reference [68]. The phase diagram describes the polariton density N in the system, which is required for polariton condensation at a given temperature T. For a finite system with the spatial extension L, the polariton density N is given by:

$$N(T, L, \mu) = \frac{N_0}{L^2} + \frac{1}{L^2} \sum_{\mathbf{k}, k > \frac{2\pi}{L}} \frac{1}{exp(\frac{E(\mathbf{k}) - \mu}{k_B T}) - 1}, \tag{4.6}$$

assuming a Bose-Einstein distribution (see equation 2.35), where the polariton dispersion relation $E(k)$ is described by equation 2.22 and N_0 is the ground state population. Defining the critical density N_c as the maximum number of particles that can be accommodated in all states but the ground state, one can write:

$$N_c(T, L) = \frac{1}{L^2} \sum_{\mathbf{k}, k > \frac{2\pi}{L}} \frac{1}{exp(\frac{E(\mathbf{k})}{k_B T}) - 1}. \tag{4.7}$$

Here, μ is set to be zero, which allows to put an unlimited number of polaritons into the ground state, while the concentration of polaritons in the upper states is constant and equal to $N_c(T, L)$. The condensate density is thus equal to $N_0 = N - N_c$. The upper limit for N is assumed to be the Mott density. For the calculation, the following parameters were assumed: $\Delta E = 0$ meV, $m_{ph} = 10^{-5}$ m_0, $m_{ex} = 0.8$ m_0 [122], $L = 10$ μm and $a_B = 2$ nm [30]. The normal mode splitting for one monolayer was assumed to be 20 meV.

Figure 4.15 presents the phase diagram calculated for one, three, five and ten, hypothetically integrated monolayers. The line for each number of monolayers shows the density of polaritons in the system that is required for polariton condensation at a given temperature. For all monolayers numbers, the density is generally increasing with temperature, because a the fraction of polariton outside the ground state grows with temperature. Consequently, a higher density is required to reach the same ground state population. The density starts to increase more rapidly with temperature at 20 K - 80 K, depending on the number of monolayers. This kink can be understood in the following way: When a significant fraction of polaritons occupies states at energies above the inflection point of the lower polariton branch (see Figure 2.7), the number of required polaritons is strongly increasing because the density of states increases when the dispersion relation flattens out. Thus, the fraction of polaritons outside the ground state increases and therefore the total number of polaritons must increase to compensate for the lower fraction in the ground state. For more monolayers, this behavior kicks in at higher temperatures, since more

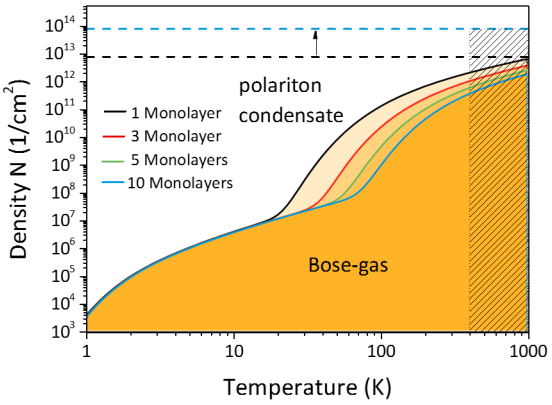

Figure 4.15: Polariton phase diagram: Required density of quasi-particles for polariton-condensation plotted as a function of temperature for different numbers of integrated monolayers. The upper density limit (Mott density) is indicated by the black/blue dashed line for one and ten integrated monolayers, respectively. The temperature range above 400 K is shaded as indication for the estimated transition from strong to weak coupling.

monolayers induce a larger normal mode splitting, which in turn increase the polariton potential between ground state and inflection point.

Most importantly though, the polariton density stays below the Mott density (10^{13} cm^{-2}, indicated by the dashed black line) at 300 K for all monolayer numbers. This means that polariton condensation could in principle be observed at room temperature and even above. The shaded area above 400 K indicates that strong coupling cannot be observed above this temperature as estimated in the previous section, meaning that no condensation would be possible anymore. An increased number of monolayers would also have the advantage that the Mott density increased by a factor equal to the number of monolayers, since excitons could be distributed among the individual monolayers. This increase is illustrated by the blue dashed line for the case of ten monolayers. It is important to note that this model assumes a Bose-Einstein-contribution of the polaritons in the thermodynamic equilibrium. This requires an efficient polariton relaxation, before the polariton population decays. At this stage, it is hard to evaluate how efficient polaritons relax by the underlying exciton-exciton interaction or polariton-phonon scattering. However, it seems certain that the radiative decay is relatively fast owing to exciton radiative decay times on the order of few hundred fs to 1 ps [123]. Thus, more experimental and theoretical work is required to evaluate the dynamics of relaxation and decay[6].

[6]The calculation of the phase diagram was carried out in close collaboration with E. Cherotchenko and A. V. Kavokin, University of Southampton, and was published in reference [8]

Chapter 5

TMDC polariton systems

5.1 Exciton-polaritons with WSe_2

WSe_2 and WS_2 monolayers were used for the first approach to observe exciton-polaritons at room temperature, since tungsten based TMDC monolayers are known to have a higher oscillator strength [96] and show brighter emission at room temperature [58] as described in chapter 4.1. Based on the simulations presented in section 4.3, a DBR-metal cavity design was chosen as it has the lowest effective cavity length of all described cavity designs and is relatively easy to fabricate. In this particular case, a WSe_2 monolayer was transfered onto a SiO_2/TiO_2 DBR (ten pairs) with a central wavelength of 680 nm (commercially available from Laseroptik GmbH). Subsequently, the full structure was capped with a 130 nm thick PMMA layer. Finally, a 35 nm thick gold layer was evaporated as the top mirror. The PMMA thickness was adjusted so that the full cavity has its resonance at 751.5 nm/1.650 eV. Figure 5.1a illustrates the final structure, including the WSe_2 monolayer. Figure 5.1b depicts the PL spectrum of the WSe_2 monolayer (before capping with PMMA and gold), which is shown in a microscope image in the inset (monolayer is marked in red for better contrast). The PL spectrum features a clear resonance at 751.5 nm/1.650 eV with a linewidth of 38 meV (FWHM). The out-of-plane, optical mode profile, obtained by a transfer matrix calculation, is illustrated in Figure 5.1c. Here, the sequence of layers (without embedded monolayer) is illustrated by their corresponding refractive indices. The position of the monolayer at the interface of the topmost SiO_2 layer and the PMMA layer coincides closely with the field maximum. However, it should be noted that the monolayer is not at the maximum of its field amplitude $|E|^2$, but at about 83 % of its maximum. Such displacement results from the bottom mirror, which is designed for a central wavelength of 680 nm and therefore the topmost SiO_2 layer is less than $\lambda/4$ with respect to the target wavelength of 751.5 nm. Consequently, the PMMA layer needs to be thicker than $\lambda/4$ to compensate for this, which in turn displaces the

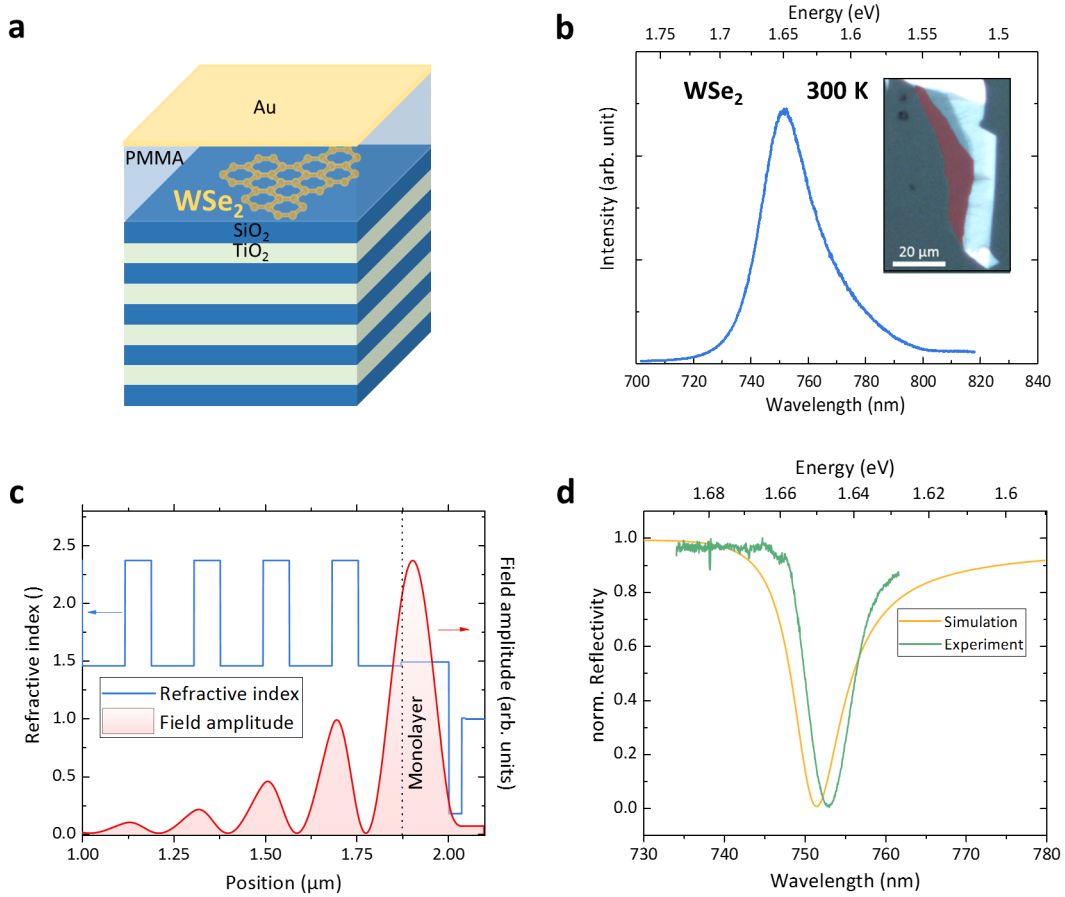

Figure 5.1: Sample structure: (a) Schematic illustration of the sample structure. (b) PL spectrum and microscope image (inset) of the WSe_2 monolayer before PMMA capping. The monolayer marked in red. (c) Simulated field distribution in the photonic structure, represented by the refractive indices of the layer sequence. The monolayer position is marked by the dotted line. (d) Simulated and experimentally acquired reflectivity spectra of the empty cavity at zero in-plane momentum (both spectra were normalized to 1).

monolayer slightly from its ideal position. This effect will ultimately reduce the normal mode splitting, which is directly proportional to the field amplitude [68] (see also equation 2.24). The simulation also provides a reflectivity spectrum shown in Figure 5.1d. The measured empty cavity resonance (also plotted in Figure 5.1d) is close to the one of the simulated structure at 752.8 nm/1.647 eV with a linewidth of 15 meV, corresponding to a Q-factor of 110.

The full system was excited non-resonantly at 532 nm with a cw-laser, an excitation power of 3 mW and a spotsize of 2 μm. Here, a 100 x magnification objective with an NA of 0.7 was used. In Figure 5.2a, PL spectra are plotted for various in-plane wave

vectors. Each spectrum shows two spectral features that were fitted with a two Gaussian

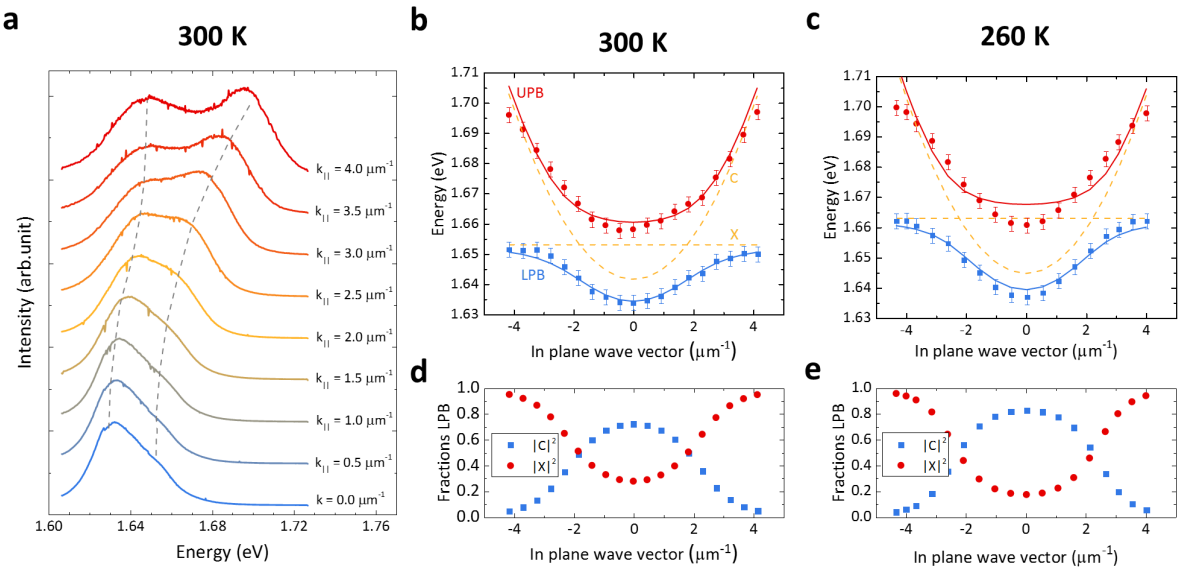

Figure 5.2: (a) PL spectra of the full structure at various in-plane wave vectors acquired at 300 K. Approximate peak positions are connected by gray dashed lines as a guide to the eye. (b) Peak positions extracted from the line spectra in (a) are plotted as a function of the in-plane wave vector. The experimental data was fitted with the coupled oscillator model (blue and red lines for the lower and upper polariton branch, respectively). The uncoupled exciton and cavity resonances are additionally plotted (yellow dashed lines) to illustrate the clear anti-crossing behavior of the two branches. The Hopfield coefficients for the lower polariton branch are plotted in (d). (c) Polariton branches for the same experiment carried out at 260 K. The uncoupled exciton has clearly shifted to a higher energy, which changes the polariton composition (e). The plot of the lower polariton branch Hopfield coefficients confirms a more photonic character.

peaks, allowing to extract the peak positions (see appendix A.10 for the detailed fitting procedure and error analysis). The peak positions were subsequently plotted as a function of the corresponding in-plane wave vector, presented in Figure 5.2b. In this plot, two distinctly anti-crossing branches can be identified. A two-coupled-oscillator fit, based on equation 2.22, is applied to the data, which demonstrates that this model can reproduce the obtained branches, namely lower and upper polariton branch. From this fit, a normal mode splitting of 23.5 ± 1 meV was extracted (see appendix A.11 for error analysis), which is close to the simulations presented in chapter 4.3 for a $MoSe_2$ monolayer (25 ± 2 meV predicted). Taking into account that the simulated splitting still needs to be reduced by 17 % (to 21.8 ± 1.8 meV) due to the reduced field amplitude at the monolayer position, experiment and prediction are in good agreement.

In addition, the fit provides a modest negative detuning $\Delta E = E_C - E_X$ of -12 meV, although the independent measurements of the exciton and cavity resonances (see Figure 5.1b and d, respectively) imply a negative detuning of only -3 meV. However, the blueshift of the exciton resonance by PMMA capping on the order of 10 meV needs to be taken into account (see Figure 4.6). Including this consideration, one would expect a negative detuning of about -13 meV, which in good agreement with extracted detuning value of -12 meV. The negative detuning condition leads to an effective lower polariton mass of 1.96 ($\pm$ 0.1) x 10^{-5} m_0. The rather photonic character of the lower polariton branch at low in-plane wave vectors is quantified in more detail by the Hopfield coefficient plot in Figure 5.2d.

The polariton fractions and the detuning can be controlled by the sample temperature. When the full structure was cooled down to 260 K, the exciton shifts by about 10 meV to a higher energy, while the cavity stays almost unaffected (see Figure 5.2c and Figure 5.3a). In this case, the detuning is -18.5 meV. Fitting of the recorded line spectra as in the previous experiment reveals that the lower polariton branch is even more photonic (see Figure 5.2e). Consequently, an effective polariton mass of 1.70 ($\pm$ 0.09) x 10^{-5} m_0 was determined. This procedure has been repeated for various temperatures from 240 K to 330 K (see appendix A.12 for the fits of the PL dispersions). Figure 5.3 shows the extracted exciton and cavity energies as well as their detuning and the effective mass of the lower polariton branch as a function of temperature. The cavity resonance remains

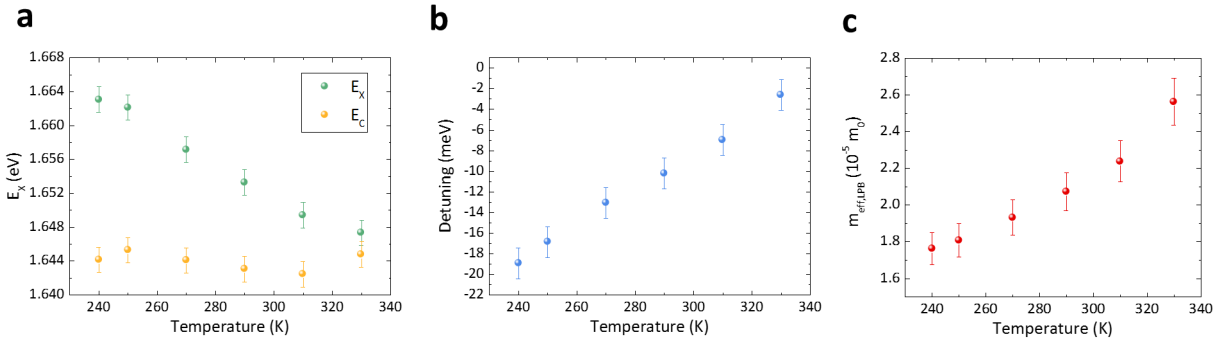

Figure 5.3: (a) Exciton and cavity energies, (b) the corresponding detuning and (c) effective, lower polariton mass as a function of temperature.

almost unchanged, while the exciton energy decreases linearly with temperature. Consequently, the negative detuning, present at lower temperature, is reduced with increasing temperature. Therefore, the lower polariton composition becomes more excitonic with temperature, which results in an increasing lower polariton mass. This experiment shows that polariton composition and mass can be adjusted by simply changing the sample temperature.

In order to address the occupation of polariton states in the system, the experimentally acquired data was modeled. Due to the comparably low particle number and the high temperature, a Boltzmann distribution law is assumed in a first approximation: $N_i \sim exp(-E_i/k_BT)$, where N_i and E_i are the population and energy of the lower polariton branch (i = 1) and the lower polariton branch (i = 2). E_i is a function of the in-plane wave vector as described by the dispersion relation (equation 2.22). In order to model the PL distribution based on the population distribution, it is assumed that the PL stems from the photon part of the polariton and therefore the population is weighted with the k-dependent cavity fraction $|C^i(k)|^2$ of LPB and UPB. The PL intensity is then approximated by:

$$I(k,E) \sim \sum_i \frac{|C^i_{ph}(k)|^2 exp(-E_i(k)/k_BT)}{(E - E_i(k))^2 + \Gamma_C^2}, \tag{5.1}$$

where Γ_C accounts for the broadening of the photonic mode (15 meV taken from experimental data) and the i-index spans over the two polariton branches. The temperature is set to 300 K. The comparison between experiment and theory is illustrated in Figure 5.4. It should be noted that the investigated system can not be expected to be in the ther-

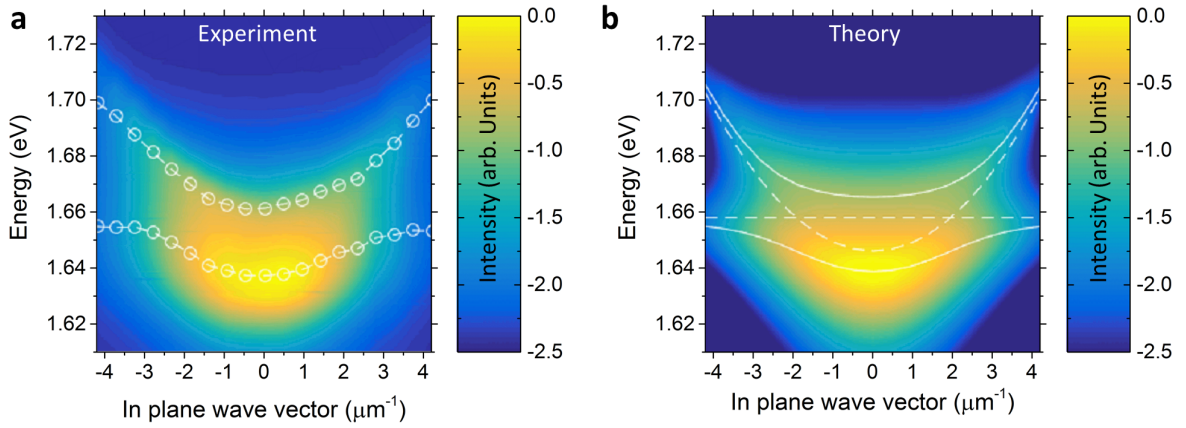

Figure 5.4: Polariton population: Experimentally acquired (a) and theoretically modeled (b) PL dispersion relation of the full structure at 300 K. The model assumes a Boltzmann distribution for the occupation of polariton-states. Although the experimentally studied system is assumed not be in thermal equilibrium (continuous pumping + fast decay), experiment and theory show a similar intensity distribution.

modynamic equilibrium due to its driven-dissipative nature (continuous wave excitation, non-radiative decay channels and continuous PL emission). Nevertheless, experiment and theory are in good agreement, which is an indicator for efficient relaxation channels to the polariton ground state[1].

[1]The calculation of the polariton population was carried out in close collaboration with E.

All in all, the investigated system demonstrates that exciton-polaritons can be observed in TMDC monolayers in a DBR-metal microcavity at room temperature. The large normal mode splitting of 23.5 meV originates from the high oscillator strength of excitons in TMDC monolayers and the strong photonic confinement (low effective cavity length). Due to the high exciton binding energy, the excitons are in fact stable enough to form exciton-polaritons even at room temperature[2]. At the time when these results were obtained, there had been a first experiment which showed indications for strong-coupling with a TMDC monolayer at room temperature [125]. In this work, a MoS_2 monolayer was integrated into a chemical vapor deposition (CVD) grown, planar microcavity consisting SiO_2/Si_3N_4 DBRs. Based on angle-resolved reflectivity and PL measurements, the observation of exciton-polaritons was claimed. However, these measurements could not fully map out the anti-crossing and even less so the full dispersion relation of the expected exciton-polariton branches. In contrast, a clear anti-crossing had been shown in a low temperature (5 K) strong coupling experiment between a $MoSe_2$ monolayer exciton and a cavity mode based on the open cavity design described in the previous chapter [107]. In this experiment, the cavity mode was detuned by adjusting the cavity length and the resulting detuning series yielded a normal mode splitting of 20 meV. This value is perfectly consistent with the observed normal mode splitting of 23.5 meV presented in this section of this thesis, considering the difference in effective cavity length and the temperature induced reduction of the normal mode splitting (see section 4.3). Nevertheless, it should be noted that a quantitative comparison between these experiments has to be treated with caution, since normal mode splitting values may even vary by 20 % for the same monolayer material, cavity design and temperature [71, 107]. Although the anti-crossing was clearly demonstrated in a detuning experiment, the experimental conditions in reference [107] did not allow to measure the dispersion relation in momentum-resolved configuration. In this context, the results presented in this section are the first demonstration of a full exciton-polariton dispersion relation with a TMDC monolayer at room temperature. A few months after this observation, room-temperature exciton-polaritons were demonstrated based on MoS_2 monolayer integrated into similar DBR-metal design [126]. The extracted normal mode splitting of 54 meV is surprisingly large, given that one could expect a difference in the normal mode splittings of about 25 % between WSe_2 and MoS_2, based on equation 2.23 and their relative exciton oscillator strengths presented in table 4.1. Even considering the slightly different effective cavity lengths (about 250 nm in reference [126] vs. 300 nm for the results presented here) and the monolayer displacement from the maximum field amplitude in this work, the quantitative difference is still on the order of 40 %. However, it should be emphasized that the exciton oscillator strength also

Cherotchenko, A.V. Nalitov and A.V. Kavokin, University of Southampton.

[2]The results presented in this section were published in reference [124]

depends on the dielectric environment of the monolayer as well as on material quality and potentially material degradation, which makes a quantitative comparison between these findings difficult. Even more so, a very recent experiment demonstrated that the normal mode splitting strongly depends on the doping level of the monolayer [127]. In this study, a WS_2 monolayer was electrostatically gated, which allowed to control the doping concentration, and the normal mode splitting was measured as a function of the free charge carrier concentration. The normal mode splitting decreased with this concentration, since the oscillator strength shifts form the exciton to the trion. For high free charge carrier concentrations (on the order of 10^{12} cm^{-2}), the system even moved from the strong to the weak coupling regime. The study also demonstrated that compensation of the naturally occurring, intrinsic doping by electrostatic gating increased the normal mode splitting by a factor of three. Since most TMDC monolayer exhibit varying degrees of intrinsic doping, it is less surprising that the reported normal mode splitting values, differ so much.

5.2 Exciton-polaritons with WS_2

In order to extend the observation of exciton-polaritons to other material systems, a SiO_2/TiO_2 DBR-metal cavity containing a WS_2 monolayer has additionally been fabricated. WS_2 is an interesting alternative to WSe_2, since it has an oscillator strength, which is a factor of 1.9 higher [96]. Fabrication of a new sample also allows to improve the spatial overlap of photonic mode and monolayer, since the available bottom DBR (stopband center at 610 nm) was designed for the resonance energy of the WS_2 monolayer (615 nm). In addition, the wavelength of the WS_2 monolayer exciton resonance (620 nm) is lower than the one of WSe_2 (750 nm) and thus the effective cavity length for the corresponding cavity modes is reduced from 300 nm (for WSe_2) to about 250 nm (for WS_2).

After transferring a WS_2 monolayer on the DBR, the full structure was spin-coated with 82 nm of PMMA and finally a 40 nm thick layer of silver was evaporated. The gold layer was replaced by silver, due to its higher reflectivity at this wavelength range (96.7 % for silver as compared to 92.5 % for gold as shown in appendix A.2). The silver layer was protected against oxidation with a 5 nm film of SiO_2. The final structure is illustrated in Figure 5.5a. The PL spectrum of the WS_2 monolayer (before capping with PMMA and silver) is plotted in Figure 5.5b, featuring a clear exciton resonance at 618.6 nm/2.004 eV with a linewidth (FWHM) of 29 meV. A microscope image of the monolayer is shown the inset of 5.5b. Figure 5.5c presents the simulated field distribution in the cavity, which has a maximum very close the monolayer position ($\sim$ 98 % of the maximum field amplitude at the monolayer). The simulation also provides a reflectivity spectrum, shown in Figure 5.5d, with a resonance at 619 nm/2.003 eV and a linewidth of 5.5 nm/17.6 meV, which corresponds to a Q-factor of 113. The measured reflectivity spectrum of the empty

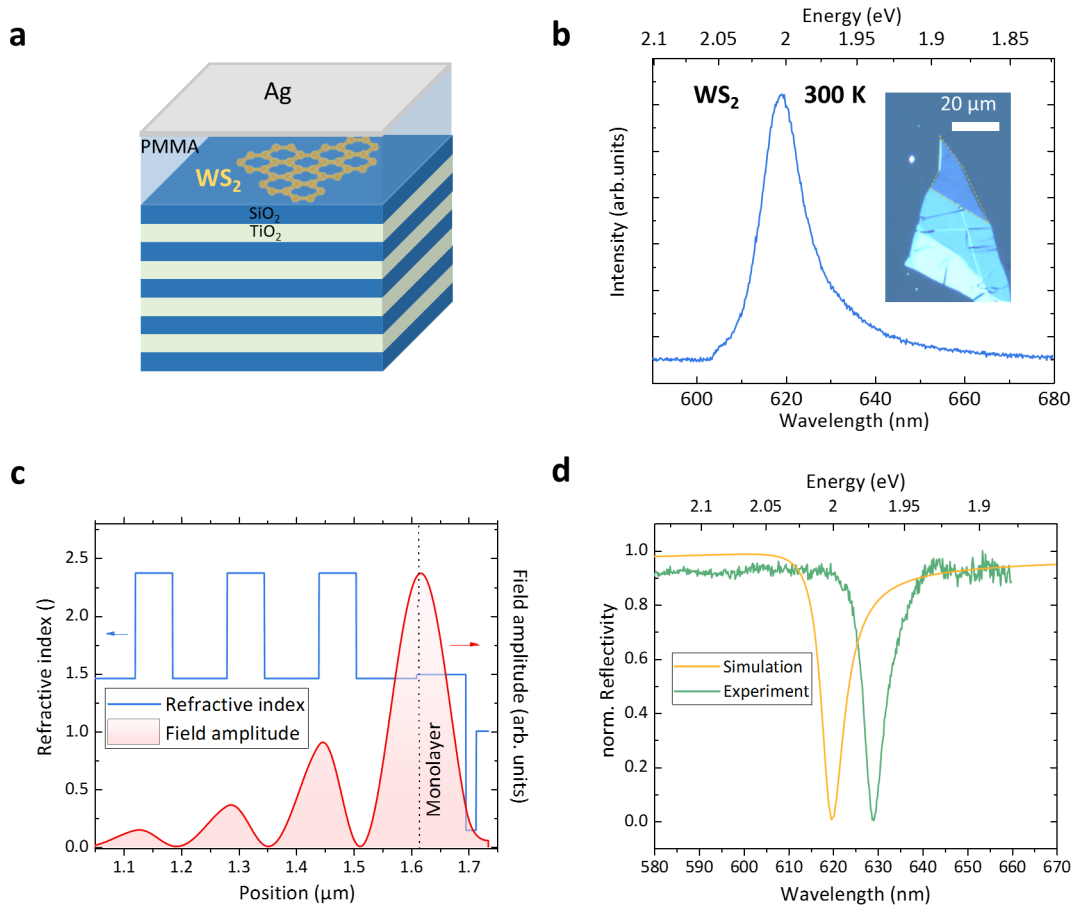

Figure 5.5: Sample structure: (a) Schematic illustration of the sample structure. (b) PL spectrum and microscope image (inset) of the WS_2 monolayer. (c) Simulated field distribution in the photonic structure, represented by the refractive indices of the layer sequence. (d) Comparison of simulated and experimentally measured reflectivity spectra (both spectra were normalized to 1).

cavity, also plotted in Figure 5.5d, exhibits a resonance at 629.4 nm/1.970 eV and a linewidth of 5.3 nm/16.5 meV (Q = 119). The discrepancy between the designed and targeted resonance position stems from the high sensitivity of the resonance position on the PMMA layer thickness. For 1 nm PMMA thickness variation, the cavity resonance shifts by 1.6 nm in this wavelength range. Although the PMMA layer thickness can be controlled by the PMMA concentration in its solvent, a thickness uncertainty of a few nanometer can be expected. In this case, the discrepancy between design and experiment indicates that the PMMA layer was 6 nm too thick. Nevertheless, exciton and cavity resonances are in principle still close enough to observe strong coupling, considering the expected coupling strength.

After completing the full structure, angle-resolved PL was measured under cw excita-

tion at 532 nm (4 mW excitation power, 2 μm spot size). Figure 5.6a shows the PL as a function of the in-plane wave vector. A clear dispersion can be resolved, which shows

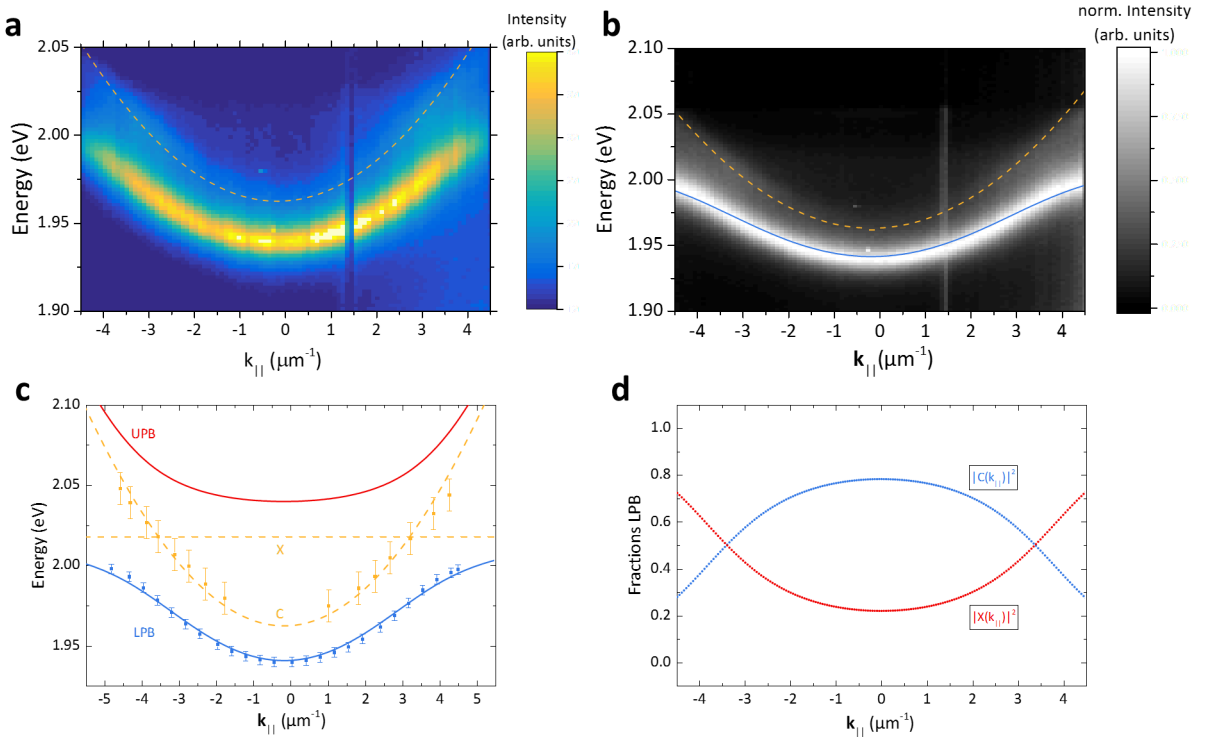

Figure 5.6: (a) Polariton dispersion measured in PL at 300 K. The empty cavity dispersion also appears as a faint branch in the background marked by the yellow dashed line. (b) Data set of (a) replotted, where line spectra, which are saved in each column of the presented data set, were normalized to 1 to better illustrate the characteristic shape of the lower branch. The lower polariton branch is marked by the blue solid line. (c) Peak positions are plotted as a function of the in-plane wave vector. The experimental data was fitted with the two-coupled-oscillator model (blue and red lines for the lower and upper polariton branch, respectively). The uncoupled exciton and cavity resonances are additionally plotted (yellow dashed lines, see appendix A.10 for error analysis). (d) Hopfield coefficients for the lower polariton branch, illustrating the photonic character of the ground state.

the typical shape of a lower polariton branch. In order to illustrate the characteristic shape of the lower branch better, the data set in Figure 5.6a, was replotted in 5.6b, where line spectra, which are saved in each column of the data set were normalized to 1 and 0. The lower polariton branch was also marked by the blue solid line as guide to the eye. In addition to the LPB, a faint, parabolic branch can be observed energetically, slightly above the LPB (indicated by the yellow, dotted line). Since its minimum energy coincides well with the empty cavity resonance, this branch was identify as the empty cavity. In

principle, the empty cavity should not be visible in the strong coupling regime, but it is assumed that PL from edge regions or from smaller monolayer pieces in close proximity may weakly couple to the cavity mode. However, no PL from the upper polariton is observed. Fitting the individual line spectra for each in-plane momentum reveals the exact spectral positions of lower polariton and empty cavity as shown in Figure 5.6b. These energies were taken as an input for a two-coupled-oscillator fit. The fit results in a detuning ($\Delta = E_C - E_X$) of -55 meV and a normal mode splitting of 80 $\pm$ 4 meV. For the best fit, the exciton energy is assumed to be 14 meV higher than measured before PMMA and silver capping. This is in good agreement with the blue-shift of the exciton resonance after PMMA capping (see Figure 4.6). According to this fit, the upper polariton branch is about 100 meV above the lower polariton ground state, which yields a very low thermal population of the UPB and thus it can not be observed in PL. The Hopfield coefficients of the lower polariton, plotted in Figure 5.6c, also reflect the negative detuning situation with a photon fraction of 72 % at zero in-plane momentum.

In this structure, an exciton-polariton is observed with a significantly higher normal mode splitting than in the previous structure. This is partly attributed to three factors. First, the optical field amplitude coincides much better with monolayer position (98 % of the maximum field amplitude as compared to 83 % in the previous structure). Moreover, the effective cavity length is reduced from 300 nm (previous structure) to 260 nm, since the physical cavity length is reduced for a lower target resonance wavelength. Finally, excitons in WS_2 monolayers have a oscillator strength which is about twice as high as in WSe_2 monolayers [96]. However, taking these three factor quantitatively into account (equations 2.23 and 2.24), the measure normal mode splitting still differs by a factor of 1.8 as compared result presented in the previous section.

Nevertheless, these results are in agreement with previous findings in reference [108], where are normal mode splitting of 70 meV was demonstrated for a WS_2 monolayer in an open cavity at room temperature. More recently, room-temperature normal mode splittings of 70 - 100 meV have been shown for WS_2 monolayer in a monolithic metal-metal cavity [128]. Excitons in WS_2 monolayer have also been coupled to metal-based, plasmonic nanostructures [129, 130]. Plasmonic nanostructures allow to confine light below the diffraction limit and thus exhibit a particular small mode volume. This way, room-temperature normal mode splitting of 101 meV [129] and 74 meV [130] could be achieved.

5.3 Trion-polaritons with $MoSe_2$

Besides excitons, most monolayers contain a significant population of trions, where the trion/exciton ratio mainly depends on intrinsic doping [100, 101], photo-doping [31] or

electrostatic gating [100]. Since the trion dissociation energy is on the order of 30 meV, trion resonances are typically observed in low temperature PL experiments. Under these conditions, trion resonances can be as pronounced as the exciton resonances. Because of this, the question arises whether trions could also be coupled strongly to a microcavity photon mode. This would imply a new quasi-particle, the trion-polariton, which distinguishes qualitatively from the exciton-polariton, due to its net charge. This net charge stems from the trion composition of three fermionic, charged particles, creating a new particle with fermionic and charged character. Consequently, such particle could be better controlled by external electric and magnetic fields. It would inherit the very low effective mass from the light component and the sensitivity on external fields from the matter component.

A $MoSe_2$ monolayer was chosen for such an experiment, since it exhibits narrow and well separated exciton and trion resonances at cryogenic temperatures, as presented in Figure 5.7a. The $MoSe_2$ monolayer was transferred onto an AlGaAs/AlAs DBR with a

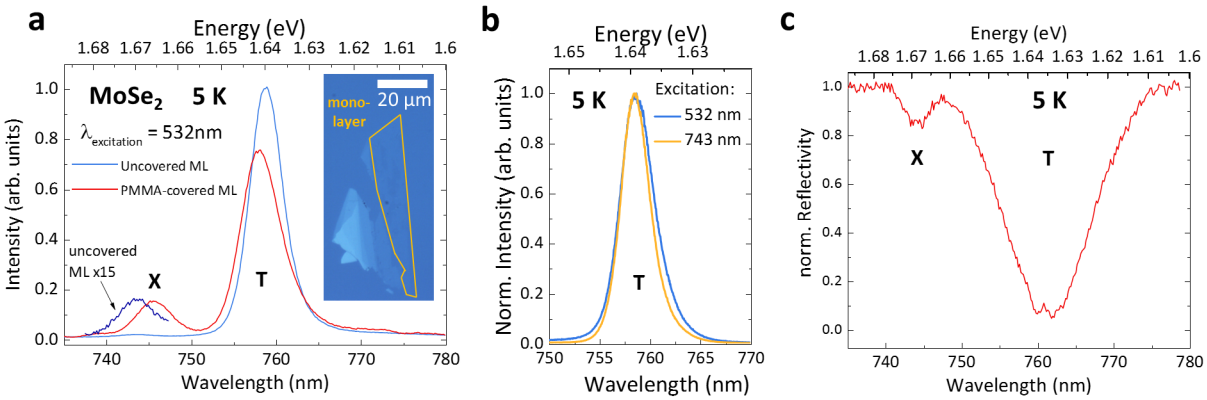

Figure 5.7: $MoSe_2$ monolayer pre-characterization: a) PL spectrum of the $MoSe_2$ monolayer taken before and after PMMA capping under 532 nm excitation at 5 K. Exciton and trion peaks are labeled with X and T, respectively. The exciton peak for the uncovered monolayer is additionally plotted multiplied by a factor of 15 for better visibility. The inset shows a microscope image of the investigated monolayer (marked by a yellow frame). b) PL spectra of the trion resonance at 5 K for excitations at 532 nm and 743 nm. c) Reflectivity spectrum of the exciton and trion resonances at 5 K (normalized to 1).

terminating GaInP layer, which enhances the trion dominance due to free carrier injection [131] as presented in section 4.1. Under 532 nm excitation (cw, 400 μW excitation power, 2 μm spot size), exciton and trion resonances were observed at 1.6681 eV $\pm$ 0.3 meV and 1.6334 eV $\pm$ 0.3 meV, respectively. The selection of GaInP as the monolayer substrate is

crucial. As elaborated in section 4.1, it results in electron doping from the substrate into the monolayer and thus also increases the probability of trion formation. Thus, the PL signal is highly trion dominant with a trion/exciton intensity ratio of 80. The presence of a free electron gas also changes the screened Coulomb potential for both the exciton and the trion. While the exciton binding energy decreases with the concentration of free charge carries, the trion binding increases [31, 102]. As a result, the trion dissociation energy increase in a system with many free electrons. Consequently, the very high trion dissociation energy of 34.7 meV ± 0.3 meV also serves as strong indicator for a large accumulation of free electrons in the monolayer. When the monolayer is covered with PMMA, a requirement for further integration into a microcavity, the trion dominance is slightly reduced. Moreover, the exciton shifts red to 1.6632 eV ± 0.3 meV and the trion shifts blue to 1.6354 eV ± 0.3 meV. While the linewidths in this experiment are 9.3 meV ± 0.3 meV and 9.7 meV ± 0.3 meV, respectively, the trion linewidth is reduced to 7.3 meV ± 0.3 meV, when the trion is excited through the exciton resonance at a laser wavelength of 743 nm (1.6688 eV ± 0.3 meV) as shown in Figure 5.7b. Although, the trion resonance is routinely observed in PL experiments, it cannot be taken for granted that the trion carries significant oscillator strength. Instead of the PL intensity, the absorption of a resonance is the relevant measure for the oscillator strength. In fact, the trion absorption feature is very weak or not observable in many absorption/reflectivity experiments [132, 59, 94]. This in an indication that the trion carries less oscillator strength than the exciton. Nevertheless, the trion may be higher populated than the exciton as it is energetically favored. Hence, the trion dominates the PL spectrum. In order to check if the high free electron concentration also increases the trion oscillator strength, a reflectivity measurement on the monolayer (after PMMA capping) was carried out as presented in Figure 5.7c. The spectrum shows both the exciton and trion resonances and in fact the trion resonance is dominant in the absorption spectrum as well. Therefore, it is concluded that the trion carries significant oscillator strength. It should be noted that the trion resonance is broadened in the absorption spectrum and the shape of the resonance indicates a convolution of two separate resonances, which could be a signature of the fine structure splitting of the trion [133, 134].

After this pre-characterization, the monolayer needs to be integrated into a microcavity. The bottom DBR with the topmost GaInP layer (10 nm) consists of a AlAs/AlGaAs DBR (30 pairs) on a GaAs substrate. After the transfer of the monolayer, the full structure is capped with PMMA (42 nm) and 60 nm of gold, evaporated on top as shown in Figure 5.8a. This structure is also illustrated in Figure 5.8b by the refractive indices of the layer sequence. The layer thicknesses were designed so that the photonic structure forms a resonance at the trion energy. The spatial overlap of the monolayer and the field maximum of the optical mode was ensured, shown by the optical mode profile and the

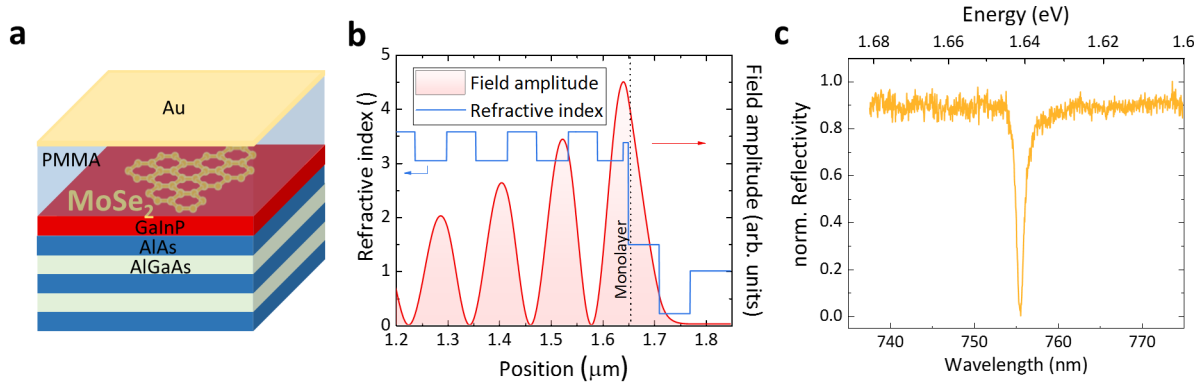

Figure 5.8: Microcavity structure: a) Schematic illustration of the investigated microcavity. b) Simulated field distribution in the microcavity plotted with respect to the refractive indices of the layer sequence. c) Reflectivity spectrum of the empty microcavity (normalized to 1).

marked monolayer position in Figure 5.8b. The reflectivity measurement of the empty cavity, presented in Figure 5.8c, reveals a photonic mode at 1.6409 eV ± 0.3 meV with a Q-factor of 720 ± 20 ($\Gamma_c = 2.28\ meV$) close to the trion resonance.

When full structure was probed under 743 nm (1.6688 eV ± 0.3 meV) cw excitation, 2 mW excitation power, 2 μm spot size, two curved branches were observed as depicted in Figure 5.9a. These branches follow the dispersion relation of the upper and lower trion-polariton as indicated by dashed lines. In order to illustrate the shape of the lower polariton more clearly, a zoom-in of the data is replotted in Figure 5.9b with a linear color scale and the line spectra, which are saved in each column of the presented data set were normalized. These line spectra can be fitted to extract the peak positions, as shown in Figure 5.9c. However, the upper polariton branch is too faint to be fit around zero in-plane momenta. The extracted energies were fitted by a two-coupled-oscillator fit, indicated by the red and blue, solid lines. This fit allowed to deduce a normal mode splitting of 5.2 ± 0.2 meV, a coupling constant of 5.7 ± 0.2 meV and a positive detuning $\Delta = E_C - E_T$ of 4.0 meV. At $k_{||} = 0\ \mu m^{-1}$, the LPB has trion and cavity fractions of 0.852 and 0.148, respectively. Also, the trion energy of 1.6358 eV ± 0.3 meV, according to the two coupled oscillator fit, is in excellent agreement with the measured trion energy under PMMA coverage (1.6354 eV ± 0.3 meV). The trion-polariton mass was determined to $2.8 \pm 0.14 \times 10^{-4}$ m_0. This is higher than for the previously observed exciton-polariton masses, because of the lower photonic fraction, but is still significantly lower than of an uncoupled trion.

Reference [71], which was published shortly after the results of this section, reports of a qualitatively similar observation. In this reference, a $MoSe_2$ monolayer was placed in an open cavity and a trion-polariton with a coupling constant of 1.3 meV was mapped out

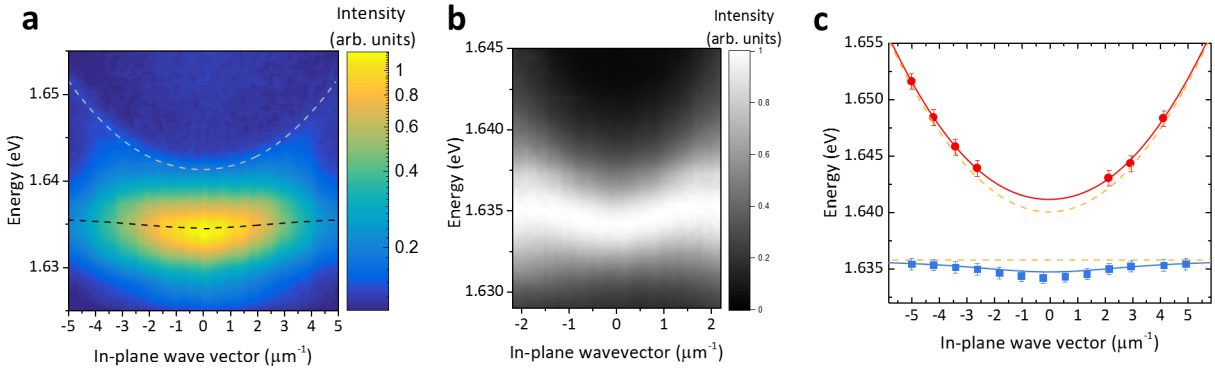

Figure 5.9: Trion-polariton: a) Angle-resolved PL measurement under 743 nm excitation at 5 K. The PL intensity is plotted with a logarithmic color scale to highlight the faint upper branch (indicated by the gray dashed line). The shape of the lower branch is indicated by the black dashed line. b) Zoom-in of the PL measurement of a) re-plotted with a linear color scale and the line spectra, which are saved in each column of the presented data set were normalized to better illustrate the characteristic shape of the lower branch. c) Extracted peak positions fitted with a two coupled oscillator fit, where the UPB is plotted as a red line, the LPB as a blue line and the uncoupled trion and cavity are indicated by yellow, dashed lines.

in a detuning series. The quantitative difference is partly explained by different effective cavity lengths (2.9 μm in [71] vs. 0.75 μm in the presented Tamm structure). However, even if this is taken into account (equation 2.23), the coupling constant in reference [71] is still a factor of 2 lower. It should be stressed that the monolayers might have a different intrinsic doping level and were investigated on different substrates (SiO_2 in [71] vs. GaInP here), which both have a strong influence on the trion oscillator strength and can therefore explain the quantitative difference. Moreover, shortly before these two studies, there had been another closely related observation for a $MoSe_2$ monolayer placed in a fiber-coupled open cavity [135]. In this work, the $MoSe_2$ monolayer was gated in a way that the density of free charge carriers could be adjusted. In the high density regime of free charge carriers, the low energy resonance was interpreted as a polaron, a quasi-particle that describes the interaction of the exciton with surrounding sea of free charge carriers. The normal mode splitting was up to 8 meV, depending on the gating voltage. Given that substrate (h-BN) and the free charge carrier density are not comparable with the results of this section, the observation in reference [135] is also in qualitative agreement with the results here.

The formation of trion-polaritons is remarkable since trions do not carry enough oscillator strength for strong coupling in GaAs quantum wells, which is one of the most common polariton material systems. In this way, extremely light charged quasi-particles

were created, which may potentially be controlled and directed by external fields[3].

[3]The results presented in this section were published in reference [102]

Chapter 6

Spin-valley properties of TMDC polaritons

6.1 Trion-polaritons with $MoSe_2$

The distinct spin-valley physics in TMDC monolayers give this material class a unique character. Manifestations of these properties, such as valley polarization or valley coherence, strongly depend on the exciton relaxation, decay and depolarization dynamics [64]. These dynamics are expected to be significantly altered in the strong coupling regime as described in section 2.4. Consequently, spin-valley effects should also change for exciton-polaritons as compared to pure excitons. Therefore, this section is dedicated to investigate the effects of strong light-matter coupling on the spin-valley properties in TMDC monolayers.

The trion-polariton system with a $MoSe_2$ monolayer, described in section 5.3, was chosen as a first sample system. Even at cryogenic temperatures, excitons and trions in $MoSe_2$ monolayers show hardly any (less than 2 %) valley polarization [58, 71]. This was confirmed in a circular polarization resolved PL measurement of a bare monolayer shown in Figure 6.1a. Under σ^- excitation at 743 nm (cw, 400 μW excitation power, 2 μm spot size), the σ^+ and σ^- components of PL spectra exhibit the same intensities, meaning that the DOCP is 0 %. In contrast, the same experiment carried out on the trion-polariton system yields a significant difference between the σ^+ and σ^- components (Figure 6.1b). For an energy that corresponds to lower polariton states at high in-plane wave vectors (> 4 μm^{-1}, see Figure 5.9c), also referred to the trion-polariton reservoir, a DOCP of 18 ± 2 % was measured (see appendix A.13 for error analysis). At an energy equivalent to the lower polariton ground ground state (zero in-plane wave vector), a DOCP value of 10 ± 2 % was determined.

It is known that the relation of relaxation, decay and depolarization dynamics are the

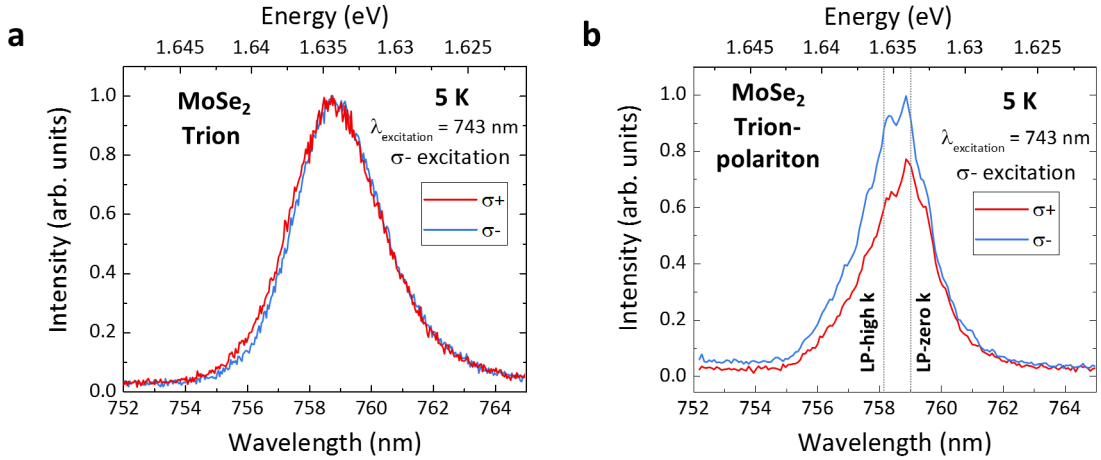

Figure 6.1: Valley polarization measurement: PL measurement of the σ^+/σ^- components of the trion (a) and the trion-polariton (b) under σ^- excitation at 743 nm and at 5 K. The energies of the LPB at zero in-plane wave vector (ground state) and at high in-plane wave vectors ($> 4\ \mu m^{-1}$) are marked by dashed lines (both taken from the dispersion presented in Figure 5.9).

determining factor for the valley polarization [64]. If relaxation and decay take place faster than the intervalley scattering (depolarization), a significant fraction of valley polarization may be conserved. Therefore, time-resolved PL measurements of the trion and the trion-polariton were performed. Figure 6.2a shows the PL time traces of trion and lower trion-polariton ground state under pulsed excitation (120 fs pulse duration, 80 MHz repetition rate) at 700 nm (100 μW average power, 1 μm spot size). Clearly, the trion response rises more rapidly, but has a much longer decay as compared to the lower trion-polariton. Figures 6.2b and c show the extracted rise and decay times of trion and trion-polariton, respectively, as a function of the averaged excitation power (see appendix A.15 for fitting and error details). The induced population density is estimated to $10^6 - 10^9 cm^{-2}$ (see appendix A.14), which is in a range where interaction process between excitons and trions should not be dominant [50]. The rise time of the trion remains on the same level of 4.5 $\pm$ 0.5 ps across the entire excitation power range. The trion-polariton rise time is significantly longer and on the order of 8.6 $\pm$ 0.5 ps with a slight drop to 7.8 $\pm$ 0.5 ps at high powers. The trion decay time shows a slight drop from about 26.5 $\pm$ 0.6 ps at low powers to 25.0 $\pm$ 0.6 ps at an intermediate power and stays on a comparable level even at high powers. The trion-polariton decay time is significantly shorter ranging from 12.8 $\pm$ 0.5 ps at low power to 11.2 $\pm$ 0.5 ps at high power.

In order to interpret these dynamics, the ground state populations of trion and trion-polariton were simulated by solving the coupled rate equation system described by equations 2.40 to 2.42. Here, the exciton index X is replaced with the trion index T and

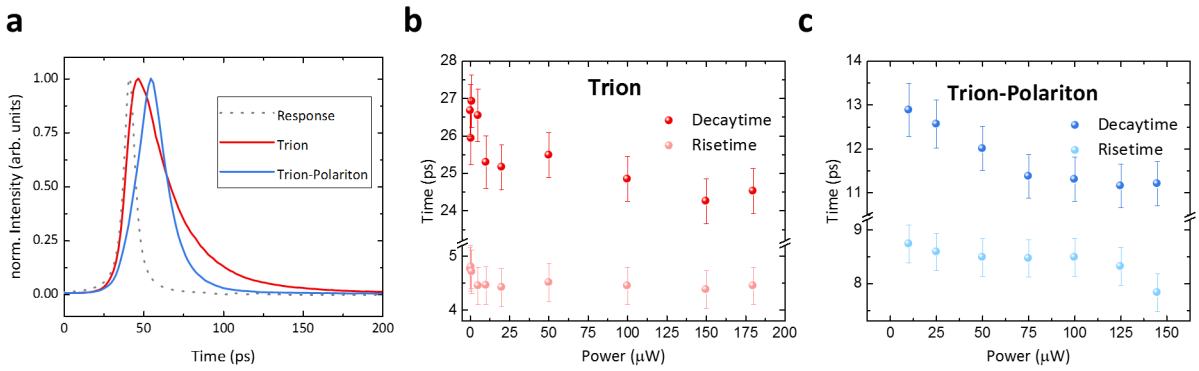

Figure 6.2: Dynamics measurements: (a) Normalized time traces of the trion (red line) and the trion-polariton (blue line) as well as the response function of the system (gray, dashed line) observed under pulsed excitation at 700 nm with an average excitation power of 100 μW. (b) Rise and decay time of the trion as a function of the average excitation power. (c) Rise and decay time of the trion-polariton as a function of the average excitation power.

the pure trion system is reduced to a two-level-system. For the trion-polariton, the non-linear terms were neglected, since the underlying stimulated scattering is not expected for trion-polaritons due to their fermionic character. N_0 is the initial electron-hole pair density, induced by the 120 fs laser pulse. Figure 6.3a schematically draws the two- and three-level model systems and the related time constants for the trion and trion-polariton, respectively.

In the pure trion case, the trion-formation and relaxation time τ_{eh-T} was set to 4.5 ps according to the measured rise time and trion decay time τ_T was set to 26 ps according to the measured decay time. The experimental rise and decay is plotted in Figure 6.3b together with the result of this simulation, showing that the simulation reproduces the experiment. Therefore, the risetime is interpreted as the trion formation and relaxation time, which is in good agreement with a pure trion formation time of 2 ps (excluding the relaxation time) [136]. This slight discrepancy in the rising tail is explained with the signal convolution with measurement system response function, which is not accounted for in the simulation. The decay time of the trion is on the same order of what has been identified as its radiative decay time τ_T at cryogenic temperatures (15 ps) [45]. The radiative decay time depends on the overlap of the charge carrier wave functions (see equation 2.7). This overlap depends in turn on the dielectric screening of the particle complex. Thus, changing the dielectric environment of the monolayer (substrate and capping) also affects the radiative decay time. Since the dielectric constant of the substrate (GaInP, 11.4 [103])) is higher than one of the substrate used in reference [45] (SiO_2, 2.1 [109]), the dielectric screening is stronger, which reduces the charge carrier overlap and leads to a

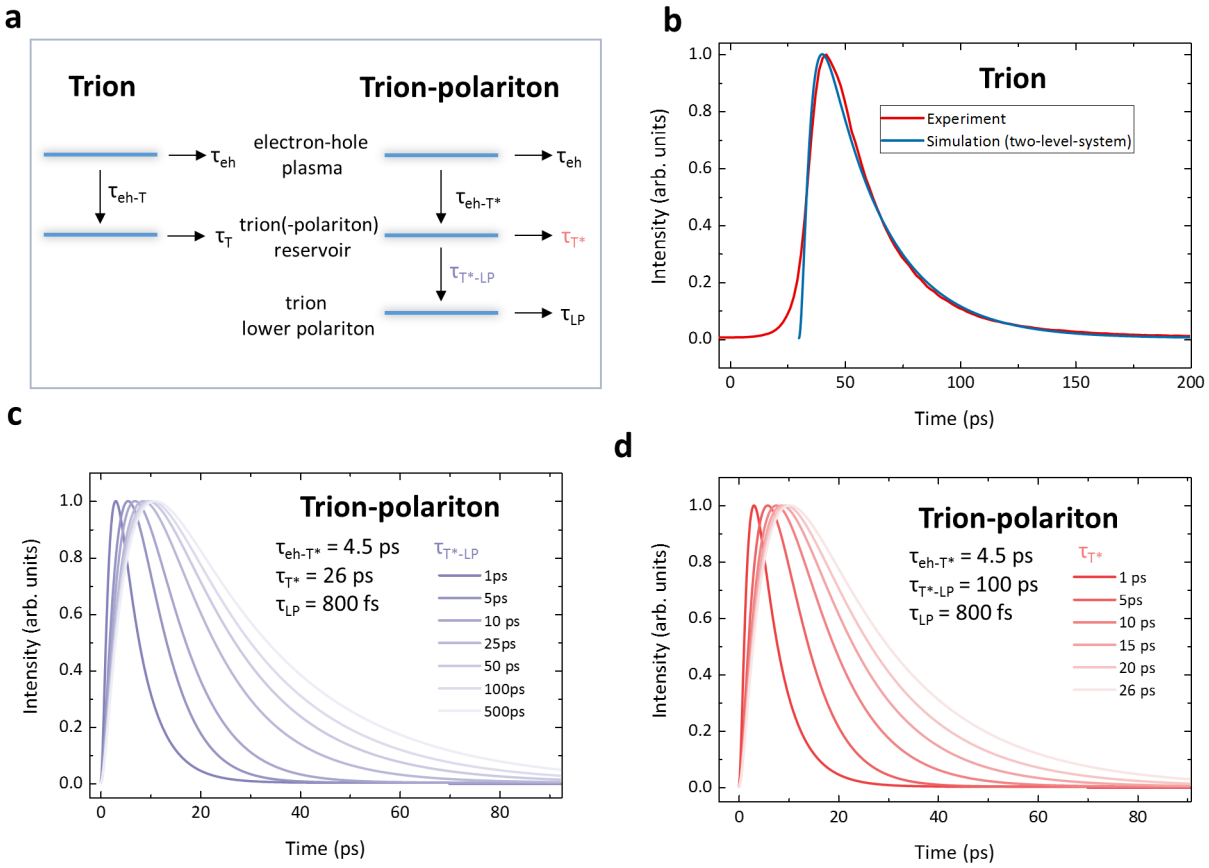

Figure 6.3: (a) Schematic illustration of dynamic models: While the trion is modeled with a two-level system, the trion-polariton dynamics are approximated with three levels, distinguishing between the trion-polariton reservoir and the lower polariton ground state. (b) Comparison of experimental and simulated trion dynamics. (c) Simulation of time-resolved ground state population for varying scattering times from the trion-polariton to the lower polariton ground state, which accounts for slowed polariton relaxation cause by suppressed phonon emission. (d) Simulation of time-resolved ground state population for varying trion-polariton decay times, which considers the faster trion-polariton reservoir depletion due to trion coupling to the cavity mode.

longer radiative decay time (26 ps). The radiative lifetime can be also calculated based on the observed normal mode splitting of the trion-polariton (5.2 meV) by using equation A.3 in appendix A.16 ($n_c = 2.453$ and $L_{eff} = 760\ nm$). This calculation yields a radiative lifetime of 28.5 ps, which is in excellent agreement with the observed decay time.

In the trion-polariton case, the trion formation and relaxation time should be mostly unaffected by the cavity since it mainly takes place outside the light cone. Therefore, τ_{eh-T^*} was kept at 4.5 ps for the trion-polariton simulations, where T^* denotes the trion-

polariton reservoir in the polariton system (for simplicity the trion reservoir outside the light cone and the trion-polariton reservoir inside the light cone are simulated as one level). Nevertheless, the measured rise time is prolonged as compared to the pure trion case. Such turn-on delay has been observed previously in GaAs based exciton-polariton samples [4] and is attributed to a longer scattering time from the trion-polariton reservoir to the lower polariton ground state τ_{T^*-LP} as compared to τ_{eh-T^*}. This behavior was explained in the following manner: The polariton relaxation into the low energy states is associated with the emission of multiple phonons. However, phonon emission is suppressed due to the inverted curvature of the in-plane dispersion relation between its two inflection points (see Figure 2.9). Consequently, the phonon-mediated relaxation is slowed and thus the PL emission from the ground state is delayed. This effect is known as the bottleneck effect [16, 137, 138]. To simulate this effect, τ_{T^*-LP} was varied from 1 ps to 500 ps as shown in Figure 6.3. In this first simulation, the decay time of trion-polariton reservoir τ_{T^*} was set to 26 ps, taken from the pure trion case as trion-polariton reservoir has a very trionic character. Furthermore, the lower polariton radiative decay time was set to 800 fs, which was calculated based on equation 2.30 ($\tau_c = 120\ fs$, $\tau_T = 26\ ps$, $|C|^2 = 0.148$ and $|T|^2 = 0.852$ with $|T|^2$ being the trion fraction). The results of the simulation are presented in Figure 6.3c. In fact, the longer scattering time τ_{T^*-LP} leads to an increasing rise time for the ground state. It is worth noting here that the very fast radiative decay time of the lower polariton ground state (800 fs) does not determine the decay time of the PL emission, as confirmed by the simulation.

While the rise time of trion-polariton is longer than for the pure trion, the decay time is shorter in the experimental observation (Figure 6.2). The shortened lower polariton decay time cannot be associated with its radiative decay time, but is rather interpreted as the depletion of the trion-polariton reservoir. Although the reservoir states have very trionic and little photonic character ($|T|^2 \geq 0.852$, $|C|^2 \leq 0.148$), they coupled to cavity photon mode and thus their radiative decay τ_{T^*} is expected to be reduced. Consequently, the reservoir is depleted faster. Therefore, the dynamics of the lower polariton population was simulated for various reservoir decay time from 1 ps to 26 ps. Here, the scattering time from the reservoir to the lower polariton was kept constant at 100 ps, taking into account the reduced polariton-phonon scattering. The results, shown in Figure 6.3d, reveal that the dynamics of the lower polariton ground state are affected by an accelerated depletion of the trion-polariton reservoir states. When the reservoir decay time is reduced, also the polariton ground state decay time decreases, which can explain the observed reduction when the trion is strongly coupled to the cavity mode. Overall, the interpretation of trion-polariton dynamics are more challenging because of the complex interplay of various scattering and decay times. This is the reason why the measured rise and decay times can not be directly attributed to certain time constants. Nevertheless, the longer rise time

can be explained by a slowed polariton scattering from the reservoir to the ground state (bottleneck effect) and the shorter decay time is associated with a faster depletion of the reservoir states because of its coupling to the cavity mode.

The dynamics measurement did not show strong dependences on the excitation power, but a slight decrease in the trion and trion-polariton decay times with power was observed. Both, trion and trion-polariton decay times, have been related to the radiative decay of the trion or the trion-like polariton reservoir. Previously, it had been observed that the exciton radiative decay time is reduced in TMDC monolayers for high densities, which was associated with exciton-exciton annihilation or Auger-type non-radiative decay processes [50, 139]. Thus, it seems reasonable that a similar non-radiative and density dependent effect reduces the decay time at higher excitation powers.

Finally, the results of the dynamics measurements should be related to the strong enhancement of the observed DOCP in the trion-polariton system. As elaborated in section 2.2, the measured DOCP and valley polarization is determined by the balance of decay and depolarization times (see also equation 2.8). The depolarization times have not been experimentally accessible here, but are still discussed based on estimations. By strong coupling between trion and cavity mode, the system benefits from both, a shorter decay time and a prolonged depolarization time. According to the dynamics experiments and their interpretation, both the trion-polariton reservoir and the ground state exhibit a faster radiative decay. However, the scattering to the ground state is slowed because of the suppressed phonon emission and thus the overall decay time is prolonged for the ground state. This is well in line with the lower DOCP value at the energy of the ground state (10 %) as compared to the trion-polariton reservoir (18 %). In order to estimate the depolarization time, equation 2.31 can be adapted to the trion-polariton depolarization time $\tau_{LP,s}$ [71]:

$$\tau_{LP,s} = \frac{1}{\beta\frac{|T|^2_{LP}}{\tau_{T,s}} + \frac{|C|^2_{LP}}{\tau_{C,s}}}, \tag{6.1}$$

where $\tau_{T,s}$ is the trion depolarization time. According to reference [71], the factor β needs to be introduced to account for reduced disorder scattering, because the polariton wave function ($\sim 1\ \mu m$) is much larger than the typical length scale of the trion disorder potentials (tens of nanometers). Thus, disorder scattering from low-k to high-k states is reduced, which also reduces the depolarization at high-k states (large LT-splitting) by the MSS mechanism [140]. The back-scattering to high-k states could be also reduced by the confinement potential of the lower polariton branch. Thus, β was estimated to about 0.05 [71]. The term $\frac{|C|^2_{LP}}{\tau_{C,s}}$ only makes up a small contribution to the denominator of equation 6.1, since the cavity fraction is relatively low (≤ 0.148) and the excepted cavity photon depolarization time (15 ps estimated for the cavity in reference [71]) is long as

compared to the trion depolarization time of 1 ps [71]. Consequently, the trion fraction ($\geq$ 0.852) and β mainly determine the prolonged trion-polariton depolarization time, which is about a factor of 20 longer than for the pure trion. The valley polarization of the trion-polariton system is therefore explained by a shortened radiative decay time and the prolonged depolarization time[1].

Overall, the relaxation, radiative decay and depolarization dynamics are significantly altered in the strong coupling regime. In comparison to pure trions, the relaxation of trion-polaritons is slowed down due to the suppressed polariton-phonon scattering, also known as the bottleneck effect. However, the radiative decay of the trion-polariton ground state and reservoir is shortened, due to the coupling to the cavity combined with the fast cavity decay time. The polariton depolarization time is slowed down, mainly due to suppressed disorder scattering. Both, the faster decay and slower depolarization help to conserve a significant fraction of valley polarization. These results are in good agreement with the findings of reference [71], published shortly after the result of this section, where DOCP values from few to almost 20 % have been measured for $MoSe_2$ monolayer trion-polaritons. The DOCP was dependent on the detuning of trion and cavity mode and the valley polarization of the lower trion-polariton decreased with a more negative detuning. This is an indication that the scattering into the lower polariton state is also slowed by a more distinct lower polariton curvature in the presented study. Although no dispersions were presented in reference [71] (polariton was identified in a detuning series), the reduced valley polarization of the lower polariton was modeled with a coupled rate equation system, which assumed a slowed scattering time into the lower polariton branch. Besides the quantitative difference between the results presented here and in reference [71], both studies demonstrate that valley polarization can be significantly increased up to 20 % by strongly coupling the trion to a cavity resonance. It should be noted that this enhancement effect might be limited by the fact that most of the depolarization takes place at high in-plane wave vectors outside the lightcone (large L-T splitting), where the trion dispersion remains unaffected by the coupling to the cavity.

6.2 Exciton-polaritons with WS_2

While the previous structure demonstrates a significant enhancement of the trion valley polarization when strongly coupled to a cavity resonance at cryogenic temperatures, it is of great interest from an application point of view to extend these studies to room temperature experiments on TMDC monolayer exciton-polaritons. Therefore, the valley polarization of the exciton-polaritons with a WS_2 monolayer, as described in chapter 5.2,

[1]The time-resolved measurements were carried out in close collaboration with P. Nagler, T. Korn and C. Schüller, University of Regensburg. Results presented in this section were published in reference [102].

was studied in more detail. In particular, the role of the dark ground state, which is energetically below the bright exciton state in WS_2 monolayer, was investigated, since it is considered crucial for preserving the valley polarization [64]. Moreover, the shape of the lower polariton branch allows a detailed investigation of the DOCP dependence on the in-plane wave vector.

As in the previous section, the exciton-polariton valley polarization should be compared to the one of excitons in bare monolayer. Thus, polarization-resolved PL measurements were carried out on bare WS_2 monolayer at various temperatures from 200 K to 290 K. Figure 6.4 depicts the polarization-resolved PL spectra (σ^+ excitation at 568 nm, 500 μW excitation power, 2 μm spot size) of the identical WS_2 monolayer (on a SiO_2 terminated SiO_2/TiO_2 DBR) that was later integrated into the investigated microcavity. At 200 K (Figure 6.4a), the PL spectrum exhibits an additional low-energy feature, which

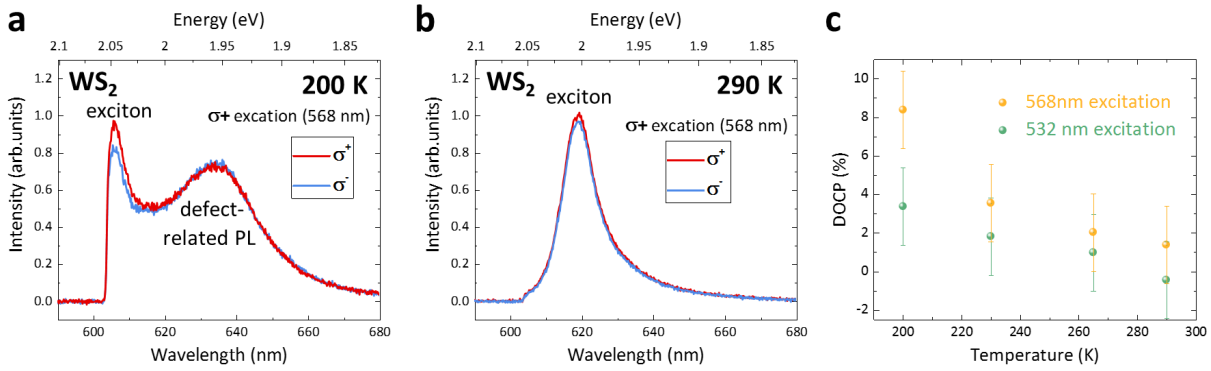

Figure 6.4: Valley polarization of the exciton: (a) PL measurement of σ^+/σ^- components of the exciton under σ^+ excitation at 568 nm and at 200 K. The high-energy tail of the exciton feature is slight cut by a high-pass filter that was used to block reflections of the excitation laser. In addition to the exciton, the spectrum shows a defect-related emission feature at lower energies. (b) σ^+/σ^- components of the exciton under σ^+ excitation at 568 nm and at 290 K. (c) Derived DOCP values from equivalent measurements under 532 nm and 568 nm excitations at various temperatures.

is associated with defect-bound excitons [134]. The σ^+ and σ^- components of the exciton emission show a slight difference, corresponding to a DOCP of 8.5 $\pm$ 2%. At 290 K (Figure 6.4b), hardly any difference of the σ^+ and σ^- components can be seen (2 $\pm$ 2% DOCP). These measurements were repeated at 230 K and 265 K and also under 532 nm excitation. Figure 6.4c compares the DOCP values for all experiments. For both excitation wavelengths, the DOCP is clearly increasing towards lower temperatures. This result is qualitatively consistent with previous findings [141], as phonon scattering enhances the mayor (MSS) depolarization mechanisms. At high temperatures, excitons are scattered

to higher in-plane wave vectors where the L-T splitting is larger and thus they depolarize faster. When comparing the excitation wavelengths, it can be seen that the higher energy excitation (532 nm) leads to a lower DOCP. A higher excitation energy means that excitons are formed at higher in-plane wave vectors and are subject to a larger L-T splitting. Furthermore, the relaxation path down to the ground state is longer, increasing the probability of intervalley scattering, which ultimately leads to a loss in valley polarization.

The same experiment was carried on the identical WS_2 monolayer at 290 K, but integrated into the DBR-metal cavity which was introduced in section 5.2. Figure 6.5 shows the σ^+ and σ^- components of the PL spectra for each excitation wavelength (532 nm vs. 568 nm) and at three different in-plane wave vectors (σ^+ excitation, 6 mW excitation power, 2 μm spot size). It should be noted that the excitation power was increased as

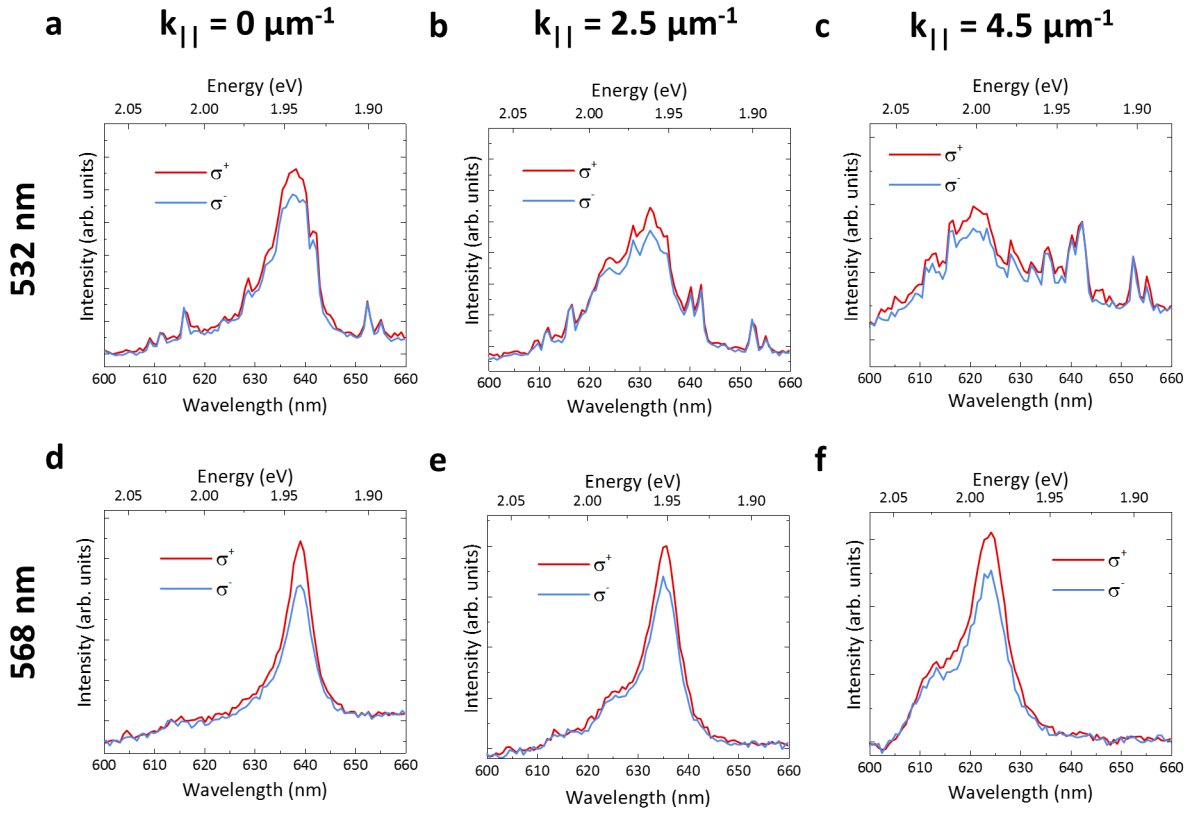

Figure 6.5: σ^+ and σ^- components of the PL spectra acquired at 290 K under σ^+ excitation at 532 nm (a - c) and at 568 nm (d - f). The measurement was carried out in the Fourier configuration, allowing to resolve the in-plane wave vector. The spectra are shown for three exemplary in-plane wave vector.

compared to the bare monolayer experiment, since the top silver layer strongly absorbs both the excitation beam and also the emitted signal, which also explains the relatively low signal-to-noise ratio of the presented data. In contrast to the 290 K measurement

of the exciton in the bare monolayer, all measurements clearly show a difference between the σ^+ and σ^- components. As before, the difference tends to be more pronounced under 568 nm excitation. Figure 6.6 depicts the a more detailed analysis of the DOCP values for various in-plane wave vectors. For a better comparison, the exciton-polariton characteristics presented in Figure 5.5a and b are replotted in Figure 6.6a. In addition,

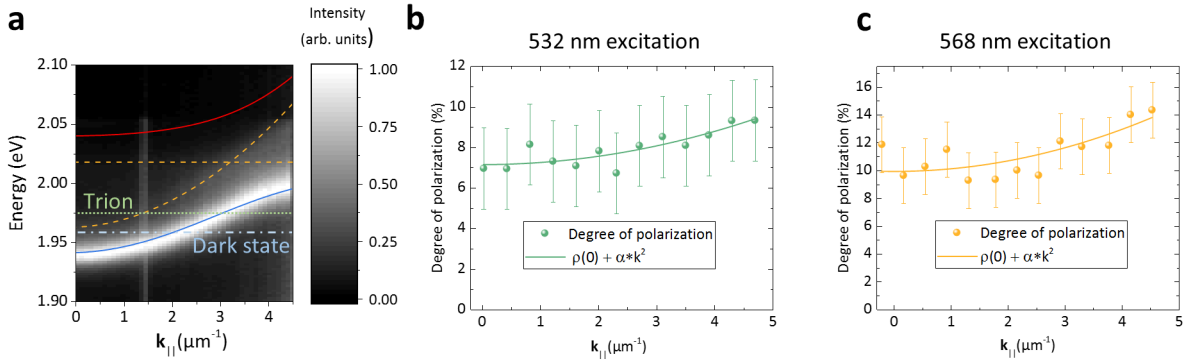

Figure 6.6: Valley polarization of the exciton-polariton: a) Re-plotted exciton-polariton dispersion relation with additional markings of the trion (green, dotted line) and dark state (light blue, dashed-dotted line) energies. b) and c) DOCP as function of the in-plane wave vector for 532 nm (b) and 568 nm (c) excitations.

the spectral positions of the trion (42 meV below the exciton [94]) and dark ground state (55 meV below the exciton [123]) were marked here. Although both states cross the lower polariton branch, they do not strongly couple to the cavity mode because of their very low oscillator strength (the trion may in fact carry enough oscillator strength for strong coupling as demonstrated in chapter 5.3, but only at cryogenic temperatures). However, both resonances may still weakly couple to the polariton mode. Figure 6.6b and c depict the DOCP as a function of the in-plane wave vector for the excitation wavelengths of 532 nm and 568 nm, respectively. Firstly, it is striking that the overall level of DOCP is significantly higher (up to 15 %) than for the pure exciton (about 2 %). The DOCP is slightly increasing with the in-plane wave vector from 7 ± 2 % to 10 ± 2 % for the 532 nm excitation and from 10 ± 2 % to 15 ± 2 % for the 568 nm excitation.

As elaborated in the previous section, the valley polarization of the exciton and exciton-polariton is determined by the balance of relaxation, decay and depolarization dynamics [64]. However, in WS_2 and WSe_2 the dynamics are more complicated because the ground state is optically inactive (dark ground state). Figure 6.7a illustrates a three-level model of the dynamics in the pure exciton case. The initial electron-hole population is distributed among the bright exciton and the dark exciton ground state during the exciton formation and relaxation. However, a transfer between the two states is possible by an effective intra-valley scattering process with a simultaneous spin flip [64]. The dynamic model for

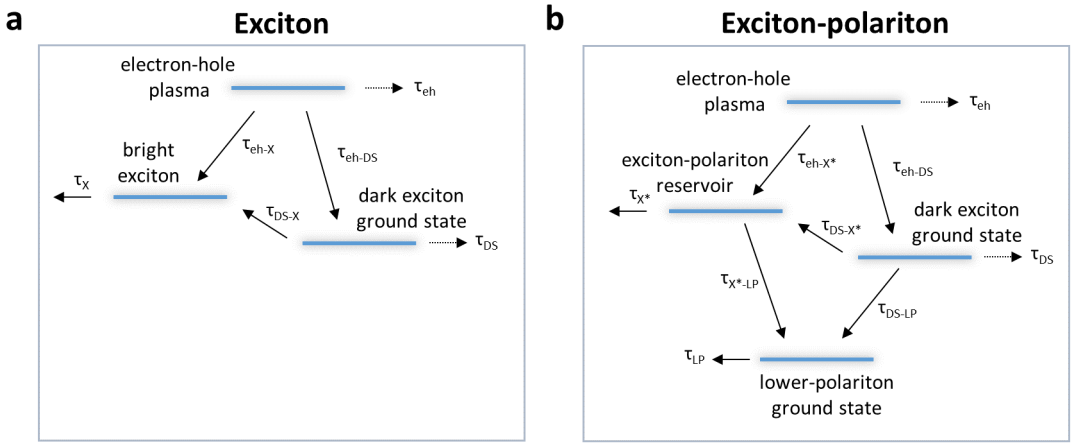

Figure 6.7: Exciton and exciton-polariton dynamics: (a) Three-level model of the exciton dynamics including the dark ground state. (b) Four-level model of the exciton-polariton dynamics including the lower-polariton ground state.

the exciton-polariton case requires a fourth level as shown in Figure 6.7b. The bright exciton at high in-plane wave vector (but already inside the lightcone) is referred to as exciton-polariton reservoir as it strongly couples to the cavity resonance. The fourth level is the ground state of the lower polariton branch. Transfer from the dark exciton ground state is possible to the exciton-polariton reservoir, to the lower polariton-ground state and also to all lower polariton states in between.

The transfer from the dark ground state plays a special role in preserving the valley polarization, since the dark state is not subject to the strong exchange interaction, which leads to the MSS-type depolarization [32]. Therefore, a transfer from the dark to a bright exciton state, followed by a fast radiative decay may lead to a significant valley polarization [64]. Thus, the role of the dark state should be considered in more detail in the investigated polariton system. While the dark ground state is situated energetically below the bright exciton state in bare WS_2 monolayer, the exciton-polariton dispersion crosses the dark state as indicated in Figure 6.6a. This already renders a transition from the dark exciton state to a bright polariton state more likely. Although the dark state has no oscillator strength at zero in-plane momentum due to its dipole orientation (hence, its name), it accumulates significant oscillator strength towards higher in-plane momenta [123]. Therefore, it is reasonable to assume that the dark state weakly couples to high-k polariton states. This coupling is enhanced by the cavity, which allows to reabsorb the emitted light form the dark state by polariton states. The relative transition probability was numerically modeled as a function of the in-plane wave vector. This model considers both the overlap integral of spectral distribution of the dark state $S_{DS}(k_{||})$ and of the bright lower polariton branch $S_{LPB}(k_{||})$, indicated in Figure 6.8a, as well as the increasing

dark state dipole moment $M(k_{||})$ towards higher wave vectors. Figure 6.8b shows the emission increase of the dark ground state as a function of emission angle, which serves as measure for the dipole moment (taken from reference [123] with permission). The transition probability $R(k_{||})$ expresses as:

$$R(k_{||}) \sim \int S_{DS}(k_{||}, E) \times S_{LPB}(k_{||}, E) dE \times M(k_{||}). \tag{6.2}$$

It was empirically shown that the dipole moment $M(k_{\|})$ has a quadratic dependence on the emission angle Θ (see Figure 6.8b) [123]. Using the relations $E = \hbar \cdot c \cdot k$ and $k_{\|} = k \sin(\Theta)$, $M(k_{\|})$ is expressed by

$$M(k_{\|}) \sim \left[arcsin \left(\frac{k_{\|} \cdot \hbar c}{E} \right) \right]^2 . \tag{6.3}$$

The spectral distributions are modeled as Lorentzian functions, where the linewidths for the lower polariton branch are calculated based on the Hopfield coefficients. The linewidth of the dark state is considered to be equal to the bright exciton linewidth at room temperature (29 meV) and the dark state energy is considered constant 55 meV below the exciton [123]. The result of this calculation is presented in Figure 6.8c. At

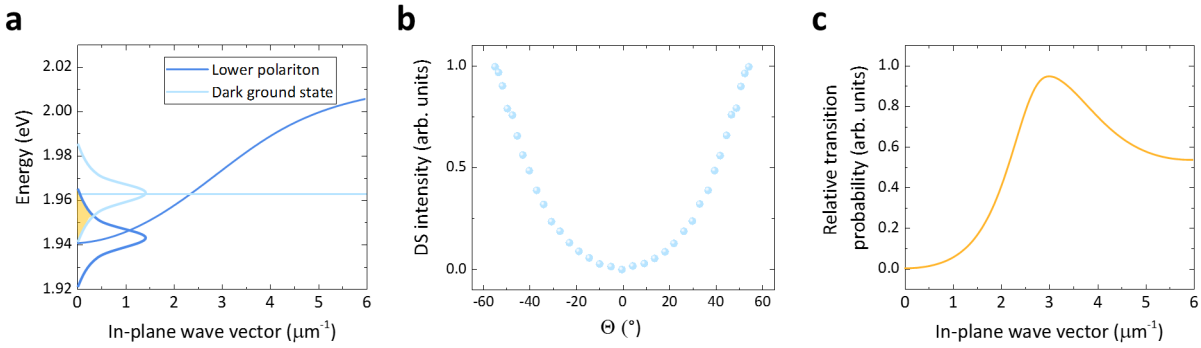

Figure 6.8: Dark state transition: (a) Dispersion of the lower polariton and the dark ground state. Both are modeled with Lorentzian function, which have an overlap depending on the in-plane wave vector as indicated by the yellow-shaded area. (b) Dark state emission intensity as a function of the emission angle. The emission intensity was taken as a measure for the dipole moment and has a quadratic dependence on the emission angle (taken and modified from reference [123] with permission). (c) Transition probability from the dark exciton state to the bright exciton-polariton state as a function of the in-plane wave vector derived from equation 6.2.

zero in-plane momentum, the transition is forbidden because the dark state has no dipole moment. The transition probability increases towards higher wave vector due to the

accumulation of oscillator strength of the dark state. The transition probability exhibits a maximum at $k_{||} \sim 3\ \mu m^{-1}$ (corresponding to 1.97 eV on the lower polariton dispersion), which is close to the crossing point of the dispersion relations of the lower polariton branch and the dark ground state. This calculation shows that the transfer from the dark ground state can be enhanced by establishing a lower polariton ground state energetically below the dark exciton ground state. Since the dark states are considered to be valley-polarized, the enhanced transfer is also expected to lead to an increased valley polarization of the bright polariton states.

In order to investigate if the formation of exciton-polariton also affects the decay dynamics, time-resolved PL measurements were taken for both a reference WS_2 monolayer and the exciton-polariton system. The samples were excited with a pulsed laser (120 fs pulse duration, 80 MHz repetition rate at 568 nm, 100 μW average power, 1 μm spot size). The time traces and extracted time constants from these measurements are presented in Figure 6.9. Fitting the time trace of the pure excitons in the reference monolayer (Figure 6.9a), reveals a double-exponential decay with the time constants $\tau_1 = 8.2 \pm 0.4$ ps and $\tau_2 = 31.6 \pm 3.0$ ps (details on the fitting can be found in appendix A.15). Figure 6.9b presents the time traces of the exciton-polariton reservoir at high in-plane wave vectors ($k_{||} = 5\ \mu m^{-1}$), and of the ground state at zero in-plane wave vector. Although the time-resolved PL configuration does not provide angle/momentum-resolution, the in-plane wave vector can be determined by its well defined energy along the dispersion relation (see Figure 5.6). The reservoir exhibits decay times of $\tau_1 = 8.8 \pm 0.4$ ps and $\tau_2 = 30.3 \pm 3.8$ ps and the lower polariton ground state shows decay times of $\tau_1 = 6.8 \pm 0.4$ ps and $\tau_2 = 23.2 \pm 3.2$ ps. Figure 6.9c and d present the values for τ_1 and τ_2, respectively, for the states along the dispersion between the ground state (value at lowest energy) and the reservoir (value at the highest energy). Both decay constants are steadily increasing with the exception of two features between 1.96 eV and 1.98 eV with a longer decay. As in the previous section, the pure radiative decay times of the exciton τ_X (200 fs [43, 41, 46]), of the exciton-polariton reservoir τ_{X^*} (50 fs) and of lower polariton ground state τ_{LP} (20 fs) do not determine the measured time constants (see also appendix A.16 for details on the radiative decay times).

As in the previous section, τ_1 is interpreted as effective depletion time of the exciton reservoir and exciton-polariton reservoir, including phonon-induced back-scattering of excitons outside the lightcone. The back-scattering leads to a much longer decay on the ps time scale compared to the pure radiative decay [41]. It is worth noting that τ_1 of the exciton (8.2 ± 0.4 ps) is comparable to τ_1 of the exciton-polariton reservoir (8.8 ± 0.4 ps). This is consistent, since the relaxation into exciton-polariton reservoir should be almost unaffected as it is close to the lightcone edge and has a very excitonic character ($|X|^2 > 0.8$).

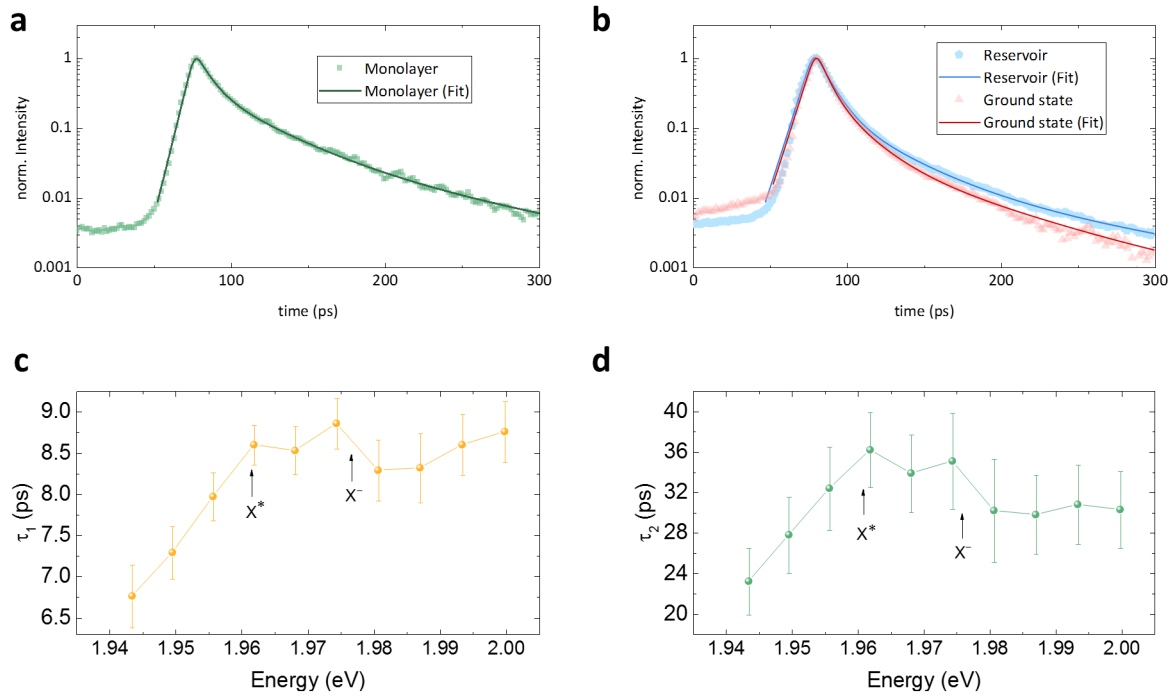

Figure 6.9: Dynamics measurement: a) Time trace and fit of exciton in bare WS_2 monolayer. b) Time traces and fits of the exciton-polariton reservoir at high in-plane k vectors (reservoir, plotted in blue) and at zero in-plane k vector (ground state, plotted in red). The initial signal (time < 50 ps) is part of the system response function and was therefore not includes in the fit in (a) and (b). c) and d) derived time constants from time traces of the exciton-polariton at various energies along the polariton branch, where the lowest energy corresponds to the ground state and the highest energy corresponds to the reservoir state.

τ_2 is attributed to the transfer from the dark state to either exciton (τ_{DS-X}), exciton-polariton reservoir (τ_{DS-X^*}) or the lower-polariton ground state (τ_{DS-LP}). Also for τ_2, no difference can be seen between the exciton (31.6 ± 3.0 ps) and the exciton-polariton reservoir (30.3 ± 3.8 ps). Again, this transfer seems mostly unaffected since the exciton-polariton reservoir is very excitonic. It should be noted that the prolonged decay times between 1.96 eV and 1.98 eV coincide with the maximum in the calculated transfer rates from the dark ground state (Figure 6.8). This is an experimental indication that the transfer from the dark ground state, potentially also from the trion, takes place and increases the lifetime of the lower polariton states, close to where the LPB and dark ground states dispersion cross.

Overall, the measured decay times are have not changed enough for the exciton-polariton to explain the significant increase in valley polarization. The exciton and

exciton-polariton reservoir show almost the same decay dynamics for example, but the measured DOCP values are very different (2 % vs. 14 %, respectively). As elaborated above, the transfer from the dark ground state provides a contribution to the measured valley polarization. Besides that, the shortened radiative decay time (20 - 50 fs for the exciton-polariton as compared to 200 fs for the free exciton inside the lightcone) is also beneficial to preserve a high DOCP. Most likely, the reduced disorder scattering to high-k state, as explained in the previous section, also favors a higher valley polarization [71, 140]. The dependence of the DOCP on the in-plane wave vector, as shown in Figure 6.6, is explained with the fact that relaxation to the lowest energy state (polariton ground state) takes longest and thus depolarization is more likely. This dependence is modeled with a stepwise polariton relaxation, taking into account that the depolarization strength decreases with smaller in-plane wave vector [142] (see appendix A.17 for more details). It should be noted that polariton depolarization mainly originates from the TE-TM splitting of cavity, which was estimated to be about two orders of magnitude larger than the excitons L-T splitting in this k-vector range [140]. According to this model, the valley polarization $\rho(k_{||})$ of polaritons can be analytically described by:

$$\rho(k_{||}) = \rho(0) + \alpha k_{||}^2, \tag{6.4}$$

where $\rho(0)$ is the DOCP at $k_{||} = 0$ and α is a constant depending of the strength of depolarization [63]. This dependence fits the experimental data presented in Figure 6.6b and c well. This modeling and experimental observation is also well in line with finding of the previous section, where the DOCP was found to be lower for the ground state than for states at higher energies.

Although strong coupling to the cavity resonance increases the valley polarization, it may not prevent most of the depolarization, if the system is excited non-resonantly, because the depolarization is strongest for high in-plane wave vectors (larger L-T splitting). This conclusion implies that the exciton-polaritons need to be excited closer to the ground state or even resonantly, which is also supported by the observation that the measured DOCP was higher for the lower excitation energy at 568 nm as compared to 532 nm.

Shortly before these results were published, there were two publications that reported on a similar enhancement of the valley polarization of TMDC monolayer based exciton-polaritons at room temperature [65, 128]. Reference [65] demonstrated strong coupling of a MoS_2 monolayer exciton to a monolithic DBR-DBR microcavity with a normal mode splitting of 39 meV. The structure exhibits a valley polarization of 13 %, while the valley polarization of the bare monolayer exciton was determined to less than 1 %. Although no time resolved measurements were presented, the measured DOCP values were reproduced with a rate equation model. The model uses a prolonged exciton-polarization depolarization time, based on the assumption that depolarization only takes place in the exciton

component of the polariton. This approach appears to be rather empirical, but nevertheless the experimental findings are in good agreement with the results presented in this section. Reference [128] presents strong coupling of a WS_2 monolayer to a microcavity consisting of a top and bottom silver layer. For a comparable detuning (-60 meV in [128], - 56 meV here), the presented normal mode splitting of 80 meV is in excellent agreement with the observations presented in this section. The DOCP values at room temperature ranged from 15 % to 19 %, depending on the detuning and in-plane wave vector. Reference [128] does not show time-resolved measurements either, but explains the enhanced degree of valley polarization with an accelerated decay time in the framework of rate equation model. However, the role of the dark ground state was not mentioned. Thus, the experimental results of this section and of references [65] and [128] are in good agreement, but the each interpretation emphasizes different aspects.

Recently, there has been another demonstration of an enhanced valley polarization in a WSe_2 monolayer based exciton-polariton in an open cavity (26.5 meV normal mode splitting) at cryogenic temperatures [143]. The maximum of the extracted DOCP was 35 % at an energy that coincided with trion state. Consequently, it was concluded that a valley polarized transfer from the trion takes place, similar to the discussed transfer from the dark state. However, no signature for a transfer from the dark ground state was observed. It should be noted that the measurement was carried out at cryogenic temperatures, where the trion contribution is more pronounced as compared to room temperature experiments. Because of that, the study can not be directly compared with the results of this section. Nevertheless, the study shows that a valley polarized transfer from another state (dark ground state or trion) is a plausible explanation for an enhanced DOCP.

In summary, the valley polarization is a complex interplay between the dynamics of exciton and exciton-polariton relaxation, intervalley scattering, radiative decay and transfer between bright and dark states. It was found that the exciton relaxation outside the light cone is almost unaffected by the cavity, yielding the conclusion that the relaxation dynamics cannot explain the strong enhancement in valley polarization. The depolarization due to the strong exchange interaction takes mainly place outside the light cone, which means that valley polarization is already strongly reduced once excitons enter the light cone. Nevertheless, the remaining valley polarization can be conserved in the polariton regime since depolarization is slowed down and the radiative decay is shortened. However, the TM-TE splitting of the cavity opens up a new spin-valley depolarization mechanism, which may explain the measured dependence of the DOCP on the in-plane wave vector. In addition, the transfer of the dark state is significantly increased due to the red-shift of the lower polariton and the cavity effect. This provides another valley-conserving relaxation channel. Overall, these finding and their interpretation provide a qualitative image of the

major contributions to the polariton enhanced valley polarization[2].

6.3 Exciton-polaritons with $MoSe_2$

Besides integrating monolayers into microcavities, quasi-resonant excitation close the exciton resonance has been a successful approach to induce a high valley polarization [141]. As shown in the previous section, excitation closer to the resonance shortens the relaxation pathway and only excites excitons at low in-plane wave vectors, where the L-T splitting is small and thus intervalley scattering/depolarization is reduced. This approach has been successively used to measure reasonably high DOCP values in MoS_2 (40 %) [145], WS_2 (90 %) [146] and WSe_2 (40 %) [133] monolayers at cryogenic temperature and DOCP values up to 30 % in WS_2 monolayer a room temperature [141]. However, in $MoSe_2$ monolayer only few percent valley polarization could be observed under such optimized conditions [58, 71]. To achieve close-to-unity valley polarization, excitons in WSe_2 have been resonantly excited in a two-photon absorption process [147]. In this section, a combination of both approaches, namely monolayer integration into a microcavity and two-photon excitation, is applied. More specifically, a $MoSe_2$ monolayer was integrated into a mechanically assembled, monolithic microcavity and the valley polarization of the LPB was probed by polarization-resolved spectroscopy under two-photon excitation.

The microcavity design is the same as described in section 4.2.2, but additionally contains a $MoSe_2$ monolayer as schematically depicted in Figure 6.10a. The structure is also shown from the top view in a microscope image in Figure 6.10b (monolayer is marked in blue for better visibility). The monolayer spatial extension is about 8 x 40 μm. A PL spectrum of the monolayer was measured at 5 K (Figure 6.10c, 532 nm excitation, 500 μW excitation power, cw, spotsize 2 μm), after PMMA coverage, but before the top DBR was placed on the sample. This spectrum shows clear exciton and trion resonances at 745.5 nm/1.663 eV and 759.8 nm/1.632 eV, respectively. Figure 6.10c also shows a reflectivity spectrum of the empty cavity measured next to the monolayer position. The spectrum confirms that the cavity mode (747.3 nm/ 1.659 eV) is close to the exciton resonance.

Subsequently, the complete system was probed under cw excitation at 740 nm/1.676 eV (1 mW excitation power, 2 μm spotsize) to acquire its PL dispersion relation as presented in Figure 6.11a. Neither the cavity mode, nor exciton or trion mode can be observed but a new mode appears with a ground state at 761.4 nm/1.628 eV. This mode has a parabolic dispersion relation at small in-plane momentum components parallel to the long monolayer axis. In contrast, if the dispersion is measured perpendicular to the mono-

[2]The time-resolved measurements were carried out in close collaboration with P. Nagler, T. Korn and C. Schüller, University of Regensburg and results presented in this section were published in reference [144]

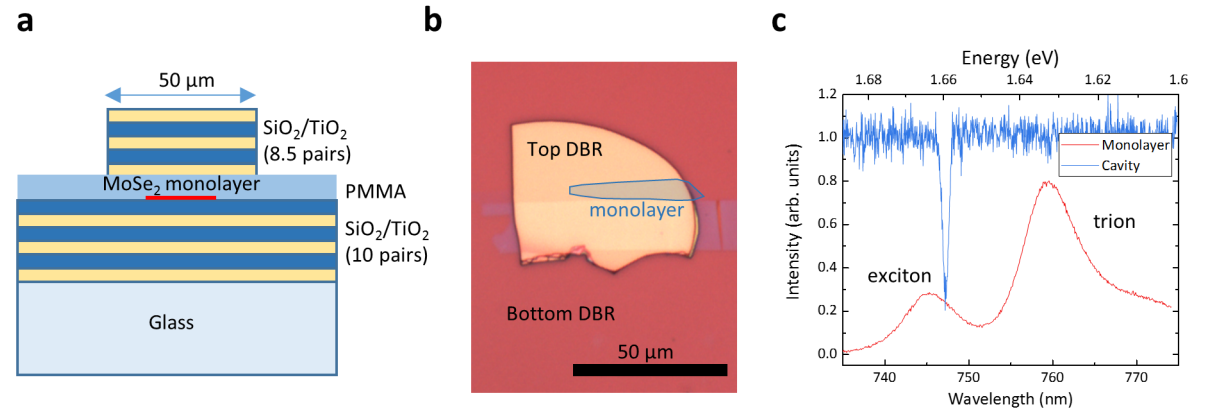

Figure 6.10: Sample structure: (a) Schematic illustration of the sample structure incl. the $MoSe_2$ monolayer. (b) Microscope image of the sample (top view), where the monolayer was marked in blue for better visibility. (c) PL spectrum of the monolayer at 5 K without top mirror and reflectivity spectrum of the empty cavity measured next to the monolayer.

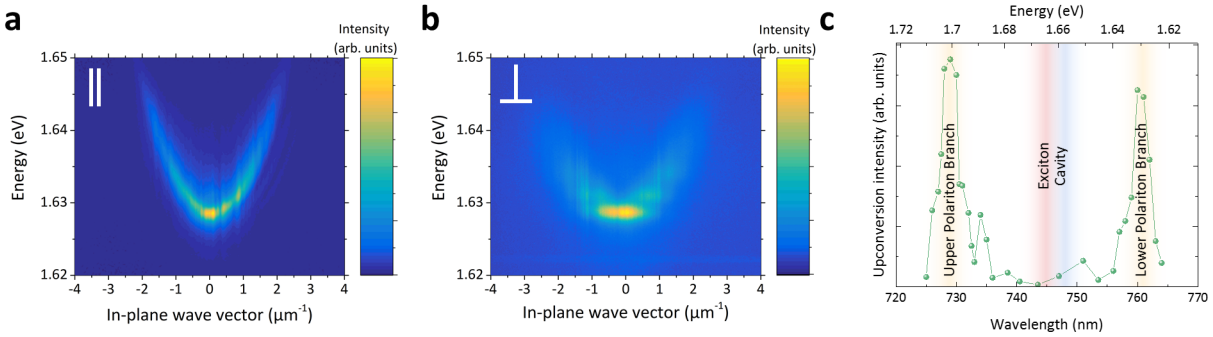

Figure 6.11: Exciton-polariton: PL dispersion relation of the full system measured along (a) and perpendicular to (b) the elongated monolayer direction. (c) Plot of upconversion intensity as a function of double the excitation energy. The energies of uncoupled cavity and exciton are marked in blue and red, respectively.

layer extension, discrete modes appear in the PL spectrum as depicted in Figure 6.11b. The mode discretization can be well explained by the lateral confinement given by the monolayer width and the confinement potential that arises from a normal mode splitting (energy difference between uncoupled exciton and lower polariton ground state). The mode splitting between fundamental and first excited mode of 2.7 meV is also quantitatively consistent with an optical mode confinement induced by the monolayer width of 8 μm. The quantization of perpendicular modes of an elongated cavity wire can be

calculated according to [148]:

$$E_m(k_x) = \sqrt{E_C^2 + \frac{h^2c^2}{4\pi^2\varepsilon_{eff}}(k_x^2 + \frac{(m+1)^2\pi^2}{L_y^2})}, \tag{6.5}$$

where $E_m(k_x)$ is the energy dispersion of the mode along the elongated direction x (no confinement) with the quantization index m (m = 0,1,2,..), ε_{eff} is the effective refractive index and L_y is the confinement length in y (perpendicular to x). The dispersion of these cavity modes was put into the coupled oscillator model. Using the measured exciton and cavity energies and the monolayer width (8 μm) as an input, the measured ground mode $E_0(k_x)$, presented in Figure 6.11a, can be reproduced with a coupling constant of 66 meV, $\epsilon_{eff} = 1.27$ as shown in Figure 6.12. The difference between $E_1(k_x)$ and $E_0(k_x)$ was calculated to be 3.0 meV, which is in excellent agreement with a measured quantization of 2.7 meV, extracted from the data set shown in Figure 6.11b.

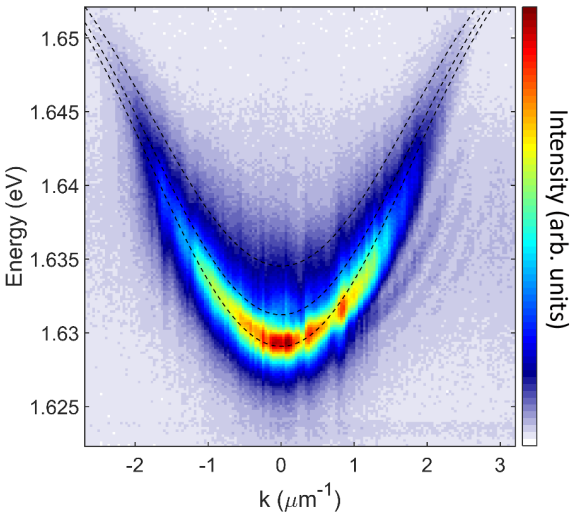

Figure 6.12: Acquired dispersion along the elongated flake direction x and calculated dispersion relations (black dashed lines) for the quantization indices 0, 1 and 2.

Therefore, this new mode was attributed to the lower polariton branch of the strongly coupled exciton-cavity system. As for the previously presented polariton systems, the upper polariton branch and also lower polariton states with large in-plane wave vectors are not observed under such experimental conditions, since their thermal population of is very low at cryogenic temperatures [149]. Assuming a Boltzmann distribution for the population of the polariton branches, the ratio of the upper polariton population P_{UP} to the lower polariton population P_{LP} was estimated by:

$$\frac{P_{UP}}{P_{LP}} = e^{-\frac{\hbar\Omega}{k_BT}}, \tag{6.6}$$

yielding a ratio of about 10^{-61}. Thus, the upper polariton can not be expected to be observed in a PL experiment. However, these states can be directly probed by a resonant second harmonic generation (SHG) process, to provide unambiguous evidence of the characteristic split-peak spectrum. The broken inversion symmetry of the monolayer crystal (a requirement of the SHG process) provides excellent conditions for efficient SHG [150, 151] and the SHG efficiency is strongly enhanced when the energy of the optical resonances coincides with twice the energy of the driving field [58, 152]. Since the SHG intensity dependence on the excitation intensity is a quadratic function, the full structure was excited by high-intensity laser pulses (Coherent Mira-OPO system, 2 ps, 82 MHz, 1.5 nm linewidth, 110 mW average power, 3 μm spotsize). The laser wavelength was scanned from 1450 nm to 1528 nm, while monitoring the signal at half the laser wavelength, as shown in Figure 6.11c.

In fact, scanning over the resonance that was found in Figure 6.11a, results in a strong enhancement of the SHG signal. In contrast, at the exciton energy, no SHG intensity enhancement is observed as could be expected in the uncoupled case [147]. Instead, another strong response of the system appears around 729 nm, evidencing the existence of a second resonance, which was identify as the upper polariton branch. To support this identification, the exciton and cavity energies (detuning of -4 meV) were used as input parameters for the two-coupled-oscillator model described in section 2.4.1 and the coupling strength was adjusted to 66 meV to match the observed LPB at 761.4 nm/1.628 eV. Figure 6.13 shows the modeled polariton dispersions. This model predicts a UPB at

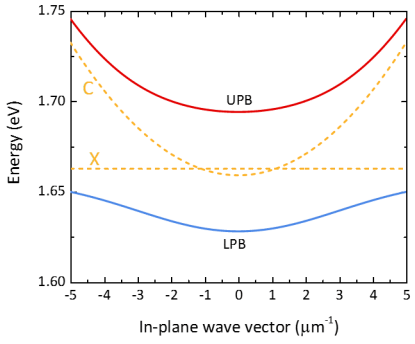

Figure 6.13: Two-coupled oscillator model for the investigated system.

730.2 nm/1.698 eV, which coincides very well with observed UPB in the two-photon excitation experiment. The model yields a normal mode splitting of 65 $\pm$ 3 meV and exciton and cavity fractions of $|X|^2 = 0.42$ and $|C|^2 = 0.58$ for the LPB at zero in-plane momentum.

In order to study the two-photon absorption process in more detail, the structure was

excited slightly above the ground state at a wavelength of 1514 nm, yielding a SHG signal at 757 nm. Figure 6.14a shows the resulting emission spectrum under such excitation. Besides the SHG emission peak at 757 nm, the spectrum is dominated by the emission

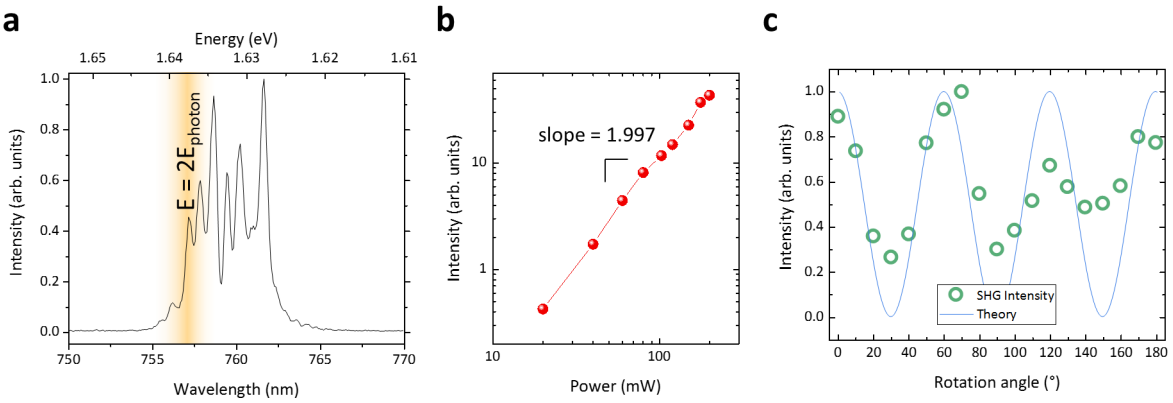

Figure 6.14: Two-photon excitation: (a) Emission spectrum under slightly off-resonant excitation at 1514 nm, showing emission features at the SHG energy (marked in orange), but also at lower energies. (b) Double-logarithmic plot of the SHG intensity (intensity from the SHG energy feature only) versus excitation power (error is covered by the symbol size). (c) Dependence of the SHG intensity on the orientation of the exciting lights linear polarization (error is corresponds to the symbol size).

from resonances that have lower energies than the SHG signal. The lowest energy resonance coincides with the ground state of the lower polariton branch. This indicates that exciton-polaritons, which are resonantly excited via two-photon absorption, can relax to the systems ground state. This is a strong indication that SHG is not the only microscopic process taking place under two-photon excitation since it should only be observable at double the excitation energy with an emission peak which has a linewidth that corresponds to the excitation laser linewidth (1.5 nm as tested on a bare $MoSe_2$ monolayer, see appendix A.18). Most likely, the emission from other energies is a result of a two-photon interband transition. In principle, such a transition is spin-forbidden for a 1s exciton (and the corresponding exciton-polariton), however the intermixing with 2p states allows a two-photon interband transition into this state [26, 153]. Following references [58, 147], the emission features below double the exciton energy are therefore referred to as two-photon-induced photoluminescence (2P-PL). Figure 6.15 schematically illustrated the difference between the two processes.

The discretization of the 2P-PL stems from the polariton mode discretization perpendicular to the monolayer extension as depicted in Figure 6.11b. The non-linear nature

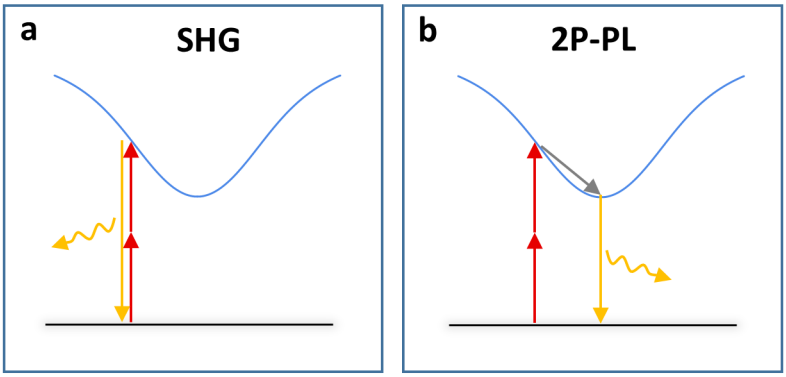

Figure 6.15: Schematic illustration of (a) the second harmonic generation (SHG) and (b) the two-photon induced photoluminescence (2P-PL) processes under two-photon excitation of the polariton system.

of the two photon absorption process is directly reflected in the dependence of the SHG emission intensity (excluding the 2P-PL signal) on the excitation power as presented in Figure 6.14b. The extracted power law coefficient is 2.00 ± 0.05, which clearly confirms the two-photon absorption nature of the process. In addition, the SHG intensity (again, excluding 2P-PL) was measured as a function of the orientation of the linearly polarized excitation light. The experiment was carried out by rotating the polarization orientation by a half-wave plate and detecting the emission in the same orientation. The selection rules for the SHG in TMDC monolayers predict that the polarization orientation is only conserved when it is aligned with one of the crystal axes [26], which leads to an oscillating intensity dependence with 60° periodicity [150, 151]. In contrast, 2P-PL does not follow these specific selections rules [147]. Figure 6.14b shows the result of this measurement. A clear intensity modulation can be seen, which is however not as distinct as on bare monolayer samples [150, 151]. Therefore, it is concluded that signal is a superposition of SHG and 2P-PL.

Finally, the strong non-linear response of the system was used to quasi-resonantly address specific valleys or a coherent superposition of different valleys in the $MoSe_2$ monolayer. In contrast to conventional one-photon PL, this techniques does not require to filter the excitation laser, which in turn allows to excite polariton states much closer or even at the ground state. At first, the DOCP was measured under 1518 nm excitation in both the $\sigma+$ and $\sigma-$ configurations. The results of this measurement are depicted in Figure 6.16. The emitted signal is strongly cross-polarized with an opposite helicity as compared to excitation polarization. Observing a counter-rotating signal is fully consistent with the SHG selection rules for crystals with broken inversion symmetry and three-fold rotation symmetry [154], which also holds true for two-photon interband transitions [147]. Figure 6.16 also contains a plot of the DOCP across the spectral features of the emission. The

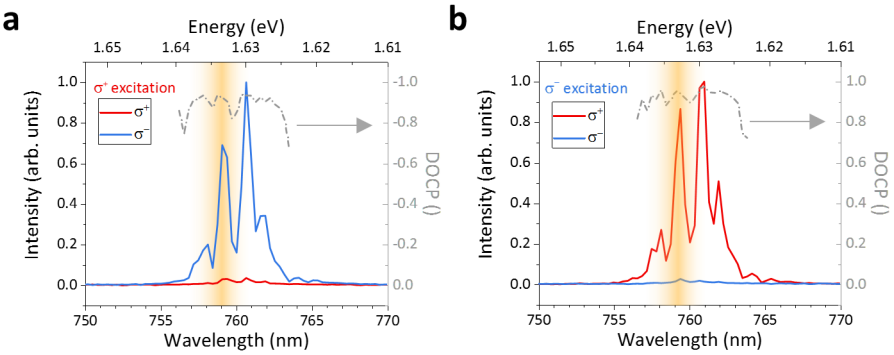

Figure 6.16: Valley-polarization: Polarization-resolved PL spectra acquired under $\sigma+$ (a) and $\sigma-$ (b) excitation at 1518 nm. Double the excitation energy is marked in orange. The extracted DOCP values are plotted for the features of interest (gray, dashed line).

extracted DOCP is higher than 90 %, even for the 2P-PL features above and below the SHG resonance.

The outstandingly high valley polarization is explained by two factors: First, the excited polariton states are situated close to the ground state, and therefore their in-plane wave vectors are low ($< 1.5\ \mu m^{-1}$). Hence, the TE-TM splitting of the cavity, which is the main mechanism of depolarization of the exciton-polariton, is small as compared to the case of non-resonant excitation. As assessed in references [71, 140] and discussed in the previous two sections, the strong coupling conditions reduces disorder scattering from low-k to high-k states. Scattering to high-k states would increase the depolarization, since the TE-TM splitting increases with the k-vector for states within the lightcone or due to the significant exciton L-T splitting for scattering outside the lightcone. Thus, the reduction of disorder scattering suppresses the depolarization and increases the depolarization time by a factor of approximately 20 [71]. In particular, the negative detuning of exciton and cavity photon mode is crucial for such suppression of disorder scattering [140]. Second, the polariton lifetime is shortened by coupling to the cavity. Using equations 2.11 and 2.30 with a cavity linewidth 1.54 meV (extracted from the reflectivity spectrum in Figure 6.10) as input, the polariton life time of 263 fs is determined, which is significantly lower than for the pure exciton (390 fs [44]). For both reasons, a strong increase in the degree of circular polarization can be expected. As described in previous sections, the resulting value of DOCP is governed by the interplay between radiative decay time and the spin-valley relaxation time and can be approximated by equation 2.8. The intervalley scattering time for the pure $MoSe_2$ monolayer exciton is 150 fs [44, 71]. Assuming a 20-fold increase due to suppressed disorder scattering as estimated in reference [71], the polariton depolarization time is calculated to 3 ps. By using the calculated polariton decay and depolarization

times, equation 2.8 yields a valley polarization of 92 %, which is in excellent agreement with the experimental observations.

While valley polarization can be generated by excitation with circular polarized light as shown above, excitation with linear polarized light may induce a coherent superposition of valley polaritons. Valley coherence has been observed in MoS_2 (55 % [95]), WS_2 (80 % [141]) and WSe_2 (40 % [152]). However, it has not been reported in $MoSe_2$ at the time this thesis was written. The degree of linear polarization (DOLP) of the decaying polaritons (2P-PL) provides a direct measure of the dephasing processes of the polariton pseudospin. The system was excited at 1514 nm (757 nm) with linearly polarized light in X- and Y-basis, where the X axis is aligned with one of the crystal axis (determined by the maxima in Figure 6.14c) and the Y axis is perpendicular to the X axis. The emitted signal is subsequently measured in the each base and the DOLP was determined with $\rho_{lin} = \frac{I(X)-I(Y)}{I(X)+I(Y)}$. Figure 6.17 depicts the acquired spectra and deduced DOLP values as a function of the detected wavelength. Indeed, the polarization of the resonantly scattered

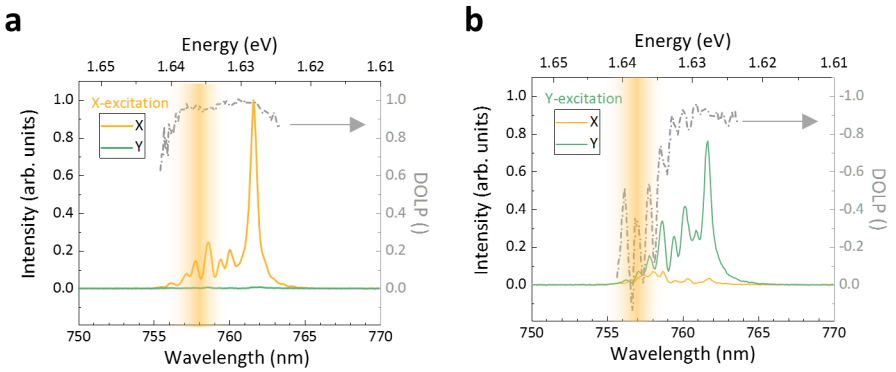

Figure 6.17: Valley-coherence: Polarization-resolved PL spectra acquired under X (a) and Y (b) excitation at 1514 nm. Double the excitation energy is marked in orange. The extracted DOLP values are plotted for the features of interest (gray, dashed line).

fraction of the signal (SHG part) is expected to be fully governed by the crystal symmetry and yields no information about the valley coherence of the polaritons. However, DOLP values of the 2P-PL signal can be interpreted as valley coherence. Although exciton-polaritons need to undergo at least one inelastic relaxation process, the valley coherence clearly exceeds 90 % in both excitation schemes even 10 meV below the energy of the SHG signal. In both excitation bases, the linear polarization of the 2P-PL follows the excitation orientation. However, the linear orientation of the SHG signal should only follow the excitation orientation if aligned with a crystal axis. This is in fact the case for the X-basis as shown in Figure 6.17a. In contrast, the DOLP signal is close to zero or even negative around the SHG frequency under Y-basis excitation. The reason is that

the Y-basis does not coincide with a crystal axis and therefore the emission orientation is rotated by 90° in this specific configuration [26]. Consequently, excitation in the Y-basis should lead to a SHG emission in X-orientation. However, the signal at the SHG energy is a superposition of the emission from both processes (SHG and 2P-PL), which makes a quantitative interpretation difficult. The high degree of valley coherence can be explained by the same arguments as for the high valley polarization: A fast radiative decay and a prolonged depolarization time [155].

In contrast to TMDC excitons, which have a diffusion length of a few hundred nanometers in high quality samples [13, 14], TMDC based polaritons are expected to expand over significantly larger distances (on the order of 10 μm) even in the linear, non-ballistic regime due to their small effective masses [15]. Figure 6.18a depicts the spatial intensity distribution of near-resonantly (1514 nm) injected polaritons on the monolayer. An in-

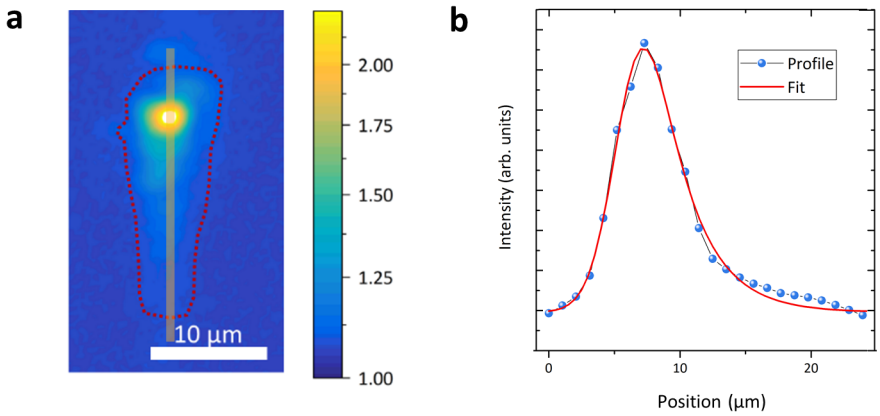

Figure 6.18: Polariton expansion length: a) intensity distribution across the monolayer. The line of the profile that is presented in b) is marked in orange. The profile was fit with a convolution of a Gaussian shaped focus with an exponential decay function to extract a polariton expansion length of 3.6 μm.

tensity profile was taken from the intensity distribution presented in Figure 6.18a (profile cut is marked by the orange line), which is plotted in Figure 6.18b. This profile was fitted with a convolution of the Gaussian shaped focus profile (FWHM of 2.5 μm) with an exponential decay function. This fit yields a decay constant of 3.6 μm, which is taken as the polariton expansion length. It should be noted that an excitation slightly above the LPB (in this case 10 meV) is essential to create polaritons with finite wave vectors and thus finite group velocities.

Such propagation lengths allow to investigate the valley dependent polariton propagation upon valley coherent initialization of the system. This is recorded via spatial- and polarization-resolved luminescence. The spatial intensity distribution (replotted in Figure

6.19a) was recorded in the σ^+ and σ^- basis and the spatial-resolved DOCP was deduced. Figure 6.19b depicts a DOCP distribution recorded under linearly polarized two-photon excitation at 1514 nm. The initial polarization angle was -75° with respect to the long

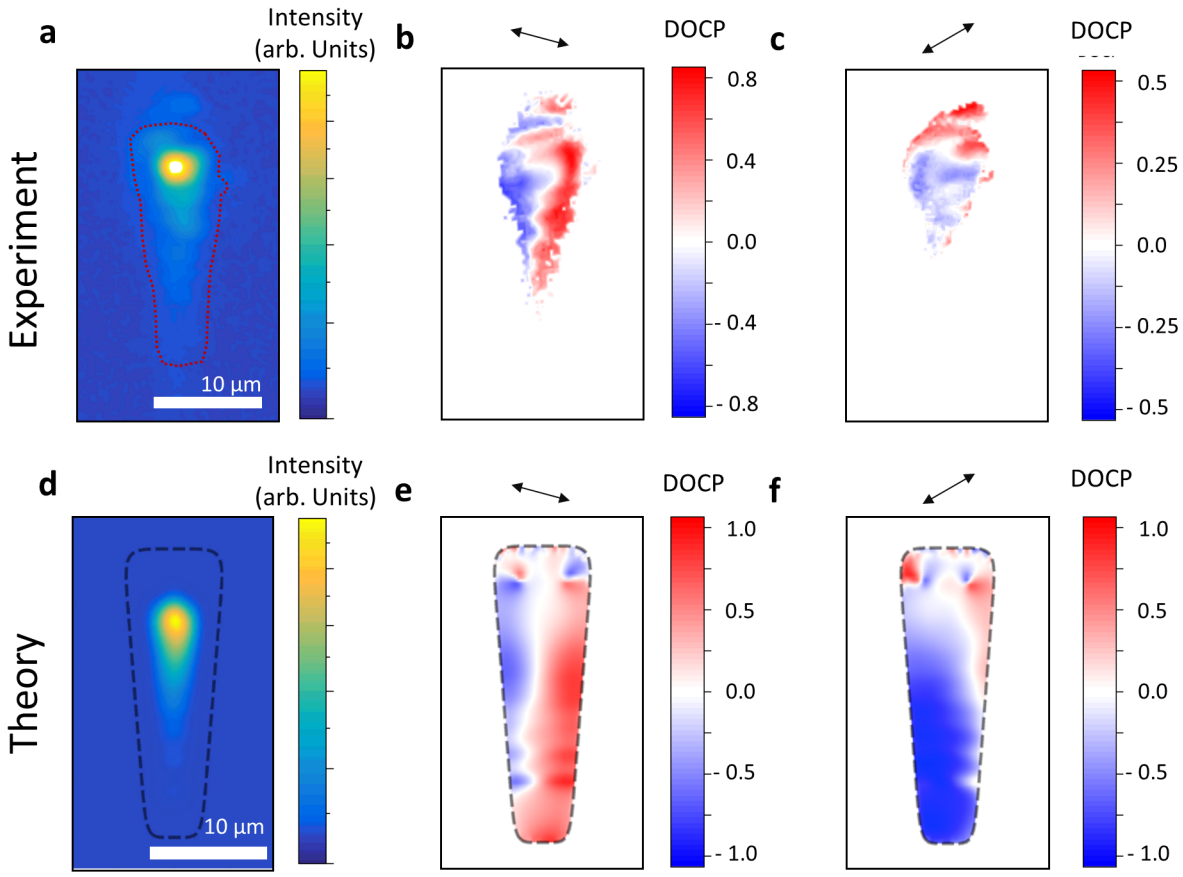

Figure 6.19: Optical valley hall effect: a) PL intensity distribution along the monolayer, observed under two-photon excitation at 1514 nm (the white point marks the excitation spot on the monolayer). b) Spatially resolved DOCP distribution across the monolayer. The polarization orientation of excitation light (-75° with respect to the long monolayer axis) is indicated by the double-headed arrow. (c) DOCP distribution across the monolayer with a polarization orientation that was rotated by -45° (-120° with respect to the long monolayer axis). d-f) Simulated intensity and DOCP distributions, each corresponding to Figure above.

monolayer axis. Clearly, the DOCP distribution shows two domains with a left-right separation that is slightly rotated clockwise, and features an oscillating pattern along the vertical stripe direction. The DOCP was not plotted for the bottom tip of the monolayer, since the signal-to-noise ratio is to weak for this region (a plot threshold was set for a signal-to-noise ratio of at least 1.5). As the initial polarization orientation was rotated by

-45° (Figure 6.19c), a dramatic change in the polarization pattern was observed with a vertical domain separation and weak σ^+ regions along the right monolayer edge. Similar pattern have been predicted [156] and observed [157] as spin domains of exciton-polaritons with GaAs QWs. The spin separation was explained as a result of the TE-TM splitting of the cavity and the L-T splitting of the exciton, whereas the latter is significantly weaker pronounced. For a in-plane wave vector of 1.5 μm^{-1}, the L-T splitting is about 6 μeV as compared to a cavity TE-TM splitting of about 280 μeV for the TMDC monolayer based polariton example described in reference [140]. These splittings act as an effective magnetic field on polaritons with finite k-vector and rotate the polariton pseudospin. The rotation depends on the propagation direction of the polariton, which ultimately leads to a four-fold spin pattern in real space. This effect is known as the optical spin hall effect (OSHE) [156, 157]. The OSHE has been predicted for TMDC monolayer exciton-polaritons [140] and was renamed to optical valley Hall effect (OVHE) because spin and valley can not be treated separately in TMDC monolayer excitons.

Based on the physics of the OVHE effect, the intensity and DOCP distributions were modelled for the measured monolayer geometry and the experimental conditions. The system is described by solving the generalized Schrödinger equation for the spinor $|\Psi(\mathbf{r},t)\rangle = (\Psi_+(\mathbf{r},t), \Psi_-(\mathbf{r},t))^{\mathrm{T}}$:

$$\mathrm{i}\hbar\partial_t|\Psi\rangle = \left[\hat{\mathbf{T}} + V(\mathbf{r})\right]|\Psi\rangle + \mathrm{i}(|P\rangle - \hbar\gamma|\Psi\rangle), \tag{6.7}$$

where $\Psi_\pm(\mathrm{r})$ represent the wave functions of polaritons with pseudo-spins $+1$ and -1, respectively. γ is the polariton decay rate. The operator $\hat{\mathbf{T}}$, given by

$$\hat{\mathbf{T}} = \begin{bmatrix} \hbar^2\hat{k}^2/2m_{eff} & \Delta(\hat{k}_x - \mathrm{i}\hat{k}_y)^2 \\ \Delta(\hat{k}_x + \mathrm{i}\hat{k}_y)^2 & \hbar^2\hat{k}^2/2m_{eff} \end{bmatrix}, \tag{6.8}$$

accounts for the kinetic energy (diagonal elements) and the polarization splitting Δ of polaritons (off-diagonal elements). $\hat{\mathbf{k}} = (\hat{k}_x, \hat{k}_y) = (-\mathrm{i}\partial_x, -\mathrm{i}\partial_y)$ is the momentum operator and m_{eff} is the effective mass of polaritons. $V(\mathbf{r})$ is the stationary confinement potential across the sample and $|P\rangle$ describes the pump of the polariton state, where $|P\rangle = f(\mathbf{r})|p\rangle$. $f(\mathbf{r})$ accounts for the spatial characteristics of the pump beam and $|p\rangle$ describes the polarization state of the pump. The polarization of the pump is characterized by the Stokes vector $\mathbf{S}_\mathrm{p} = (S_{\mathrm{p}x}, S_{\mathrm{p}y}, S_{\mathrm{p}z})$, where the components are given by $S_{\mathrm{p}x} = \langle p|\hat{\sigma}_x|p\rangle$, $S_{\mathrm{p}y} = \langle p|\hat{\sigma}_y|p\rangle$, $S_{\mathrm{p}z} = \langle p|\hat{\sigma}_z|p\rangle$. For the simulation, the following realistic set of parameters was assumed: $\Delta = 225$ μeV, $m_{eff} = 4.2 \times 10^{-5} m_e$, $\hat{\mathbf{k}} = 1.5$ μm^{-1} (corresponding to the excitation energy of 1.638 eV, according to the dispersion relation presented in Figure 6.11a) and a FWHM of the excitation spot of 2.5 μm. The polariton decay time was increased to 750 fs to cover the full monolayer extension and to allow polaritons to reflect

at the monolayer edges and to interfere[3].

The simulated intensity distribution plotted in Figure 6.19d shows a polariton propagation tail along the monolayer similar as in the experiment. The simulated DOCP distributions are depicted in Figure 6.19e and f for the same polarization orientations that were used in the experiments (Figure 6.19b and c, respectively) . In the case of the -75° orientation, the simulation qualitatively reproduces the valley separation of the experiment. As in the experiment, the DOCP is increasing towards the flake edges. Polaritons that decay further away from the excitation spot are associated with a higher in-plane wave vector, which in turn results in a higher splitting and a stronger effective magnetic field. Consequently, the precession of the pseudo-spin, which is equivalent to the polarization Stokes vector, is more pronounced, leading to a larger valley polarization. Moreover, the wavy domain separation line is also seen in the simulation. This can be explained by interfering polaritons that are reflected at the monolayer edges. It should be noted that the DOCP distribution is less clearly defined in the top most part monolayer. The reason for that is the proximity of the excitation spot to the rather undefined monolayer top edge. Polariton decay and reflection at such edges make an exactly reproducing simulation very challenging. The simulation of the -120° orientation case is in good agreement with the experimental data as well. The bottom section of the monolayer is dominated by a σ^- domain with small σ^+ regions a the right monolayer edge. Here again, the top section is not exactly reproduced but is predominantly composed of σ^+ domains in both, experiment and simulation.

The good agreement of the experimental data with the theoretical modeling allows to interpret these findings as the first manifestation of the optical valley Hall effect in a TMDC exciton-polariton system. It should be noted that the experimentally observed valley polarized domains yield DOCP up to 80 %, which itself is a remarkable consequence of the strong valley polarization and valley coherence, preserved by in this experimental approach.

It has been demonstrated that exciton-polaritons are formed when $MoSe_2$ monolayer is integrated into a mechanically assembled monolithic microcavity. A valley polarization of more than 90 % can be induced by addressing these polaritons by a chiral two-photon absorption process. This method can be also used to induce valley coherence on the order of 90 % under two-photon excitation with linearly polarized light. The high degrees of valley polarization and coherence are explained by exciting close to the resonance, where depolarization mechanisms are weak and which reduces relaxation steps. Moreover, the decay dynamics are accelerated, while both intervalley scattering and dephasing times are prolonged. These findings are remarkable since valley polarization in $MoSe_2$ monolayer

[3]The theoretical modeling and simulation was carried out in close collaboration with E. Sedov and A. V. Kavokin, University of Southampton and M. Glazov, Ioffe Physical-Technical Institute, Russia.

is typically on the order of few percent under off-resonant excitation [58, 71] and valley coherence has not been demonstrated thus far in $MoSe_2$ monolayer. Due to the light effective mass, polaritons may propagate along the monolayer. The polariton expansion is strongly valley-dependent due to the optical valley Hall effect. The latter is induced by the cavity TE-TM splitting and the exciton L-T splitting, both acting as an effective magnetic field on propagating polaritons. The observed spin-valley patterns could be reproduced qualitatively by a simulations that assumes the OVHE as the underlying mechanism. In principle, such spatial separation of valley-tagged polaritons could possibly be used for future valleytronic devices [11][4].

[4]The results presented in this sections were published in [158]

Chapter 7

Hybrid-polaritons

7.1 Hybrid-polaritons with $MoSe_2$ and GaAs quantum wells

The previous sections have presented strong coupling of one, either exciton or trion, species to a cavity mode. However, strong coupling two different exciton species to one photon mode is also possible. This requires that each of the two exciton resonances strongly couples individually to the photon mode, but no direct coupling between the excitons is required. In this particular case, the coupling of a GaAs quantum well (QW) exciton, a $MoSe_2$ monolayer exciton and a photon mode in a DBR-metal Tamm structure was studied. The hybridization of the three modes confers an admixture of the individual resonances' properties to the hybrid-polariton. This is of particular interest, because GaAs QW and $MoSe_2$ monolayer excitons have distinctly different character. As compared to TMDC monolayers, excitons in GaAs QWs exhibit a significantly longer radiative lifetime ($\approx$ 500 ps [159]) and interact more strongly with each other. Aiming at polariton condensation, a longer radiative lifetime is highly beneficial to build up an initial population in the ground state. A stronger exciton-exciton interaction is also helpful, because it facilitates polariton relaxation into the ground state by polariton-polariton scattering [4]. Still, the $MoSe_2$ monolayer exciton contribution is very relevant to add its unique spin-valley properties to the polariton system and to increase the Mott density. To investigate such a system, a DBR-metal Tamm design, including both GaAs QWs and $MoSe_2$ monolayer, was chosen.

The bottom part of the investigated structure, shown in Figure 7.1a, starts with a AlAs/$Al_{0.25}Ga_{0.75}As$ DBR (62.5 nm and 56 nm thickness, respectively, 30 pairs), supporting a very high reflectivity of 99.9 % between 740 nm/1.675 eV and 765nm/1.621 eV. This is followed by an AlAs layer (112 nm) with four embedded GaAs QWs (5 nm thick, 10 nm spacings) and a top layer of GaInP (63 nm) as oxidation protection layer. The

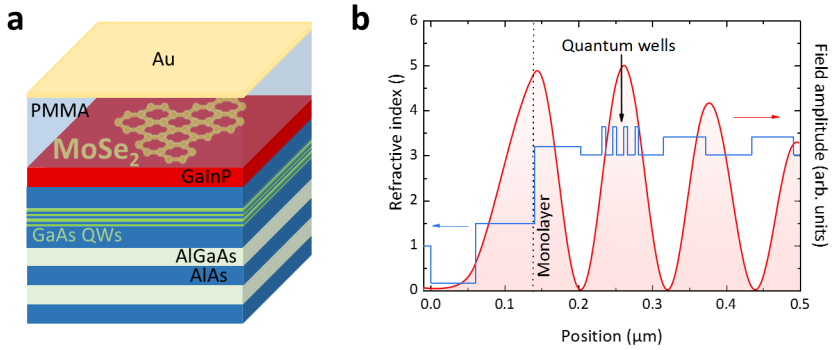

Figure 7.1: Sample design: (a) Schematic illustration of the sample structure. (b) The layer sequence of the structure is illustrated the corresponding refractive indices. The field distribution within the structure is plotted in red, showing field maxima at the monolayer and quantum well positions.

GaAs QW thickness was adjusted to 5 nm so that the QW and monolayer exciton have the almost the same energy. This bottom structure was grown by gas-source molecular beam epitaxy. Then, a $MoSe_2$ monolayer was transfered on this bottom part, which was subsequently spin-coated with 80 nm of PMMA and finally 60 nm of gold were evaporated on top. The structure was designed in a way that the optical field distribution has maxima at the monolayer and quantum well positions, as shown in 7.1b. The photon resonance is controlled by the PMMA layer thickness. It was adjusted to yield a photon mode at 1.63 eV, close to the excitonic resonances of $MoSe_2$ monolayer and GaAs QW at 150 K.

For this system, the pre-characterization of the $MoSe_2$ monolayer is more challenging since the GaAs QWs dominate all PL measurements due to their very high quantum yield (> 90 % [160]) and their spectrally close proximity to the monolayer resonance. Moreover, the QWs extend over the full sample dimensions and are therefore always probed. Thus, white light reflectivity measurements were carried out (after PMMA capping, but before the gold evaporation) on a sample positions with monolayer (QW + monolayer) and without monolayer (QW only). The absorption dips of both measurements are distinctly different, as shown in Figure 7.2a. This allows to extract the bare monolayer contributions (subtraction of normalized spectra), presented in 7.2b. It should be noted that, despite of using the same substrate as for the trion-polariton system (GaInP) described in section 5.3, here the exciton is the dominating species instead of the trion. Most likely, this is explained by an imperfect adhesion to the substrate due to organic residuals. This reflectivity measurement was repeated at various temperatures and the peak positions of the monolayer and QW resonances were plotted in Figure 7.2c. The temperature dependences were then fitted by a typical Varshni curve [161] to inter- and extrapolate the exciton energies for the full temperature range from 0 K to 160 K.

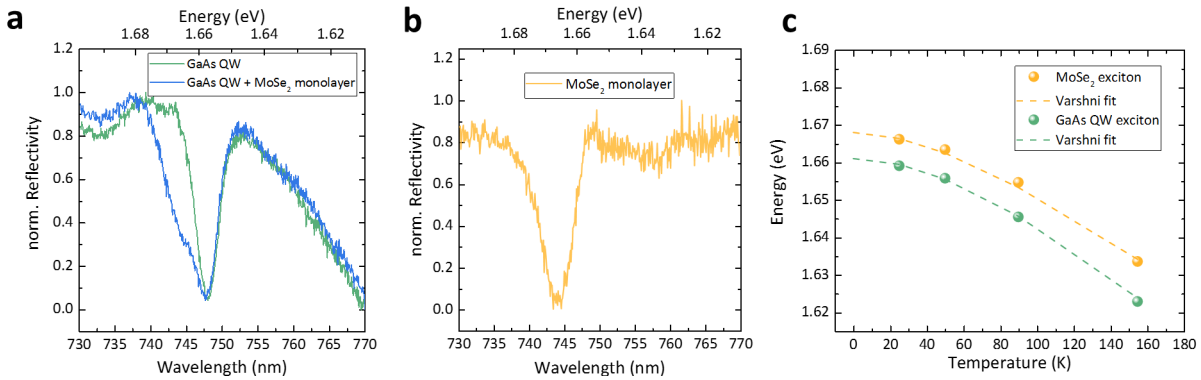

Figure 7.2: $MoSe_2$ monolayer and GaAs quantum well excitons: (a) Reflectivity spectrum taken next to the monolayer (QW excitons) and on the monolayer ($MoSe_2$ + QW excitons), showing pronounced absorption dips. (b) Reconstructed $MoSe_2$ monolayer contribution to the reflectivity spectrum shown in (a). (c) $MoSe_2$ and QW exciton energies at various temperatures fitted with a Varshni curve (fitting error of ± 1.5 meV corresponds to the symbol size).

The pre-characterization of the photon mode is not as straight forward either, since the cavity always contains the QWs, which does not allow a reflectivity measurement of the empty cavity. The QW excitons are expected to strongly couple to the cavity mode even without the $MoSe_2$ monolayer. Thus, any measurement off the monolayer position needs to be interpreted in the strong coupling context. Therefore, angle-resolved PL measurements (532 nm excitation, cw, 2 mW excitation power, 2 μm spot size) of the full structure were carried out at a position close to but not on the monolayer. The resulting dispersion relations at 10 K and at 150 K, depicted in Figure 7.3 a and b, respectively, show the typical shapes of polariton dispersions. A two-coupled-oscillator fit was applied to the dispersion relations, which provides information about the bare photonic mode and the coupling strength of the QWs to the cavity. According to this, the photonic modes are situated at 1.633 eV and at 1.626 eV at 10 K and 150 K, respectively. The shift of the cavity mode is explained with the temperature-dependent refractive indices of the constituent semiconductor materials [162]. The bare cavity mode is also affected by the relatively high real part of the monolayer refractive index (∼5 [120]), which increases the effective cavity length. Consequently, the bare cavity mode is red-shifted by a about 3.6 meV on the monolayer position (estimation based on transfer matrix calculation with and without the monolayer real part of its refractive index). In the 10 K measurement, the lower polariton branch has a very high cavity fraction of 0.967 at $k_{||} = 0\ \mu m^{-1}$, which allows to reliably calculate the Q-factor (equation 2.10) to 650 ± 20. The effective photon mass is 4.2 (± 0.21) x 10^{-5} m_0. Both fits of the measurements at 10 K and at 150 K independently yield a coupling strength of 9 ± 0.4 meV, which is in good agreement with

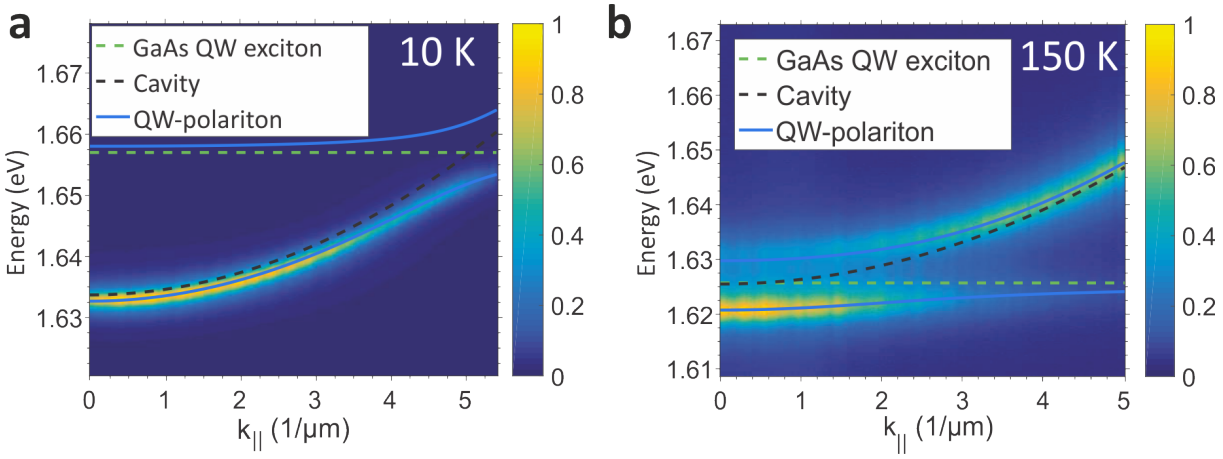

Figure 7.3: Quantum well exciton-polariton: PL spectra taken next to the monolayer showing strong coupling of the QW excitons with the cavity at 4 K (a) and at 150 K (b).

literature on similar cavities containing GaAs QWs [114].

Finally, the full structure on the monolayer position was investigated at 4 K. Figure 7.4a presents an angle-resolved PL measurement of this position under pulsed laser excitation (2 ps pulse duration, 82 MHz) at 745 nm/1.664 eV. Two curved branches were

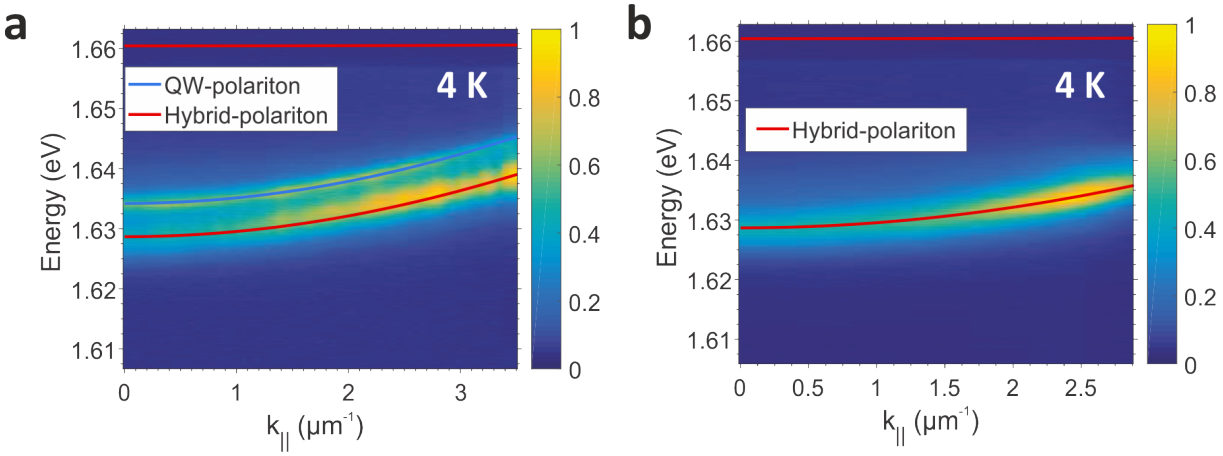

Figure 7.4: Hybrid polariton at 4 K: PL spectra taken on the monolayer without spatial filtering (a) and with spatial filtering applied (b). Without spatial filtering a clear contribution from outside the monolayer position (QW-polariton) is observed.

observed. The upper of the two branches is identical with the LPB of the pure QW exciton-polariton, shown in Figure 7.3a. Therefore, it is assumed that this signal stems from regions outside the monolayer position. Presumably, the hybrid-polariton mode expands in the in-plane directions either due to the photon mode propagation (very light effective mass) or due to GaAs QW exciton diffusion on the order of several microns

[163]. When the hybrid-polariton propagates out of the monolayer region is excites the QW exciton-polariton mode. Consequently, even though the system is only excited on the monolayer position with a laser spot size much smaller (2 μm) than the monolayer extension (about 10 μm), GaAs QW exciton-polaritons contribute to observed signal. In order to verify this assumption, a tight spatial filtering was applied to the measurement. This was done by placing a pinhole aperture in the first real space plane after the collecting objective (see Figure 3.2). The aperture was positioned in a way that any PL signal outside the monolayer was blocked. For this measurement, a 20 x magnification objective (NA = 0.42) was used, which facilitates the tight spatial filtering. In this configuration, the same measurement was repeated resulting in the dispersion depicted in 7.4b. In fact, the upper of the two branches vanished. The remaining dispersion is red-shifted with respect to the pure QW-polariton. Adding the monolayer exciton to this strongly coupled system pushes the lower most branch to lower energies. However, it is hard to observe the middle polariton branch (and even less to the upper polariton branch) in such PL experiment because the middle polariton branch is lies 32 meV above the ground state in this detuning configuration (-25 meV detuning between QW exciton and cavity). Consequently, the middle and upper polariton branches are not thermally populated at 4 K [149].

In order to verify this result, the system was also investigated at 140 K, where the photon and exciton resonances are much closer (-4 meV detuning with respect to the QW exciton and -13 meV with respect to the monolayer exciton). Here again, spatial filtering was applied in all measurements. The PL measurement at this temperature is presented in Figure 7.5a. Despite of the reduced detuning and the elevated temperature, which in principle facilitates the occupation of higher energy states, there is still only one branch visible, which lies significantly below the LPB of the pure QW exciton-polariton (see Figure 7.3b). To confirm this observation, a theoretical PL spectrum, based on a thermal population (see equation 5.1), was calculated for comparison with the experimental results. The calculation, shown in Figure 7.5c, verifies that only the LPB can be expected to be seen in a PL experiment. Therefore, a white light reflectivity measurement was acquired under the same conditions, since the absorption from high energy states does not required their occupation. In fact, three branches are observed in this experiment, as depicted in Figure 7.5b (a median and Fourier filter was applied to the raw data in order to enhance the branch visibility). The three branches were identified as lower, middle and upper polariton branch of a hybrid-polariton composed of excitons in $MoSe_2$ monolayer, GaAs QW and a DBR-metal Tamm mode. As a consistency check, a three-coupled-oscillator model was applied to the measurements using the excitons energies from the pre-characterization presented in Figure 7.2 (E_X, QW = 1.630 eV, E_X, ML = 1.639 eV) and the coupling constant between QW exciton and cavity deduced from the measurements

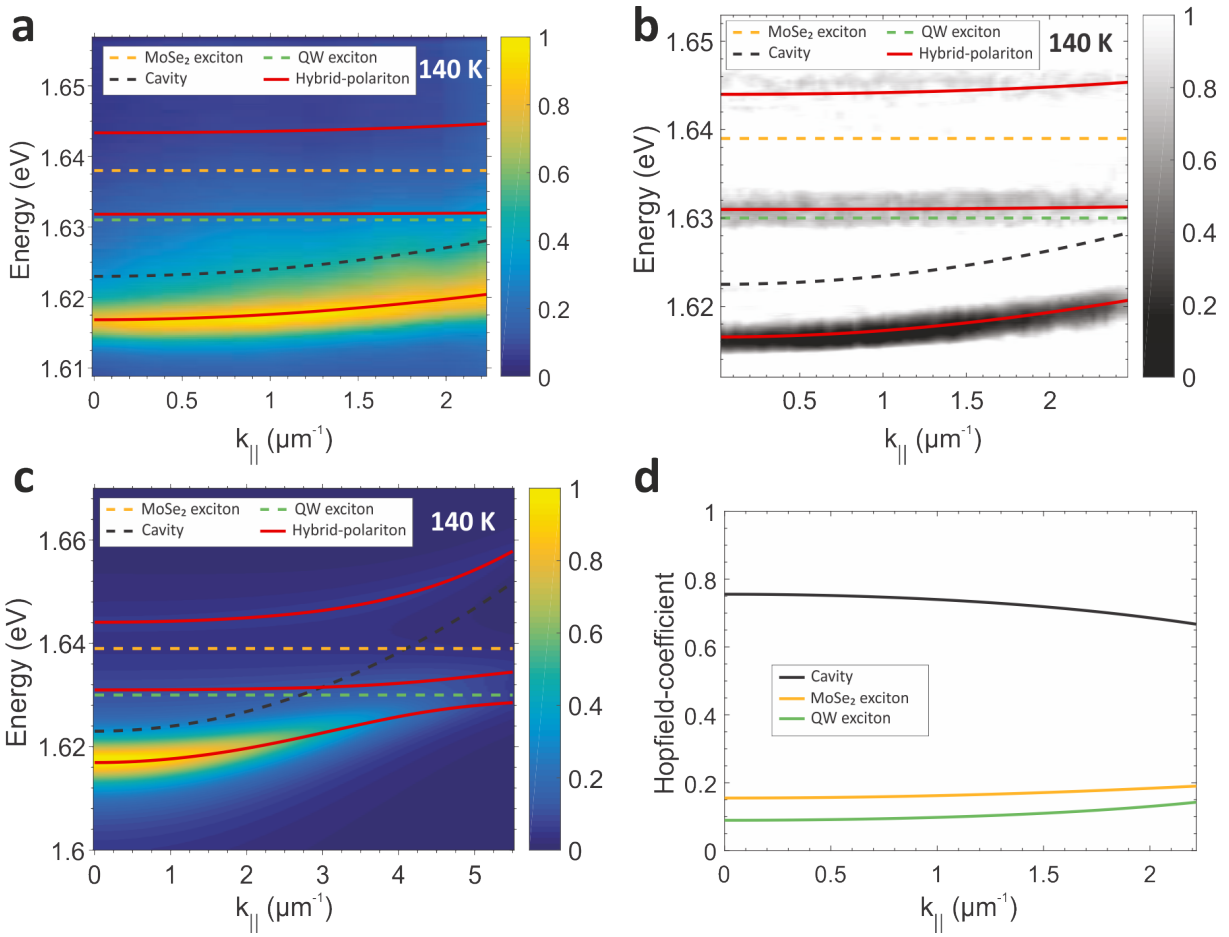

Figure 7.5: Hybrid polariton at 140 K: PL (a) and reflectivity (b) spectra taken on the monolayer with spatial filtering applied. (c) Calculated PL spectrum of the hybrid-polariton. (d) Hopfield coefficients of the lower polariton branch.

show in Figure 7.3 (7.0 meV). The photon mode was adjusted by -3.5 meV from 1.626 eV to 1.6223 meV to account for the increased effective cavity length by the real part of the monolayer refractive index as described above. The only remaining free fitting parameter is the coupling strength of the monolayer exciton to the cavity, which was determined to 20 ± 1 meV, in good agreement with literature [107]. These fitting results were overlaid with the experimental PL and reflectivity results in Figure 7.5a and b. Figure 7.5d depicts the Hopfield coefficients of the LPB. Even at 140 K, at $k_{||} = 0\ \mu m^{-1}$ the hybrid-polariton is still highly photonic (75.6 %) with GaAs QW and $MoSe_2$ monolayer excitons fractions of 8.9 % and 15.5 %, respectively. The Hopfield coefficient allows to calculate the hybrid-polariton life time according to equation 2.34. Taking $\tau_c = 110$ fs, $\tau_{X,monolayer} = 390$ fs [44] and $\tau_{X,QW} = 500$ ps [159] yields a life time of 137 fs. In fact, this is not much longer as compared to the comparable cavity, but without the QW contribution, yielding a radiative lifetime of 133 fs. The reason is that the radiative term of the cavity dominates

the polariton lifetime (see equation 2.34). In order to significantly increase the polariton life time, a cavity with higher Q-factor would thus be required[1].

The first observations of hybrid exciton-polaritons were based on excitons hosted in organic and inorganic materials [165, 166]. The great advantage of this hybridization has been the admixture of excitons with different character, namely localized Frenkel-type excitons with small Bohr radius in organics and delocalized Wannier-Mott type excitons with larger Bohr radius in inorganic semiconductors. By adjusting the exciton fractions the overall polariton properties can be tuned. Moreover, hybrid-polariton systems, which contain semiconductor quantum well can be driven electrically by integrating the QW into a $p-i-n$ heterostructure, which acts as a the QW light emitting diode [167]. More recently, there has been a first demonstration of room-temperature hybrid-polaritons between excitons in a WS_2 monolayer, excitons in an organic dye and an optical mode of an open cavity. Although the demonstration at room temperature is attractive from an application point of view, the choice of materials does not allow an established and efficient integration of optoelectronic functionalities. In contrast, using GaAs QW excitons for the hybridization with TMDC monolayer excitons, as presented in this section, allows to modify the system for an efficient electrical injection. More importantly, the interparticle interaction strength M of GaAs QW excitons is larger than in TMDC monolayers because of the lower reduced mass μ ($M \sim \frac{1}{\mu}$ [52]). For GaAs QWs $\mu = 0.056\ m_0$ [7] and for TMDC monolayers $\mu = 0.25\ m_0$. Consequently, the interparticle interaction of the presented hybrid-polaritons is expected to be enhanced as compared to a pure TMDC monolayer exciton-polariton system. This becomes relevant for an efficient polariton relaxation, required for polariton-condensation. The very high quantum yield of GaAs QWs (> 90 % [160]) also allows to build up an exciton reservoir, which can be depleted in the stimulated scattering process to form a polariton-condensate. Hence, the additional hybridization with GaAs QW is expected to facilitate the condensation process. Thus, a condensation experiment was carried out on such hybrid-polariton system, as described in the next section.

7.2 Condensation of hybrid-polaritons

As discussed in previous section, the additional hybridization with GaAs QWs increases the exciton-exciton interaction and the effective quantum yield of the system. Both are important aspects for building up a significant ground state population that may initiate bosonic scattering and polariton condensation. In this section, a hybrid-polariton system, as described in section 7.1, was investigated under high power, pulsed excitation to study whether bosonic condensation is possible under these conditions. The experiment

[1] The results presented in this section were published in reference [164]

is carried out at cryogenic temperatures (5 K) since the required condensation density is lower as elaborated in sections 2.4.3 and 4.4. The investigated system has the same sample design as described in section 7.1, but is not the identical sample. Here again, the monolayer and cavity pre-characterization is more challenging, since the PL from the GaAs QWs and their strong coupling to the cavity mode are always present. Thus, before capping the structure with gold, a white-light reflectivity spectrum was taken on and off the monolayer position, which allows to extract the monolayer and QW exciton energies. Figure 7.6 shows the resulting white light reflectivity spectra of the sample prior to gold

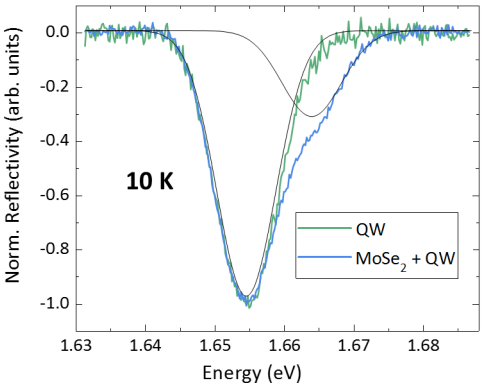

Figure 7.6: White light reflectivity spectrum of on and off the monolayer taken at 10 K.

evaporation, but after PMMA capping. Next to the monolayer position, only the absorption feature of the QWs is visible. A shoulder appears on the monolayer at the high energy side of this feature, stemming from the convolution of QW and monolayer absorption features. The shoulder is not very pronounced because of the small monolayer size (about 2 x 2 μm). Nevertheless, fitting the spectrum with two Lorentzian functions provides the QW and monolayer exciton energies (1.655 eV and 1.666 eV, respectively). This procedure is repeated as an PL experiment after finalizing the structure with the top gold layer. Figure 7.7a presents PL spectra at various in-plane wave vectors together with corresponding Lorentzian fits, acquired next to the monolayer at 5 K (pulsed excitation, 2 ps pulse time, 82 MHz repetition rate, 2 μm spot size, 0.17 pJ/pulse at 741 nm/1.6733 eV). The fitted peak positions are replotted in Figure 7.7b (blue circles) along with a two-coupled-oscillator fit of the lower and upper polaritons (solid lines). Exciton and cavity resonances are indicated by gray dashed lines. The exciton energy extracted from the fit is slightly different form the previous measurement, which is due to fluctuating QW energies across the sample. Nevertheless, the fit provides a reasonable value for the cavity energy of 1.659 eV. The fit yields a normal mode splitting of 9.2 $\pm$ 0.4 meV at a positive detuning of 5.9 meV, which is fully consistent with the hybrid system presented in section

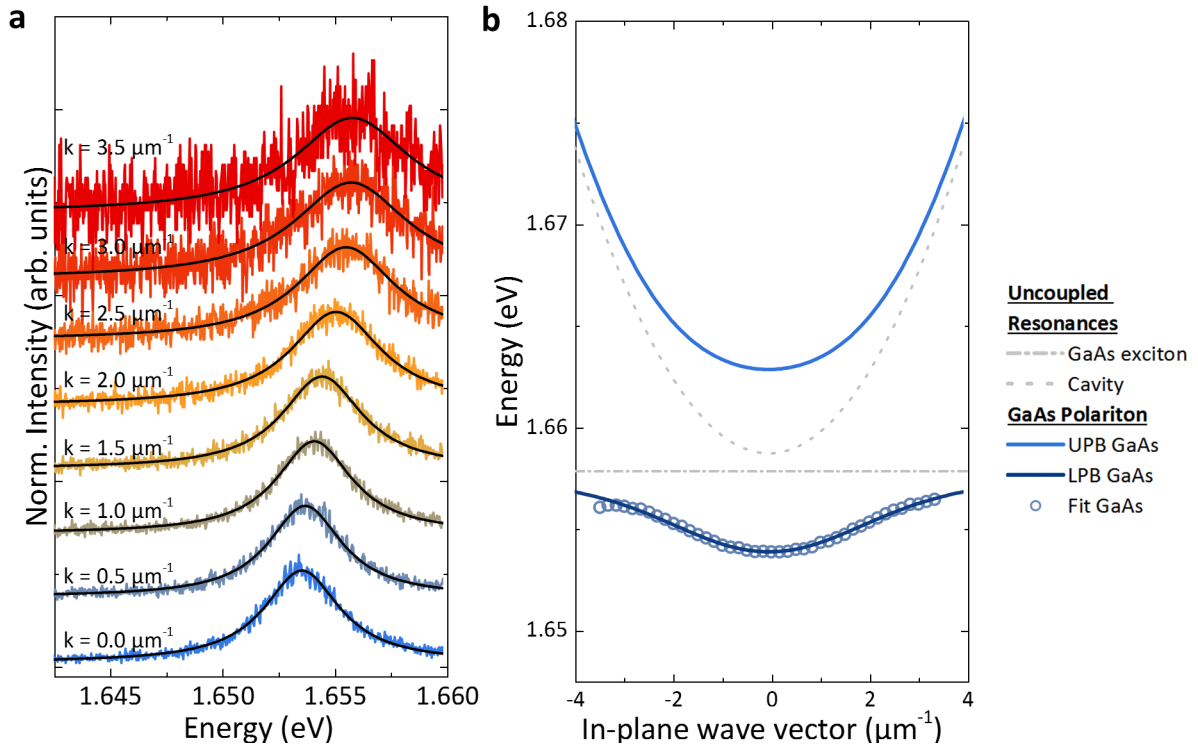

Figure 7.7: Dispersion relation of the GaAs QW exciton-polariton: (a) PL line spectra at various in-plane vectors. (b) Corresponding peak energies are plotted as function of $k_{||}$ (blue circles, fitting error of $\pm$ 0.3 meV corresponds to the circle size) together with a two-coupled-oscillator fit for the upper and lower polariton (solid lines). The uncoupled exciton and cavity modes are indicated by gray dashed lines.

7.1. However, it should be noted that here, QW exciton and cavity mode are close to in resonance at 5 K, which was the case at 150 K for previously investigated sample.

Finally, the full system including the monolayer is probed (Figure 7.8). As in the previous hybrid system, the captured signal is a superposition of PL from the monolayer position and PL from regions outside the monolayer, due to the high, lateral diffusion lengths of the QW excitons. However, here the spatial filtering that was previously applied (see Figure 7.4) to suppress the outside signal, does not work properly anymore because of the small monolayer size. The resulting signal is depicted in Figure 7.8. The line spectra at various in-plane wave vectors show two peaks. Fitting these spectra with a two-Lorentzian functions allows to extract the peak energies, which are plotted in 7.8b as a function of $k_{||}$. The upper dispersion follows the same fit as for the pure GaAs QW exciton-polariton case (blue solid lines). Thus, this feature is attributed to the signal from outside the monolayer area. The lower feature has a dispersion-less appearance and spreads up to 2.5 μm^{-1} in momentum space, which is an indication for a localized state. For comparison, a three-coupled-oscillator fit is drawn here (red solid lines). The fit

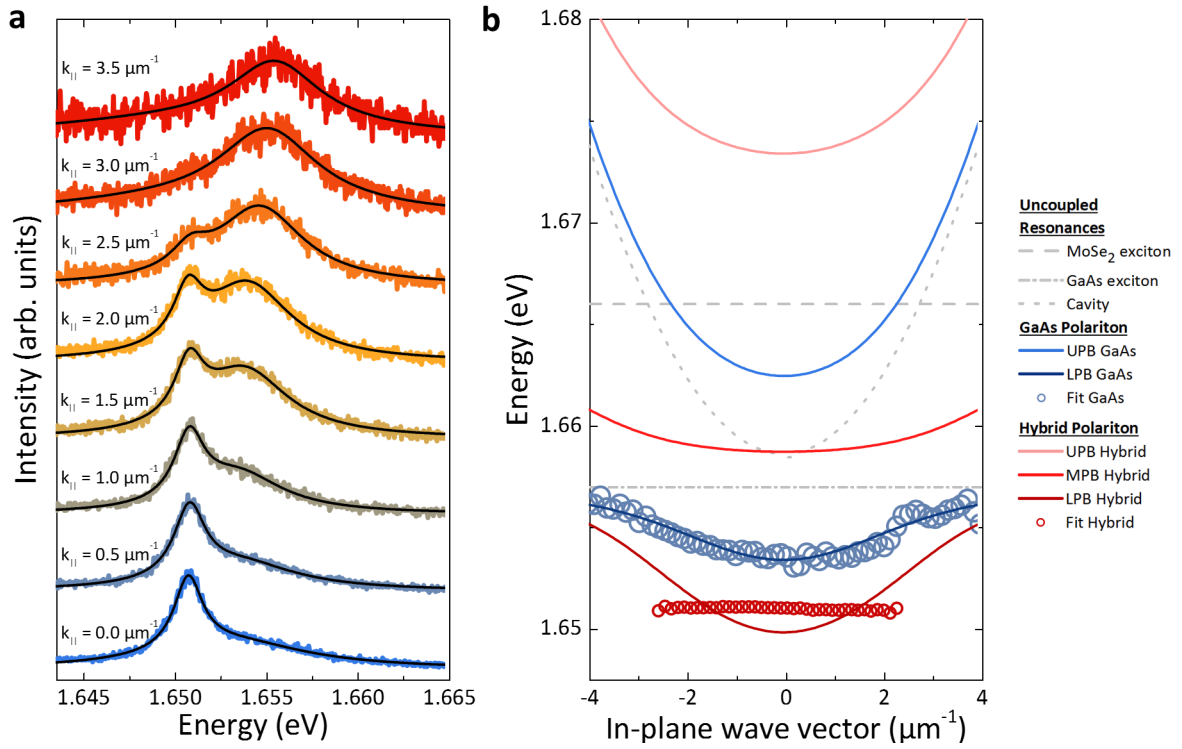

Figure 7.8: Dispersion relation of the hybrid-polariton: (a) PL line spectra at various in-plane vectors featuring two separate peaks. (b) Corresponding peak energies are plotted as function of $k_{||}$ (blue and red circles, fitting errors of 0.2 meV and 0.4 meV correspond to the circle sizes). The high energy dispersion is fitted with a two-coupled-oscillator fit for the upper and lower polariton (blue solid lines). The low energy dispersion is compared with three-coupled-oscillator model (red solid lines). The uncoupled excitons and the cavity mode are indicated by gray, dashed lines.

used the uncoupled resonance parameters, a QW exciton coupling strength from the pre-characterization and a monolayer exciton coupling strength from section 7.1 (20 meV) as model parameters. The measured feature lies 1.21 meV above the lower polariton branch of this hybrid-model. This can be well explained by a lateral confinement and quantization in a potential, which is given by the difference between the LPB of the QW polariton and the LPB of the hybrid polariton (2.38 meV). The determined quantization energy can be reproduced by using a finite-potential-well model with a lateral monolayer extension of 1.7 μm, which is close to the actual monolayer size. Overall, a localized hybrid-polariton was identified with fractions of 21.0 % GaAs QW, 21.5 % $MoSe_2$ monolayer and 57.5 % cavity at $k_{||} = 0\ \mu m^{-1}$.

In order to induce a condensation phenomenon, the pulsed laser excitation is an important mean to inject a high density of hybrid-polaritons, while keeping the thermal input relatively low. The excitation energy was tuned to be in resonance with the UPB

of the hybrid polariton (741 nm/1.6733 eV) for an enhanced injecting efficiency. For the condensation experiment, the excitation power was consecutively increased, starting at 0.17 pJ/pulse going up to 394 pJ/pulse. The dispersions for four selected excitation powers are depicted in Figure 7.9. For an increasing excitation power, the hybrid-polariton

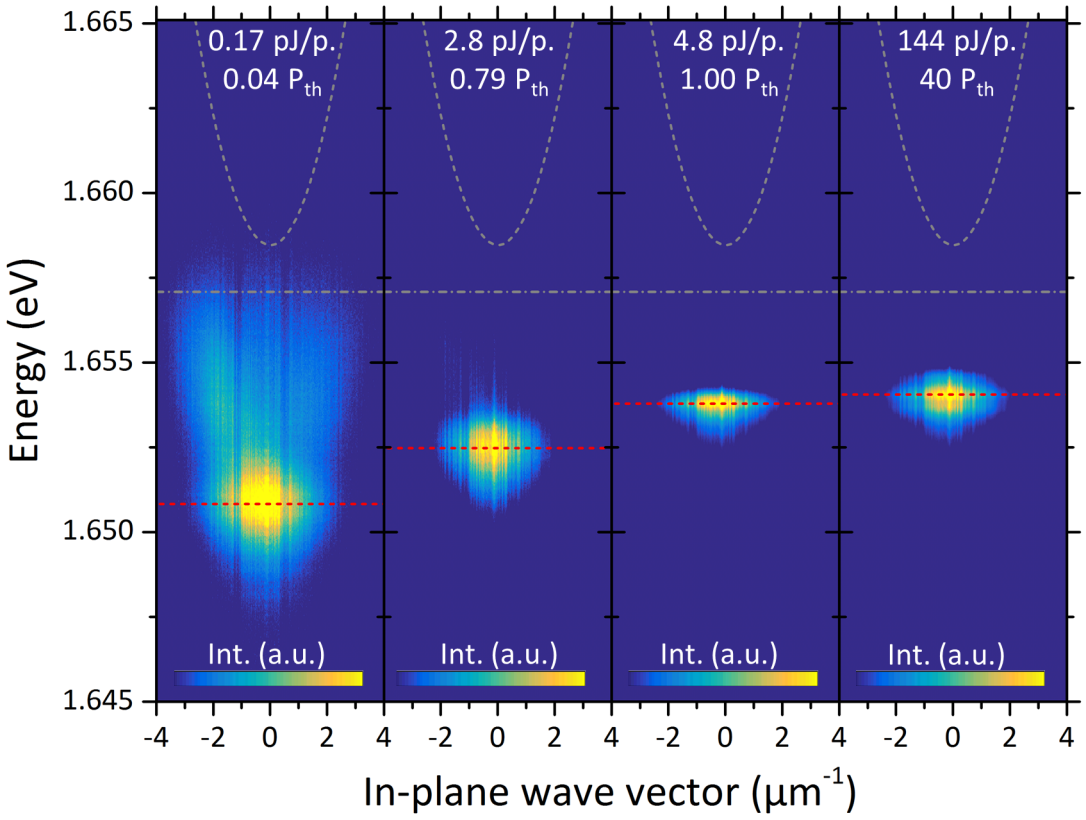

Figure 7.9: Polariton condensation: PL polariton dispersions at various excitation powers below, close to, at and above the threshold, respectively. With increasing power the polariton ground state shift to higher energies (indicated by red-dashed lines) and becomes more distinct.

feature becomes more dominant. In addition, a blue shift occurs and the feature spectrally narrows. This behavior is a strong indication for a condensation phenomenon. To support this indication, the dispersion spectra were analyzed more closely as depicted in Figure 7.10. By varying the excitation power as shown in Figure 7.10a, a clear threshold behavior becomes apparent at 4.8 pJ/pulse, which is shaded grayly and labeled P_{th} (threshold power). This non-linearity coincides with a sharp linewidth drop from 2.1 meV to 0.7 meV. The non-linear intensity development is a well explained by stimulated-scattering into the ground state, which makes the polariton relaxation much more efficient, while the

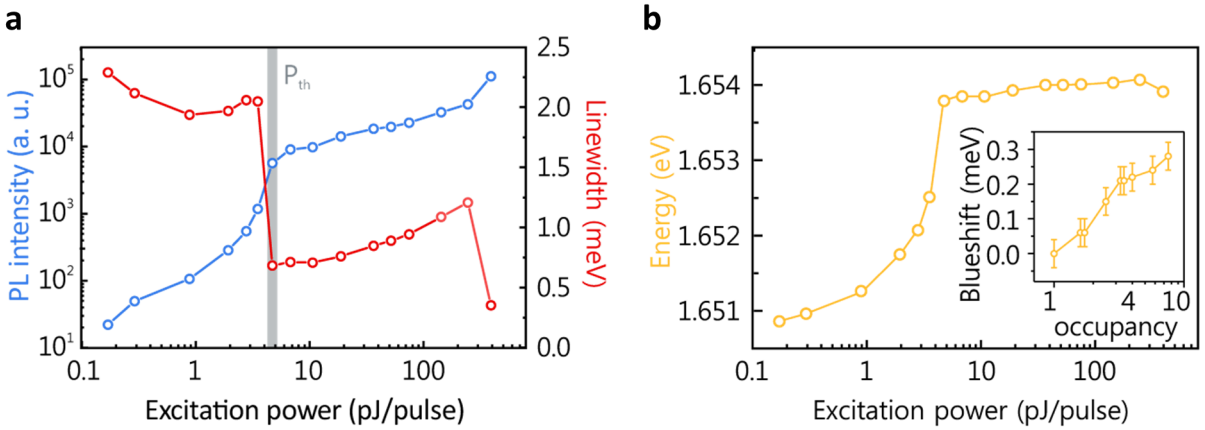

Figure 7.10: Power series: (a) PL intensity and linewidth of the polariton ground state as a function of the excitation power. The condensation threshold, which is identified by a strong non-linear intensity increase and a significant drop in linewidth, is indicated by the grayly shaded bar. Error bars are on the order of data point symbol extension. (b) Plot of the energy-power dependence in same power range. Again, the error is on the order of data point symbol extension. The energy shift above the threshold is replotted in the inset as a function of the polariton occupancy to illustrate the in continuing blue shift more clearly.

linewidth drop evidences the onset of temporal coherence in the system [84]. To distinguish polariton-condensation from classical lasing, the spectral shift of the hybrid-mode was analyzed in detail (Figure 7.10b). The blue shift below the threshold on the order of 3 meV is a typical sign for an increasing exciton-exciton interaction of the reservoir excitons. More importantly though, even above the threshold the modes continues to blueshift (by about 300 μeV). To illustrate the blue shift more clearly, the energy is replotted as a function of the occupancy above the threshold. The occupancy is obtained by normalizing emission intensity to the intensity at the threshold, which better reflects the number of polaritons in the condensate [168]. Here, the blue shift can be seen more clearly. This behavior is very different to classical lasing (fixed energy above the threshold), allowing to identify the observed non-linearity as polariton condensation [7].

Finally, it should be investigated to which degree the valley index of the monolayer exciton can be conserved in the hybrid-polariton condensate. Therefore, the PL intensity of the LPB mode was measured above and below the threshold in the σ^+ and σ^- configurations. Figure 7.11 presents the resulting spectra for σ^+ and σ^- excitations, which yield 9.8 $\pm$ 2 % and 7.2 $\pm$ 2 % DOCP below the threshold and 17.9 $\pm$ 2 % and 16.4 $\pm$ 2 % DOCP above the threshold. Bare $MoSe_2$ monolayers exhibits hardly any valley polarization under the described experimental conditions [58, 71]. Thus, even below the threshold

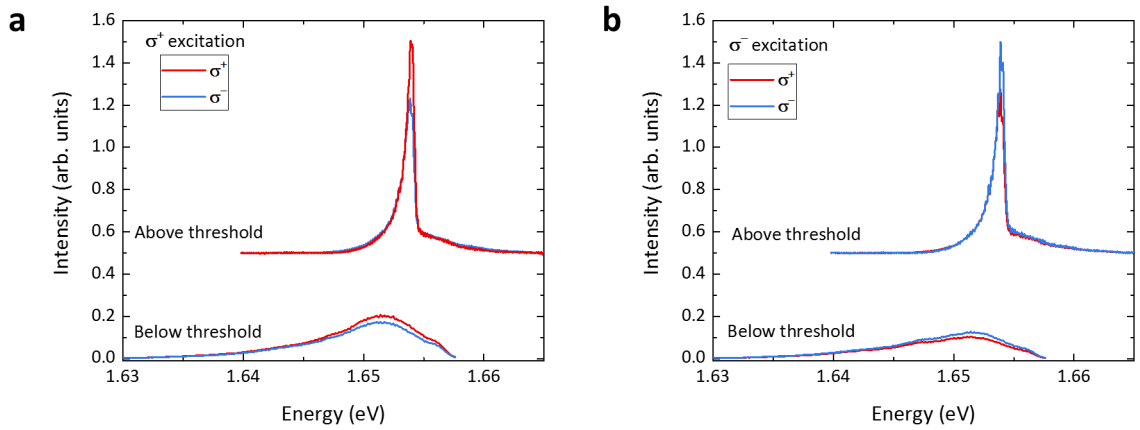

Figure 7.11: Valley polarization: Polarization-resolved PL measurements of the hybrid-polariton below and above the threshold under σ^+ (a) and σ^- (b) excitation.

the valley polarization is strongly increased. Following the results from sections 6.1 and 6.2, this increase is attributed to a shorter radiative polariton lifetime and a longer intervalley scattering time due to the cavity fraction. It should be mentioned that pure GaAs QW exciton-polaritons may also show a finite DOCP on the order of a few percent under comparable conditions [169], which is associated to pure spin polarization. Thus, also the GaAs QWs may contribute to the measured DOCP. Above the threshold, the DOCP increases by a factor of about two. This increase can be well explained by the effective relaxation channel that is provided by the stimulated scattering mechanism. In this case, not only the polariton lifetime is reduced, but also the relaxation time is accelerated. Both effects are highly beneficial to conserve the valley polarization.

Overall, the additional hybridization with GaAs QW excitons facilitates the condensation process for a number of reasons. Firstly, the high quantum efficiency of the QW excitons helps to build up an initial ground state population. In addition, the polariton-polariton interaction is stronger due the larger spatial extension of the QW excitons, making the polariton relaxation more efficient. Moreover, the Mott density of the system is increased since the excitons can be distributed among the QWs and the monolayer. In particular, the monolayer may host a high exciton density, because of the small exciton Bohr radius. Consequently, the full system can be excited more strongly before the Mott density is reached. Finally, in this particular case, the lateral confinement of the polaritons due to the small flake size might be also helpful. Because the ground state has a finite extension in k-space, the conditions for phonon-scattering induced relaxation are loosened, which in turn makes the overall relaxation more efficient [7]. At the same time, the $MoSe_2$ monolayer provides a high degree of valley polarization, which strongly

benefits from the effective relaxation by the stimulated scattering mechanism[2].

[2]The results presented in this section were published in reference [169]

Summary

The aim of this work was to elaborate if strong coupling between excitons in TMDC monolayers and optical resonances in photonic microstructures provides additional benefit to exploit the physics of exciton-polaritons and 2D materials. More specifically, it was studied if TMDC monolayers may serve as a material platform for room-temperature polaritonics. Equally important, it was investigated if strong coupling helps to observe spin-valley related phenomena in TMDC monolayers.

In order to integrate TMDC monolayer into a microcavity, three new cavity fabrication processes have been developed. The DBR-metal based design is easy to fabricated and offers acceptably good mode confinement. However, the Q-factors are limited to a few hundred and the top metal layer is strongly absorbing. In contrast, DBR-DBR microcavities (either mechanically assembled or fully grown) are more challenging to fabricated, but also provide much higher Q factors up to 5000.

In two first approaches, it was demonstrated that excitons-polaritons can be observed with WSe_2 and WS_2 monolayers in DBR-metal microcavities at room temperature. The strong coupling is manifested in the distinct anti-crossing behavior of the dispersion relations. The small optical mode volume of the cavities and high oscillator strength of both monolayer materials were the most important conditions for this observation. The demonstration of WSe_2 monolayer exciton-polaritons was the first clear evidence of room-temperature strong coupling with TMDC monolayer and is therefore important from the perspective of potential applications. Moreover, it was shown that not only excitons, but also trions in a $MoSe_2$ monolayer strongly couple to optical resonances in a DBR-metal Tamm structure at cryogenic temperatures. Trion-polaritons are particularly interesting, since their interaction with external fields should be significantly stronger than for exciton-polaritons due to the charged character of the trion.

Beyond the demonstration of exciton- and trion-polaritons, their spin-valley physics were studied in more detail. While the trion resonance in bare $MoSe_2$ monolayer does not exhibit any valley polarization under non-resonant excitation, a valley polarization of up to 18 % was measured for the trion-polariton system. This enhancement was explained by the accelerated radiative decay dynamics and the prolonged depolarization of the exciton-polariton as compared to the excitons in the bare monolayer. A similar enhance-

ment from 2 % to 15 % was observed when comparing excitons and exciton-polaritons in WS_2 monolayer at room temperature. In addition to the previous explanations, the transfer from the valley-polarized dark ground state contributes to the observed enhancement. This room-temperature valley polarization enhancement is in good agreement with other publications that were published only briefly before these results [65, 128]. Lastly, an exciton-polariton system consisting of a $MoSe_2$ monolayer in a DBR-DBR monolithic microcavity, was probed under two-photon excitation at cryogenic temperatures. Strikingly, this system shows valley polarization and valley coherence of more than 90 %. In this case, it was important to excite the system close to the ground state, where the depolarization mechanisms are weak. Here again, the faster decay and slower depolarization time are also highly beneficial to extract such high degrees of valley polarization and coherence. The high valley coherence and long polariton propagation lengths also allow to investigate the valley-dependent polariton propagation. Owing to the cavity TE-TM splitting, propagating polaritons spatially separate depending on their valley index. This is known as the optical valley Hall effect, which had been predicted and theoretically modeled [140], but not demonstrated.

The last chapter of this work covers the formation of hybrid-polaritons and their condensation. Two different exciton species, namely excitons in $MoSe_2$ monolayer and in GaAs quantum wells, were coupled strongly to a cavity resonance. This results in a hybridization of all three resonances and manifests in three anti-crossing polariton branches. The admixture of the GaAs quantum well excitons contributes with an improved quantum efficiency and enhanced exciton-exciton interaction, which are important aspects for polariton-condensation. Consequently, the investigated sample system was excited with high-intensity laser pulses in a low-temperature condensation experiment to inject a significant polariton density. Above a threshold power of 4.8 pJ/pulse, a strongly non-linear intensity increase and drop in the emission linewidth was observed. This behavior was attributed to the stimulated scattering process and the onset of coherence, which are initiated by a polariton condensation. The condensate exhibits an enhanced valley polarization (17 %) as compared to hybrid-polaritons below the threshold (8 %), because the relaxation channel through the stimulated scattering process is more efficient. It was concluded that the increased quantum and relaxation efficiency, which was added by the GaAs component, enables the condensate formation, which has not been observed in exciton-polariton systems containing only a TMDC monolayer.

When having actual applications of exciton-polaritons in mind, the demonstration of strong coupling with TMDC monolayers at room temperature has been an important milestone. However, to fully take advantage of the polariton physics, future investigations need to transfer the more advanced effects such as near unity valley polarization/coherence or polariton condensation, to systems that operate and exhibit such effects even at room

temperature.

This step could be challenging for the demonstrated trion-polaritons since trion decompose quickly at room temperature due to their low dissociation energy of about 30 meV. Nevertheless, trion-polaritons could be quite interesting as they combine their charged, fermionic character with the low effective mass of the cavity mode. One could think of electro-optical transistor concepts that control the quasi-particle by its charge and take advantage its high velocity. In addition, the inter-particle interaction is expected to be much stronger due to their charged character, which could principally allow to isolate individual particles. Moreover, trion-polaritons are discussed in the context of superconducting effects based on collective fermionic excitations [135, 170].

With respect to the spin-valley properties, the combination of monolayer integration into a DBR-DBR monolithic microcavity and the two-photon excitation has proven to be a very successful approach. In principle, this combination should also work at room temperature. However, it might be purposeful to replace $MoSe_2$ by WSe_2. WSe_2 monolayers naturally exhibit higher degrees of valley polarization/coherence and have a higher PL yield under ambient conditions. With the established cavity fabrication and the experimental techniques described in this work, this could be implemented in the near future. Also, the optical valley Hall effect could principally observed at room temperature.

Transferring the condensation effect to a room temperature experiment with a sample system that contains only TMDC monolayer could be more challenging. The fast radiative decay and the weak exciton-exciton interaction make polariton condensation more difficult than in other material systems. Although polariton condensation requires lower densities at cryogenic temperatures, moving to higher temperatures could also facilitate the polariton relaxation by an increased polariton-phonon scattering. Moreover, establishing new high-Q cavity designs and improving the material quality by h-BN encapsulation have been important steps towards more sophisticated condensation experiments. Combining these advances and the acquired knowledge on exciton-polaritons could make such condensation experiments possible. Having all these results in mind, it can be concluded that 2D materials, in particular TMDC monolayers, have certainly justified their existence particularly in the field of polariton physics.

Zusammenfassung

Ziel dieser Arbeit war die Untersuchung des Effekts der starken Kopplung zwischen einer Übergangsmetalldichalkogenidmonolage und der optischen Resonanz einer photonischen Mikrostruktur. Dabei ging es zunächst darum die Bildung von Exziton-Polaritonen nachzuweisen und darauf basierend zu untersuchen welche Vorteile 2D Materialien für die Bildung von Exziton-Polaritonen haben. Genauer wurde untersucht, ob Übergangsmetalldichalkogenidmonolagen ein geeignetes Materialsystem für Polaritonen bei Raumtemperatur sind. Ebenso wichtig war auch die Frage, ob starke Kopplung dabei hilft Spin-Valley (Valley engl. für Tal) Phänomene in Übergangsmetalldichalkogenidmonolagen zu beobachten.

Um eine Übergangsmetalldichalkogenidmonolage in eine Mikrokavität zu integrieren, wurden drei neue Kavitätsherstellungsverfahren entwickelt. Kavitäten auf DBR-Metall Basis können leicht hergestellt werden und bieten ein geringes Modenvolumen. Allerdings ist ihr Qualtitätsfaktor auf wenige Hundert beschränkt und die Metallschicht ist stark absorbierend. Im Gegensatz dazu sind Kavitäten auf DBR-DBR Basis (mechanisch gestapelt oder komplett gewachsen) schwerer herzustellen, bieten dafür aber Qualitätsfaktoren bis zu 5000.

In den ersten beiden Versuchen wurde gezeigt, dass man Exziton-Polaritonen mit WSe_2 und WS_2 Monolagen in einer DBR-Metall basierten Mikrokavität bei Raumtemperatur beobachten kann. Die starke Kopplung zeigt sich im anti-kreuzenden Verhalten der beiden Dispersionsrelationen. Das kleine Modenvolumen der Kavität sowie die hohe Oszillatorstärke der Exzitonen waren die wichtigsten Voraussetzungen für diese Beobachtung. Diese Ergebnisse stellen den ersten, eindeutigen Nachweis von starker Kopplung mit einer Übergangsmetalldichalkogenidmonolage beim Raumtemperatur dar. Dies hat vor allem aus Sicht möglicher Anwendungen große Relevanz. Darüber hinaus wurde gezeigt, dass auch Trionen in einer $MoSe_2$ Monolage bei Tieftemperatur stark an die optische Mode einer DBR-Metall basierte Tammstruktur koppeln können. Trion-Polaritonen sind besonders interessant, da ihre Wechselwirkung mit äußeren Feldern durch ihre Ladung deutlich stärker sein sollte als bei Exziton-Polaritonen.

Im darauffolgenden Kapitel wurden die Spin-Valley Eigenschaften der Exziton- und Trion-Polaritonen genauer untersucht. Während Trionen in einer reinen $MoSe_2$ Mono-

lage unter nicht-resonanter Anregung keine Valley-Polarization zeigen, wurde bei Trion-Polaritonen eine Valley-Polarisation von bis zu 18 % gemessen. Diese Steigerung wird durch eine beschleunigte, radiative Zerfallszeit und eine verlängerte Depolarisationszeit erklärt. Eine ähnliche Erhöhung der Valley-Polarisation von 2 % auf 15 % wurde bei Raumtemperatur an einem Exziton-Polariton mit einer WS_2 Monolagen beobachtet. Zusätzlich zu den vorherigen Erklärungen, trägt hier der Transfer von dem dunklen Grundzustand zu der Valley-Polarisation bei. Diese Beobachtung deckt sich gut mit Ergebnissen, die kurz vor den Ergebnissen dieser Dissertation veröffentlicht wurden [65, 128]. Abschließend wurde ein Exziton-Polariton System mit einer $MoSe_2$ Monolage in einer DBR-DBR basierten Mikrokavität mittels Zwei-Photonen-Anregung untersucht. Besonders hervorzuheben war hier die Beobachtung von über 90 % Valley-Polarisation und -Koheränz. Für diese Beobachtung war es besonders wichtig das System nah am Grundzustand anzuregen, wo die Valley-Depolarisationsmechanismen schwach ausgeprägt sind. Auch in diesem Fall waren der verschnellerte Zerfall und verlängerte Depolarisationszeit ausschlaggebend für das Erreichen solch hoher Werte. Außerdem ermöglichten die hohe Valley-Koheränz und die verlängerte Ausbreitungsslänge eine Valley-abhängige Ausbreitung der Polaritonen zu beobachten. Aufgrund der TE-TM Aufspaltung der Kavität breiten sich Polaritonen in Abhängigkeit ihres Valley-Indexes aus. Dieser Effekt ist als optischer Valley Hall Effekt bekannt und war bereits vorhergesagt, aber noch nicht beobachtet worden [140].

Das letzte Kapitel beschäftigt sich mit der Bildung von Hybrid-Polaritonen und deren Kondensation. Hierbei wurden zwei unterschiedliche Arten von Exzitonen stark an eine Kavitätsresonanz gekoppelt. Es handelte sich um Exzitonen in einer $MoSe_2$ Monolage und in GaAs Quantentrögen. Dies führt zu einer Hybridisierung der drei Resonanzen, die sich durch drei anti-kreuzende Polaritonäste zeigt. Die Beimischung der GaAs Quantentrog Exzitonen trägt zu einer erhöhten Quanteneffizienz und einer verstärken Exziton-Exziton Wechselwirkung bei, was sich beides positive auf die Polariton-Kondensation auswirkt. Um letztere zu untersuchen wurde das gekoppelte System bei Tieftemperatur mit einem gepulsten Laser angeregt, was eine hohe Polaritondichte erzeugt. Ab einem Schwellwert von 4.8 pJ/Puls zeigt sich ein stark nicht-linearer Anstieg in der Intensität und eine Verschmälerung der Emission. Dieses Verhalten wird durch stimulierte Streuung in den Grundzustand und die Koheränz des Polariton-Kondensats erklärt. Das Kondensat zeigt eine erhöhte Valley-Polarisation (17 %) im Vergleich zu dem Hybrid-Polariton unter der Schwelle (8 %), da der Relaxationskanal durch die stimulierte Streuung effizienter ist. Demnach liefert die erhöhte Quanteneffizienz und die verstärte Exziton-Exziton-Wechselwirkung durch die Beimischung der GaAs Exziton den entscheidenden Beitrag zu der Polariton-Kondensation, die im Gegensatz dazu noch nicht bei reinen Übergangsmetalldichalkogenidmonolagen Exziton-Polaritonen beobachtet wurde.

Im Hinblick auf mögliche Anwendungen von Exziton-Polaritonen ist die Beobachtung von starker Kopplung mit einer Übergangsmetalldichalkogenidmonolage bei Raumtemperatur ein wichtiger Schritt. Um jedoch tatsächlichen Nutzen aus solchen Polaritonen zu ziehen, müssten auch die weiterführenden Experimente wie die Valley-Polarisation und -Koheränz nahe 100 % oder die Polariton-Kondensation auf Raumtemperaturexperimente übertragen werden. Dieser Schritt könnte für Trion-Polaritonen schwer sein, da Trionen aufgrund ihrer geringen Bindungsenergie bei Raumtemperatur sehr schnell zerfallen. Nichtsdestotrotz könnten Trion-Polaritonen interessant sein, da sie sowohl geladenen als auch sehr leicht sind. Grundsätzlich wäre ein elektro-optischer Transistor mit solchen Trion-Polaritonen vorstellbar. Außerdem ist zu erwarten das deren gegenseitige Wechselwirkung deutlich stärker ist, was prinzipiell die Auftrennung in einzelne Polaritonen ermöglicht. Darüber hinaus werden Trion-Polaritonen im Zusammenhang mit supraleitenden Effekten diskutiert, die auf kollektiven, fermionischen Anregungen basieren [135, 170].

Im Bezug auf die Spin-Valley Eigenschaften hat sich die Monolagenintegration in DBR-DBR Mikrokavitäten und die gleichzeitige Zwei-Photonen-Anregung als sehr erfolgreich erwiesen. Grundsätzlich lässt sich diese Kombination auch auf Raumtemperaturexperimente übertragen. In diesem Fall wäre es jedoch sinnvoll $MoSe_2$ durch WSe_2 zu ersetzten. WSe_2 Monolagen weisen grundsätzlich einen höheren Grad an Valley-Polarisation und -Koheränz auf und haben eine höhere Quantenausbeute bei Raumtemperatur. Mit den hier beschrieben Methoden wäre eine solche Umsetzung bereits in naher Zukunft möglich. Grundsätzlich könnte auch der optische Valley Hall Effekt bei Raumtemperatur gezeigt werden.

Die Ausweitung des Kondensationsexperiments auf Raumtemperatur und auf Systeme, die ausschließlich Monolagen als aktives Material enthalten, könnte allerdings deutlich herausfordernder sein. Der schnelle, radiative Zerfall sowie so schwache Exziton-Exziton Wechselwirkung erschweren die Polariton-Kondensation in diesem Materialsystem. Obwohl die Kondensation eine geringere Dichte bei niedrigen Temperaturen erfordert, könnten höhere Temperaturen die Polaritonrelaxation durch Phononstreuung vereinfachen. Darüberhinaus stellen die hier präsentieren, neuen Kavitätskonzepte mit hohem Qualitätsfaktor, sowie die Verbesserung der Materialqualität durch Verkappselung mit h-BN wichtige Schritte in Richtung weiterführender Kondensationsexperimente dar. Unter Berücksichtigung aller Ergebnisse dieser Arbeit lässt sich abschließend zusammenfassen, dass das große wissenschaftliche Interesse an Übergangsmetalldichalkogenidmonolagen, vor allem im Bezug auf Exziton-Polaritonen, durchaus gerechtfertigt ist.

Bibliography

[1] E. Gibney, "2D or not 2D," *Nature*, vol. 522, no. 7556, p. 274, 2015.

[2] W. Shakespeare, *The Tradegy of Hamlet*. The Shakespear Press, 1603.

[3] C. Weisbuch, M. Nishioka, A. Ishikawa, and Y. Arakawa, "Observation of the coupled exciton-photon mode splitting in a semiconductor quantum microcavity," *Physical Review Letters*, vol. 69, no. 23, p. 3314, 1992.

[4] H. Deng, H. Haug, and Y. Yamamoto, "Exciton-polariton Bose-Einstein condensation," *Reviews of Modern Physics*, vol. 82, no. 2, p. 1489, 2010.

[5] A. Imamoglu, A., R. Ram, S. Pau, Y. Yamamoto, *et al.*, "Nonequilibrium condensates and lasers without inversion: Exciton-polariton lasers," *Physical Review A*, vol. 53, no. 6, p. 4250, 1996.

[6] C. C. Bradley, C. Sackett, J. Tollett, and R. G. Hulet, "Evidence of Bose-Einstein condensation in an atomic gas with attractive interactions," *Physical Review Letters*, vol. 75, no. 9, p. 1687, 1995.

[7] D. Bajoni, "Polariton lasers: Hybrid light–matter lasers without inversion," *Journal of Physics D: Applied Physics*, vol. 45, no. 31, p. 313001, 2012.

[8] N. Lundt, S. Klembt, E. Cherotchenko, S. Betzold, O. Iff, A. V. Nalitov, M. Klaas, C. P. Dietrich, A. V. Kavokin, S. Höfling, *et al.*, "Room-temperature Tamm-plasmon exciton-polaritons with a WSe_2 monolayer," *Nature communications*, vol. 7, p. 13328, 2016.

[9] T. Cao, G. Wang, W. Han, H. Ye, C. Zhu, J. Shi, Q. Niu, P. Tan, E. Wang, B. Liu, *et al.*, "Valley-selective circular dichroism of monolayer molybdenum disulphide," *Nature communications*, vol. 3, p. 887, 2012.

[10] D. Xiao, G.-B. Liu, W. Feng, X. Xu, and W. Yao, "Coupled spin and valley physics in monolayers of MS_2 and other group-VI dichalcogenides," *Physical Review Letters*, vol. 108, no. 19, p. 196802, 2012.

[11] J. R. Schaibley, H. Yu, G. Clark, P. Rivera, J. S. Ross, K. L. Seyler, W. Yao, and X. Xu, "Valleytronics in 2D materials," *Nature Reviews Materials*, vol. 1, no. 11, p. 16055, 2016.

[12] S. Wolf, D. Awschalom, R. Buhrman, J. Daughton, S. Von Molnar, M. Roukes, A. Y. Chtchelkanova, and D. Treger, "Spintronics: A spin-based electronics vision for the future," *Science*, vol. 294, no. 5546, pp. 1488–1495, 2001.

[13] F. Cadiz, C. Robert, E. Courtade, M. Manca, L. Martinelli, T. Taniguchi, K. Watanabe, T. Amand, A. Rowe, D. Paget, *et al.*, "Exciton diffusion in WSe_2 monolayers embedded in a van der Waals heterostructure," *Applied Physics Letters*, vol. 112, no. 15, p. 152106, 2018.

[14] M. Kulig, J. Zipfel, P. Nagler, S. Blanter, C. Schüller, T. Korn, N. Paradiso, M. M. Glazov, and A. Chernikov, "Exciton diffusion and halo effects in monolayer semiconductors," *Physical Review Letters*, vol. 120, no. 20, p. 207401, 2018.

[15] F. Barachati, A. Fieramosca, S. Hafezian, J. Gu, B. Chakraborty, D. Ballarini, L. Martinu, V. Menon, D. Sanvitto, and S. Khena-Cohen, "Interacting polariton fuids in a monolayer of tungsten disulfide," *Nature Nanotechnology*, vol. 11, pp. 18–22, 2018.

[16] P. Senellart, J. Bloch, B. Sermage, and J. Marzin, "Microcavity polariton depopulation as evidence for stimulated scattering," *Physical Review B*, vol. 62, no. 24, p. R16263, 2000.

[17] M. B. Peterson and R. L. Johnson, "Friction of possible solid lubricants with various crystal structures," *National Advisory Committee for Aeronautics*, vol. 3334, 1954.

[18] R. Frindt, "Single crystals of MoS_2 several molecular layers thick," *Journal of Applied Physics*, vol. 37, no. 4, pp. 1928–1929, 1966.

[19] J. A. Wilson and A. Yoffe, "The transition metal dichalcogenides discussion and interpretation of the observed optical, electrical and structural properties," *Advances in Physics*, vol. 18, no. 73, pp. 193–335, 1969.

[20] W. Jamison and S. Cosgrove, "Friction characteristics of transition-metal disulfides and diselenides," *ASLE TRANSACTIONS*, vol. 14, no. 1, pp. 62–72, 1971.

[21] R. Bromley, R. Murray, and A. Yoffe, "The band structures of some transition metal dichalcogenides. III. Group VI: trigonal prism materials," *Journal of Physics C: Solid State Physics*, vol. 5, no. 7, p. 759, 1972.

[22] K. S. Novoselov, A. K. Geim, S. V. Morozov, D. Jiang, Y. Zhang, S. V. Dubonos, I. V. Grigorieva, and A. A. Firsov, "Electric field effect in atomically thin carbon films," *Science*, vol. 306, no. 5696, pp. 666–669, 2004.

[23] K. Novoselov, D. Jiang, F. Schedin, T. Booth, V. Khotkevich, S. Morozov, and A. Geim, "Two-dimensional atomic crystals," *Proceedings of the National Academy of Sciences*, vol. 102, no. 30, pp. 10451–10453, 2005.

[24] K. F. Mak, C. Lee, J. Hone, J. Shan, and T. F. Heinz, "Atomically thin MoS_2: a new direct-gap semiconductor," *Physical Review Letters*, vol. 105, no. 13, p. 136805, 2010.

[25] A. Splendiani, L. Sun, Y. Zhang, T. Li, J. Kim, C.-Y. Chim, G. Galli, and F. Wang, "Emerging photoluminescence in monolayer," *Nano Letters*, vol. 10, p. 1271, 2010.

[26] M. Glazov, L. Golub, G. Wang, X. Marie, T. Amand, and B. Urbaszek, "Intrinsic exciton-state mixing and nonlinear optical properties in transition metal dichalcogenide monolayers," *Physical Review B*, vol. 95, no. 3, p. 035311, 2017.

[27] A. Kuc, N. Zibouche, and T. Heine, "Influence of quantum confinement on the electronic structure of the transition metal sulfide TeS_2," *Physical Review B*, vol. 83, no. 24, p. 245213, 2011.

[28] A. Chernikov, T. C. Berkelbach, H. M. Hill, A. Rigosi, Y. Li, O. B. Aslan, D. R. Reichman, M. S. Hybertsen, and T. F. Heinz, "Exciton binding energy and non-hydrogenic Rydberg series in monolayer WS_2," *Physical Review Letters*, vol. 113, no. 7, p. 076802, 2014.

[29] D. Bimberg, M. Grundmann, and N. N. Ledentsov, *Quantum Dot Heterostructures*. Wiley, 2001.

[30] M. M. Ugeda, A. J. Bradley, S.-F. Shi, H. Felipe, Y. Zhang, D. Y. Qiu, W. Ruan, S.-K. Mo, Z. Hussain, Z.-X. Shen, *et al.*, "Giant bandgap renormalization and excitonic effects in a monolayer transition metal dichalcogenide semiconductor," *Nature Materials*, vol. 13, no. 12, p. 1091, 2014.

[31] F. Cadiz, C. Robert, G. Wang, W. Kong, X. Fan, M. Blei, D. Lagarde, M. Gay, M. Manca, T. Taniguchi, *et al.*, "Ultra-low power threshold for laser induced changes in optical properties of 2D molybdenum dichalcogenides," *2D Materials*, vol. 3, no. 4, p. 045008, 2016.

[32] G. Wang, A. Chernikov, M. M. Glazov, T. F. Heinz, X. Marie, T. Amand, and B. Urbaszek, "Colloquium: Excitons in atomically thin transition metal dichalcogenides," *Reviews of Modern Physics*, vol. 90, no. 2, p. 021001, 2018.

[33] A. Raja, A. Chaves, J. Yu, G. Arefe, H. M. Hill, A. F. Rigosi, T. C. Berkelbach, P. Nagler, C. Schüller, T. Korn, *et al.*, "Coulomb engineering of the bandgap and excitons in two-dimensional materials," *Nature communications*, vol. 8, p. 15251, 2017.

[34] M. Shinada and S. Sugano, "Interband optical transitions in extremely anisotropic semiconductors. i. Bound and unbound exciton absorption," *Journal of the Physical Society of Japan*, vol. 21, no. 10, pp. 1936–1946, 1966.

[35] L. Keldysh, "Coulomb interaction in thin semiconductor and semimetal films," *Soviet Journal of Experimental and Theoretical Physics Letters*, vol. 29, p. 658, 1979.

[36] P. Cudazzo, I. V. Tokatly, and A. Rubio, "Dielectric screening in two-dimensional insulators: Implications for excitonic and impurity states in graphene," *Physical Review B*, vol. 84, no. 8, p. 085406, 2011.

[37] T. C. Berkelbach, M. S. Hybertsen, and D. R. Reichman, "Theory of neutral and charged excitons in monolayer transition metal dichalcogenides," *Physical Review B*, vol. 88, no. 4, p. 045318, 2013.

[38] A. V. Stier, K. M. McCreary, B. T. Jonker, J. Kono, and S. A. Crooker, "Exciton diamagnetic shifts and valley Zeeman effects in monolayer WS_2 and MoS_2 to 65 tesla," *Nature communications*, vol. 7, p. 10643, 2016.

[39] C. Schneider, K. Winkler, M. Fraser, M. Kamp, Y. Yamamoto, E. Ostrovskaya, and S. Höfling, "Exciton-polariton trapping and potential landscape engineering," *Reports on Progress in Physics*, vol. 80, no. 1, p. 016503, 2016.

[40] P. Y. Yu and M. Cardona, *Fundamentals of Semiconductors*. Springer, 2010.

[41] M. Palummo, M. Bernardi, and J. C. Grossman, "Exciton radiative lifetimes in two-dimensional transition metal dichalcogenides," *Nano Letters*, vol. 15, no. 5, pp. 2794–2800, 2015.

[42] G. Moody, C. Kavir Dass, K. Hao, C.-H. Chen, L.-J. Li, A. Singh, K. Tran, G. Clark, X. Xu, G. Berghäuser, E. Malic, A. Knorr, and X. Li, "Intrinsic homogeneous linewidth and broadening mechanisms of excitons in monolayer transition metal dichalcogenides," *Nature communications*, vol. 6, p. 8315, 2015.

[43] C. Pöllmann, P. Steinleitner, U. Leierseder, P. Nagler, G. Plechinger, M. Porer, R. Bratschitsch, C. Schüller, T. Korn, and R. Huber, "Resonant internal quantum transitions and femtosecond radiative decay of excitons in monolayer WSe_2," *Nature Materials*, vol. 14, no. 9, p. 889, 2015.

[44] T. Jakubczyk, V. Delmonte, M. Koperski, K. Nogajewski, C. Faugeras, W. Langbein, M. Potemski, and J. Kasprzak, "Radiatively limited dephasing and exciton dynamics in $MoSe_2$ monolayers revealed with four-wave mixing microscopy," *Nano Letters*, vol. 16, no. 9, pp. 5333–5339, 2016.

[45] C. Robert, D. Lagarde, F. Cadiz, G. Wang, B. Lassagne, T. Amand, A. Balocchi, P. Renucci, S. Tongay, B. Urbaszek, *et al.*, "Exciton radiative lifetime in transition metal dichalcogenide monolayers," *Physical Review B*, vol. 93, no. 20, p. 205423, 2016.

[46] T. Jakubczyk, K. Nogajewski, M. R. Molas, M. Bartos, W. Langbein, M. Potemski, and J. Kasprzak, "Impact of environment on dynamics of exciton complexes in a WS_2 monolayer," *2D Materials*, vol. 5, no. 3, p. 031007, 2018.

[47] H. Wang, C. Zhang, W. Chan, C. Manolatou, S. Tiwari, and F. Rana, "Radiative lifetimes of excitons and trions in monolayers of the metal dichalcogenide MoS_2," *Physical Review B*, vol. 93, no. 4, p. 045407, 2016.

[48] B. Deveaud, F. Clérot, N. Roy, K. Satzke, B. Sermage, and D. Katzer, "Enhanced radiative recombination of free excitons in GaAs quantum wells," *Physical Review Letters*, vol. 67, no. 17, p. 2355, 1991.

[49] L. C. Andreani, F. Tassone, and F. Bassani, "Radiative lifetime of free excitons in quantum wells," *Solid state communications*, vol. 77, no. 9, pp. 641–645, 1991.

[50] N. Kumar, Q. Cui, F. Ceballos, D. He, Y. Wang, and H. Zhao, "Exciton-exciton annihilation in $MoSe_2$ monolayers," *Physical Review B*, vol. 89, no. 12, p. 125427, 2014.

[51] C. F. Klingshirn, *Semiconductor Optics*. Springer, 2007.

[52] C. Schneider, M. M. Glazov, T. Korn, S. Höfling, and B. Urbaszek, "Two-dimensional semiconductors in the regime of strong light-matter coupling," *Nature Communications*, vol. 9, 2018.

[53] V. Shahnazaryan, I. Iorsh, I. Shelykh, and O. Kyriienko, "Exciton-exciton interaction in transition-metal dichalcogenide monolayers," *Physical Review B*, vol. 96, no. 11, p. 115409, 2017.

[54] T. Li and G. Galli, "Electronic properties of MoS_2 nanoparticles," *The Journal of Physical Chemistry C*, vol. 111, no. 44, pp. 16192–16196, 2007.

[55] Z. Zhu, Y. Cheng, and U. Schwingenschlögl, "Giant spin-orbit-induced spin splitting in two-dimensional transition-metal dichalcogenide semiconductors," *Physical Review B*, vol. 84, no. 15, p. 153402, 2011.

[56] G.-B. Liu, W.-Y. Shan, Y. Yao, W. Yao, and D. Xiao, "Three-band tight-binding model for monolayers of group-VIB transition metal dichalcogenides," *Physical Review B*, vol. 88, no. 8, p. 085433, 2013.

[57] K. Kośmider, J. W. González, and J. Fernández-Rossier, "Large spin splitting in the conduction band of transition metal dichalcogenide monolayers," *Physical Review B*, vol. 88, no. 24, p. 245436, 2013.

[58] G. Wang, I. Gerber, L. Bouet, D. Lagarde, A. Balocchi, M. Vidal, T. Amand, X. Marie, and B. Urbaszek, "Exciton states in monolayer $MoSe_2$: impact on interband transitions," *2D Materials*, vol. 2, no. 4, p. 045005, 2015.

[59] A. Arora, K. Nogajewski, M. Molas, M. Koperski, and M. Potemski, "Exciton band structure in layered $MoSe_2$: from a monolayer to the bulk limit," *Nanoscale*, vol. 7, no. 48, pp. 20769–20775, 2015.

[60] F. Withers, O. Del Pozo-Zamudio, S. Schwarz, S. Dufferwiel, P. Walker, T. Godde, A. Rooney, A. Gholinia, C. Woods, P. Blake, *et al.*, "WSe_2 light-emitting tunneling transistors with enhanced brightness at room temperature," *Nano Letters*, vol. 15, no. 12, pp. 8223–8228, 2015.

[61] M. Glazov, T. Amand, X. Marie, D. Lagarde, L. Bouet, and B. Urbaszek, "Exciton fine structure and spin decoherence in monolayers of transition metal dichalcogenides," *Physical Review B*, vol. 89, no. 20, p. 201302, 2014.

[62] H. Yu, G.-B. Liu, P. Gong, X. Xu, and W. Yao, "Dirac cones and Dirac saddle points of bright excitons in monolayer transition metal dichalcogenides," *Nature communications*, vol. 5, p. 3876, 2014.

[63] M. Maialle, E. d. A. e Silva, and L. Sham, "Exciton spin dynamics in quantum wells," *Physical Review B*, vol. 47, no. 23, p. 15776, 1993.

[64] M. Baranowski, A. Surrente, D. Maude, M. Ballottin, A. Mitioglu, P. Christianen, Y. Kung, D. Dumcenco, A. Kis, and P. Plochocka, "Dark excitons and the elusive valley polarization in transition metal dichalcogenides," *2D Materials*, vol. 4, no. 2, p. 025016, 2017.

[65] Y.-J. Chen, J. D. Cain, T. K. Stanev, V. P. Dravid, and N. P. Stern, "Valley-polarized exciton–polaritons in a monolayer semiconductor," *Nature Photonics*, vol. 11, no. 7, p. 431, 2017.

[66] Z. Ye, D. Sun, and T. F. Heinz, "Optical manipulation of valley pseudospin," *Nature Physics*, vol. 13, no. 1, p. 26, 2017.

[67] S. F. Yu, *Analysis and Design of Vertical Surface Emitting Lasers*. John Wiley and Sons, 2003.

[68] A. V. Kavokin, J. J. Baumberg, G. Malpuech, and F. P. Laussy, *Microcavities*. Oxford University Press, 2007.

[69] J. Hopfield, "Theory of the contribution of excitons to the complex dielectric constant of crystals," *Physical Review*, vol. 112, no. 5, p. 1555, 1958.

[70] V. Savona, L. Andreani, P. Schwendimann, and A. Quattropani, "Quantum well excitons in semiconductor microcavities: Unified treatment of weak and strong coupling regimes," *Solid State Communications*, vol. 93, no. 9, pp. 733–739, 1995.

[71] S. Dufferwiel, T. Lyons, D. Solnyshkov, A. Trichet, F. Withers, S. Schwarz, G. Malpuech, J. Smith, K. Novoselov, M. Skolnick, *et al.*, "Valley-addressable polaritons in atomically thin semiconductors," *Nature Photonics*, vol. 11, no. 8, p. 497, 2017.

[72] D. Lidzey, J. Wenus, D. Whittaker, G. Itskos, P. Stavrinou, D. Bradley, and R. Murray, "Hybrid polaritons in strongly coupled microcavities: experiments and models," *Journal of luminescence*, vol. 110, no. 4, pp. 347–353, 2004.

[73] T. Fliessbach, *Statistische Physik*. Spektrum Akademischer Verlag Heidelberg, 2010.

[74] A. Einstein, *Quantentheorie des einatomigen idealen Gases*. Sitzungsbericht der Koeniglich Preussischen Akademie der Wissenschaften zu Berlin, 2. Abhandlung, 1925.

[75] A. Kavokin and G. Malpuech, *Thin films and nanostructures*. Elsevier, 2003.

[76] P. C. Hohenberg, "Existence of long-range order in one and two dimensions," *Physical Review*, vol. 158, no. 2, p. 383, 1967.

[77] N. D. Mermin and H. Wagner, "Absence of ferromagnetism or antiferromagnetism in one-or two-dimensional isotropic heisenberg models," *Physical Review Letters*, vol. 17, no. 22, p. 1133, 1966.

[78] M. Richard, J. Kasprzak, R. André, R. Romestain, L. S. Dang, G. Malpuech, and A. Kavokin, "Experimental evidence for nonequilibrium Bose condensation of exciton polaritons," *Physical Review B*, vol. 72, no. 20, p. 201301, 2005.

[79] F. Manni, K. G. Lagoudakis, T. C. Liew, R. André, and B. Deveaud-Plédran, "Spontaneous pattern formation in a polariton condensate," *Physical Review Letters*, vol. 107, no. 10, p. 106401, 2011.

[80] H. Haug, T. Doan, H. T. Cao, and D. T. Thoai, "Temporal first-and second-order correlations in a polariton condensate," *Physical Review B*, vol. 85, no. 20, p. 205310, 2012.

[81] V. Savona and D. Sarchi, "Bose-Einstein condensation of microcavity polaritons," *physica status solidi (b)*, vol. 242, no. 11, pp. 2290–2301, 2005.

[82] F. Tassone and Y. Yamamoto, "Exciton-exciton scattering dynamics in a semiconductor microcavity and stimulated scattering into polaritons," *Physical Review B*, vol. 59, no. 16, p. 10830, 1999.

[83] F. Tassone and Y. Yamamoto, "Lasing and squeezing of composite bosons in a semiconductor microcavity," *Physical Review A*, vol. 62, no. 6, p. 063809, 2000.

[84] N. Wiener, *Time Series*. M.I.T. Press, 1964.

[85] J.-S. Tempel, F. Veit, M. Aßmann, L. E. Kreilkamp, A. Rahimi-Iman, A. Löffler, S. Höfling, S. Reitzenstein, L. Worschech, A. Forchel, *et al.*, "Characterization of two-threshold behavior of the emission from a GaAs microcavity," *Physical Review B*, vol. 85, no. 7, p. 075318, 2012.

[86] Y.-H. Lee, X.-Q. Zhang, W. Zhang, M.-T. Chang, C.-T. Lin, K.-D. Chang, Y.-C. Yu, J. T.-W. Wang, C.-S. Chang, L.-J. Li, *et al.*, "Synthesis of large-area MoS_2 atomic layers with chemical vapor deposition," *Advanced materials*, vol. 24, no. 17, pp. 2320–2325, 2012.

[87] M. Chhowalla, H. S. Shin, G. Eda, L.-J. Li, K. P. Loh, and H. Zhang, "The chemistry of two-dimensional layered transition metal dichalcogenide nanosheets," *Nature Chemistry*, vol. 5, no. 4, p. 263, 2013.

[88] R. Lv, J. A. Robinson, R. E. Schaak, D. Sun, Y. Sun, T. E. Mallouk, and M. Terrones, "Transition metal dichalcogenides and beyond: synthesis, properties, and applications of single-and few-layer nanosheets," *Accounts of chemical research*, vol. 48, no. 1, pp. 56–64, 2014.

[89] Y. Zhang, T.-R. Chang, B. Zhou, Y.-T. Cui, H. Yan, Z. Liu, F. Schmitt, J. Lee, R. Moore, Y. Chen, *et al.*, "Direct observation of the transition from indirect to direct bandgap in atomically thin epitaxial $MoSe_2$," *Nature Nanotechnology*, vol. 9, no. 2, pp. 111–115, 2014.

[90] L. K. Tan, B. Liu, J. H. Teng, S. Guo, H. Y. Low, and K. P. Loh, "Atomic layer deposition of a MoS_2 film," *Nanoscale*, vol. 6, no. 18, pp. 10584–10588, 2014.

[91] A. Castellanos-Gomez, M. Buscema, R. Molenaar, V. Singh, L. Janssen, H. S. Van Der Zant, and G. A. Steele, "Deterministic transfer of two-dimensional materials by all-dry viscoelastic stamping," *2D Materials*, vol. 1, no. 1, p. 011002, 2014.

[92] N. G. McCrum, C. P. Buckley, and C. B. Bucknall, *Principles of Polymer Engineering*. Oxford University Press, 1988.

[93] M. A. Meyers and K. K. Chawla, *Mechanical Behavior of Materials*. Cambridge University Press, 2009.

[94] J. Jadczak, J. Kutrowska-Girzycka, P. Kapuściński, Y. Huang, A. Wójs, and L. Bryja, "Probing of free and localized excitons and trions in atomically thin WSe_2, WS_2, $MoSe_2$ and MoS_2 in photoluminescence and reflectivity experiments," *Nanotechnology*, vol. 28, no. 39, p. 395702, 2017.

[95] F. Cadiz, E. Courtade, C. Robert, G. Wang, Y. Shen, H. Cai, T. Taniguchi, K. Watanabe, H. Carrere, D. Lagarde, *et al.*, "Excitonic linewidth approaching the homogeneous limit in MoS_2-based van der Waals heterostructures," *Physical Review X*, vol. 7, no. 2, p. 021026, 2017.

[96] Y. Li, A. Chernikov, X. Zhang, A. Rigosi, H. M. Hill, A. M. van der Zande, D. A. Chenet, E.-M. Shih, J. Hone, and T. F. Heinz, "Measurement of the optical dielectric function of monolayer transition-metal dichalcogenides: MoS_2, $MoSe_2$, WS_2, and WSe_2," *Physical Review B*, vol. 90, no. 20, p. 205422, 2014.

[97] G. Wang, C. Robert, A. Suslu, B. Chen, S. Yang, S. Alamdari, I. C. Gerber, T. Amand, X. Marie, S. Tongay, *et al.*, "Spin-orbit engineering in transition metal dichalcogenide alloy monolayers," *Nature communications*, vol. 6, p. 10110, 2015.

[98] B. Y. University, *InGaP Band Structure Calculation*. 2016.

[99] F. A. Rasmussen and K. S. Thygesen, "Computational 2D materials database: electronic structure of transition-metal dichalcogenides and oxides," *The Journal of Physical Chemistry C*, vol. 119, no. 23, pp. 13169–13183, 2015.

[100] K. F. Mak, K. He, C. Lee, G. H. Lee, J. Hone, T. F. Heinz, and J. Shan, "Tightly bound trions in monolayer MoS_2," *Nature materials*, vol. 12, no. 3, p. 207, 2013.

[101] B. Radisavljevic, A. Radenovic, J. Brivio, i. V. Giacometti, and A. Kis, "Single-layer MoS_2 transistors," *Nature nanotechnology*, vol. 6, no. 3, p. 147, 2011.

[102] N. Lundt, S. Stoll, P. Nagler, A. Nalitov, S. Klembt, S. Betzold, J. Goddard, E. Frieling, A. Kavokin, C. Schüller, *et al.*, "Observation of macroscopic valley-polarized monolayer exciton-polaritons at room temperature," *Physical Review B*, vol. 96, no. 24, p. 241403, 2017.

[103] C. Liedenbaum, A. Valster, A. Severens, and G. Hooft, "Determination of the GaInP/AlGaInP band offset," *Applied Physics Letters*, vol. 57, no. 25, pp. 2698–2700, 1990.

[104] R. Schmidt, G. Berghäuser, R. Schneider, M. Selig, P. Tonndorf, E. Malic´, A. Knorr, S. Michaelis de Vasconcellos, and R. Bratschitsch, "Ultrafast coulomb-induced intervalley coupling in atomically thin WS_2," *Nano Letters*, vol. 16, no. 5, pp. 2945–2950, 2016.

[105] O. A. Ajayi, J. V. Ardelean, G. D. Shepard, J. Wang, A. Antony, T. Taniguchi, K. Watanabe, T. F. Heinz, S. Strauf, X. Zhu, *et al.*, "Approaching the intrinsic photoluminescence linewidth in transition metal dichalcogenide monolayers," *2D Materials*, vol. 4, no. 3, p. 031011, 2017.

[106] J. Wierzbowski, J. Klein, F. Sigger, C. Straubinger, M. Kremser, T. Taniguchi, K. Watanabe, U. Wurstbauer, A. W. Holleitner, M. Kaniber, *et al.*, "Direct exciton emission from atomically thin transition metal dichalcogenide heterostructures near the lifetime limit," *Scientific reports*, vol. 7, no. 1, p. 12383, 2017.

[107] S. Dufferwiel, S. Schwarz, F. Withers, A. Trichet, F. Li, M. Sich, O. Del Pozo-Zamudio, C. Clark, A. Nalitov, D. Solnyshkov, *et al.*, "Exciton–polaritons in van der Waals heterostructures embedded in tunable microcavities," *Nature communications*, vol. 6, p. 8579, 2015.

[108] L. C. Flatten, Z. He, D. M. Coles, A. A. Trichet, A. W. Powell, R. A. Taylor, J. H. Warner, and J. M. Smith, "Room-temperature exciton-polaritons with two-dimensional WS_2," *Scientific reports*, vol. 6, p. 33134, 2016.

[109] Filmetrics, *Refractive Index Database*. https://www.filmetrics.com/refractive-index-database, 15.10.2015.

[110] Ioffe-Physical-Technical-Institute, *n-k-database*. http://www.ioffe.ru/SVA/NSM/nk/, 15.10.2015.

[111] A. Kavokin, G. Malpuech, and M. Glazov, "Optical spin Hall effect," *Physical Review Letters*, vol. 95, no. 13, p. 136601, 2005.

[112] M. Kaliteevski, I. Iorsh, S. Brand, R. Abram, J. Chamberlain, A. Kavokin, and I. Shelykh, "Tamm plasmon-polaritons: Possible electromagnetic states at the interface of a metal and a dielectric Bragg mirror," *Physical Review B*, vol. 76, no. 16, p. 165415, 2007.

[113] M. Sasin, R. Seisyan, M. Kalitteevski, S. Brand, R. Abram, J. Chamberlain, A. Y. Egorov, A. P. Vasilev, V. Mikhrin, and A. Kavokin, "Tamm plasmon polaritons: Slow and spatially compact light," *Applied Physics Letters*, vol. 92, no. 25, p. 251112, 2008.

[114] J. Gessler, V. Baumann, M. Emmerling, M. Amthor, K. Winkler, S. Höfling, C. Schneider, and M. Kamp, "Electro optical tuning of Tamm-plasmon exciton-polaritons," *Applied Physics Letters*, vol. 105, no. 18, p. 181107, 2014.

[115] Y. Yamamoto, F. Tassone, and H. Cao, *Semiconductor Cavity Quantum Electrodynamics*. Springer, 2000.

[116] P. Tsotsis, P. Eldridge, T. Gao, S. I. Tsintzos, Z. Hatzopoulos, and P. G. Savvidis, "Lasing threshold doubling at the crossover from strong to weak coupling regime in gaas microcavity," *New Journal of physics*, vol. 14, no. 2, p. 023060, 2012.

[117] A. Hanbicki, M. Currie, G. Kioseoglou, A. Friedman, and B. Jonker, "Measurement of high exciton binding energy in the monolayer transition-metal dichalcogenides WS_2 and WSe_2," *Solid State Communications*, vol. 203, pp. 16–20, 2015.

[118] A. Ramsay, T. Godden, S. Boyle, E. M. Gauger, A. Nazir, B. W. Lovett, A. Fox, and M. Skolnick, "Phonon-induced Rabi-frequency renormalization of optically driven single InGaAs/GaAs quantum dots," *Physical Review Letters*, vol. 105, no. 17, p. 177402, 2010.

[119] P. Tonndorf, R. Schmidt, P. Böttger, X. Zhang, J. Börner, A. Liebig, M. Albrecht, C. Kloc, O. Gordan, D. R. Zahn, *et al.*, "Photoluminescence emission and Raman response of monolayer MoS_2, $MoSe_2$, and WSe_2," *Optics express*, vol. 21, no. 4, pp. 4908–4916, 2013.

[120] Y. V. Morozov and M. Kuno, "Optical constants and dynamic conductivities of single layer MoS_2, $MoSe_2$, and WSe_2," *Applied Physics Letters*, vol. 107, no. 8, p. 083103, 2015.

[121] A. Auffèves, D. Gerace, J.-M. Gérard, M. F. Santos, L. Andreani, and J.-P. Poizat, "Controlling the dynamics of a coupled atom-cavity system by pure dephasing," *Physical Review B*, vol. 81, no. 24, p. 245419, 2010.

[122] M. I. Vasilevskiy, D. G. Santiago-Pérez, C. Trallero-Giner, N. M. Peres, and A. Kavokin, "Exciton polaritons in two-dimensional dichalcogenide layers placed in a planar microcavity: Tunable interaction between two Bose-Einstein condensates," *Physical Review B*, vol. 92, no. 24, p. 245435, 2015.

[123] G. Wang, C. Robert, M. Glazov, F. Cadiz, E. Courtade, T. Amand, D. Lagarde, T. Taniguchi, K. Watanabe, B. Urbaszek, *et al.*, "In-plane propagation of light in transition metal dichalcogenide monolayers: optical selection rules," *Physical Review Letters*, vol. 119, no. 4, p. 047401, 2017.

[124] N. Lundt, A. Maryński, E. Cherotchenko, A. Pant, X. Fan, S. Tongay, G. Sęk, A. Kavokin, S. Höfling, and C. Schneider, "Monolayered $MoSe_2$: a candidate for room temperature polaritonics," *2D Materials*, vol. 4, no. 1, p. 015006, 2016.

[125] X. Liu, T. Galfsky, Z. Sun, F. Xia, E.-c. Lin, Y.-H. Lee, S. Kéna-Cohen, and V. M. Menon, "Strong light–matter coupling in two-dimensional atomic crystals," *Nature Photonics*, vol. 9, no. 1, p. 30, 2015.

[126] T. Hu, Y. Wang, L. Wu, L. Zhang, Y. Shan, J. Lu, J. Wang, S. Luo, Z. Zhang, L. Liao, *et al.*, "Strong coupling between Tamm plasmon polariton and two dimensional semiconductor excitons," *Applied Physics Letters*, vol. 110, no. 5, p. 051101, 2017.

[127] B. Chakraborty, J. Gu, Z. Sun, M. Khatoniar, R. Bushati, A. L. Boehmke, R. Koots, and V. M. Menon, "Control of strong light-matter interaction in monolayer WS_2 through electric field gating," *Nano letters*, 2018.

[128] Z. Sun, J. Gu, A. Ghazaryan, Z. Shotan, C. R. Considine, M. Dollar, B. Chakraborty, X. Liu, P. Ghaemi, S. Kéna-Cohen, *et al.*, "Optical control of room-temperature valley polaritons," *Nature Photonics*, vol. 11, no. 8, p. 491, 2017.

[129] S. Wang, S. Li, T. Chervy, A. Shalabney, S. Azzini, E. Orgiu, J. A. Hutchison, C. Genet, P. Samorì, and T. W. Ebbesen, "Coherent coupling of WS_2 monolayers with metallic photonic nanostructures at room temperature," *Nano letters*, vol. 16, no. 7, pp. 4368–4374, 2016.

[130] J. Cuadra, D. G. Baranov, M. Wersa?ll, R. Verre, T. J. Antosiewicz, and T. Shegai, "Observation of tunable charged exciton polaritons in hybrid monolayer WS_2 - plasmonic nanoantenna system," *Nano letters*, vol. 18, no. 3, pp. 1777–1785, 2018.

[131] O. Iff, Y.-M. He, N. Lundt, S. Stoll, V. Baumann, S. Höfling, and C. Schneider, "Substrate engineering for high-quality emission of free and localized excitons from atomic monolayers in hybrid architectures," *Optica*, vol. 4, no. 6, pp. 669–673, 2017.

[132] J. S. Ross, S. Wu, H. Yu, N. J. Ghimire, A. M. Jones, G. Aivazian, J. Yan, D. G. Mandrus, D. Xiao, W. Yao, *et al.*, "Electrical control of neutral and charged excitons in a monolayer semiconductor," *Nature communications*, vol. 4, p. 1474, 2013.

[133] A. M. Jones, H. Yu, N. J. Ghimire, S. Wu, G. Aivazian, J. S. Ross, B. Zhao, J. Yan, D. G. Mandrus, D. Xiao, *et al.*, "Optical generation of excitonic valley coherence in monolayer WSe_2," *Nature Nanotechnology*, vol. 8, no. 9, p. 634, 2013.

[134] G. Plechinger, P. Nagler, A. Arora, R. Schmidt, A. Chernikov, A. G. Del Águila, P. C. Christianen, R. Bratschitsch, C. Schüller, and T. Korn, "Trion fine structure and coupled spin–valley dynamics in monolayer tungsten disulfide," *Nature communications*, vol. 7, p. 12715, 2016.

[135] M. Sidler, P. Back, O. Cotlet, A. Srivastava, T. Fink, M. Kroner, E. Demler, and A. Imamoglu, "Fermi polaron-polaritons in charge-tunable atomically thin semiconductors," *Nature Physics*, vol. 13, no. 3, p. 255, 2017.

[136] A. Singh, G. Moody, K. Tran, M. E. Scott, V. Overbeck, G. Berghäuser, J. Schaibley, E. J. Seifert, D. Pleskot, N. M. Gabor, *et al.*, "Trion formation dynamics in monolayer transition metal dichalcogenides," *Physical Review B*, vol. 93, no. 4, p. 041401, 2016.

[137] F. Tassone, C. Piermarocchi, V. Savona, A. Quattropani, and P. Schwendimann, "Bottleneck effects in the relaxation and photoluminescence of microcavity polaritons," *Physical Review B*, vol. 56, no. 12, p. 7554, 1997.

[138] A. Tartakovskii, M. Emam-Ismail, R. Stevenson, M. Skolnick, V. Astratov, D. Whittaker, J. J. Baumberg, and J. Roberts, "Relaxation bottleneck and its suppression in semiconductor microcavities," *Physical Review B*, vol. 62, no. 4, p. R2283, 2000.

[139] M. Amani, P. Taheri, R. Addou, G. H. Ahn, D. Kiriya, D.-H. Lien, J. W. Ager III, R. M. Wallace, and A. Javey, "Recombination kinetics and effects of superacid treatment in sulfur- and selenium-based transition metal dichalcogenides," *Nano Letters*, vol. 16, no. 4, pp. 2786–2791, 2016.

[140] O. Bleu, D. Solnyshkov, and G. Malpuech, "Optical valley Hall effect based on transitional metal dichalcogenide cavity polaritons," *Physical Review B*, vol. 96, no. 16, p. 165432, 2017.

[141] A. T. Hanbicki, G. Kioseoglou, M. Currie, C. S. Hellberg, K. M. McCreary, A. L. Friedman, and B. T. Jonker, "Anomalous temperature-dependent spin-valley polarization in monolayer WS_2," *Scientific reports*, vol. 6, p. 18885, 2016.

[142] K. V. Kavokin, I. A. Shelykh, A. V. Kavokin, G. Malpuech, and P. Bigenwald, "Quantum theory of spin dynamics of exciton-polaritons in microcavities," *Physical Review Letters*, vol. 92, no. 1, p. 017401, 2004.

[143] M. Król, K. Lekenta, R. Mirek, K. Łempicka, D. Stephan, K. Nogajewski, M. R. Molas, A. Babiński, M. Potemski, J. Szczytko, and B. Pietka, "Valley polarization of exciton-polaritons in monolayer WSe_2 in a tunable microcavity," *arXiv preprint arXiv:1809.09571*, 2018.

[144] N. Lundt, P. Nagler, A. Nalitov, S. Klembt, M. Wurdack, S. Stoll, T. Harder, S. Betzold, V. Baumann, A. Kavokin, *et al.*, "Valley polarized relaxation and upconversion luminescence from Tamm-plasmon trion–polaritons with a $MoSe_2$ monolayer," *2D Materials*, vol. 4, no. 2, p. 025096, 2017.

[145] G. Kioseoglou, A. Hanbicki, M. Currie, A. Friedman, D. Gunlycke, and B. Jonker, "Valley polarization and intervalley scattering in monolayer MoS_2," *Applied Physics Letters*, vol. 101, no. 22, p. 221907, 2012.

[146] B. Zhu, H. Zeng, J. Dai, Z. Gong, and X. Cui, "Anomalously robust valley polarization and valley coherence in bilayer WS_2," *Proceedings of the National Academy of Sciences*, vol. 111, no. 32, pp. 11606–11611, 2014.

[147] K. L. Seyler, J. R. Schaibley, P. Gong, P. Rivera, A. M. Jones, S. Wu, J. Yan, D. G. Mandrus, W. Yao, and X. Xu, "Electrical control of second-harmonic generation in a WSe_2 monolayer transistor," *Nature Nanotechnology*, vol. 10, no. 5, p. 407, 2015.

[148] A. I. Tartakovskii, V. D. Kulakovskii, A. Forchel, and J. P. Reithmaier, "Exciton-photon coupling in photonic wires," *Physical Review B*, vol. 57, no. 12, p. 6807, 1998.

[149] V. Kulakovskii, A. Larionov, S. Novikov, S. Höfling, C. Schneider, and A. Forchel, "Bose-Einstein condensation of exciton polaritons in high-Q planar microcavities with GaAs quantum wells," *JETP Letters*, vol. 92, no. 9, pp. 595–599, 2010.

[150] Y. Li, Y. Rao, K. F. Mak, Y. You, S. Wang, C. R. Dean, and T. F. Heinz, "Probing symmetry properties of few-layer MoS_2 and h-BN by optical second-harmonic generation," *Nano Letters*, vol. 13, no. 7, pp. 3329–3333, 2013.

[151] L. M. Malard, T. V. Alencar, A. P. M. Barboza, K. F. Mak, and A. M. de Paula, "Observation of intense second harmonic generation from MoS_2 atomic crystals," *Physical Review B*, vol. 87, no. 20, p. 201401, 2013.

[152] G. Wang, X. Marie, I. Gerber, T. Amand, D. Lagarde, L. Bouet, M. Vidal, A. Balocchi, and B. Urbaszek, "Giant enhancement of the optical second-harmonic emission of WSe_2 monolayers by laser excitation at exciton resonances," *Physical Review Letters*, vol. 114, no. 9, p. 097403, 2015.

[153] P. Gong, H. Yu, Y. Wang, and W. Yao, "Optical selection rules for excitonic Rydberg series in the massive Dirac cones of hexagonal two-dimensional materials," *Physical Review B*, vol. 95, no. 12, p. 125420, 2017.

[154] H. Simon and N. Bloembergen, "Second-harmonic light generation in crystals with natural optical activity," *Physical Review*, vol. 171, no. 3, p. 1104, 1968.

[155] S. Dufferwiel, T. Lyons, D. Solnyshkov, A. Trichet, F. Withers, G. Malpuech, J. Smith, K. Novoselov, M. Skolnick, D. Krizhanovskii, *et al.*, "Valley coherent exciton-polaritons in a monolayer semiconductor," *arXiv preprint arXiv:1804.09108*, 2018.

[156] A. Kavokin, I. Shelykh, and G. Malpuech, "Optical Tamm states for the fabrication of polariton lasers," *Applied Physics Letters*, vol. 87, no. 26, p. 261105, 2005.

[157] C. Leyder, M. Romanelli, J. P. Karr, E. Giacobino, T. C. Liew, M. M. Glazov, A. V. Kavokin, G. Malpuech, and A. Bramati, "Observation of the optical spin Hall effect," *Nature Physics*, vol. 3, no. 9, p. 628, 2007.

[158] N. Lundt, L. Dusanowski, E. Sedov, P. Stepanov, M. M. Glazov, S. Klembt, M. Klaas, J. Beierlein, Y. Qin, S. Tongay, M. Richard, A. V. Kavokin, S. Hoefling, and C. Schneider, "Optical valley hall effect for highly valley-coherent exciton-polaritons in an atomically thin semiconductor," *Nature Nanotechnology*, vol. 492, 2019.

[159] J. Feldmann, G. Peter, E. Göbel, P. Dawson, K. Moore, C. Foxon, and R. Elliott, "Linewidth dependence of radiative exciton lifetimes in quantum wells," *Physical Review Letters*, vol. 59, no. 20, p. 2337, 1987.

[160] J. Andersson and L. Lundqvist, "Near-unity quantum efficiency of AlGaAs/GaAs quantum well infrared detectors using a waveguide with a doubly periodic grating coupler," *Applied Physics Letters*, vol. 59, no. 7, pp. 857–859, 1991.

[161] Y. P. Varshni, "Temperature dependence of the energy gap in semiconductors," *physica*, vol. 34, no. 1, pp. 149–154, 1967.

[162] N. W. Ashcroft and N. D. Mermin, *Solid State Physics*. Cengage Learning, 2011.

[163] J. Hegarty, L. Goldner, and M. Sturge, "Localized and delocalized two-dimensional excitons in GaAs-AlGaAs multiple-quantum-well structures," *Physical Review B*, vol. 30, no. 12, p. 7346, 1984.

[164] M. Wurdack, N. Lundt, M. Klaas, V. Baumann, A. V. Kavokin, S. Höfling, and C. Schneider, "Observation of hybrid Tamm-plasmon exciton-polaritons with GaAs quantum wells and a $MoSe_2$ monolayer," *Nature communications*, vol. 8, no. 1, p. 259, 2017.

[165] G. Lanty, S. Zhang, J. Lauret, E. Deleporte, P. Audebert, S. Bouchoule, X. Lafosse, J. Zuñiga-Pérez, F. Semond, D. Lagarde, *et al.*, "Hybrid cavity polaritons in a ZnO-perovskite microcavity," *Physical Review B*, vol. 84, no. 19, p. 195449, 2011.

[166] M. Slootsky, X. Liu, V. M. Menon, and S. R. Forrest, "Room temperature frenkel-wannier-mott hybridization of degenerate excitons in a strongly coupled microcavity," *Physical review letters*, vol. 112, no. 7, p. 076401, 2014.

[167] G. Paschos, N. Somaschi, S. Tsintzos, D. Coles, J. Bricks, Z. Hatzopoulos, D. Lidzey, P. Lagoudakis, and P. G. Savvidis, "Hybrid organic-inorganic polariton laser," *Scientific Reports*, vol. 7, no. 1, p. 11377, 2017.

[168] D. Bajoni, P. Senellart, E. Wertz, I. Sagnes, A. Miard, A. Lemaître, and J. Bloch, "Polariton laser using single micropillar GaAs-GaAlAs semiconductor cavities," *Physical Review Letters*, vol. 100, no. 4, p. 047401, 2008.

[169] M. Waldherr, N. Lundt, M. Klaas, S. Betzold, M. Wurdack, V. Baumann, E. Estrecho, A. Nalitov, E. Cherotchenko, H. Cai, E. Ostrovskaya, A. V. Kavokin, S. Tongay, S. Klembt, S. Hoefling, and C. Schneider, "Observation of bosonic condensation in a hybrid monolayer $MoSe_2$-GaAs microcavity," *Nature communications*, vol. 9, pp. 1–6, 2018.

[170] O. Cotleţ, S. Zeytinoglu, M. Sigrist, E. Demler, and A. Imamoglu, "Superconductivity and other collective phenomena in a hybrid Bose-Fermi mixture formed by a

polariton condensate and an electron system in two dimensions," *Physical Review B*, vol. 93, no. 5, p. 054510, 2016.

[171] D. Rosales, T. Bretagnon, B. Gil, A. Kahouli, J. Brault, B. Damilano, J. Massies, M. Durnev, and A. Kavokin, "Excitons in nitride heterostructures: From zero-to one-dimensional behavior," *Physical Review B*, vol. 88, no. 12, p. 125437, 2013.

Publications of the author

Sorted by date in reverse chronological order:

N. Lundt, L. Dusanowski, E. Sedov, P. Stepanov, M. M. Glazov, S. Klembt, M. Klaas, J. Beierlein, Y. Qin, S. Tongay, M. Richard, A. V. Kavokin, S. Höfling, and C. Schneider; *Optical valley Hall effect for highly valley-coherent exciton-polaritons in an atomically thin semiconductor*, Nature Nanotechnology (492), 2019

O. Iff, N. Lundt, S. Betzold, L. N. Tripathi, M. Emmerling, S. Tongay, Y. J. Lee, S.-H. Kwon, S. Höfling, and C. Schneider; *Deterministic coupling of quantum emitters in WSe_2 monolayers to plasmonic nanocavities*, Optics Express (26), 2018

M. Waldherr*, N. Lundt*, M. Klaas*, S. Betzold, M. Wurdack, V. Baumann, E. Estrecho, A. Nalitov, E. Cherotchenko, H. Cai, E. A. Ostrovskaya, A. V. Kavokin, S. Tongay, S. Klempt, S. Höfling and C. Schneider; *equal contribution; *Observation of bosonic condensation in a hybrid monolayer $MoSe_2$-GaAs microcavity*, Nature communications (9) 2018

E. Krauss, R. Kullock, X. Wu, P. Geisler, N. Lundt, M. Kamp and B. Hecht, *Controlled Growth of High-Aspect-Ratio Single-Crystalline Gold Platelets*; Crystal Growth and Design" (18) 2018

N. Lundt, E. Cherotchenko, O.Iff, X.Fan, Y. Shen, P. Bigenwald, A. Kavokin, S. Höfling and C. Schneider; *The interplay between excitons and trions in a monolayer of $MoSe_2$*, Applied Physics Letters (112) 2018

N. Lundt, S. Stoll, P. Nagler, A. Nalitov, S. Klembt, S. Betzold, J. W. Goddard, E. Frieling, A.V. Kavokin, C. Schüller, T. Korn, S. Höfling and C. Schneider, *Observation of macroscopic valley-polarized monolayer exciton-polaritons at room temperature*; PRB rapid communications (96), 2017

M. Wurdack, N. Lundt, M. Klaas, V. Baumann, A. V. Kavokin, S. Höfling and C. Schnei-

der; *Observation of hybrid Tamm-plasmon exciton-polaritons with GaAs quantum wells and a $MoSe_2$ monolayer*; Nature Communications (8), 2017

O. Iff, Y.-M. He, N. Lundt, S. Stoll, V. Baumann, S. Höfling, and C. Schneider; *Substrate engineering for high-quality emission of free and localized excitons from atomic monolayers in hybrid architectures*; Optica (4), 2017

N. Lundt, P. Nagler , A. Nalitov , S. Klembt , M. Wurdack , S. Stoll , T. H. Harder, S. Betzold , V. Baumann, A. V. Kavokin, C. Schüller, T. Korn, S. Höfling and C. Schneider; *Valley polarized relaxation and upconversion luminescence from Tamm-plasmon trion-polaritons with a $MoSe_2$ monolayer*; 2D Materials (4), 2017

Y.-M. He, O. Iff, N. Lundt, V. Baumann, M. Davanco, K. Srinivasan, S. Höfling and C. Schneider; *Cascaded emission of single photons from the biexciton in monolayered WSe_2*; Nature Communications (7), 2016

N. Lundt, A. Marynski, E. Cherotchenko, A. Pant, X. Fan, S. Tongay, G. Sek, A. V. Kavokin, S. Höfling and C. Schneider; *Monolayered $MoSe_2$: a candidate for room temperature polaritonics*; 2D Materials (4), 2016

N. Lundt, S. Klembt, E. Cherotchenko, S. Betzold, O. Iff, A. V. Nalitov, M. Klaas, C. P. Dietrich, A. V. Kavokin, S. Höfling, C. Schneider; *Room-temperature Tamm-plasmon exciton-polaritons with a WSe_2 monolayer*; Nature Communications (7), 2016

R. E. O'Brien, B. Wang, S. T. Kelly, N., Lundt, Y. You, A. K. Bertram, S. R. Leone, A. Laskin, M. K. Gilles; *Liquid-liquid phase separation in aerosol particles: Imaging at the nanometer scale*; Environmental science and technology (49), 2015

N. Lundt, S.T. Kelly, T. Rodel, B. Remez, A. M. Schwartzberg, A. Ceballos, C. Baldasseroni, P. A. F. Anastasi, M. Cox, F. Hellman, S. R. Leone, M. K. Gilles; *High spatial resolution Raman thermometry analysis of TiO_2 microparticles*; Reviews of Scientific Instruments (48), 2013

A. Osvet, M. Batentschuk, M. Milde, N. Lundt, C. Gellermann, S. Dembski, A. Winnacker, C. J. Brabec; *Photoluminescent and storage properties of photostimulable core/shell type silicate nanoparticles*; Physica Stuatus Solidi c (10), 2013

Acknowledgement

This work was conducted with a lot of support from others that has always been highly appreciated. Therefore, the author likes to thank:

Dr. C. Schneider for the supervision of this work, guidance of this project and for the fruitful discussions and his advice.

Prof. Dr. B. Hecht and Prof. Dr. T. Brixner for their co-supervision in the frame of the Graduate School of Science and Technology (GSST).

Prof. Dr. S. Höfling as the chair holders of the Chair of Technisch Physik for providing the working environments and means that were required for this work.

Dr. S. Schröder-Köhne for his administrative support at the GSST.

V. Wegmann for her administrative support at the Chair of Technisch Physik.

M. Klaas, T. Harder and Dr. H. Lundt for proof-reading of this work.

O. Iff, S. Stoll, M. Wurdack for their contributions and assistance in the frame of their master projects to this work.

I. Kim, E. Frieling and J. Goddard for their contributions and assistance to this work in the frame of the exchange program with the University of British Columbia, Canada.

S. Stoll, M. Jörg, M. Rödel and J. Michl for their contributions as assistant students to this work.

A. Wolf, M. Emmerling, T. Bausenwein, M. Wagenbrenner, S. Kuhn and G. Heller for their technical support.

Prof. Dr. A. V. Kavokin, Dr. A. Nalitov, Dr. E. Cherotchenko and Dr. E. Sedov from the University of Southampton, UK for their theory support.

Prof. Dr. S. Tongay and his students, Arizona State University, Prof. Dr.T. Taniguchi and Prof. Dr.K. Watanabe, National Institute for Materials Science, Japan for providing bulk materials.

Prof. Dr. T. Korn, Prof. Dr. C. Schüller and Dr. P. Nagler, University of Regensburg, for their collaboration on time-resolved measurements and for my enjoyable stay at their lab.

Prof. Dr. Sek and A. Marynski, Wroclaw University of Science and Technology for their collaboration on first monolayer reflectance measurements and for my enjoyable stay at their lab.

Dr. U. Schulz, Dr. F. Eilenberger, Dr. F. Rickelt and H. Knopf, Fraunhofer Insitute IOF, Jena for their collaboration on oxide material deposition.

S. Betzold, S. Brodbeck, T. Harder and U. Müller for providing software-based simulation and data analysis tools.

Dr. S. Klembt for his instructions and advice on various spectroscopy related topics.

All other members of the Institute of Applied Physics for the enjoyable working atmosphere.

All co-authors that contributed to the publications listed above.

My friends and family for their unconditional support throughout this work.

Affidavit

I hereby confirm that my thesis entitled "Strong light-matter coupling with 2D materials" is the result of my own work. I did not receive any help or support from commercial consultants. All sources and / or materials applied are listed and specified in the thesis.

Furthermore, I confirm that this thesis has not yet been submitted as part of another examination process neither in identical nor in similar form.

Würzburg, den .....

Nils Lundt

Eidesstattliche Erklärung

Hiermit erkläre ich an Eides statt, die Dissertation "Starke Licht-Materie Kopplung mit 2D Materialien" eigenständig, d.h. insbesondere selbständig und ohne Hilfe eines kommerziellen Promotionsberaters, angefertigt und keine anderen als die von mir angegebenen Quellen und Hilfsmittel verwendet zu haben. Ich erkläre außerdem, dass die Dissertation weder in gleicher noch in ähnlicher Form bereits in einem anderen Prüfungsverfahren vorgelegen hat.

Würzburg, den .....

Nils Lundt

Curriculum vitae

Personal data

Date/place of birth	21.10.1988, Burghausen
Address	Heinestrasse 12, 97070 Würzburg
Telephone	0151/28243089
Email	nils.lundt@gmail.com

Education

09/1995 - 07/1999	Hans-Kammerer elementary school, Burghausen
09/1999 - 07/2008	High school with A-level, Aventinus-Gymnasium, Burghausen
10/2009 - 05/2012	Bachelor of Science in nanotechnology and nanoscience at the University of Erlangen, Germany
04/2012 - 03/2015	Master of Science in nanotechnology and nanoscience at the University of Würzburg, Germany
Since 10/2015	Ph.D. program at the Graduate School of Science and Technology, University of Würzburg, Germany

Research and working experience

07/2008 - 03/2009	Civilian service in the department of environment of the Town of Burghausen, Germany
04/2009 - 05/2009	Engineering internship at Siltronic AG in Portland, Oregon, USA
05/2010 - 03/2012	Research assistant at the Institute for Materials of Electronics and Energy Technology, University of Erlangen, Germany
08/2010 - 09/2010	Internship at the Nanoelectronic Material Laboratory gGmbH, Dresden, Germany
02/2011 - 03/2011	Research internship at the Institute of Multidisciplinary Research for Advanced Materials, Tohoku University, Sendai, Japan
08/2012 - 07/2013	Research internship at the University of California, Berkeley and Lawrence Berkeley National Laboratory, Berkeley, USA

Würzburg, den .....

Nils Lundt

Appendix A

Appendix

A.1 Error anaylsis for single-peak fits

When fitting a single resonance, the error of peak energy and linewidth (FWHM) is partly determined by the energy resolution of the spectrometers optical gratings. In this work, gratings with either 150, 600 or 1200 lines/mm have been used, corresponding to energy resolutions of 1.1, 0.26 and 0.11 meV for the reference wavelength of 750 nm. Peaks were fitted (peak analysis of OriginPro 2016) by either a Lorentzian function for resonances measured at cryogenic temperature experiments or by a Gaussian function for resonances measured at room temperature. The fitting error is typically well below the energy resolution of the used grating. If not stated differently, the error is smaller or on the order of the last digit precision of the energy and linewidth values stated in the maintext and thus the error values are not explicitly stated in these cases.

A.2 Reflectivities of gold and silver

In order to choose the appropriate metal for DBR-metal cavity designs for different target resonance wavelengths, the reflectivity spectra of gold and silver were calculated here by the transfer matrix method as shown in Figure A.1 (refractive indices were taken from [109]).

A.3 Error analysis for Q-factors

The Q-factors were determined by taking individual line spectra of the empty cavity reflectivity dispersion relations (as shows in Figure 4.8 for example) around zero in-plane wave vector. The cavity resonance absorption dips were fitted with a Lorentzian function and the Q-factor was calculated by $Q = \frac{\lambda_C}{\Gamma_C}$. Because of the varying white-light background

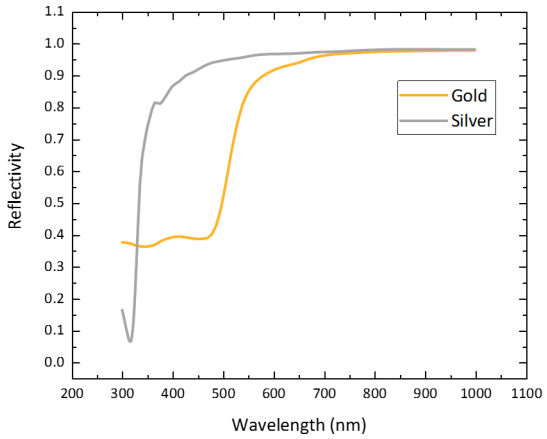

Figure A.1: Comparison of the reflectivity spectra of gold and silver.

of the signal, the determined values vary. Therefore, several line spectra were fitted and the error of the Q-factor was estimated based of the variance of individual line spectra results.

A.4 Reflectivity spectra data treatment

First, a manual background substraction (peak analysis tool of OriginPro 2016) was carried out for the recorded reflectivity spectra. Subsequently, the spectra were normalized to 1. Finally, the cavity resonance absorption feature was fit with a Lorentzian function to determined its linewidth and Q-factor. Figure A.2 compares the recorded raw data with the final spectrum for a fully grown DBR-DBR cavity.

A.5 Error analysis for cavity and lower polariton effective masses

The effective cavity masses were extracted from the curvature of the dispersion relations (see equation 2.16). The dispersions were fitted around zero in-plane wave vectors with a quadratic function to deduce the curvature. Since the dispersion diverges from the parabolic behavior towards higher in-plane wave vectors, in particular for a lower polariton branch, the error for the curvature determination was estimated to about 5 %.

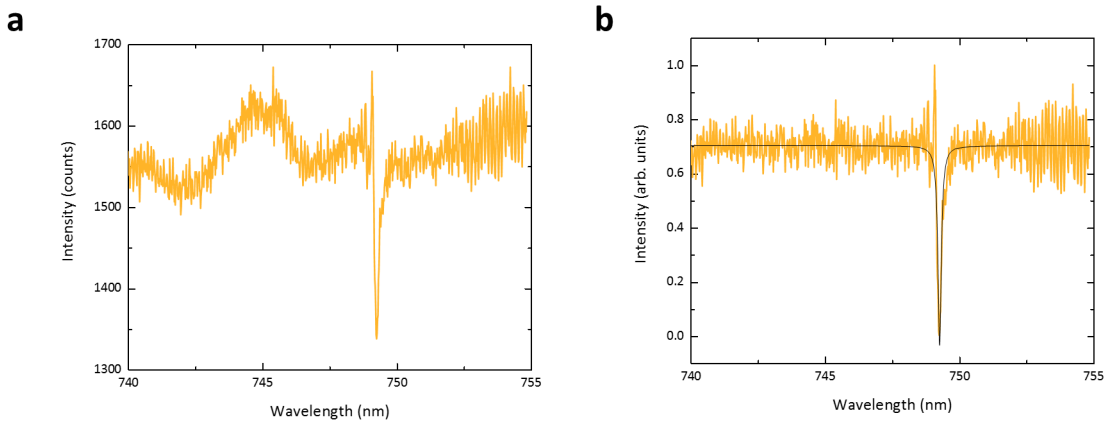

Figure A.2: Reflectivity spectra before (a) and after (b) background substraction and normalization to 1. In addition, (b) shows the cavity mode fit with a Lorentzian peak, which is used to determine the cavity Q factor (see appendix A.3)

A.6 Reflectance contrast spectra

The reflectance contrast spectra is obtained as $\Delta R/R = (R_{sample} - R_{substrate})/R_{substrate}$, where R_{sample} is the reflectivity measured on the monolayer position and $R_{substrate}$ is the reflectivity measured on the bare substrate. Figure A.3a shows reflectivity spectra on bare SiO_2 substrate and of a $MoSe_2$ monolayer on the same substrate, recorded at 5 K. Figure A.3b presents the derived reflectance contrast spectrum.

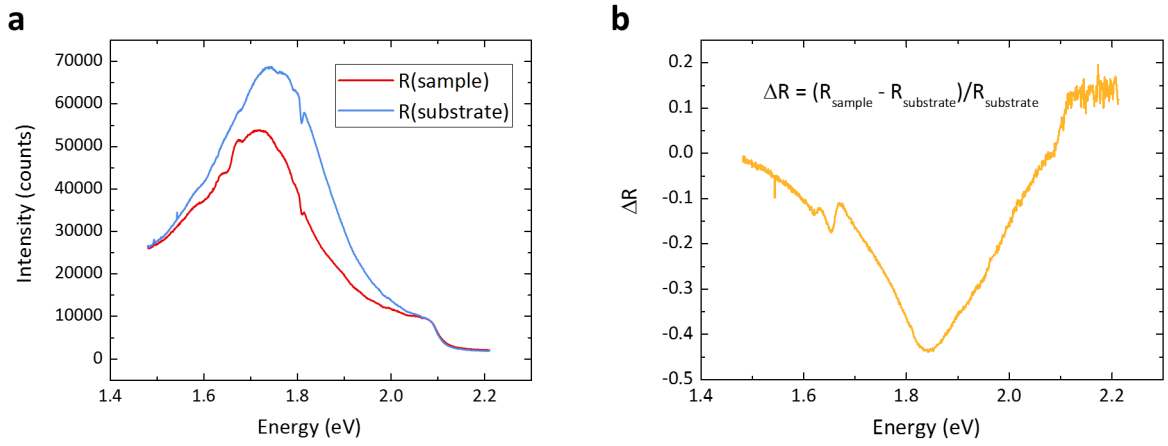

Figure A.3: (a) Reflectivity spectra of bare SiO_2 substrate and of a $MoSe_2$ monolayer on the same substrate at at 5 K. (b) Derived reflectance contrast spectrum based on the spectra presented in (a).

A.7 Fitting of reflectance spectra

In this section, details on the fitting procedure and the error analysis of the reflectance spectra presented in section 4.3 are described. Linewidth and amplitude were deduced by fitting a Gaussian function to the reflectance contrast spectra after a background subtraction. In order to carry out an appropriate background subtraction, the reflectance contrast spectra were simulated without excitonic absorptions (imaginary part of the refractive index k of $MoSe_2$ was set to 0). The transfer matrix simulations were carried out for a Si substrate thickness of 200 μm, 285 nm for SiO_2 and 0.65 nm for $MoSe_2$. Optical constants were taken from reference [120] and the exciton resonances were modeled with a Lorentz oscillator according to equation 4.3. For comparison, a Gaussian shaped dip centered at the resonance was subtracted from the simulated background spectrum. In Figure A.4, the latter is compared to a simulated background spectrum. The spectra describe the experimentally acquired spectra presented in Figure 4.12a very well. The shoulders above and below the resonance provide an excellent orientation in the background subtraction process. It should be noted that these shoulders are not as distinct in the spectra for 200 K and higher temperatures. Therefore, a higher error was assumed in the subtraction and fitting process. The error from the subtraction process was evaluated by conducting the subtraction and fitting multiple times for an identical spectrum. According to this, the amplitude typically varies by ± 5% and the linewidth by ± 0.75 meV. The total error is composed of the background subtraction error and the fitting error (quadratic error propagation).

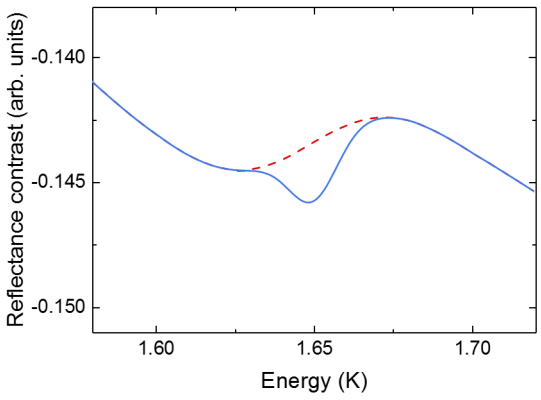

Figure A.4: Simulated reflectance contrast of the sample structure with (blue solid line) and without (red dashed line) the excitonic absorption

A.8 Modeling of the exciton resonance as Lorentz oscillator

Figure A.5 presents real and imaginary part of the refractive index (n and k) deduced from the Lorentz oscillator model (equation 4.3) and the experimental results of linewidth and relative oscillator strength. It should be noted that the integral $\int_0^\infty k(E,T)dE$ follows exactly the same temperature evolution as f(T), which justifies to deduce f from the product of dip amplitude and linewidth, which is in turn proportional to the integrated dip area.

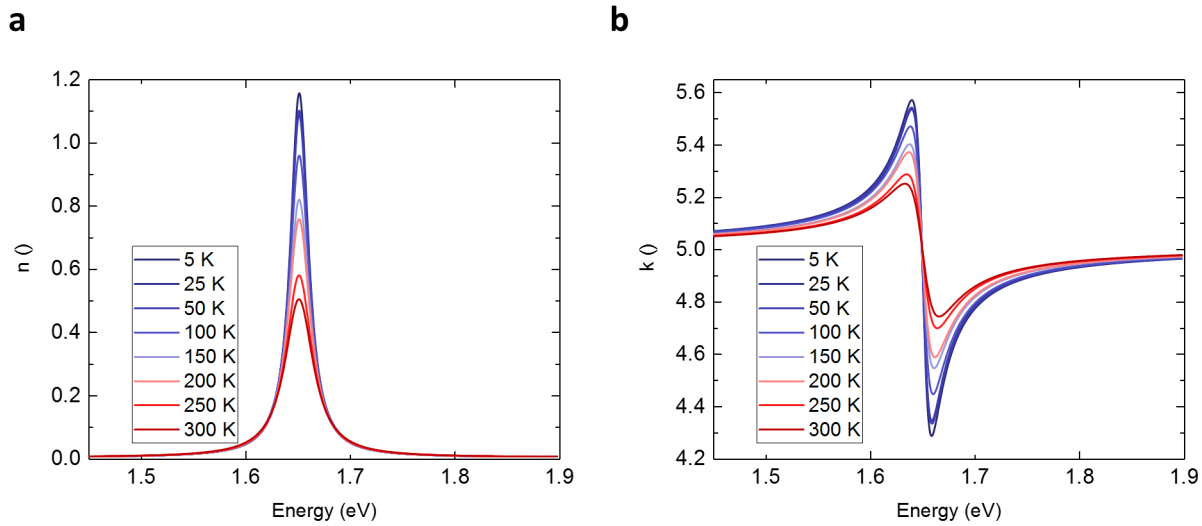

Figure A.5: Real (a) and imaginary (b) parts of refractive index of monolayer $MoSe_2$, used for transfer matrix calculations

A.9 Modeling of temperature-induced decrease of oscillator strength

The oscillator strength of the exciton is determined by both the optical matrix element and the available bright exciton states inside the light cone. While the optical matrix element is not affected by the temperature, the available exciton states inside the light cone are a function of temperature. Therefore, the overall reduction of oscillator strength with temperature naturally follows from the reduced fraction of bright excitons inside the light cone at higher temperatures [159]. The remaining fraction occupies optically dark states. Excitons absorbed inside the light cone may thermalize and redistribute in the

reciprocal space before being re-emitted and thus contributing to the optical reflectivity. The temperature dependence of this effect stems from the temperature-induced decrease of the phonon scattering time in $MoSe_2$ monolayers [44]. The radiative decay rate Γ_0, which is proportional to the oscillator strength, enters the expression for the integrated absorption $\alpha = \frac{2\pi\Gamma\Gamma_0}{\Gamma_0+\Gamma}$ and must be averaged over the exciton ensemble. Assuming the Boltzmann distribution of excitons, the radiative decay rate is estimated as $\Gamma_0(T) = \Gamma_0(T = 0)(1 - exp(-\frac{T_0}{T}))$, where T_0 is the characteristic temperature which depends on the exciton frequency and effective mass [171]. The integrated absorption of light by excitons is linear in the averaged radiative decay rate under the condition that the radiative broadening is small compared to the non-radiative broadening, which can be assumed above 100 K[44]. Thus, the relative oscillator strength in Figure 4.12d can be fitted by $(1 - exp(-\frac{T_0}{T}))$, with $T_0 = 300\ K$ because of its proportionality to the radiative decay rate[1]

A.10 Fitting procedure and error analysis double-peak fit

In this work, some acquired disperison relations include more than one branch (for example upper and lower polariton branch). Consequently, the line spectra for each in-plane momentum are composed of two peaks. Here, the detailed fitting procedure of momentum-resolved two-peak spectra and the resulting error analysis are exemplarily discussed for the results presented in section 5.1 (diverging error values for two-peak fits for results presented in other section are given at the end of this section). Each spectrum was fitted with two Gaussian peaks. Initially, two peak energies were manually selected and then a fitting algorithm (OriginPro 2016) optimized peak energies, linewidths, intensities and a constant offset. The iterative process minimized the standard deviation of the global fit to a Chi value of below 10^{-12}, allowing up to 500 iterations (all fits converged before reaching this limit). Figure A.6 illustrates the results of this fitting procedure for five selected spectra that are presented in Figure 5.2 in the main text. For each spectrum, the experimental data, the fits for each peak and the global fit are shown. For all spectra the global fit exhibits good agreement with the experimental data. A closer analysis of the individual spectra shows that the peak positions of the global fit do not always perfectly coincide with the experimental data. For example Figure A.7 shows the uppermost spectrum of Figure A.6 in detail. This closer analysis suggests an error of approximately 2 meV for the fit. Furthermore, the starting conditions for the fitting process have a slight

[1]The modeling of the temperature dependence was carried out in close collaboration with E. Cherotchenko and A. V. Kavokin, University of Southampton.

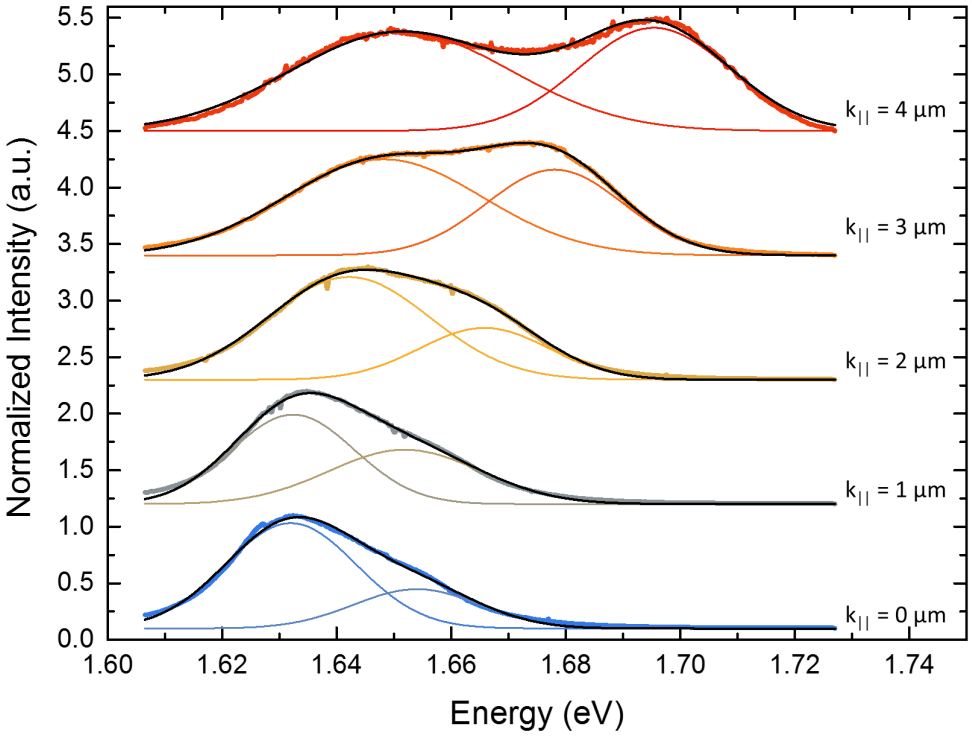

Figure A.6: Selected line spectra from Figure 5.2 including the global fit (black line) and the individual Gaussian peaks.

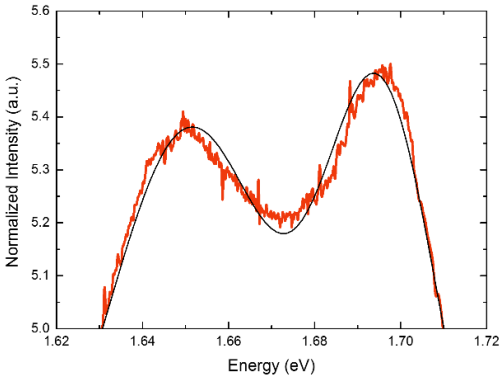

Figure A.7: Uppermost line spectrum of Figure A.6 and the corresponding global fit, showing slight deviations.

influence on the final peak energy result. Therefore, the error for each data point was estimated to be 2.5 meV, added as error bars to Figure 5.2b and c. The estimated error

for the empty cavity branch presented in figure 5.6 has been increase to 10 meV due to the low intensity of the branch.

A.11 Error analysis for normal mode splittings

The normal mode splittings were determined by fitted upper and lower polariton branch (or alternatively only the lower polariton branch is the upper one was not observed) with the two-coupled-oscillator model described in section 2.4.1. For this fit, a maximum of fixed fitting parameters such as exciton and cavity energies was used. Exciton and cavity energies were taken from pre-characterization measurements. The error of the normal mode splitting mainly depends on the peak fitting error of the observed branches (see appendix A.1 and A.10). In addition, the uncoupled exciton and cavity energies might have been shifted in the cavity fabrication process (strain induced energy shift of the exciton resonance for example) and thus diverge from the pre-characterization value. Adjusting these values for a best fit is another source of uncertainty. Thus, the error for the normal mode splitting is estimated to 4 - 5 %.

A.12 Fits for WSe_2 exciton-polariton temperture series

The peak position of upper and lower polariton branch were extracted by a double-Gaussian peak fit and were subsequently fitted by a two-coupled-oscillator. Extracted peak positons and fits are presented in Figure A.8

A.13 Error analysis for the degrees of polarization

Although a polarimeter was used to adjust and compensate for losses of the degree of polarization at the optics (beam splitter, objective), the error due to imperfections of the optics is still estimated to be on the order of 1 %. Moreover, the excitation laser power is typically fluctuating of the on the order of 2 %. The two contributions result in an absolute error of 2.2 % (quadratic error propagation).

A.14 Estimation of exciton, trion and polariton densities

The trion and trion-polariton densities were estimated according to following equation:

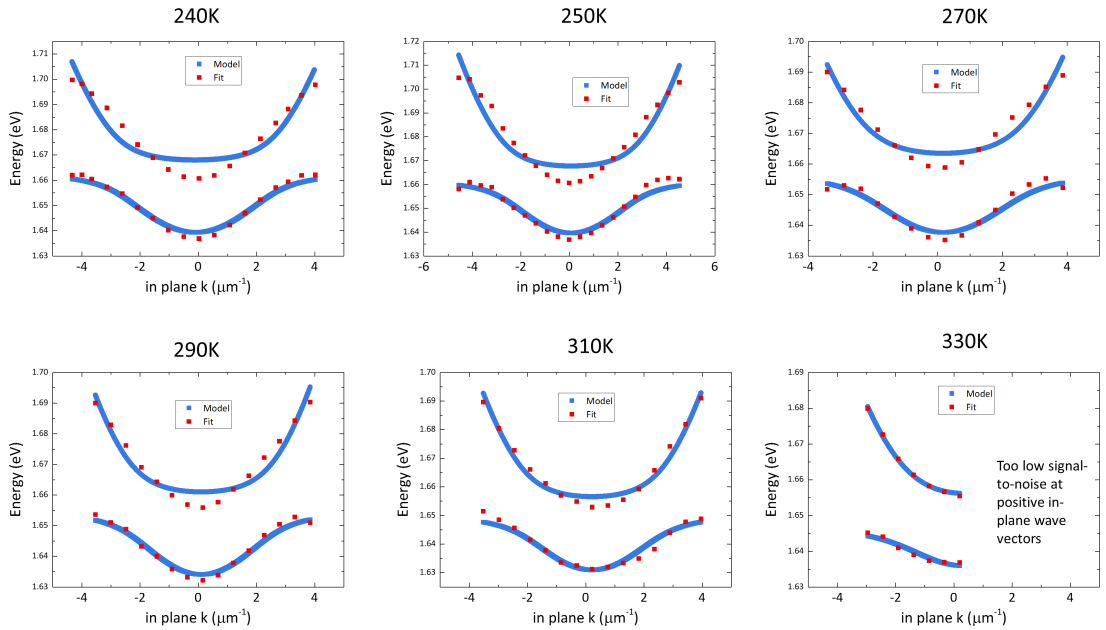

Figure A.8: Extracted lower and upper polariton branch peak positions and two-coupled-oscillator fits for PL dispersion recorded at various temperatures.

$$n = C\frac{P_{Peak}\tau_{puls}a}{E_{photon}A}, \tag{A.1}$$

where P_{Peak} is the peak power of the laser, τ_{puls} is the pulse length of the laser (180 fs), parameter a is the absorption of the $MoSe_2$ monolayer (4 % at 700 nm), E_{photon} is the photon energy and A is the excitation area for a spot size of 1 μm. C is a correction factor that accounts for the reflectivity and absorption of the top gold layer of the Tamm structure. It was set to 1 for the bare monolayer and to $6.4*10^{-4}$ for the polariton sample, using this value from the correspond transfer matrix calculation.

A.15 Fitting procedure for time-resolved photoluminescence measurement

In order to fit the time traces, a convolution of an exponential growth function with the streak camera response function and with either one exponential decay in the case of $MoSe_2$ trion/trion-polariton (chapter 6.1) or three exponential decays in the case of the WS_2 exciton/exciton-polariton (chapter 6.2) was used. The streak camera response function has a line width (FWHM) of 8 ps. Since both, rise and decay time were fitted, the camera temporal resolution is 4 ps (HWHM) for each time constant. Figure A.9

shows two exemplary time traces and the corresponding fits. The error values provided by this fitting procedure are actually very low. Therefore, the fitting error was estimated by slightly varying the starting conditions of fitting. The variation of the fitting results were then used to determine more realistic error values.

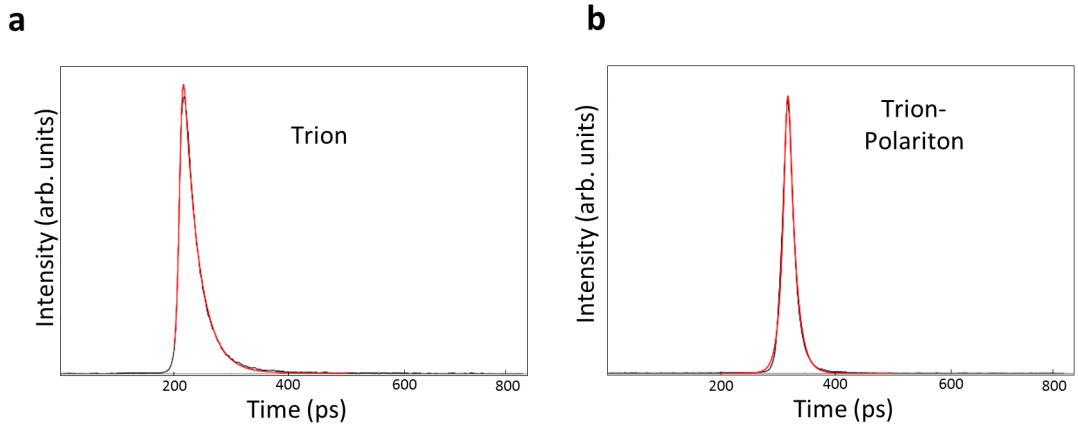

Figure A.9: Time traces of of trion and trion-polariton (black line) and corresponding fits (red lines)

A.16 Radiative lifetimes of WS_2 excitons and exciton-polaritons

By measuring the normal mode splitting $\hbar\Omega$ of the two coupled modes, the radiative life time τ_{ex} of the exciton can be accessed by applying the following equation [81]:

$$\hbar\Omega = 2\sqrt{\frac{2\gamma_{ex}c}{n_c L_{eff}}}. \tag{A.2}$$

With $\tau_{ex} = \frac{1}{\gamma_{ex}}$, This can be re-written to:

$$\tau_{ex} = \frac{8c}{\hbar^2\Omega^2 n_c L_{eff}}. \tag{A.3}$$

Taking $\hbar\Omega = 82\ meV$, $n_c = 1.471$ (arithmetic mean of 82 nm PMMA layer and 105 nm SiO_2 layer) and $L_{eff} = 247\ nm$, a radiative lifetime of 220 fs is obtained, which is in good agreement with previous findings [43, 41, 46].

Then, equation 2.30 was used to calculate the radiative polariton lifetime τ_{pol} as a function of its Hopfield coefficients and its in-plane wave vector. For this, equation 2.11 was used to determined the cavity life to 20 fs. Figure A.10 shows that τ_{pol} is on the order of 20 - 50 fs depending on the polariton in-plane wave vector.

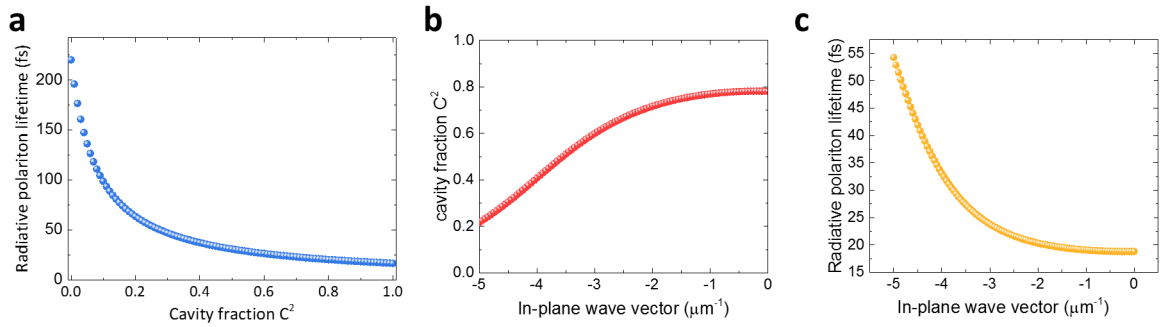

Figure A.10: a) Radiative polariton lifetime as a function of its Hopfield coefficients. b) Hopfield coefficients of the exciton-polariton presented in section 5.2 as function of its in-plane wave vector. c) Relating a) and b) yields the radiative polariton lifetime as a function of the in-plane wave vector.

A.17 Valley polarization relaxation

In order to model the dependence of valley polarization on the in-plane wave vector, it is assumed that polaritons relax stepwise down the dispersion. The model considers a gas of free polaritons with parabolic dispersion, created by a circularly polarized non-resonant pump at high energies. The model accounts for (1) acoustic phonon-assisted energy relaxation, which is dominant below the condensation threshold, and (2) Maialle-Silva-Sham type spin relaxation stemming from the interplay of momentum-dependent effective magnetic field acting on polariton pseudospin and stochastic elastic momentum scattering. The system has been treated by numerically solving the full set of Boltzmann kinetic equations as described in reference [142]. For the stationary state, corresponding to cw pumping, the model provides an analytical solution for the circular polarization of polariton emission in dependence on the wave-vector.

Firstly, the continuous problem is discretizesd and reformulated in terms of a ladder of bosonic energy levels, where direct transitions are only allowed between the neighboring levels. In order to do so, possible phonon assisted inelastic transitions of a polariton with momentum $\mathbf{p}$ are considered. In the limit of slow speed of sound $u \ll p/m$, where m is the polariton effective mass, the maximal energy which can be emitted by the polariton to the thermal bath in one transition is $\Delta E_{\max} = 2pu$.

However, the average over the scattering angle energy dissipation may be estimated as $\langle \Delta E \rangle = pu$. This argument allows to set the energy distance of the bosonic ladder $E_{i+1} - E_i = up_{i+1}$, where E_i and $p_i = \sqrt{2mE_i}$ are the energy and momentum value of the i-th level respectively. Contrary to bosonic cascades, it is not constant and increases from the bottom to the top in parabolic quantum wells. This energy discretization corresponds

to homogeneous grid in the momentum value: $p_i = imu$ with the resolution being the momentum of a polariton at the speed of sound.

The occupation numbers of twice degenerate in spin energy levels $n_i^{\pm}$ is introduced. Then, the model focuses on the linear regime of the bosonic ladder $n_i^{\pm} \ll 1$. In this case, the effect of bosonic stimulation are be neglected and the model is reduced to a set of semiclassical Boltzmann kinetic equations:

$$\frac{\mathrm{d}n_i^{\pm}}{\mathrm{d}t} = \alpha_{i+1} n_{i+1}^{\pm} - \alpha_i n_i^{\pm} - \gamma_i \left(n_i^{\pm} - n_i^{\mp}\right) - \gamma n_i, \tag{A.4}$$

where γ is the universal rate of polariton decay, α_i and γ_i are the level-specific rates of phonon-assisted spin-conserving transitions between the levels and spin relaxation, stemming from elastic momentum scattering within the level. Introducing the level population $n_i = n_i^+ + n_i^-$ and degree of circular polarization $P_i = (n_i^+ - n_i^-)/n_i$, the time derivatives in (A.4) is set to zero to find the stability condition:

$$n_{i+1} = n_i \frac{\alpha_i + \gamma}{\alpha_{i+1}}, \tag{A.5}$$

$$P_{i+1} = P_i \left(1 + \frac{2\gamma_i}{\alpha_i + \gamma}\right). \tag{A.6}$$

From this recursively defined sequence are expressed

$$P_i = P_0 \prod_{l=0}^{i} \left(1 + \frac{2\gamma_l}{\alpha_l + \gamma}\right), \tag{A.7}$$

which can be simplified in the case of slow spin relaxation $\gamma_i \ll \alpha_i$:

$$P_i = P_0 \left(1 + \sum_{l=0}^{i} \frac{2\gamma_l}{\alpha_l + \gamma}\right). \tag{A.8}$$

The interlevel transition rates α_i are given by the product of the squared transition matrix element and the number of states involved in the transition. The exciton-phonon scattering matrix element in Van-der-Waals structures is linear in the phonon momentum on the scale of characteristic polariton wave-vectors. Unlike the QW case, where the main exciton energy relaxation mechanism is due to emission of phonons in the growth direction, here the active layer is mechanically isolated from the substrate, therefore the excitons can only emit in-plane phonons. In turn, the Hopfield coefficient governing the excitonic fraction of polariton also slowly varies in the vicinity of the polariton dispersion bottom, faraway from the anti-crossing point. Finally, the number of states taking part in the transition can be approximated by $\rho(E_i)\,(E_{i+1} - E_i)$, where $\rho(E)$ is the density of states. Since in the two-dimensional case $\rho(E) = const$, the transition rate $\alpha_i = \alpha p_i^3$ is qubic in the polariton momentum.

The spin relaxation rate γ_i is governed by the dominating contribution of the Maialle-Silva-Sham mechanism $\gamma_i = \Omega_i^2 \tau$, where Ω_i is the value of stochastic effective magnetic field and τ is the polariton transport time, which is assumed constant. The effective field Ω_i, in which the polariton pseusospin precesses, originates from TE-TM splitting of the photonic polariton component and the long-range part of the electron-hole exchange acting on the excitonic component. In the vicinity of the polariton dispersion bottom the photonic component is dominant, hence, the effective field is given by the TE-TM splitting, which is quadratic in polariton momentum, allowing us to put $\gamma_i = \beta p_i^4$.

Assuming fast polariton energy relaxation $\alpha_i \gg \gamma$, one can therefore derive from (A.8):

$$P_i = P_0 \left(1 + 2\frac{\beta}{\alpha} \sum_{l=0}^{i} p_l \right) \tag{A.9}$$

Finally, approximating the sum by an integral and coming back to continuous momentum value p, the model yields the expression for the circular polarisation as a function of momentum:

$$P(p) = P(0) + \frac{\beta}{2\alpha} p^2. \tag{A.10}$$

The neighboring level transition approximation is employed, which allows us to derive the recurrent relation (A.8) for the circular polarisation of the emission from the i-th level, is based on several assumptions. Firstly, it is assumed that the characteristic speed of sound u is much slower then the characteristic velocity of polaritons with wave vectors in the region of interest. This implies only one acoustic phonon mode, however, the approximation works in the case of many acoustic modes as long the fastest of them is still slow compared to polariton velocities. Secondly, the argument is based on the existence of the characteristic energy, transferred from the polariton to the phonon bath, depending on the polariton momentum. Finally, it is assumed that the dominance of Maialle-Silva-Sham type mechanism in the spin relaxation. This allows to describe the simultaneous energy and spin relaxation with two separate terms in the kinetic equations (A.4), one of them stemming from the spin-conserving instantaneous energy relaxation steps, and the other one describing elastic process of spin relaxation within each energy level [2].

A.18 SHG response of bare $MoSe_2$ monolayer

In order to extract the SHG characteristic that arise from bare $MoSe_2$ monolayer, the SHG (1509 nm excitation) of $MoSe_2$ monolayer, encapsulated in h-BN, was compared

[2] This model has been worked out by A. Nalitov and A. V. Kavokin, University of Southampton, and was subsequently applied to experimental results presented in section 6.2

to conventional PL (532 nm excitation) as presented in Figure A.11. While exciton and trion resonances exhibit a linewidths of 8 - 10 meV in PL, the SHG signal carries the laser linewidth of about 3.3 meV.

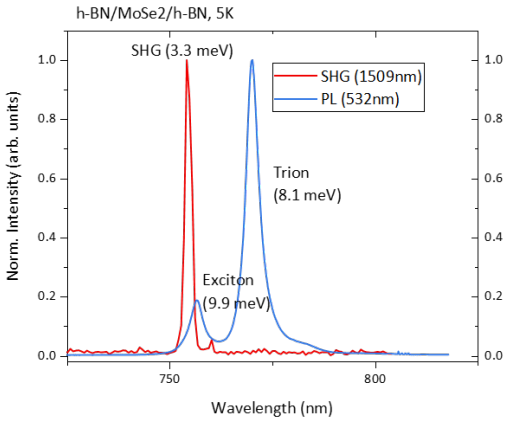

Figure A.11: Comparison of the photoluminescence (in blue) and SHG (in red) response of bare $MoSe_2$ monolayer